

PULSAR RADIO EMISSION MODULATION
IN RELATION TO
ROTATIONAL INSTABILITY

A THESIS SUBMITTED TO THE UNIVERSITY OF MANCHESTER
FOR THE DEGREE OF DOCTOR OF PHILOSOPHY
IN THE FACULTY OF ENGINEERING AND PHYSICAL SCIENCES

2012

By
Neil James Young
School of Physics and Astronomy

Contents

Abstract	13
Declaration	15
Copyright	16
Acknowledgements	17
The Author	19
1 Introduction	23
1.1 Pulsar Physics	26
1.1.1 The Pulsar Environment	26
1.1.2 Emission Models	28
1.1.3 Spin Evolution	33
1.2 Pulsar Timing	35
1.2.1 Pulse Arrival Time Measurement	36
1.2.2 The Timing Model	37
1.2.3 Timing Irregularities	39
1.3 Thesis Outline	43
2 Pulse Intensity Modulation of Radio Pulsars	45
2.1 Interstellar Scintillation	46
2.2 Drifting Subpulses	48
2.3 Microstructure and Giant Pulses	51
2.4 Mode Changes	52
2.5 Pulse Nulling	54
2.5.1 The ‘Death Valley’	58

CONTENTS

2.5.2	Magnetospheric Switching	61
2.5.3	Orbital Companions	65
2.5.4	Geometrical Models	66
3	The Emission Modulation Properties of PSR B0823+26	69
3.1	Background	70
3.2	Observations	71
3.3	Emission Modulation	72
3.4	Periodicity Analysis	80
3.4.1	Periodogram Analysis	80
3.4.2	WWZ Analysis	82
3.5	Timing Behaviour	87
3.6	Simulations	88
3.6.1	Overview	88
3.6.2	Analysis	89
3.6.3	Switching Timescale Dependency	92
3.7	Discussion	94
3.8	Conclusions	96
4	Further Investigation into the Emission Modulation Characteristics of PSR B1931+24	97
4.1	Background	98
4.2	Why look at PSR B1931+24 Again?	100
4.3	Observations	100
4.4	Emission Modulation	101
4.5	Periodicity Analysis	112
4.5.1	Periodogram Analysis	112
4.5.2	WWZ Analysis	118
4.6	Residual Fitting and Measurement of the Braking Index	121
4.7	Long-term Evolution in Spin-down Rate	125
4.8	Discussion	128
4.9	Conclusions	130
5	Radio Emission Moding and Nulling in PSR J1107-5907	133
5.1	Background	133
5.2	Observations	135

5.3	Emission Modulation	136
5.3.1	Single-pulse Emission Mode Characterisation	144
5.3.2	Pulse-energy Distributions	148
5.3.3	Fluctuation Spectra	159
5.4	Timing Analysis	163
5.5	Discussion	164
5.5.1	Nulling Statistics and Detection Probability	165
5.5.2	A RRAT connection?	167
5.5.3	What Is Driving PSR J1107–5907?	169
5.5.4	Future Prospects	171
5.6	Conclusions	172
6	The Single-pulse Characteristics of PSR B0823+26	173
6.1	Observations	173
6.2	Single-pulse Modulation Properties	174
6.2.1	Scintillation Effects	176
6.2.2	Nulling Fraction Estimation	177
6.2.3	Main-pulse and Post-cursor Component Variability	180
6.3	Discussion	188
6.4	Conclusions	189
7	Conclusions	191
7.1	PSR B0823+26	191
7.2	PSR B1931+24	192
7.3	PSR J1107–5907	193
7.4	Distinctions Between the Different Types of Nulling Pulsars	194
7.5	Future Prospects	195
A	The Energy Loss Model of PSR B1931+24	197
B	Periodicity Analysis of Astronomical Signals	201
B.1	Periodicity Analysis Basics	201
B.1.1	Time-frequency Localisation	202
B.1.2	The Wavelet Transform	203
B.2	Periodicity Analysis of Unevenly Sampled Data	207
B.2.1	Autocorrelation and Welch Periodogram Method	207

CONTENTS

B.2.2	Weighted Wavelet Z-Statistic	210
B.3	WWZ Error Analysis	211
B.3.1	Confusion Limit Estimation	211
B.3.2	Data Windowing Method	211
B.3.3	Resampling Methods	212
References		217

List of Tables

3.1	Observed and derived properties of PSR B0823+26.	70
3.2	System characteristics of observations of PSR B0823+26.	72
3.3	The observation properties for PSR B0823+26 during the continuous observing intervals.	72
3.4	The main results obtained from the flux density analysis of PSR B0823+26.	80
3.5	Median-peak WWZ values and fluctuation frequencies for the PSR B0823+26 data.	85
3.6	The properties of PSR B0823+26 obtained from timing measurements of the 153-day Analogue Filter Bank data-set.	87
4.1	The properties of PSR B1931+24.	98
4.2	System characteristics of observations of PSR B1931+24.	101
4.3	Properties of the nine data intervals chosen to characterise the correlation between the radio-on and -off emission phase durations of PSR B1931+24.	107
4.4	Peak WWZ values and fluctuation frequencies for 12 years of observation of PSR B1931+24.	121
4.5	Results from the residual fitting of PSR B1931+24 observations. .	124
4.6	Derived spin properties of PSR B1931+24 from linear regression. .	125
4.7	The linear fit parameters for the long-term spin-down rate study of PSR B1931+24.	127
5.1	Observed and derived properties of PSR J1107–5907.	134
5.2	Observation characteristics of PSR J1107–5907.	136
5.3	The system characteristics of the single-pulse observations of PSR J1107–5907.	137

LIST OF TABLES

5.4	The single-pulse observation statistics of PSR J1107–5907	144
5.5	The best-fit parameters to the pulse-energy distributions of PSR J1107–5907	154
5.6	The best-fit trial nulling fractions for observations of PSR J1107–5907	156
5.7	The predicted detection statistics for the strong mode of emission for PSR J1107–5907	167
6.1	The single-pulse observation properties of PSR B0823+26.	174
6.2	The single-pulse nulling properties of PSR B0823+26.	180

List of Figures

1.1	The distribution of pulsars in $P - \dot{P}$ space.	25
1.2	Schematic diagram depicting the co-rotating magnetosphere and wind zone of a pulsar.	27
1.3	Schematic diagram of the pulsar acceleration regions.	29
1.4	Cartoon depicting the subbeam carousel model.	31
1.5	Schematic diagram of the polar cap region in the slot gap emission model.	32
1.6	Examples of timing noise in a number of normal pulsars.	40
1.7	The timing stability of a sample of pulsars versus various physical properties.	42
2.1	Sketch depicting the thin screen model of the interstellar medium.	46
2.2	Pulse stacks showing examples of the drifting subpulse phenomenon.	49
2.3	An example of the mode changing phenomenon, as seen in the pulsar J1826–6700.	53
2.4	Examples of pulse nulling in six pulsars.	55
2.5	The distribution of radio-on fractions against mean null length for a sample of radio pulsars.	56
2.6	The distribution of pulsars in $P - B_s$ space, with overlaid lines denoting the theoretical limits on pair production.	59
2.7	The rotational frequency evolution and timing residuals of the pulsar B1931+24 over a 160-day period.	62
2.8	The variation in average pulse shape versus spin-down rate against time, for six pulsars which exhibit mode changing.	64
2.9	Schematic diagram of the pulsar magnetosphere, describing how mode changes and nulls could manifest.	65

LIST OF FIGURES

3.1	An example of the radio emission cessation behaviour of PSR B0823+26.	73
3.2	Average profiles of PSR B0823+26 during the radio-on and radio-off phases of emission.	74
3.3	The sequence of observations of PSR B0823+26 carried out over the 153-day period.	75
3.4	Three sequences of continuous observations of PSR B0823+26.	77
3.5	The emission durations of PSR B0823+26 for the radio-on and radio-off phases of emission.	78
3.6	The evolution of the pulse flux density of PSR B0823+26.	79
3.7	Welch periodogram analysis of the radio emission activity of PSR B0823+26.	81
3.8	WWZ transform of the radio emission activity of PSR B0823+26.	83
3.9	Peak fluctuation frequencies and periods from the PSR B0823+26 WWZ data.	86
3.10	Post-fit timing residuals for PSR B0823+26 from the 153-day Analogue Filter Bank data-set.	88
3.11	A comparison between the observed and simulated timing residuals of PSR B1931+24.	90
3.12	Constraints on the spin-down rate variation of PSR B0823+26 from simulations.	91
4.1	Sequence of observations of PSR B1931+24.	102
4.2	Emission phase durations for PSR B1931+24.	105
4.3	The evolution of the activity duty cycle of PSR B1931+24 over approximately 13 years of data.	106
4.4	The correlation between the radio-on and -off emission phase durations of PSR B1931+24.	108
4.5	The evolution of the flux density of PSR B1931+24.	109
4.6	Average pulse profiles of PSR B1931+24 showing the characteristics of the radio-on and -off emission.	111
4.7	The evolution in the ratio of the first peak to second peak intensities of PSR B1931+24.	112
4.8	Welch periodogram analysis of 12 years of observations of PSR B1931+24.	114

4.9	Welch periodogram analysis of the first 4-year segment of observations of PSR B1931+24.	115
4.10	Welch periodogram analysis of the second 4-year segment of observations of PSR B1931+24.	116
4.11	Welch periodogram analysis of the third 4-year segment of observations of PSR B1931+24.	117
4.12	WWZ analysis of 12 years of observations of PSR B1931+24. . . .	119
4.13	Peak WWZ fluctuation frequencies and periods for 12 years of observations of PSR B1931+24.	120
4.14	Least-squares, weighted fit to timing residuals of PSR B1931+24. . . .	122
4.15	Linear fits to the spin-down rate values of PSR B1931+24 with respect to time.	125
4.16	The timing residuals of PSR B1931+24, over approximately 80 days of data, depicting the change in rotational frequency fitting procedure.	127
4.17	A linear fit to the change in rotational frequency against radio-on phase length for PSR B1931+24.	128
5.1	The emission profiles of PSR J1107–5907.	135
5.2	Long-term emission modulation of PSR J1107–5907.	138
5.3	Emission phase durations for PSR J1107–5907.	139
5.4	An observation showing the transition timescales for the source J1107–5907.	140
5.5	Examples of the emission modulation observed in the pulsar PSR J1107–5907.	141
5.6	Dynamic spectra for three observations of PSR J1107–5907. . . .	143
5.7	Pulse intensity fluctuations with respect to pulse longitude for PSR J1107–5907.	146
5.8	The average pulse profiles of PSR J1107–5907, formed from single-pulse data.	147
5.9	Integrated pulse-energy distributions for two single-pulse observations of PSR J1107–5907.	149
5.10	Longitude-resolved pulse-energy distributions for six single-pulse observations of PSR J1107–5907.	151

LIST OF FIGURES

5.11	Best-fit pulse-energy distributions for single-pulse observations of PSR J1107–5907.	155
5.12	Residual histograms for single-pulse observations of the pulsar J1107–5907.	158
5.13	The modulation properties of PSR J1107–5907 in the strong mode of emission.	160
5.14	The modulation properties of PSR J1107–5907 in the weak mode of emission.	161
5.15	Timing residuals of PSR J1107–5907 over an ~ 7.5 -year period of observations.	164
6.1	Two single-pulse observations of PSR B0823+26.	175
6.2	The scintillation properties of PSR B0823+26.	177
6.3	Two pulse stacks of PSR B0823+26, demonstrating its single-pulse variability.	178
6.4	Integrated pulse-energy distributions for PSR B0823+26.	179
6.5	Results from the nulling fraction analysis of observations of PSR B0823+26.	181
6.6	Pulse stacks of the 1-hour, single-pulse observation of PSR B0823+26 at 1532 MHz.	183
6.7	The pulse intensity variation of PSR B0823+26.	184
6.8	The average pulse shape of PSR B0823+26 for increasing post-cursor peak-intensity.	185
6.9	Longitude-resolved pulse-energy distributions for PSR B0823+26. .	186
6.10	The subpulse modulation properties of PSR B0823+26.	187
B.1	A schematic diagram depicting the basic principle of a short-time Fourier transform.	203
B.2	Examples of the different types of wavelet functions used in wavelet analysis.	204
B.3	The local matching of a wavelet function to a time-series signal. .	205
B.4	An illustration showing the basic principles of wavelet analysis. .	206
B.5	A number of common window functions used in spectral analysis and their corresponding spectral leakage functions.	209
B.6	The basic principles of the bootstrap method.	213

The University of Manchester

ABSTRACT OF THESIS submitted by Neil James Young
for the Degree of Doctor of Philosophy and entitled
“Pulsar Radio Emission Modulation in Relation to
Rotational Instability”, March 2012.

The magnetospheric conditions responsible for radio emission in pulsars are still not clearly understood. Through studying the modulation of this emission, in relation to the rotational properties of these stars, the observer can obtain insight into the mechanism which governs the radio emission in pulsars, as well as their magnetospheric environments. Nulling pulsars are instrumental in this study due to their meta-stable configurations, which result in abrupt cessation or reactivation of their radio emission. As the observed modulation timescales in these sources vary from seconds to years, several theories have been proposed to explain their behaviour. However, no consensus has been reached on what triggers their magnetospheric reconfigurations, nor whether they are all governed by the same processes. In this work, we have studied three extreme nulling pulsars to help determine how these objects can be best classified, and what the most viable processes responsible for their behaviour could be.

Using approximately 13 years of high-cadence observations, we confirm that the prototype ‘intermittent’ pulsar, PSR B1931+24, has a variable spin-down rate which is correlated with the presence (absence) of radio emission. The spin-down rates of the pulsar, attributed to the radio-on and -off emission phases, do not exhibit any evidence for time evolution and, as such, retain a constant difference of $\sim 50\%$ throughout the 13-year data-set. We find that the radio-on and -off emission phases last approximately 8 days and 22 days on average respectively. They are also found to repeat quasi-periodically, over an average timescale of 36 days. We find no evidence for any interruptions to a given emission phase, that is the pulsar appears to switch between emission phases over long timescales (\sim days) only. Using our unprecedented data span, we find the object has an overall nulling fraction of $74 \pm 6\%$.

We use an unparalleled 153-day set of observations to show that the pulsar B0823+26 exhibits a bimodal distribution of nulling timescales, that is short nulls ($\sim 1 - 3$ pulse periods) and long nulls ($\sim 10^{2-4}$ pulse periods) that are not periodic in nature. Remarkably, the longest nulls observed in PSR B0823+26

can be as extreme as those found in rotating radio transients (RRATs). The pulsar is shown to undergo pre-ignition periods of emission bursts and nulls before transitioning to a reasonably steady radio-on phase. Through characterising the emission variability of the source in the radio-on phases, we find that the post-cursor emission component exhibits a remarkable degree of variability. We do not obtain any direct evidence for spin-down rate variation in this pulsar, but we do place an upper limit of $\lesssim 6\%$ on any change.

We also investigate the radio emission characteristics of PSR J1107–5907, and find that it exhibits a wide range of nulling timescales (i.e. seconds to many hours). Coupled with its highly irregular bright emission, these nulling properties suggest a strong link between this object and RRAT-like sources. Although the pulsar undergoes both nulls and dramatic pulse shape changes, no evidence for spin-down rate variation is obtained.

The nulling properties of the sources studied suggest a close relationship between conventional nulling pulsars, RRATs and intermittent pulsars. We find that the existing characterisation of the different types of nulling pulsars, based on their initial detection properties, is unsuitable. We also predict that, in addition to those yet undetected, a significant number of nulling objects are located in the existing known pulsar population, but have not yet been fully characterised.

Declaration

No portion of the work referred to in this thesis has been submitted in support of an application for another degree or qualification of this or any other university or other institution of learning.

Copyright

The author of this thesis (including any appendices and/or schedules to this thesis) owns certain copyright or related rights in it (the “Copyright”) and s/he has given The University of Manchester certain rights to use such Copyright, including for administrative purposes.

Copies of this thesis, either in full or in extracts and whether in hard or electronic copy, may be made only in accordance with the Copyright, Designs and Patents Act 1988 (as amended) and regulations issued under it or, where appropriate, in accordance with licensing agreements which the University has from time to time. This page must form part of any such copies made.

The ownership of certain Copyright, patents, designs, trade marks and other intellectual property (the “Intellectual Property”) and any reproductions of copyright works in the thesis, for example graphs and tables (“Reproductions”), which may be described in this thesis, may not be owned by the author and may be owned by third parties. Such Intellectual Property and Reproductions cannot and must not be made available for use without the prior written permission of the owner(s) of the relevant Intellectual Property and/or Reproductions.

Further information on the conditions under which disclosure, publication and commercialisation of this thesis, the Copyright and any Intellectual Property and/or Reproductions described in it may take place is available in the University IP Policy (see <http://www.campus.manchester.ac.uk/medialibrary/policies/intellectual-property.pdf>), in any relevant Thesis restriction declarations deposited in the University Library, The University Library’s regulations (see <http://www.manchester.ac.uk/library/aboutus/regulations>) and in The University’s policy on presentation of Theses.

Acknowledgements

Throughout the course of my PhD, I have benefited greatly from the company of many people.

First, and foremost, I would like to extend the utmost gratitude to my supervisor, Dr. Ben Stappers, whose knowledge, support and encouragement has been immensely helpful. He has always given sound advice and has shown incredible patience, even when answering my silliest questions. Thanks for everything Ben.

I thank Dr. Patrick Weltevrede and Professors Andrew Lyne and Michael Kramer for their many extremely useful discussions, and extensive feedback during the preparation of this thesis. I would also like to thank Professors Albert Zijlstra and Anvar Shukurov for their guidance on wavelets, as well as Dr. Ismaël Cognard for providing the Nançay data used in this thesis.

Many thanks to all the postdocs (Cristóbal Espinoza, Cees Bassa, Rob Ferdinand, Gemma Janssen and Roy Smits) and students (Mark Purver, Evan Keane, Sam Bates, Tom Hassall, Sotirios Sanidas, Kuo Liu, Dan Thornton, Monika Obrocka and Phrudth ‘Math’ Jaroenjittichai) in the pulsar group who have provided me with a stimulating research environment, as well as a source of knowledge and expertise which has helped me to overcome coding bugs and difficult concepts. Thanks also to several people in the department (Jen Gupta, Adam Avison, David Jones, Nadya Kunawicz, Matias Vidal, Sarah Bryan, Adam Stanier, Mark McCulloch and Matthew Penny) for providing the pleasant environment.

During my PhD, I have made some great friends who, along with old friends, have consistently provided me with humour, support and, most importantly, drinking companionship. To name but a few, I would like to thank Peter Liddle, James McNaughton, Reuben Loffman, Chris Rushton, Pete and Pearl Brunt, Damien Jeanmaire, Nichol Cunningham, Jenny Fisher, Nick Crowney, Pete Daymond, Tim Wuttig, Stephanie Martin, Karlene van Opdorp, Rossina Miller, Mel Irfan and Michael Bareford. I would particularly like to thank: Scott Lewis for

his anecdotes, Welsh-English jokes, party tricks and for generally being a funny guy; Andrey Paska for introducing me to some of my favourite music, reintroducing me to Donkey Kong, and the frustrations therein, as well as for being a great flatmate; and Liz Guzman for being so eccentric and fun.

Lastly, I would like to thank my family for their constant support and confidence in me, as well as their ability to make me laugh at the most unexpected times. I am also eternally grateful for the invaluable perspective on life which they have given me.

The Author

The author was born in April 1986 in Bolton, Greater Manchester. He studied an MPhys in Physics with Astrophysics at the University of Leeds, during which he spent half a year in Jena, Germany, for a research project. He graduated in July 2008 with a Second Class, Division i Hons. The same year he began a PhD at the Jodrell Bank Centre for Astrophysics, for which this thesis is submitted.

To my friends and family.

The diversity of the phenomena of nature is so great, and the treasures hidden in the heavens so rich, precisely in order that the human mind shall never be lacking in fresh nourishment.

Johannes Kepler, Mysterium Cosmographicum

Chapter 1

Introduction

After more than four decades of study, the basic nature of pulsars has long been confirmed, that is pulsars are rapidly rotating neutron stars (NSs) that are formed through the collapse of a massive star ($\gtrsim 8 - 20M_{\odot}$) during a supernova explosion (e.g. Glen-denning 2000). They are so dense ($1.2 - 2M_{\odot}$ within a radius of $10 - 15$ km; Janssen et al. 2008; Demorest et al. 2010; Lattimer & Prakash 2007) and highly magnetised (10^{8-15} G¹) that they represent one of the most extreme and energetic environments in the known universe. As a result, they can be used to probe physical regimes which are far beyond any achievable in a terrestrial experiment.

In 1934, Baade and Zwicky were the first to propose the idea of neutron stars, suggesting the now established fact, that their formation is indicated by a supernova event. However, it was not until 1967 that their existence was confirmed through the detection of PSR B1919+21 in an all-sky survey (Hewish et al. 1968). Since then, almost 2000 pulsars have been discovered and catalogued, allowing insight into the characteristics of the various populations of neutron stars.

Neutron stars come in a variety of flavours and are separated into a number of classes - rotation-powered pulsars (RPPs), magnetars, X-Ray Dim Isolated NSs and central compact objects (CCOs) - each of which have particular emission and rotational properties, and can be subdivided into different types (e.g. Kaspi 2010). The majority of these sources are RPPs, which are subdivided into young, normal pulsars, old recycled or millisecond pulsars (MSPs) and more extreme objects such as Rotating Radio Transients (RRATs; McLaughlin et al. 2006) and intermittent pulsars (see §2). These objects can be plotted in rotational period versus rotational period-derivative space, in the so-called $P - \dot{P}$ diagram (Fig. 1.1), which conveniently allows a distinction

¹Data taken from the ATNF pulsar catalog (Manchester et al. 2005). See also <http://www.atnf.csiro.au/research/pulsar/psrcat> for more details.

1: INTRODUCTION

to be made between their different types according to the regions they occupy. From Fig. 1.1, we see that the pulsar population comprises mainly two distinct distributions. Namely, the normal RPPs which represent the majority of the known pulsars, with $P \sim 0.5$ s and typical $\dot{P} \sim 10^{-15}$ s/s, and MSPs with periods 1.4 ms $\lesssim P \lesssim 30$ ms and typical spin-down rates $\dot{P} \sim 10^{-19}$ s/s.

It is predicted that a total of approximately 10^5 active pulsars populate the Galaxy (Keane & Kramer 2008), which are preferentially distributed along the Galactic plane (Mdzinarishvili & Melikidze 2004). In addition, they are found to have high space velocities (typically several hundred km s^{-1} ; e.g. Sun & Han 2004) due to their supernova kicks at birth (Tutukov 2005). Although they are capable of emitting across the entire electromagnetic spectrum, most of what is known about pulsars comes from observations in the radio regime. This is mainly due to the detection sensitivity of pulsar surveys at these wavelengths, which enable the discovery and coherent timing (see §1.2) of these objects. Since the launch of the *Fermi Gamma-ray Space Telescope* in June 2008, however, this observational bias has slowly decreased; *Fermi* has facilitated the discovery of over 80 γ -ray pulsars, increasing the known population by more than an order of magnitude (Abdo et al. 2010; Takata et al. 2012). These recent discoveries have provided new insight into the magnetospheric physics, energetics and evolution of Galactic neutron stars (e.g. Abdo et al. 2010; Venter et al. 2012). With the expectation of many more γ -ray pulsars to be discovered in the coming years (e.g. Watters & Romani 2011), it is very likely that high-energy studies of pulsars will help to provide a better understanding of the nature of these fascinating objects.

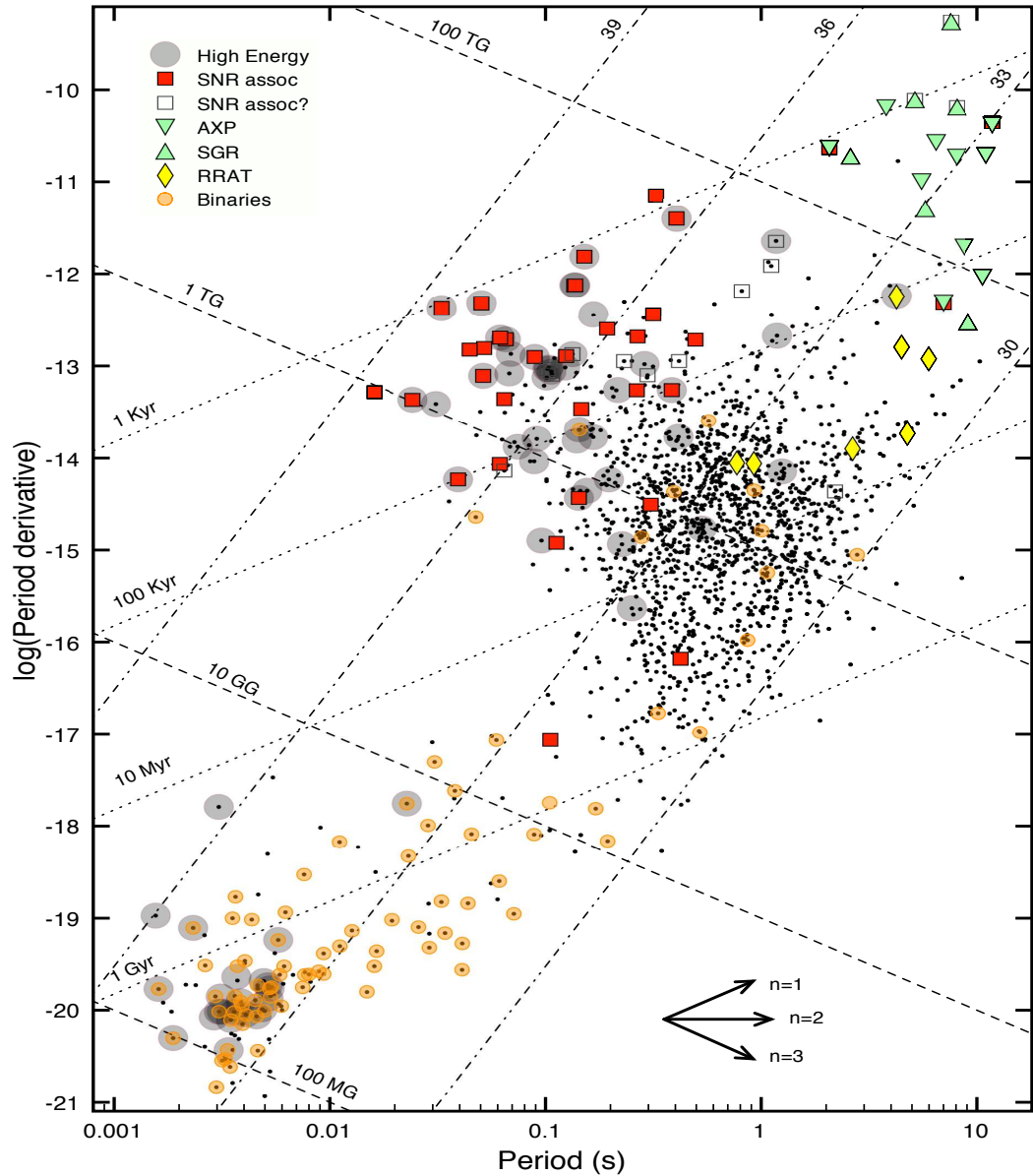


Figure 1.1: The distribution of pulsars in $P - \dot{P}$ space (figure provided by Cristóbal Espinoza). The majority of normal pulsars are found to cluster around the central region i.e. $0.1 \text{ s} \lesssim P \lesssim 3 \text{ s}$, $10^{-17} \lesssim \dot{P} \lesssim 10^{-13}$. The millisecond pulsar population is preferentially distributed towards the lower left corner of the plot, with pulse periods as low as 1.4 ms. Lines of characteristic age (*dotted lines*), magnetic field strength (*dashed lines*) and spin-down luminosity (*dot-dashed lines*) are also plotted. Pulsars move through $P - \dot{P}$ space according to their braking indices, as shown by the arrows in the lower right corner. (We refer to §1.1.3 for the definitions of these parameters.)

1.1 Pulsar Physics

It is safe to say that pulsars are still relatively poorly understood, even after more than 43 years of research. Major difficulties arise in trying to understand not only the composition of neutron stars (due to their immense density), but also their electromagnetic field configurations (given their extreme magnitudes) and, hence, the structure of their magnetospheres and mechanism(s) responsible for emission. Despite these difficulties, sufficient progress has been made to form a basic model of a pulsar which will be discussed below.

1.1.1 The Pulsar Environment

Pulsars are thought to consist of two main components: a crystalline solid crust (1 km thick, made up primarily of iron nuclei and free degenerate electrons) and a superfluid liquid interior of free neutrons (e.g. Lyne & Smith 2006). They possess a strong dipolar magnetic field ($B = 10^{8-15}$ G), which is formed from the amplification and reconfiguration of their progenitor polar fields during the collapse phase². Pulsars are threaded by this magnetic field which, subsequently, tightly couples their superfluid interior and rigid crust.

A pulsar is most commonly modelled as an axisymmetric rotator based on the successful Goldreich-Julian model (Goldreich & Julian 1969). In this model, the simplest case of a rotating NS in which the magnetic dipole moment is aligned with the rotation axis is assumed. The expanding shell of the initial supernova outburst is proposed to create an interstellar cavity, which spans a distance D and contains the remnant NS that rotates with an angular velocity Ω . The exterior of the neutron star is separated into distinct zones as shown in Fig. 1.2.

The *light cylinder* encloses the *near zone* of the neutron star, which comprises the *co-rotating magnetosphere*, and is defined as

$$R_{\text{LC}} = \frac{c}{\Omega} = \frac{cP}{2\pi}, \quad (1.1)$$

which is the maximum distance out to which particles can co-rotate with the neutron star at a velocity equal to the speed of light c . The *wind zone* encloses the *near zone* and merges into the *boundary zone* at $r \sim \frac{D}{10}$. The boundary zone is considered to encompass the outer 90 % of the supernova cavity and, therefore, makes up most of the

²Magnetic flux is conserved during the collapse of the supernova (SN) progenitor, which enables the parent polar field to be amplified. Differential rotation also acts to amplify and reconfigure this magnetic field, which is able to permeate the NS through stratification of magnetic flux due to magnetic buoyancy (Spruit 2008).

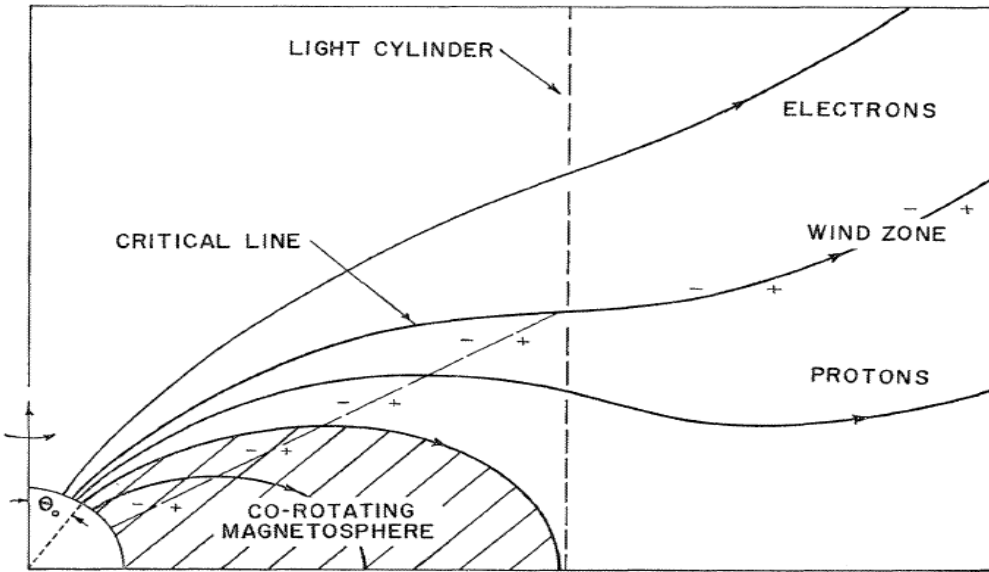


Figure 1.2: Schematic diagram depicting the *co-rotating magnetosphere* and the *wind zone*, with the star lower left (figure taken from Goldreich & Julian (1969)).

resolvable extent of young supernova remnants.

The rotation of the neutron star (essentially a magnetic dipole) is proposed to induce electromagnetic forces which extract charged particles from the stellar surface. Particles enclosed in the closed field lines subsequently co-rotate with the motion of the B field and, thus, comprise the co-rotating magnetosphere (a.k.a. the closed zone). Particles are allowed to stream out along the open magnetic field lines, which pass through the light cylinder (a.k.a. the open zone). These escaping particles are primarily thought to take the form of the observable radio emission and pulsar wind.

The electric potential on the surface is predicted to be highest at the equator and to decrease towards the poles, creating charge separation at the *critical line* (a.k.a the null surface, where the charge density $\rho = 0$). In order to conserve charge, electrons are assumed to stream out along the higher latitude lines (*electron lines*), and protons along the lower open lines (*proton lines*), until they reach the boundary zone where the Lorentz force and influence of the magnetic field diminishes. Subsequent acceleration of the escaping charges in the boundary zone creates an electromagnetically driven wind which propagates into the interstellar gas surrounding the supernova shell or pulsar wind nebula (if the shell has been disassociated by high energy radiation from the central neutron star).

1.1.2 Emission Models

Despite over four decades of research, no fully consistent model of pulsar emission has emerged. This is primarily because of the difficulties involved in modelling the structure of the pulsar magnetosphere, which has seen recent new impetus (e.g. Contopoulos et al. 1999; Spitkovsky 2006; Timokhin 2006; Kalapotharakos & Contopoulos 2009; Kalapotharakos et al. 2011), as well as the complexity of emission phenomena (e.g. subpulse drift, mode-changing and nulling; Weltevrede et al. 2006; Wang et al. 2007; Lyne et al. 2010; see also §2) which has to be explained and the broadband nature of the emission mechanism (from the radio to the multi-GeV γ -ray regime). The Goldreich-Julian model is seen as a simple visualisation of a pulsar and its magnetosphere and, as such, does not lend itself to a realistic emission model (e.g. an aligned rotator does not pulsate; see also Michel 1982; Beskin et al. 1993; Meyer & Lauroesch 1999; Timokhin 2006 for several other reasons). However, it does demonstrate some basic principles which are useful to understand the structure of the pulsar magnetosphere. Therefore, the Goldreich-Julian model has been used to form the basis of models which incorporate more realistic assumptions (e.g. oblique rotator models; Ostriker & Gunn 1969; Spitkovsky 2006; Kalapotharakos & Contopoulos 2009).

Most current models of global pulsar magnetospheres involve either an inclined vacuum dipole (Deutsch 1955), or ‘force-free’ electrodynamics (FFE)³ for both aligned (e.g. Contopoulos et al. 1999; Timokhin 2006; Komissarov 2006) and oblique rotators (e.g. Spitkovsky 2006; Kalapotharakos & Contopoulos 2009). While the vacuum dipole model has a quantitative and analytical solution and, therefore, can be used to provide a framework for the determination of pulsar properties, it does not offer a realistic description of pulsar emission (a vacuum cannot produce a plasma flow; see e.g. Li et al. 2012a). The force-free model, on the other hand, is more readily reconciled with a realistic pulsar magnetosphere (due to the abundance of plasma), but does not yet have an analytic solution (e.g. Kalapotharakos et al. 2011). Furthermore, it is uncertain how currents and electric fields are generated and sustained in this model (Viganò et al. 2011) and, as such, how particle acceleration would occur (Kalapotharakos et al. 2011). As a result, it has been suggested that a real magnetosphere, that is one which facilitates particle acceleration, will be between the vacuum limit and the ideal magnetohydrodynamic (MHD) force-free limit i.e. containing ‘resistive plasma’ (Kalapotharakos et al. 2011; Wada & Shibata 2011; Li et al. 2012a,b). However, more

³FFE assumes the abundance of infinitely conducting plasma, which shorts out all accelerating electric fields so that the ideal MHD condition $\mathbf{E} \cdot \mathbf{B} = 0$ (see e.g. Eqn. 3 of Gruzinov (1999)) holds everywhere. In this regime, the structure of the magnetosphere is determined by the balance of electromagnetic forces in the absence of plasma inertia and pressure terms (e.g. Gruzinov 1999; Komissarov 2002; Spitkovsky 2006; Kalapotharakos et al. 2011).

work is required in this field before the macrophysics of the global magnetosphere can be consolidated with the microphysics of particle acceleration and radiation emission.

Despite these difficulties, some consensus has been reached on the nature of the emission regions. Namely, it is generally accepted that particle acceleration, and subsequent photon emission, occurs in charge-depleted regions (a.k.a. ‘gaps’) in the open zone of the magnetosphere, where particles are able to escape the light cylinder. However, it is unclear where exactly these gap regions should preferentially be located. Correspondingly, emission models are primarily differentiated by the location of the gap regions, of which three are favoured in the literature i.e. the *polar gap*, *slot gap* and *outer gap* regions (as shown in Fig. 1.3).

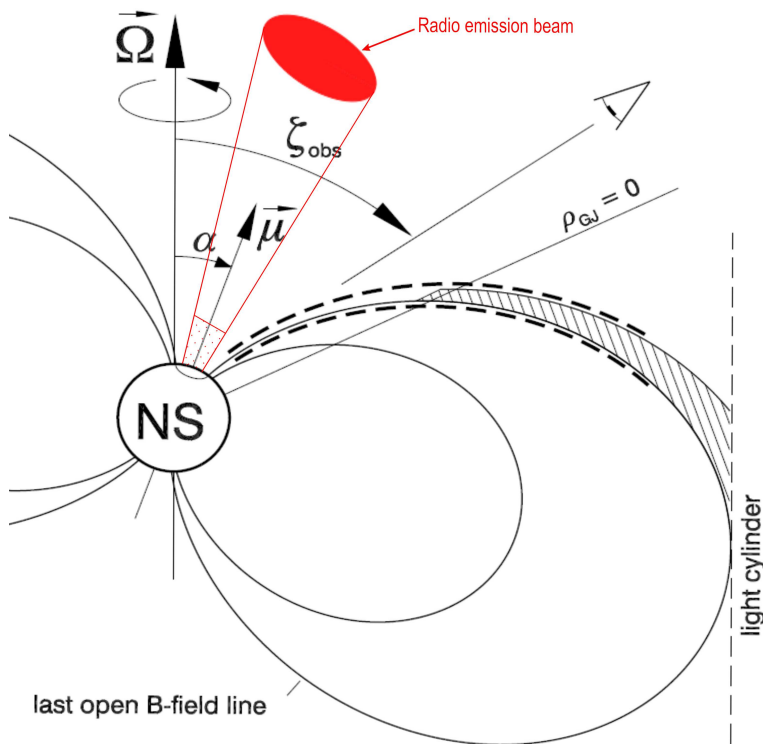


Figure 1.3: Model depiction of a rotating neutron star, its magnetosphere and acceleration regions (*not to scale*; adapted from Dyks & Rudak (2003)). The conventional polar gap is shown (*dotted line area*) and extends from the polar cap surface up to about 10^4 cm, from above which coherent radio emission is expected to arise ($\sim 10^2$ km; see e.g. Cordes 1978). The slot-gap (*dashed lines*) is confined to the surface of the last open field lines, and extends from the polar cap to the light cylinder. The outer gap is shown (*shaded area*), extending from the null surface ($\rho = 0$) to the light cylinder. The angle between the magnetic and rotational axes is denoted by α . The magnetic moment is denoted by μ and ζ_{obs} is the angle between the rotational axis of the NS and the observer’s line-of-sight (i.e. the impact angle).

1: INTRODUCTION

The polar gap (PG) model is widely discussed in the literature, as it is most commonly used to describe the coherent radio emission observed from pulsars. In this model, a vacuum gap is proposed to build up from the polar cap surface up to $\sim 10^4$ cm, due to the outflow of charged particles from the stellar surface along the open field lines (Ruderman & Sutherland 1975). Particles extracted from the surface are subsequently accelerated by the large ($\sim 10^{13-15}$ V) residual electric field which develops, enabling them to reach relativistic energies ($\gamma \sim 10^{6-7}$; see e.g. Arons (1983) and references therein). As they move along the curved magnetic field lines, these particles produce γ -ray photons via synchro-curvature emission (Ruderman & Sutherland 1975) and inverse Compton Scattering (ICS) on lower-energy photons (Daugherty & Harding 1986). These γ -ray photons interact with the strong magnetic field and create pairs (e^\pm) within the gap which, subsequently, results in an avalanche of less energetic and $\sim 10^{3-4}$ times denser secondary pair plasma that is responsible for the coherent radio emission (e.g. Lyne & Smith 2006). It is important to note, however, that the gap region is unstable against the avalanche growth of pairs and continually ‘breaks-down’ over short timescales (\lesssim ms; Ruderman & Sutherland 1975); pair cascades in the gap discharge the large potential drop through a group of short-lived plasma columns called ‘sparks’ (Ruderman & Sutherland 1975; Cheng & Ruderman 1977; Beskin 1982; Filippenko & Radhakrishnan 1982) which, subsequently, provide the necessary return current to the stellar surface to close the circuit (Ruderman & Sutherland 1975). In most models of pulsar radio emission, these sparks are associated with the *subbeam* structure of the overall flux tube of the open field lines and, therefore, are expected to rotate slowly about the magnetic pole (like a ‘carousel’) to account for subpulse modulation (e.g. Gil & Sendyk 2000; Deshpande & Rankin 2001; see also Fig. 1.4). As the pulsar rotates, the observer samples the subbeam structure of the emission beam and detects a pulse each time the beam crosses the line-of-sight (LOS) each rotation.

While the polar gap model naturally accounts for the coherent radio emission observed in pulsars⁴, it does not present a favourable scenario for high-energy emission (i.e. optical, X-ray and γ -ray). In the polar gap model, high-energy emission is proposed to come from near the neutron star surface ($\lesssim 1 - 2$ stellar radii; e.g. Ruderman & Sutherland 1975; Daugherty & Harding 1996), where the maximum energy of γ -ray photons is restricted by the magnetic field strength; the rate of magnetic-pair creation increases with magnetic field strength and, therefore, is greatest in the polar gap region which causes attenuation in the maximum photon energy that can be achieved. As a result, a hard spectral cut-off is expected in the polar gap emission model (Baring 2004; Lee et al. 2010). This theoretical argument is supported by the recent detection

⁴See §2, however, for a discussion on how this model can fail in extreme cases.

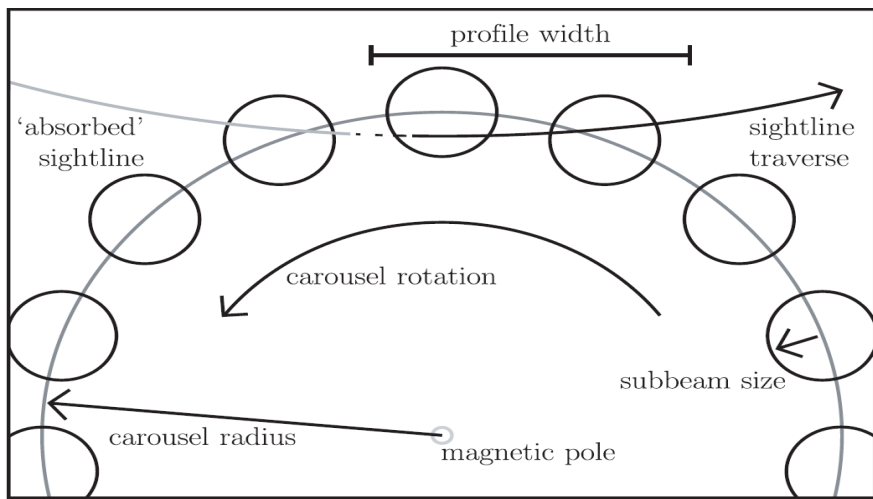


Figure 1.4: Cartoon showing the proposed geometry of a subbeam carousel (figure taken from van Leeuwen et al. (2003)). The observer samples radio emission through several *subbeams* and, therefore, obtains a radio pulse profile according to their morphology.

of pulsed emission at a maximum energy above a few GeV, which is inconsistent with the polar gap model (Abdo et al. 2010).

As such, high-energy emission has conventionally been proposed to occur in the outer gap (OG) of the magnetosphere, near the edge of the light cylinder (see Fig. 1.3), where plasma no longer co-rotates with the magnetosphere. Here, charge-depleted regions are thought to develop due to global current flows in the magnetosphere (Cheng et al. 1986a). Similar to at the polar gap, particles are electrostatically accelerated to high Lorentz factors which, in turn, radiate photon emission via the synchro-curvature and ICS processes (Cheng et al. 1986a,b; Hirotani 2008). As the magnetic field strength is weaker towards the light cylinder, higher energy emission is permitted in this region and is allowed to escape the magnetosphere, towards an observer on Earth.

In addition to the outer gap model, the slot gap (SG, or two-pole caustic) model has been proposed to explain the high-energy emission in pulsars. This model is an extension of the polar gap model, in so far that an additional charge-depleted region is proposed to exist between the pair plasma, produced from the pair cascades above the polar cap (*pair formation front*), and the last open field lines (*outer boundary*). Charge depletion occurs in this region due to the curvature of the pair formation front; the acceleration of electrons is thought to be insufficient for pair production at low altitudes and, subsequently, leaves a thin vacuum gap around the pair plasma column (Arons & Scharlemann 1979; Muslimov & Harding 2003, 2004; see also Fig. 1.5). Although slower acceleration is proposed to occur in the SG, it is thought to extend up to very

1: INTRODUCTION

high altitudes (i.e. towards the light cylinder) due to relativistic frame-dragging and geometrical screening of the electric field. This prolonged acceleration facilitates high-energy curvature emission up to several (or more) NS radii, which results in a hollow-cone beam of high-energy emission above the interior edge of the slot gap (Muslimov & Harding 2003; see also Fig. 1.5).

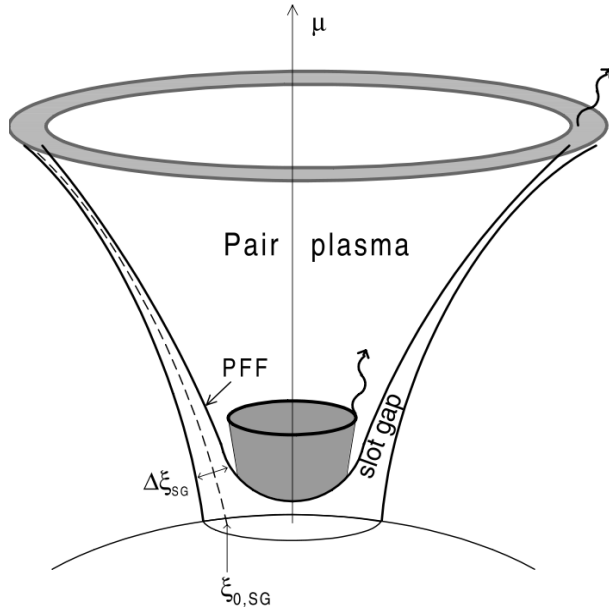


Figure 1.5: Schematic diagram illustrating the geometry of the polar cap region in the slot gap model (figure taken from Muslimov & Harding (2003)). The pair formation front is shown above the polar cap, which asymptotically approaches the outer boundary of the open field line region (where the parallel electric field component $E_{\parallel} = 0$) at high altitude. The slot gap arises between the pair plasma and the outer boundary. High energy emission at high altitudes results in a broad hollow-cone beam above the interior of the slot gap. ζ_{SG} is the slot gap thickness, $\zeta_{0,\text{SG}}$ is the central colatitude of the slot gap and μ is the magnetic moment of the neutron star.

Given the multiplicity in the possible high-energy emission models, it is natural to try to determine the most viable, based on their predictions. Recent observations with *Fermi*, however, suggest that both the SG and OG models can reproduce the emission properties (i.e. beaming fractions, light curves and spectra) of the observed γ -ray pulsar population (e.g. Watters et al. 2009; Abdo et al. 2010). Therefore, there is some ambiguity as to which emission model takes precedence⁵. This is further complicated by the recent discovery of phase alignment in the radio and γ -ray light curves of a select number of MSPs, which cannot be explained in the context of these models (e.g.

⁵Despite some preference towards the SG model in the Abdo et al. (2010) results, a greater observation sample is required to infer a significant correlation.

Abdo et al. 2010; Guillemot et al. 2012; Venter et al. 2012); phase alignment implies the co-location of radio and high-energy emission which is not readily explained by the OG and SG models. This suggests that a number of different emission mechanisms may be in operation in the pulsar population (e.g. Venter et al. 2012).

Despite the difficulties involved in determining a definitive (or population wide) high-energy emission model, significant progress has been made in the γ -ray regime thanks to *Fermi* (see e.g. Abdo et al. 2010). We now know that high-energy emission is associated with the outer magnetosphere in the majority of energetic pulsars, and that the γ -ray luminosity of such objects constitutes a large fraction of their spin-down luminosity (\dot{E} , see §1.1.3). We also find that approximately half of the Galactic birthrate of neutron stars can be attributed to γ -ray-selected pulsars i.e. radio-quiet or γ -ray loud pulsars. This indicates that observations of pulsars in the high-energy regime are imperative to not only improving our understanding of the magnetospheric physics and evolution of pulsars, but also in reducing the observational bias on their demographics. With continued observations of these objects using *Fermi*, coupled with the development of new more sensitive radio instruments such as LOFAR and the Square Kilometre Array (SKA)⁶, as well as more realistic magnetospheric modelling, we can expect significant progress in this field in the coming years.

1.1.3 Spin Evolution

The rotational periods of pulsars are observed to increase with time due to the loss of rotational kinetic energy. Only a very small amount ($\sim 10^{-6} - 10^{-4}$; Kramer 2009) of the total energy budget from this spin-down is actually converted into radio emission. In fact, the majority of the rotational energy is converted into magnetic dipole radiation and a pulsar wind (in the form of low frequency electromagnetic waves), as well as some high-energy radiation (Lyne et al. 1995; Abdo et al. 2010). As a consequence, the electromagnetic torque which is generated at the polar caps opposes the rotation of the neutron star and, thus, causes it to decelerate as it spins down (Harding et al. 1999). The rate of increase of $\dot{P} = \frac{dP}{dt}$ can be related to the rate of energy loss by

$$\dot{E} \equiv -\frac{dE_{\text{rot}}}{dt} = -\frac{d}{dt} \left(\frac{1}{2} I \Omega^2 \right) = -I \Omega \dot{\Omega}, \quad (1.2)$$

where $\Omega = 2\pi/P$ is the rotational angular frequency, I the moment of inertia and \dot{E} is defined as the *spin-down luminosity* or total power output available from rotation

⁶Phase 1 science operations with the SKA are projected to commence in 2020, with full operation of the telescope proposed in 2024. See also <http://www.skatelescope.org/about/project/> for more details.

1: INTRODUCTION

(e.g. Lorimer & Kramer 2005). Relating \dot{E} to the magnetic dipole radiation power (e.g. Jackson 1962)

$$\dot{E}_{\text{dipole}} = \frac{2}{3c^3} |\mu|^2 \Omega^4 \sin^2 \alpha, \quad (1.3)$$

the expected evolution of the rotational angular frequency can be derived

$$\dot{\Omega} = -\frac{2|\mu|^2 \sin^2 \alpha}{3Ic^3} \Omega^3. \quad (1.4)$$

Here α is the angle between the rotation and magnetic axes and μ is the magnetic dipole moment. This relationship can also be expressed as a general power law

$$\dot{\Omega} = -\kappa \Omega^n, \quad (1.5)$$

where n is the braking index, which is 3 for pure magnetodipole braking, and κ is a constant.

The spin-down of a pulsar is largely a function of the surface magnetic field strength B_s (e.g. Lorimer & Kramer 2005). From Jackson (1962), the magnetic moment is related to the magnetic field strength according to

$$B \propto \frac{|\mu|}{R^3}. \quad (1.6)$$

Through rearrangement of Eqn. 1.4 and assuming that a pulsar is an orthogonal rotator (i.e. $\alpha = 90^\circ$) with a radius $R = 10$ km, and moment of inertia $I = 10^{38}$ kg m⁻², the spin evolution \dot{P} of a pulsar can be related to the minimum B_s ⁷ as follows

$$B_s = \sqrt{\frac{3Ic^3 P \dot{P}}{8\pi^2 R^6 \sin^2 \alpha}} = 3.2 \times 10^{19} \sqrt{P \dot{P}} \text{ Gauss.} \quad (1.7)$$

Assuming a high angular velocity at birth, Ω_i , integration of Eqn. 1.5 gives a relation between Ω , $\dot{\Omega}$ and the time interval t since the pulsar was rotating at Ω_i (i.e. the age of the pulsar):

$$t = -\frac{\Omega}{(n-1)\dot{\Omega}} \left[1 - \left(\frac{\Omega}{\Omega_i} \right)^{n-1} \right]. \quad (1.8)$$

Although we do not know Ω_i , we can approximate a ‘characteristic age’ τ provided that $n > 1$ and $\Omega_i \gg \Omega$:

$$\tau = -\frac{1}{n-1} \frac{\Omega}{\dot{\Omega}} = \frac{1}{n-1} \frac{P}{\dot{P}}. \quad (1.9)$$

⁷The field strength at the magnetic equator (Eqn. 1.6) is half that at the poles, which has a more dominant role in the physics of the magnetosphere (Shapiro & Teukolsky 1983; Lyne & Smith 2006).

The accepted definition for the characteristic age of a pulsar is $\tau = P/2\dot{P}$, assuming that its spin-down is governed solely by pure magnetic dipole braking (i.e. $n = 3$; see Eqn. 1.4). However, this only serves to provide an upper limit on the actual age of a pulsar due to the idealisations; it is possible that $n \neq 3$ and (or) the spin-period of a pulsar is not far from its initial value.

Through differentiation of Eqn. 1.5, using $\nu = P^{-1}$, and measurement of a second spin derivative $\ddot{\nu}$ (Taylor & Manchester 1977), the value for n can be determined:

$$n = \frac{\nu\ddot{\nu}}{\dot{\nu}^2}. \quad (1.10)$$

When this quantity is determined accurately, we can derive important information about how a pulsar undergoes its energy loss i.e. whether or not the pulsar spin-down is dominated by magnetic dipole braking. Measurement of $n \neq 3$ has strong implications on the nature of a pulsar and its energy loss. For example, deviations from pure magnetic dipole spin-down can imply the presence of additional torques by a particle outflow or wind (e.g. Xu & Qiao 2001; Wu et al. 2003), changes in inclination angle (e.g. Blandford & Romani 1988) or magnetic field configuration (e.g. Chen & Li 2006; Geppert & Rheinhardt 2002; Ruderman 2005), as well as field reconnection processes in the pulsar magnetosphere (e.g. Contopoulos 2007).

Unfortunately, however, accurate determination of a braking index is notoriously hard to achieve; only 12 out of ~ 2000 pulsars have significant measured braking indices (Lyne et al. 1993, 1996; Livingstone et al. 2007; Chukwude et al. 2010; Weltevrede et al. 2011; Espinoza et al. 2011). For the vast majority of pulsars, this quantity is dominated by the effect of timing noise and (or) glitch events which contaminate $\ddot{\nu}$ attributed to pure magneto-dipole radiation, or some other systematic rotational energy loss (Hobbs et al. 2010; see also §1.2.3).

1.2 Pulsar Timing

A remarkable amount of information about pulsars can be acquired from timing measurements of their radio pulses. This includes insight into the emission and rotational properties of these objects, accurate position measurements, companion identification and information about the composition of the interstellar medium (ISM) traversed by the pulses. Although the concept of pulsar timing is simple, we shall see that its implementation is by no means trivial.

1.2.1 Pulse Arrival Time Measurement

As a pulsar acts like a lighthouse, radio pulses are (generally) coincident with every rotation⁸. This enables an observer to track their rotation over time. Due to their short rotational periods, radio emission variability and low flux densities⁹, very high sensitivity receivers and sophisticated backends are required to process their radio signals so that accurate timing measurements can be obtained. Crucially, this hardware is used to amplify incoming signals and, in combination with software, mitigate the effect of radio frequency interference (RFI) and compress data, so that high-sensitivity data suitable for storage and further processing can be obtained (see e.g. Lorimer & Kramer (2005) for more details on observations).

Once these initial steps have been performed, pulsar signals are required to be corrected for the effect of interstellar dispersion so that accurate arrival times can be determined. During their transit through the ISM, pulsar signals are refracted due to their frequency dependent phase velocity which, in turn, results in frequency dispersion of their arrival times i.e. a time delay (Δt) which increases with decreasing observing frequency (ν) and scales as $\Delta t \propto \text{DM} \nu^{-2}$ (where the dispersion measure $\text{DM} = \int_0^L n_e dl$; e.g. Lyne & Smith 2006). To correct for this effect, i.e. de-disperse the data, the observing bandwidth is split into a number of frequency channels which have an appropriate time delay applied to them (e.g. Lorimer & Kramer 2005).

As accurate pulsar timing requires very high measurement precision, which depends mainly on the signal-to-noise ratio (SNR) of an observed profile, a time-of-arrival (TOA) is usually defined as the arrival time of a fiducial point on an *integrated profile* (formed from the coherent addition of several hundred or even thousand pulses) with respect to the start-point (mid-point) of an observation. A TOA is then determined by cross-correlating an observed profile with a high SNR template¹⁰ at a given observing frequency, i.e. the time shift between a template and profile, relative to the start time (mid-point) of an observation (e.g. Lorimer & Kramer 2005).

The uncertainty in a TOA measurement, σ_{TOA} , is given by the ratio of the pulse width W to the profile SNR (Lorimer & Kramer 2005) which scales as:

$$\sigma_{\text{TOA}} \simeq \frac{W}{\text{SNR}} \propto \frac{S_{\text{sys}}}{\sqrt{t_{\text{obs}} \Delta \nu}} \times \frac{P \delta^{3/2}}{S_{\text{mean}}}. \quad (1.11)$$

⁸In §2.5 we will discuss various phenomena which result in the cessation of radio pulses.

⁹Measured flux densities in the ATNF pulsar catalog (Manchester et al. 2005) vary between 6 μJy and 1.1 Jy at 1400 MHz (1 Jy $\equiv 10^{-26} \text{ W m}^{-2} \text{ Hz}^{-1}$).

¹⁰Profile templates are usually formed from the addition of prior observations, which ideally have very high SNR and may also be smoothed to reduce noise. Alternatively, analytic templates can be used to represent ‘ideal’ profiles, which are formed typically from the sum of Gaussian or von Mises functions to minimise systematic noise (Purver 2010).

Here, S_{sys} is the equivalent system flux density, t_{obs} is the integration time, $\Delta\nu$ is the observing bandwidth, P is the pulse period, $\delta = \frac{W}{P}$ is the pulse duty cycle and S_{mean} is the mean flux density of the source. Consequently, the greatest timing precision is obtained from observations of short-period pulsars with large flux densities and narrow pulses (i.e. small duty cycles) using sensitive wide-band systems (low S_{sys} and high $\Delta\nu$) (Lorimer & Kramer 2005).

1.2.2 The Timing Model

Due to the Earth's rotation and orbital motion around the Sun, an observatory on Earth experiences acceleration with respect to a pulsar and therefore is not an inertial frame. To a good approximation, the solar system centre-of-mass (barycentre) can be considered to be an inertial frame of reference (Backer & Hellings 1986). Therefore, topocentric TOAs (i.e. arrival times measured at Earth) are transformed to Barycentric Dynamical Time (TDB) in order to ascertain rotational information about a pulsar. The conversion is summarised as the difference between barycentric (t_B) and topocentric (t_{topo}) TOAs:

$$\Delta t = t_B - t_{\text{topo}} = \Delta_{\text{corr}} - \Delta_{\text{DM}} + \Delta_{R\odot} + \Delta_{S\odot} + \Delta_{E\odot}. \quad (1.12)$$

where Δ_{corr} is a clock correction, Δ_{DM} is a dispersion correction, $\Delta_{R\odot}$ is the Römer delay, $\Delta_{S\odot}$ is the Shapiro delay and $\Delta_{E\odot}$ is the Einstein delay. The clock correction term incorporates variations in the observatory time standard with respect to idealised topocentric time i.e. Terrestrial Time (TT)¹¹. TOAs are transformed into the equivalent time that would be observed at infinite frequency, via the term Δ_{DM} , in order to account for dispersive delays due to the ISM (e.g. Lorimer 2008; see also §1.2.1). $\Delta_{R\odot}$ corrects for the light travel time between an observatory and the barycentre. $\Delta_{S\odot}$ accounts for the delay due to the curvature of space-time (Shapiro 1964) and $\Delta_{E\odot}$ describes the contributions due to time dilation and gravitational redshift, which result from the influence of other bodies in the solar system (e.g. Lorimer & Kramer 2005).

Once TOAs have been converted to TDB, we can use a Taylor expansion to model

¹¹TOAs are obtained using an observatory clock (e.g. a hydrogen maser), which is synchronised with the global positioning of satellites (GPS), and are converted to Universal Coordinated Time (UTC) (Backer & Hellings 1986). However, as the rotation of the Earth is not uniform, UTC is offset from International Atomic Time (TAI) by leap seconds to keep it close to mean solar time. Once these leap seconds are removed, timing measurements can be obtained in a smoothly running timescale of TAI. This is analogous to Terrestrial Time (TT), TT = TAI + 32.184 s, which represents the time kept by an ideal atomic clock at the mean sea-level of the Earth (Lorimer & Kramer 2005).

the time evolution in spin-frequency (ν) via

$$\nu(t) = \nu_0 + \dot{\nu}_0(t - t_0) + \frac{1}{2}\ddot{\nu}_0(t - t_0)^2 + \dots, \quad (1.13)$$

where t_0 is a reference epoch (in TDB), $\nu_0 = \nu(t_0)$, $\dot{\nu}_0 = \dot{\nu}(t_0)$ and $\ddot{\nu}_0 = \ddot{\nu}(t_0)$ (Manchester & Taylor 1977). The parameters ν , $\dot{\nu}$ and $\ddot{\nu}$ are related to the pulsar spin-down mechanism. However, $\ddot{\nu}$ is usually too small to be measured apart from in the very young pulsars, which have large spin derivatives and low timing noise activity (Lyne et al. 1995; Hobbs et al. 2006; see also §1.2.3).

As the rotational frequency of a pulsar ν is the rate of change of pulse number N , we can use a similar Taylor expansion to model the evolution in N and, subsequently, construct a timing model:

$$N = N_0 + \nu_0(t - t_0) + \frac{1}{2}\dot{\nu}(t - t_0)^2 + \frac{1}{6}\ddot{\nu}(t - t_0)^3 + \dots, \quad (1.14)$$

where N_0 is the initial pulse number at t_0 . For a well defined $\dot{\nu}$, N is expected to be an integer at an observed TOA if t_0 coincides with the arrival of a pulse (e.g. Lorimer & Kramer 2005).

In order to construct a timing model, we first have to estimate the spin (for example ν and $\dot{\nu}$) and astrometric parameters (i.e. position, proper motion and parallax¹², which are incorporated in Δ_{R_\odot} and Δ_{S_\odot}) of a pulsar which are not known a priori to high precision. For binary pulsar systems (e.g. MSPs), we also need to model extra Römer, Shapiro and Einstein delays due to the additional motion of a pulsar as it orbits the companion centre-of-mass e.g. (Lorimer & Kramer 2005). It naturally follows that we can compare the observed pulse numbers with those calculated using our model, whose differences are represented in terms of arrival time i.e. ‘timing residuals’ ($\text{TOA}_{\text{obs}} - \text{TOA}_{\text{pred}}$). Least-squares fitting is then employed to determine more accurate model parameters, by matching measured arrival times to pulse numbers, through minimising the expression

$$\chi^2 = \sum_i \left(\frac{N(t_i) - n_i}{\sigma_i} \right)^2. \quad (1.15)$$

Here, $N(t_i)$ describes the model pulse number at a measured arrival time t_i , which n_i is the nearest integer to, and σ_i is the uncertainty in the TOA in units of pulse number.

After the accumulation of TOAs and iterating over fits, initially for period and period-derivative for isolated pulsars, a model can be refined to obtain phase connection between TOAs (a.k.a. a ‘timing solution’). Additional systematic trends not

¹²Typically, proper motion and parallax terms are only required to be incorporated into a timing model after a year of observations, when their effect becomes measurable.

incorporated into the initial model can also be eliminated by adding additional parameters.

1.2.3 Timing Irregularities

Ideally, the application of a timing model should result in uncorrelated timing residuals which have zero mean and a Gaussian scatter that is dominated by instrumental uncertainties (Hobbs et al. 2010). In practice, this requires a very good description of the astrometric, rotational and binary (if necessary) parameters of a pulsar. For the most part, pulsars are incredibly stable rotators, whose emission times can be modelled to high precision¹³. However, the residuals of many pulsars exhibit erratic behavioural features distinguishable from this idealistic case, generically coming to be known as ‘timing noise and glitches’ (Lyne et al. 1995; Hobbs et al. 2006).

Pulsar timing noise is identified as low frequency oscillations in timing residuals, which are not introduced by observing systems or data processing. Therefore, noise features in timing residuals are interpreted as real, physical processes in a neutron star and (or) its environment¹⁴. Timing noise cannot be modelled by continuous, random walk processes in pulse phase, frequency or spin-down rate relative to the general slow-down model (Eqn. 1.14). Rather, timing noise is found to manifest in a large number of pulsars due to (quasi-)periodic oscillation between typically two spin-down rates (Hobbs et al. 2010; Lyne et al. 2010; see also §2.5.2 for more details). The timescales of these oscillations vary dramatically between pulsars (i.e. days to years) and, subsequently, result in timing residual features which differ according to the time-span of observations; systematic features become more prominent as more data is obtained (Hobbs et al. 2010). However, it is not clear exactly as to why and how these variations in spin-down rate occur (see §2.5.2 for an overview of the theory). Figure 1.6 shows some examples of the various manifestations of timing noise in residuals.

As timing residuals are generally found to be dominated by a cubic term, which corresponds to a period or frequency second derivative, the measurement of $\ddot{\nu}$ usually indicates the prevalence of timing noise (Arzoumanian et al. 1994; Lyne 1999). The Δ_8 parameter relies on this assumption and is used to estimate the cumulative phase contributed by timing noise over a time period, t , using an arbitrary reference time of

¹³Especially millisecond pulsars, whose rotation period can be measured accurately down to one part in 10^{13} or better (e.g. Davis et al. 1985).

¹⁴In some cases, timing noise can manifest due to inaccurate model parameters (e.g. \dot{P}) and unmodelled effects (e.g. orbital companions). However, these ‘pseudo-noise’ signatures can usually be quickly identified and removed.

1: INTRODUCTION

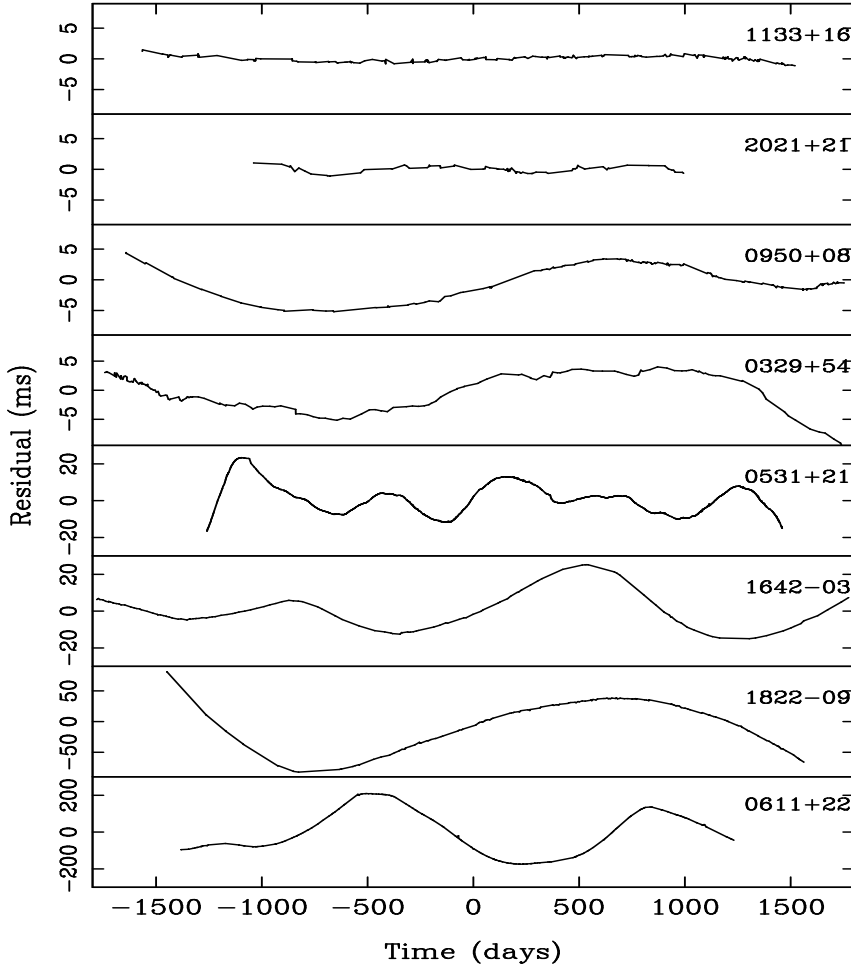


Figure 1.6: Examples of timing noise in the residuals of a number of normal pulsars, ranked (*from top to bottom*) in increasing order of timing activity (figure taken from Lyne et al. (1995)). The label on the right hand side of each residual shows the pulsar's name. Note the varying timing residual scales.

10^8 s (equivalent to the typical data span of observations in Arzoumanian et al. (1994)):

$$\Delta(t) = \log \left(\frac{1}{6\nu} |\ddot{\nu}| t^3 \right), \quad (1.16)$$

where $\Delta_8 \equiv \Delta(10^8$ s). Note the similarity with the fourth term in Eqn. 1.14.

Timing noise is also quantified using the stability parameter σ_z , which is based on the Allan variance. This acts as a measure of the ‘amount’ of noise through fitting third-order polynomials to measured time offsets in residuals (Matsakis et al. 1997;

Hobbs et al. 2006) as follows

$$\sigma_z(\tau) = \frac{\tau^2}{2\sqrt{5}} \langle c^2 \rangle^{1/2}, \quad (1.17)$$

where c is the magnitude of the cubic polynomials fitted to the data of length τ .

Both of these methods are complementary. However, the Δ_8 parameter only allows timing noise to be quantified over a single timescale. Consequently, the stability parameter has become more widely accepted as the standard parametrisation of timing noise.

Recently, Hobbs et al. (2010) analysed the timing stability of 366 pulsars in relation to various physical properties using σ_z as an indicator of timing noise. They found that timing noise is most prevalent among young pulsars with large spin-down rates (see Fig. 1.7) and can be modelled by

$$\log_{10}[\sigma_z(10 \text{ yr})] = -1.37 \log_{10}[\nu^{0.29} |\dot{\nu}|^{-0.55}] + 0.52. \quad (1.18)$$

They also measured $\ddot{\nu}$ for their sample of pulsars. From Eqn. 1.10, pulsars which undergo energy loss that is dominated by magnetodipole braking should have a positive $\ddot{\nu}$ which yields $n = 3$. Despite the long observation spans ($\gtrsim 10$ years), it was not possible to measure any realistic braking indices; braking indices ranged from approximately -3×10^5 to $+4 \times 10^4$, with a median of 22. In addition, almost half (47%) of the pulsars studied had negative $\ddot{\nu}$ values. Consequently, they came to the conclusion that $\ddot{\nu}$ is dominated by timing noise in residuals and is biased by the time-span of observations, rather than it being attributed to pure magnetodipole radiation or some other energy loss mechanism.

When faced with timing irregularities in residuals, we can often model and remove their effects (i.e. ‘whiten’ residuals) through least-squares fitting of harmonically related sinusoids (Hobbs et al. 2004). However, for discrete changes in residuals such as those due to glitches (sudden discontinuous decreases in period; e.g. Lyne et al. 1995; Lyne 1999; Lyne et al. 2000; Melatos et al. 2008) this technique fails (Hobbs et al. 2006).

1: INTRODUCTION

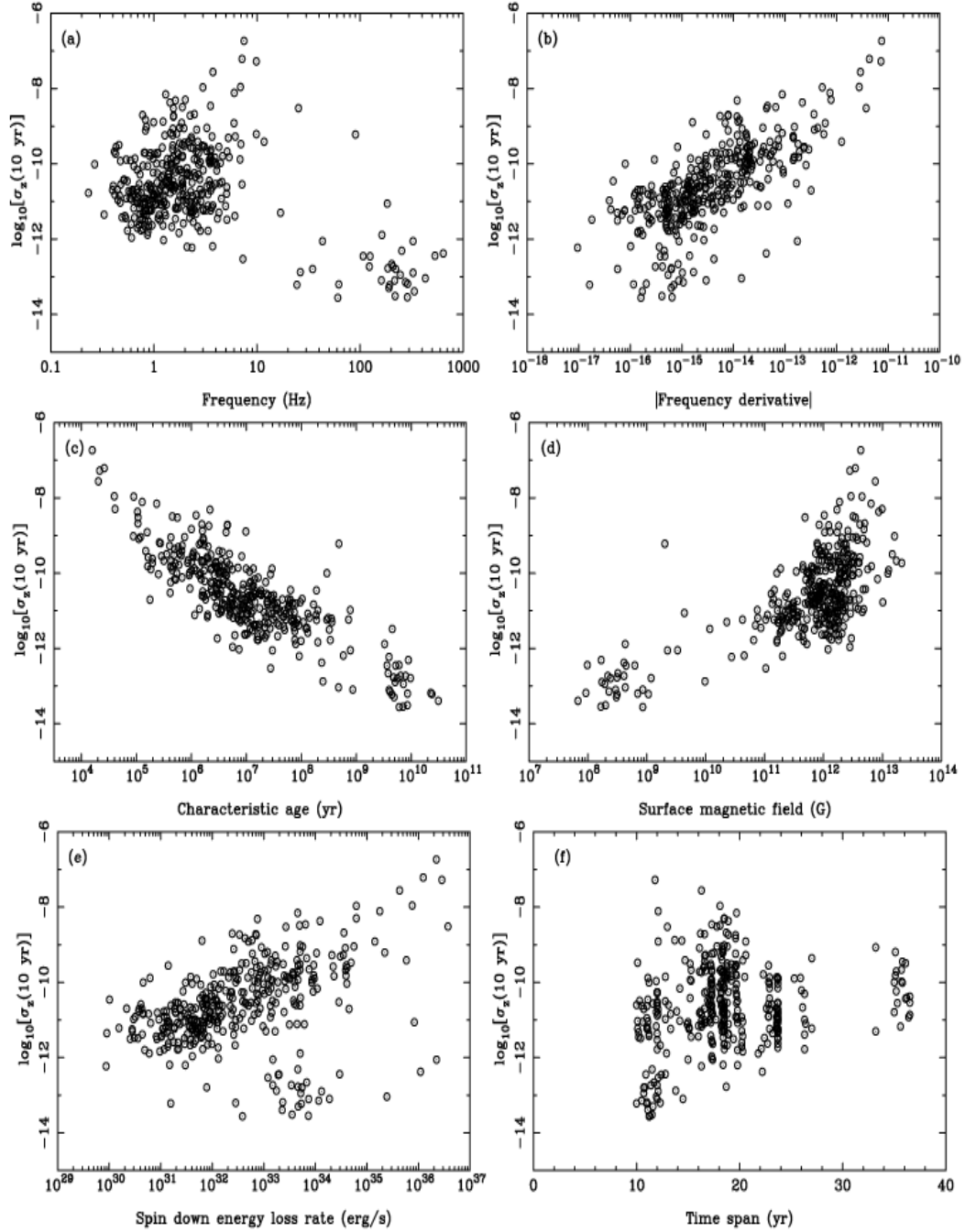


Figure 1.7: Plots showing the σ_z parameter measured over 10 years against *a*) pulse frequency, *b*) frequency derivative, *c*) characteristic age, *d*) surface magnetic field strength, *e*) spin-down luminosity and *f*) the time-span of observations (figure taken from Hobbs et al. (2010)). Greater timing noise activity is indicated by larger values of σ_z . The most prominent timing noise is observed in young pulsars with large spin-down rates and high spin-down luminosity.

1.3 Thesis Outline

This thesis is structured as follows:

- **Chapter 2** presents an overview of pulsar radio emission irregularities and their relation to rotational stability.
- **Chapter 3** investigates the nulling behaviour of PSR B0823+26 and its relation to intermittent pulsars.
- **Chapter 4** describes an in-depth study of the emission and rotational properties of the archetypal intermittent pulsar PSR B1931+24.
- **Chapter 5** examines the radio emission behaviour of PSR J1107–5907.
- **Chapter 6** provides further insight into the radio emission properties of PSR B0823+26 through the analysis of single-pulse observations.
- **Chapter 7** discusses the conclusions of this work and the future prospects.
- **Appendix A** presents the energy loss model of PSR B1931+24.
- **Appendix B** outlines the periodicity analysis techniques applied in this thesis.

1: INTRODUCTION

Chapter 2

Pulse Intensity Modulation of Radio Pulsars

Since the discovery of pulsars, radio observations have been used to probe their rotational and magnetospheric physics. Most of this work has focused on analysing integrated pulse profiles, which provide insight into the properties of these sources over relatively long timescales (i.e. $\gtrsim 10^3$ pulse periods). The inherent stability of integrated emission profiles, in the majority of pulsars, has given these objects their reputation as being remarkably stable and predictable rotators. However, it has become increasingly evident over recent years that this portrayal is not entirely correct. This is primarily due to the increase in the sensitivity of observing systems, as well as improvements in high-time resolution signal processing - made possible by advancements in computational facilities - which have enabled more detailed insight into the emission modulation properties of a much larger population of pulsars. It is now understood that these objects exhibit a plethora of periodic, and more transient, emission phenomena over a wide range of timescales (i.e. nanoseconds to years), which are thought to be linked with their rotational stability and magnetospheric structure. As such, substantial focus is now being placed on detecting and characterising their emission variation (i.e. pulse intensity modulation) in order to better understand their morphology and the physics governing their emission. In this chapter, we will present an overview of the various radio emission phenomena which have been observed in pulsars, as well as the effects of the interstellar medium on their emission, thus providing context for the observational studies presented later in this thesis.

2.1 Interstellar Scintillation

The interstellar medium (ISM) consists of a cold (of the order of ~ 10 K) plasma which has an inhomogeneous electron density distribution. As the electron density concentration of the ISM varies on a wide range of length scales, it exhibits random refractive index fluctuations which affect the phase coherence of emission from pulsars. Subsequent constructive and destructive interference between the scattered rays causes modulation in pulse intensity as a function of frequency and position in the observer plane (e.g. Rickett 1977, 1990). Due to a relative motion between the pulsar, the scattering medium and the observer, this spatial variation is transformed into an irregular temporal variation of signal intensity (Wang et al. 2005). This is known as *interstellar scintillation* and is observed over a range of timescales (seconds to months; e.g. Cole et al. 1970; Rickett et al. 1984; Labrecque et al. 1994; Bhat et al. 1999b; Wang et al. 2005). For most practical purposes, this behaviour can be described well by a simple *thin screen* model (Scheuer 1968; Rickett 1990; see Fig. 2.1).

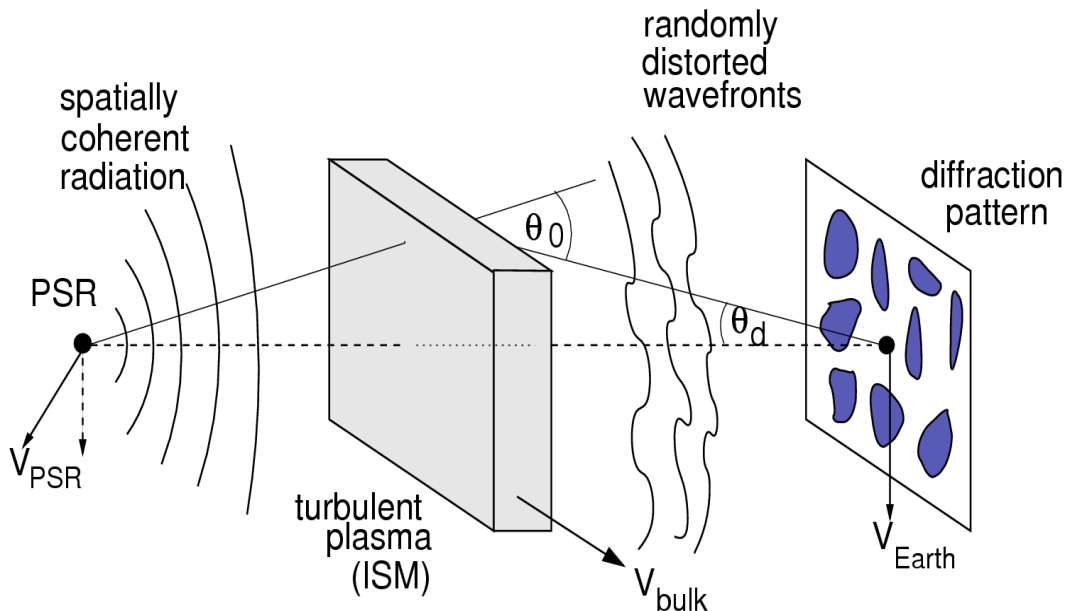


Figure 2.1: Sketch depicting the thin screen model of the interstellar medium (figure taken from Lorimer & Kramer (2005)). Coherent radiation from a pulsar is scattered (by an angle θ_0) by a thin screen of electron density irregularities, which is located midway between an observer and a source. This results in random phase perturbations in the radiation wavefronts and, subsequently, produces a scatter-broadened image of radius θ_d , which scales with distance to the observer. Scintillation is observed due to interference between the randomly distorted wavefronts. See text also for details.

There are three types of interstellar scintillation: a) *weak* scintillation, b) *strong*

diffractive scintillation and c) *strong refractive* scintillation. In order to differentiate between the weak scintillation and strong diffractive scintillation regimes, it is useful to define the scintillation strength (u) of the scattering medium at the distance of the observer (Lorimer & Kramer 2005):

$$u \equiv \frac{l_F}{s_0}, \quad (2.1)$$

Here, $s_0 = 1/k\theta_d$ is the radius of the circular scattering region around the source, which depends on the total phase perturbations of the light rays ($\Delta\Phi \propto \theta_0$), and the radius of the first Fresnel zone is given by

$$l_F = \sqrt{\frac{d}{k}} \approx 1.2 \times 10^9 \text{ m} \left(\frac{d}{\text{kpc}} \right)^{1/2} \left(\frac{\nu}{\text{GHz}} \right)^{-1/2}. \quad (2.2)$$

where d is the total distance between the pulsar and the observer, k is the wavenumber and ν is the observing frequency.

Weak scintillation is observed when $s_0 \gg l_F$ ($u < 1$) and $\Delta\Phi < 1$ radian. As such, this effect arises due to rays passing through different parts of the scattering screen as the pulsar moves relative to it with a speed V_{ISS} . Weak scintillation appears as a low intensity modulation over time ($\Delta t_{\text{weak}} \approx l_F/V_{\text{ISS}} \sim \text{hours}$), which is most prominent for nearby sources (< 1 kpc) at high observing frequencies (a few GHz or above) (Lorimer & Kramer 2005). Therefore, most pulsar observations do not experience this effect.

Strong diffractive interstellar scintillation (DISS), however, is commonly observed in pulsars. This effect occurs when $s_0 \ll l_F$ ($u > 1$) and $\Delta\Phi > 1$ radian, due to the interaction of radiation with small-scale irregularities in the ISM (Lorimer & Kramer 2005). This phenomenon appears as strong intensity variations in frequency and time, and is characterised by a typical modulation timescale (Δt_{DISS}) of minutes to hours and a decorrelation bandwidth¹ ($\Delta\nu_{\text{DISS}}$) ranging from kHz to MHz (Wang et al. 2005). For a Kolmogorov spectrum, these quantities scale as $\Delta\nu_{\text{DISS}} \propto \nu^{4.4}d^{-2.2}$ and $\Delta t_{\text{DISS}} \propto \nu^{1.2}d^{-0.6}$. However, these scaling relationships are not always observed (e.g. Wang et al. 2005). Due to the wide range of decorrelation bandwidths in pulsars, DISS can be particularly prominent when observations are obtained over narrow frequency ranges. Therefore, wideband observing systems are often used to mitigate the effect of this phenomenon; pulse intensity can be averaged over large observing bandwidths to decrease the magnitude of variations and increase the signal-to-noise ratio (SNR).

Longer timescale variations in pulse intensity may also be observed in pulsars due to

¹The decorrelation (or scintillation) bandwidth represents the maximum frequency range over which wave interference can occur (e.g. Lorimer & Kramer 2005).

refractive interstellar scintillation (RISS). This phenomenon arises due to the presence of large-scale inhomogeneities in the ISM, which cause the focusing and defocussing of radiation (e.g. Wang et al. 2005). However, this is typically only observed as a secondary effect. This is mainly because RISS results in broadband, small-amplitude intensity variations over long timescales ($\Delta t_{\text{DISS}} \propto \nu^{1.2} d^{-0.6} \sim$ days to months; Cole et al. 1970; Lorimer & Kramer 2005), which are intrinsically difficult to resolve in short observations. RISS is most notably responsible for random modulations in Δt_{DISS} and $\Delta\nu_{\text{DISS}}$, as well as unusual features in dynamic spectra (2D plots of pulse intensity versus time and frequency; e.g. Rickett 1990).

2.2 Drifting Subpulses

In pulsars, the emission profiles of individual pulses generally consist of one or more components that are significantly narrower than the average profile (i.e. $1^\circ - 3^\circ$, compared with $\sim 10^\circ$ for a typical average profile; Lyne & Smith 2006). These *subpulses* represent radiation from discrete locations within the entire emission region, which is covered by the average profile (e.g. Wright 1981; Ashworth 1988). When observed², the brightness, width, number and location of subpulses, within the pulse longitude window of the average profile, can be seen to frequently vary from pulse to pulse (e.g. Drake & Craft 1968; Backer 1970a; Weltevrede et al. 2006, 2007). In some cases, these variations are purely chaotic and, subsequently, appear as random fluctuations in the average profile shape. This is analogous to pulse phase jitter, which is observed as random phase fluctuations in individual pulses and, hence, in average profiles (see for example Cordes & Downs (1985); Cordes (1993))³.

In several pulsars, however, subpulse modulation is observed to be systematic in nature. This was first recognised by Drake & Craft (1968), who discovered a fast (~ 10 ms), secondary periodicity in the radio emission of two pulsars. This appeared as a progressive, organised ‘drift’ of subpulses in successive pulses across the average pulse profile window, which is now commonly referred to as subpulse ‘drifting’ (e.g. Weltevrede et al. 2006). Such drifting behaviour can most readily be seen in a so-called ‘pulse stack’ (i.e. a stack of successive pulses on top of each other), where subpulses form ‘drift bands’ (see left panel of Fig. 2.2). This modulation is characterised

²Some pulsars may be too weak to provide a sufficient SNR to detect individual pulses and, hence, subpulse structure. Other sources might not also exhibit emission profiles which can be characterised with multiple components.

³As pulsar timing precision is dependent on the stability of average profiles, this effect can introduce a timing measurement uncertainty in addition to radiometer noise (Cordes & Shannon 2010; Liu et al. 2012).

by two parameters: the vertical time separation between drift bands P_3 , which is expressed in units of pulse period P_0 , and the horizontal drift band separation P_2 in pulse longitude units. While P_3 is always a positive quantity, P_2 can be either positive or negative. Conventionally, a negative P_2 value (i.e. negative drifting) represents subpulses appearing earlier with each successive rotation (Weltevrede et al. 2006).

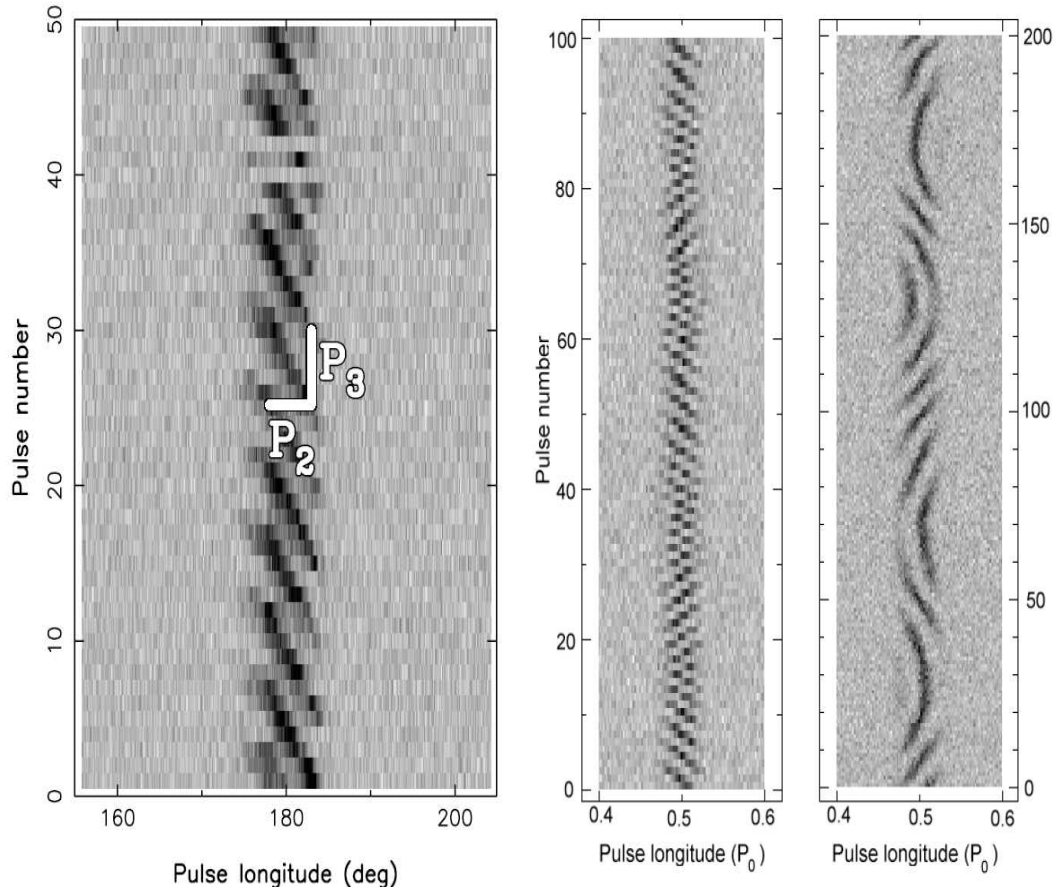


Figure 2.2: Pulse stacks showing examples of the drifting subpulse phenomenon. *Left:* A pulse stack of fifty consecutive pulses from an observation of PSR B0818–13 at 92-cm (figure taken from Weltevrede et al. (2007)). The separation between successive drift bands is denoted vertically by P_3 and horizontally by P_2 . *Right:* Two artificially generated pulse stacks, showing examples of drift reversals which are caused by changing alias order (figure taken from Weltevrede et al. (2006)). See main text also for details.

The first systematic, large-scale study of subpulse drifting was conducted by Weltevrede et al. (2006, 2007). In this work, they categorised all the pulsars in their sample which exhibited some form of modulation (170 out of a total of 187 pulsars at 21-cm) based on their drifting behaviour. Subsequently, the most stable drifters, which have the least variable P_3 values, were classified as *coherent drifters* and were also found

to be on average older than less organised drifters⁴. Pulsars which exhibited broad, diffuse drift (i.e. a drift feature with a width $\Delta P_3 > 0.05$ cycles per period (cpp)) were separated into two subclasses, based on whether their drift is clearly separated from the alias borders ($P_0/P_3 = 0$ cpp and $P_0/P_3 = 0.5$ cpp) or not. Interestingly, the latter objects were often found to exhibit a constantly changing drift direction, due to presence of multiple alias modes (Weltevrede et al. 2006, 2007; see also the right panel of Fig. 2.2). Lastly, a number of sources in this study were found to exhibit longitude stationary modulation, that is drift with a P_3 value but no finite P_2 value.

Of those pulsars which had a sufficient SNR to characterise their modulation, a remarkable 55 % were found to exhibit drifting subpulses. As such, it is likely that this phenomenon is an intrinsic mechanism of radio emission in pulsars, and the non-detection of drifting in pulsars might be due to mitigating factors (e.g. viewing geometry, insufficient SNR or refractive distortion; Weltevrede et al. 2006, 2007). Due to the high proportion of drifting pulsars, and absence of any correlation with magnetic field strength, it is thought that the physical conditions responsible for drifting are not too dissimilar from those required for the radio emission mechanism (Weltevrede et al. 2006, 2007). Indeed, in several pulsars, drifting has been directly related to the emission mechanism; several pulsars which have been observed to null (i.e. switch off their radio emission for successive pulses; see §2.5 for more details) have also experienced a correlated change in the number and shape of subpulses (c.f. mode changing; see §2.4), as well a change in the drift rate after (before) a null (e.g. Page 1973; Lyne & Ashworth 1983; van Leeuwen et al. 2002; Rankin et al. 2006; Force & Rankin 2010; Kloumann & Rankin 2010). This indicates that these phenomena are all linked (see also §2.5).

The drifting subpulse phenomenon is generally understood in terms of the widely adopted ‘carousel’ model, where subpulses are associated with a ring of equi-distant emission entities (‘sparks’) near the stellar surface (e.g. Ruderman & Sutherland 1975; Cheng & Ruderman 1980; Gil & Sendyk 2000; see also §1.1.2). As the pulsar rotates, the line-of-sight (LOS) of the observer makes a tangential pass of the subbeam structure of the carousel which, subsequently, results in the detection of a subpulse sequence. In the Ruderman & Sutherland (1975) model, the carousel slowly rotates about the magnetic axis of the star due to an $\mathbf{E} \times \mathbf{B}$ drift⁵. This accounts for a monotonic drift in the

⁴Coherent drifters are also associated with lower spin-down luminosity on average (Serylak 2011).

⁵In the gap region, where particle acceleration occurs, the corotation condition $\mathbf{E} \cdot \mathbf{B} = 0$ is not satisfied (e.g. Goldreich & Julian 1969; Ruderman & Sutherland 1975; see also §1.1.2). Consequently, particles are thought to experience an azimuthal drift relative to the surface of the star with a velocity $\mathbf{v} = \frac{\mathbf{E} \times \mathbf{B}}{B^2} c$ (Ruderman & Sutherland 1975; see also Fung et al. (2006) for more recent work on this topic), which can be attributed to the contribution of the electric field vector to the Lorentz Force. This, in turn, translates to a drift in the location of spark discharges due to the flow of current back to the stellar surface (Ruderman & Sutherland 1975).

pulse longitude of a given spark over time, which is thought to be greater further away from the magnetic pole due to an increased distance between sparks (Edwards et al. 2003). As such, this model predicts a tertiary subpulse modulation periodicity that corresponds to the circulation time of the carousel. Indeed, a number of pulsars have an associated long timescale variation, compared with P_0 (i.e. up to several hundred pulse periods), that can be explained well by this model (e.g. Deshpande & Rankin 2001; Asgekar & Deshpande 2005; Gil et al. 2003; Gupta et al. 2004; Force & Rankin 2010). However, not all drift features can be explained with this model (e.g. subpulse phase steps; Edwards et al. 2003; Edwards & Stappers 2003). As such, a number of alternative theories have been suggested to explain these features (e.g. non-radial oscillations; see Kuiper 2009 for a concise review). These models benefit from not having to rely on the presence of plasma rotation relative to the neutron star. However, they also lack self-consistency, as other drift features cannot be reconciled (e.g. drift band curvature in the context of non-radial oscillation models; Weltevrede et al. 2006). Therefore, significant work is required to either consolidate the existing carousel model, or extend alternative models, before the relationship between the drifting phenomenon and the radio emission mechanism can be fully realised.

2.3 Microstructure and Giant Pulses

Individual pulses are also seen to exhibit structure on much shorter timescales than subpulses (\sim ns – ms; e.g. Cordes 1979; Popov et al. 2002; Kramer et al. 2002; Hankins et al. 2003), which is referred to as *microstructure*. These features were first discovered by Craft et al. (1968) in two pulsars, whose pulse profiles were shown to exhibit subpulse intensity fluctuations on timescales below 200 μ s. Since then, this phenomenon has also been observed in several other pulsars, which are bright enough to allow their shortest-term variability to be resolved. As such, the general properties of microstructure are now known: microstructure exhibits a typical width of the order of 100 μ s (see e.g. Kramer et al. (2002) and references therein), is broadband in frequency (Rickett et al. 1975; Boriakoff et al. 1981), does not contribute to the average profile shape (Petrova 2004) and often occurs in short quasi-periodic groups (sometimes within the same pulse), with a periodicity of about 0.5 – 1 ms (Hankins 1971; Boriakoff et al. 1981; Kramer et al. 2002; Lyne & Smith 2006). Furthermore, the fraction of pulses in pulsars which show this phenomenon can be quite large i.e. approximately 30 – 80 % (Lange et al. 1998; Kramer et al. 2002). As a result, microstructure is believed to be a fundamental feature of the radio emission mechanism, rather than an additional feature of only a subset of sources, and is typically explained by spatial and (or) temporal

fluctuations in the subbeam structure (e.g. Cordes 1979; Petrova 2004).

Microstructure can also take the form of particularly intense (i.e. up to 100 times the average peak intensity; Johnston & Romani 2002) and narrow (e.g. 50 – 400 μ s in Vela; Johnston et al. 2001) micropulses, which can occur at pulse longitudes not covered by the average profile (Johnston et al. 2001). These ‘giant micropulses’ occur less frequently than normal micropulses and have an intensity distribution which can be described by a power law (Kramer et al. 2002)⁶. Despite these differences, however, giant micropulses are still thought to be related to normal radio emission, that is they can still be explained under the normal micropulse emission mechanism (Petrova 2004).

Remarkably, pulsars such as the Crab also show even more intense (up to 2000 times the average peak intensity; Lundgren et al. 1995; Karuppusamy et al. 2010) and narrow (0.4 ns – 120 μ s; Hankins & Eilek 2007; Karuppusamy et al. 2010) emission components, which are known as ‘giant pulses’. Conventionally, giant pulses (GPs) are defined as pulses which have a flux 10 times greater than the mean flux density of the profile, and are also much narrower than the average emission (Knight 2007). Like giant micropulses, GPs are broadband (Sallmen et al. 1999; Karuppusamy et al. 2012) and exhibit an energy distribution that is best described by a power law (Argyle & Gower 1972). However, they are observed less frequently ($\sim 1.25 \text{ s}^{-1}$ for the Crab at 1400 MHz), appear typically as isolated bursts⁷ and are not found to be periodic i.e. they occur at random time intervals (Karuppusamy et al. 2010). In addition, giant pulses are typically highly constrained in pulse longitude (e.g. Kuzmin & Ershov 2004), particularly in millisecond pulsars, and are sometimes coincident with high energy emission; GPs in some objects (e.g. the Crab) are observed to be phase aligned with optical, X-ray and γ -ray peaks (Lundgren et al. 1995; Sallmen & Backer 1995). Strikingly, enhanced optical emission has also been observed in coincidence with GPs in the Crab pulsar (Shearer et al. 2003), thus indicating that radio giant pulses are more related to high-energy emission than the normal radio emission mechanism (see also Romani & Johnston 2001; Kuzmin 2007).

2.4 Mode Changes

Pulsars are typically associated with having very stable, average emission profiles (Helfand et al. 1975). In some remarkable pulsars, however, their average profiles are observed to switch abruptly between two (or more) quasi-stable states (Backer 1970b;

⁶This is in contrast to normal micropulse emission, which follows a lognormal intensity distribution (Kramer et al. 2002).

⁷In very few cases, ‘double giant pulses’ have been seen in the Crab pulsar, where both the main-pulse and inter-pulse longitudes exhibit GP emission (Karuppusamy et al. 2010).

Wang et al. 2007). This phenomenon is aptly referred to as *mode changing* and has been observed in a few dozen pulsars to date (e.g. Bartel et al. 1982; Rankin 1986; Wang et al. 2007; Lyne et al. 2010; Chen et al. 2011). Mode changing is most common among pulsars with complex (multi-component) emission profiles (e.g. Rankin 1986; Esamdin et al. 2005; Force & Rankin 2010) and is observed to be a broadband phenomenon (Bartel et al. 1982; Gil et al. 1994). Mode changes manifest most notably as variations in the relative intensity, number, width and phase locations of profile components (see Fig. 2.3). They are also related to changes in polarisation properties, microstructure and subpulse drift rates (Taylor et al. 1975; Bartel et al. 1982; Rankin 1986; Gil et al. 1994). As such, this phenomenon represents a fundamental alteration to the emission mechanism (c.f. pulse nulling; see §2.5).

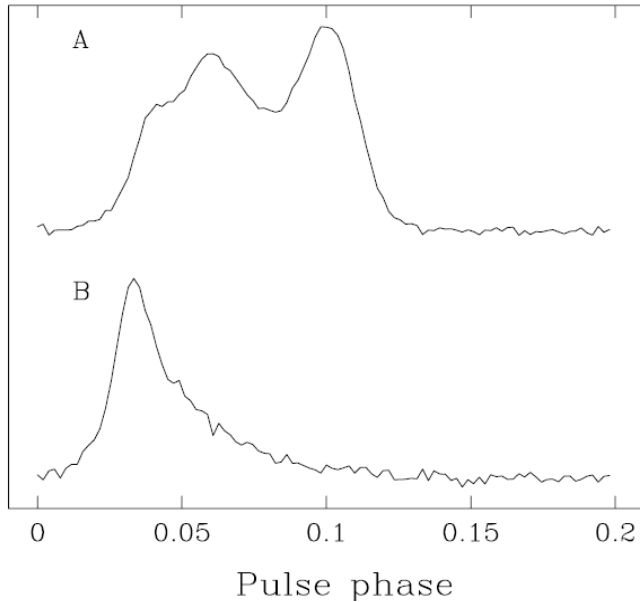


Figure 2.3: An example of the mode changing phenomenon, as seen in PSR J1826–6700 (figure taken from Wang et al. (2007)). The average profiles of the normal and abnormal modes are denoted by A and B respectively.

Typically, mode changing pulsars exhibit a dominant or preferred emission mode, which is called the *normal* mode. Other modes, therefore, are called *abnormal*. The time in which a pulsar spends in these modes can vary from one to several thousand (or more) pulse periods (e.g. Backer 1970b; Bartel et al. 1982; Chen et al. 2011). Although the mechanism which governs mode changes is not fully understood, it is thought that magnetospheric state changes are responsible for their occurrence (Contopoulos 2005; Timokhin 2010; Lyne et al. 2010; Li et al. 2012a; see also §2.5)

2.5 Pulse Nulling

In numerous pulsars, radio emission appears to ‘switch off’ abruptly, via a dramatic decrease in pulse intensity to (or very close to) zero, and then returns to its normal state after a number of successive pulse periods (Backer 1970c; see also Fig. 2.4). This phenomenon, called *pulse nulling*, affects all components of emission (Backer 1970c; Ritchings 1976) and is thought to be a severe manifestation of mode changing, that is a variation between active and quiescent emission modes. It is most commonly observed as a broadband phenomenon (Bartel et al. 1982; Rankin 1986)⁸, thus suggesting that it represents a global disruption of the emission mechanism⁹.

Pulse nulling can be observed over a wide range of timescales, that is from just one or two pulses to many days (e.g. Rankin 1986; Biggs 1992; Wang et al. 2007; Kramer et al. 2006). The fraction of time that a pulsar is in a null state, the nulling fraction (NF), can range from less than 1 % up to in excess of 95 % (Deich et al. 1986; Wang et al. 2007) and is found to be correlated with characteristic age (Wang et al. 2007). This suggests an increased prevalence of nulling activity in older pulsars. However, no significant correlation has been found with other basic pulsar properties or geometry (Rankin & Wright 2007). This is most likely due to an incomplete sample of nulling statistics, where not only are we biased by a relatively small number of sources - $\lesssim 200$ objects are known, but far fewer have been characterised (e.g. Wang et al. 2007; Palliyaguru et al. 2011 and references therein) - we are also subject to a deficit in long period and high magnetic field strength pulsars (Keane et al. 2011). Furthermore, there is a distinct dearth of objects which have been observed to undergo long-timescale ($\gtrsim 1$ hour) nulls (Burke-Spolaor et al. 2011; see also Fig. 2.5). It is possible that a deficit of neutron stars with large P , high surface magnetic field strength and long nulling timescales (t_{off}) exists. However, it is probable that we are subject to data windowing effects, which will impart an observational bias on long t_{off} pulsars; detections of nulling pulsars in surveys inherently favour those with shorter t_{off} and, hence, typically lower NF as the combined detection and confirmation probability of pulsars decreases with increasing t_{off} (Burke-Spolaor et al. 2011). As such, a complete census of nulling pulsars across the $P - \dot{P}$ diagram is required before any significant conclusions can be drawn about the general properties of nulling sources.

⁸In PSR B1133+16, nulls do not always occur simultaneously in frequency. However, it has been suggested that this can be explained by additional radio emission production in the outer gap, which is comparable to giant pulse emission (Bhat et al. 2007).

⁹In some cases, however, we may observe apparent nulls or ‘pseudo-nulls’ due to insufficient instrument sensitivity (c.f. weak emission in PSR B0826–34 ‘null’ intervals; Esamdin et al. 2005) or empty sightline traverses through the carousel (Deshpande & Rankin 2001; see also §2.5.4).

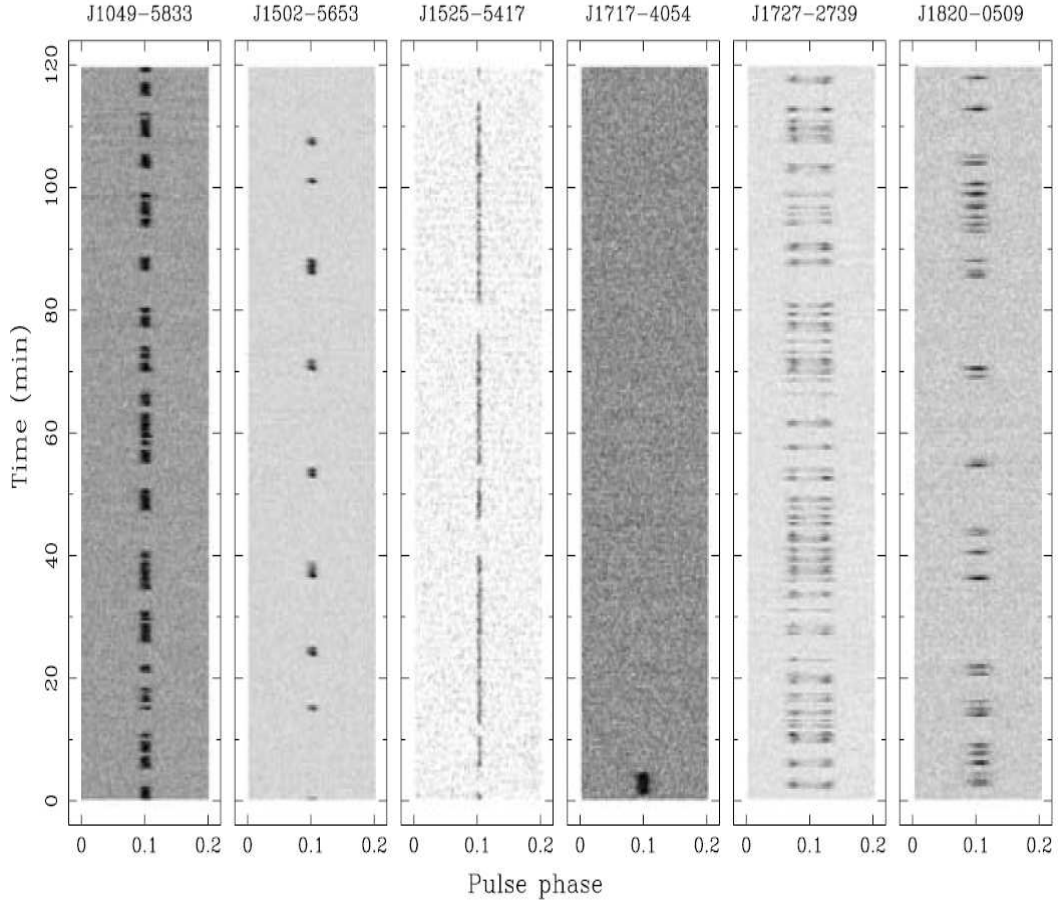


Figure 2.4: Pulse stacks of six pulsars, showing examples of the nulling phenomenon (figure taken from Wang et al. (2007)).

Recently, it has been shown that single-pulse (SP) searches, in addition to conventional periodicity searches (i.e. Fourier analysis of data), can significantly improve the probability of detection of pulsars with large NFs (e.g. McLaughlin et al. 2006; Keane 2010; Burke-Spoloar & Bailes 2010; Burke-Spoloar et al. 2011). This is particularly applicable to rotating radio transients (RRATs; McLaughlin et al. 2006), which are pulsars that are more significantly detectable through their single, isolated pulses (Burke-Spoloar et al. 2011; Keane & McLaughlin 2011). On average, these objects emit detectable pulses at a rate of between one every few minutes to a few hours, and have pulse widths of about 2 – 30 ms (Palliyaguru et al. 2011). Therefore, they are typically detectable for less than a second per day. As such, these objects lie towards the extreme end of the ‘nulling continuum’ (Keane 2010; Keane et al. 2011) and can be extremely difficult to find, primarily due to SNR limitations and spurious radio frequency interference (RFI) (McLaughlin et al. 2006). Due to the inherent transient

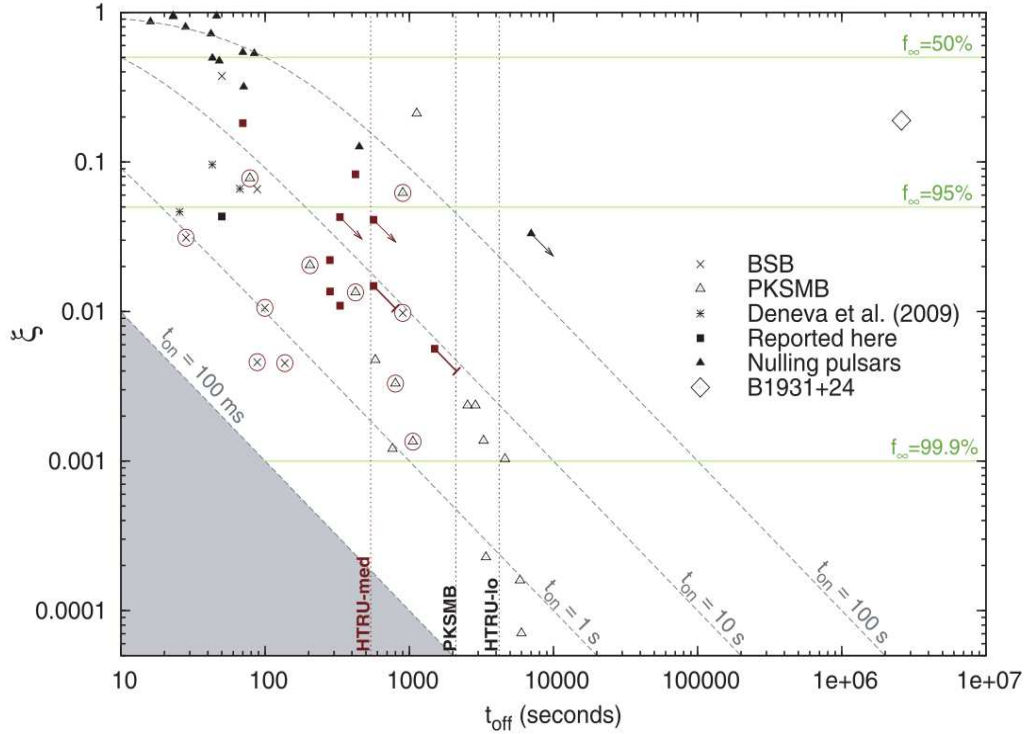


Figure 2.5: The distribution of on-fractions (ζ) against mean null length (t_{off}), for a sample of pulsars whose emission cessation behaviour has been characterised (figure taken from Burke-Spoliar et al. (2011)). The statistics for the ‘nulling pulsars’ are taken from Wang et al. (2007). The maroon points denote pulsars discovered in single-pulse searches (squares), as well as redetections (enclosed circles) in the High Time Resolution Universe (HTRU) intermediate-latitude survey. Points with arrows designate objects whose on timescale t_{on} is known, but which only have a lower limit on t_{off} . The solid green lines demarcate constant NF measured over infinite time (f_{∞}). The vertical dotted lines show the observation pointing lengths for the Parkes Multi-beam (PKSMB) and HTRU high (hi) latitude surveys (equal pointings), as well as the HTRU intermediate (med) and low (lo) latitude surveys. The shaded region denotes the area for which t_{on} is outside the period range of the SP search discoveries. Although the distribution of pulsars appears to be continuous towards larger f_{∞} , there is a clear deficit of sources which exhibit $t_{\text{on}} > 100$ s or particularly long off timescales i.e. $\gtrsim 1$ hour.

behaviour of RRATs, only a small subset (14 out of approximately 70 in total¹⁰; Keane et al. 2011) of these objects have timing solutions. As a result, the general properties of RRATs (e.g. distributions of P , \dot{P} , τ and \dot{E}) are not well characterised and, as such, nor is their connection with the normal pulsar population (see Keane et al. (2011) for a discussion on this topic).

¹⁰See <http://www.as.wvu.edu/~pulsar/rratalog/> for a complete list of the known RRAT sources.

In addition to ‘normal’ nulling pulsars ($t_{\text{off}} \sim 1–10 P$) and ‘RRATs’ ($t_{\text{off}} \sim 10^{1–4} P$; Keane et al. 2011), there are also ‘intermittent pulsars’. These objects exhibit behaviour unlike any typical nulling or RRAT-like source: 1) they undergo very long-duration ($\sim 10^{4–7} P$), quasi-periodic emission phases; and 2) they assume distinctly different spin-down rates in their opposing radio emission states (Kramer et al. 2006; Camilo et al. 2012). Due to their unprecedented emission cessation timescales, there are only a handful of these sources which have been discovered and characterised i.e. PSR B1931+24 (Kramer et al. 2006), PSR J1832+0029 (D. Lorimer, private communication) and PSR J1841–0500 (Camilo et al. 2012). The archetype of this pulsar ‘class’ (PSR B1931+24) has been studied the most extensively and, perhaps therefore, offers the best insight into their peculiar behaviour. This pulsar is observed to undergo cyclical phases of emission cessation (radio-off phases, hereafter) over timescales of $\sim 25 – 35$ days, and active phases of emission (radio-on phases, hereafter) which last approximately $5 – 10$ days¹¹. During radio-on phases, PSR B1931+24 behaves as a normal isolated radio pulsar and does not exhibit any pulse profile changes. Like conventional nulling, the absence of emission in the radio-off phases is observed to be a broadband phenomenon (at 430 MHz and 1400 MHz), and is also highly significant; the flux density of the pulsar in the radio-off state is less than 1 % of the mean radio-on flux density (Kramer et al. 2006). Coupled with the fact that the pulsar has a $\sim 50\%$ greater spin-down rate in the radio-on phase (compared with that in the radio-off phase), and emission phase transitions occur over timescales less than 10 seconds (Kramer et al. 2006), there is little doubt that the radio emitting region experiences a significant and sudden alteration between the different emission phases. As the spin-down rate is thought to be intimately related to the magnetospheric structure, it has been suggested that this behaviour has a magnetospheric origin (see §2.5.2). However, no complete model, or accepted governing mechanism, for this type of pulsar activity exists.

Due to the wide range of nulling timescales, and sparsity of known objects which exhibit temporary radio emission failure, a multitude of different and competing theories are used to explain the observations. In the following sections, we provide an overview of the dominant models and compare them with observations. Although none are conclusive, we stress that future observations and simulations of nulling pulsars, RRATs and intermittent pulsars should provide significant insight into the nature of transient phenomena and, hence, the mechanism(s) responsible for radio emission in pulsars.

¹¹In this thesis, we use the terminology ‘radio-on’ and ‘radio-off’ phases to denote sequences of active and quiescent radio observations. Whereas, we use the phrases ‘bursts’ and ‘nulls’ when referring to series of active and quiescent single pulses.

2.5.1 The ‘Death Valley’

Pulsar radio emission is conjectured to arise from copious pair production in the inner magnetosphere, above the polar cap, due to the presence of vacuum gaps (Sturrock 1971; Ruderman & Sutherland 1975; see also §1.1.2). As such, a significant amount of work has been devoted to separating the pulsars which can support pair production in their magnetospheres from those that cannot (Ruderman & Sutherland 1975; Arons & Scharlemann 1979; Chen & Ruderman 1993; Qiao & Zhang 1996; Zhang et al. 2000; Arons 2000). Not surprisingly, the criteria for pair production are inherently model dependent and vary significantly for different magnetic field configurations (Chen & Ruderman 1993; Zhang et al. 2000).

It has been suggested that so-called radio pulsar ‘death lines’, according to given models, can be drawn in a 2-D pulsar parameter phase space ($P - \dot{P}$ diagram or $P - B_s$ diagram, where P is the pulse period, \dot{P} is the spin-down rate and B_s is the surface magnetic field strength) to differentiate such pulsars. Due to the prevalence of model variables, however, the parameter space in which pulsars are thought to transition between an active and quiescent state of emission, i.e. where they can no longer produce e^\pm pairs, is defined as a ‘valley’ rather than a single line (Chen & Ruderman 1993; Zhang et al. 2000). Here, it is assumed that the potential drop achieved in the magnetosphere is limited by the rotational period (c.f. electromagnetic induction in a dynamo). If the pulsar period exceeds a certain value, then a sufficient potential drop for pair production cannot be achieved above the polar cap, and the radio emission mechanism is proposed to switch off (Chen & Ruderman 1993). However, this is dependant upon the magnetic field strength and configuration of the pulsar; more complicated field configurations allow longer period pulsars to still be emitting at radio frequencies (see e.g. Chen & Ruderman (1993) for more details).

Figure 2.6 shows the distribution of pulsars against the conventional boundary conditions for pair production. It is interesting to note that approximately half of the pulsar population sits in the ‘death valley’. As can be seen, the distribution of nulling pulsars seems quite arbitrary. Therefore, the concept of a death valley only acts as a simple model for radio emission cessation.

As previously mentioned, the condition for radio emission depends on the pulsar period as well as the magnitude and configuration of the surface magnetic field. Unfortunately, however, only the dipolar component B_d can be deduced from the observed \dot{P} , instead of near the surface where the emission arises from (Arons 1993). With this in mind, several authors have invoked the presence of more complex surface fields than

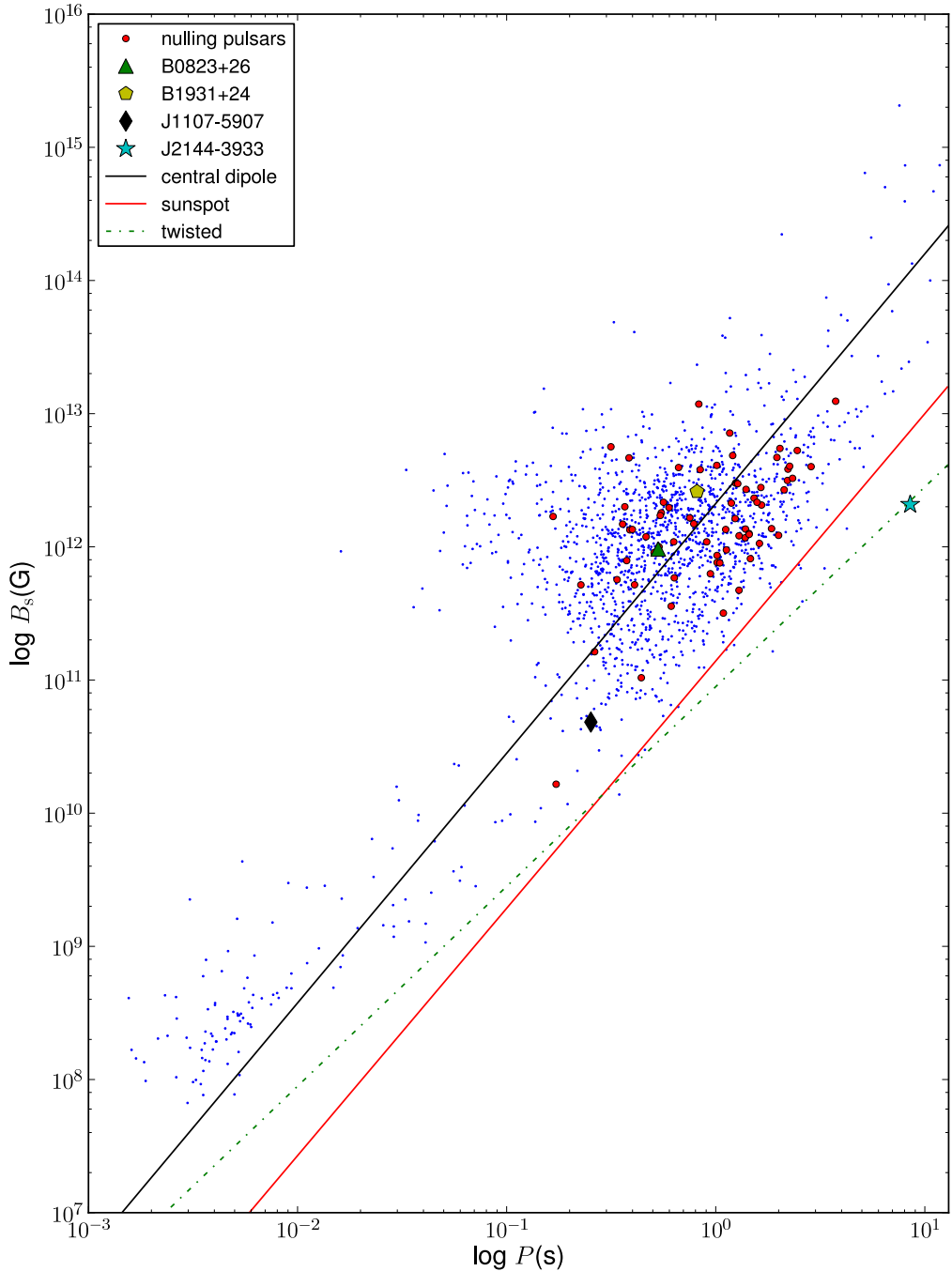


Figure 2.6: The $P - B_s$ diagram for the known population of pulsars with measured P and B_s values. Overlaid are lines denoting the theoretical pair production limits for radio emission, corresponding to a given magnetic field configuration. The conventional ‘death valley’, proposed by Chen & Ruderman (1993), is enclosed by the two solid lines. These lines represent the cut-off points for radio-emission for a star-centred dipole and a sunspot magnetic field configuration respectively. The nulling pulsars are marked by the red circles. The pulsars B0823+26, B1931+24 and J1107–5907 are discussed later in this work (see §3 – 6). Note that the location of a few pulsars in the diagram, including PSR J2144–3933, can only be explained by invoking an extreme magnetic field configuration (i.e. extremely twisted B_s).

a pure dipole¹², including sunspot-like magnetic anomalies, to explain the radio emission in nulling pulsars and solve the ‘death line problem’ in long period pulsars (e.g. PSR J2144–3933 with $P \sim 8.5$ s; see also Fig. 2.6) (Arons & Scharlemann 1979; Goldreich & Reisenegger 1992; Shalybkov & Urpin 1997; Young et al. 1999; Gil & Mitra 2001; Asseo & Khechinashvili 2002). Under the assumption that such field configurations exist, with $B_s \gg B_d$, the radius of curvature of accelerating particles can be reduced to a magnitude much less than the stellar radius ~ 10 km (Gil & Mitra 2001), thus allowing the periods at which pulsar death occurs to be brought into agreement with observations (Arons 1993). Furthermore, magnetic instabilities on the stellar surface, such as sunspot-like fields, are thought to significantly amplify (weaken) the magnetic fields there and, hence, cause the criteria for radio emission to be temporarily satisfied (dissatisfied) (Chen & Ruderman 1993; Gil & Mitra 2001; Gil et al. 2002; Geppert et al. 2003).

There are several mechanisms by which such non-dipolar field configurations could arise e.g. due to Hall drift instabilities (Flowers & Ruderman 1977; Jones 1988; Goldreich & Reisenegger 1992; Urpin & Muslimov 1992; Shalybkov & Urpin 1997; Geppert et al. 2003; Rheinhardt et al. 2004), ambipolar diffusion and magnetic buoyancy (Goldreich & Reisenegger 1992; Rheinhardt et al. 2004), as well as thermomagnetic instabilities (Blandford et al. 1983; Thorsett & Dewey 1993; Miralles et al. 2000; Urpin & Gil 2004). However, there is not a substantial amount of observational evidence to support their existence: 1) non-dipolar field configurations are tentatively supported by observed discrepancies between X-ray spectral lines and associated dipolar field strengths in a few pulsars (see e.g. Becker et al. (2003); Haberl et al. (2003)); 2) transient outbursts in White Dwarfs are not inconsistent with theoretical models (Zhang & Gil 2005). Furthermore, it is still unclear over what timescales such field configurations would modulate the radio emission in pulsars (see e.g. Urpin & Gil 2004; Rheinhardt et al. 2004 for a discussion on predicted timescales), and how exactly regulated spin-down rate variation would occur. Consequently, it is difficult to explain the radio emission behaviour of nulling pulsars.

Alternatively, it has been suggested that a dead (zombie) pulsar could be reactivated by the episodic injection of circumstellar material into the outer magnetosphere (Cordes & Shannon 2008), or via the absorption of high-energy photons from the cosmic γ -ray background (so-called ‘lightnings’; Istomin & Sobyanin 2011). Unfortunately, however, it is again unclear how the wide range of timescales can be explained by these models, or how highly periodic oscillations in the spin-down rate of intermittent pulsars can be

¹²Pulsars are normally assumed to have dipolar magnetic fields, in order to simplify models of magnetospheric emission, and because observations of pulsar rotational behaviour can be adequately modelled using this assumption (Arons 1993).

reconciled.

These models all share common predictions that high-energy emission, e.g. X-ray and optical, will be produced as a secondary product of the reactivation mechanism. However, this emission is thought to present itself in different ways, e.g. non-thermal X-ray emission will be accompanied by enhanced polar cap heating in the magnetic instability model (Zhang et al. 2007). In order to determine the viability of these models, therefore, further observations of transient pulsars, particularly at high energies, are required to provide insight into the properties of their magnetospheres and, hence, their nulling behaviour.

2.5.2 Magnetospheric Switching

Recently, it has been suggested that pulsar magnetospheres can switch between meta-stable states (Bartel et al. 1982; Contopoulos 2005; Kramer et al. 2006; Lyne et al. 2010; Hobbs et al. 2010; Timokhin 2010; Li et al. 2012a,b). This ‘magnetospheric switching’ refers to a process in the magnetosphere which causes moding between different global current distributions and, hence, different radio emission states (Lyne et al. 2010). This work centres on the discovery of the first intermittent pulsar, PSR B1931+24, whose quasi-periodic radio emission phases have been directly linked to variation in the spin-down rate (Kramer et al. 2006). These spin-down rate ($\dot{\nu}$) variations are clearly demonstrated in Fig. 2.7, where active radio emission phases are shown to be accompanied by an increase in $\dot{\nu}$, with respect to the average long-term spin-down. In their work, Kramer et al. (2006) developed a timing model which incorporated two spin-down rates to fit the observations (see bottom panel of Fig. 2.7). This model was found to fit the data extremely well, thus leading to profound implications about the nature of this pulsar and others like it (see e.g. §A for the energy loss model of this pulsar).

Motivated by these findings, Hobbs et al. (2010) conducted a systematic investigation into the timing behaviour of 366 pulsars which were observed with the Lovell Telescope over a 36-year period. This work constituted the first large-scale analysis of pulsar timing noise over a timescale > 10 years. Remarkably, the authors found that a large number of pulsars show significant irregularities in their rotation rate, which often appear as (quasi-)periodic features in their timing residuals (after a cubic polynomial is fitted and removed). This lead to the conclusion that a significant number of pulsars may possess multiple spin-down rates. These findings were further supported by Lyne et al. (2010), who analysed the spin-down variation of 17 pulsars from this sample, and found that their timing behaviour can be described by quasi-periodic switching between

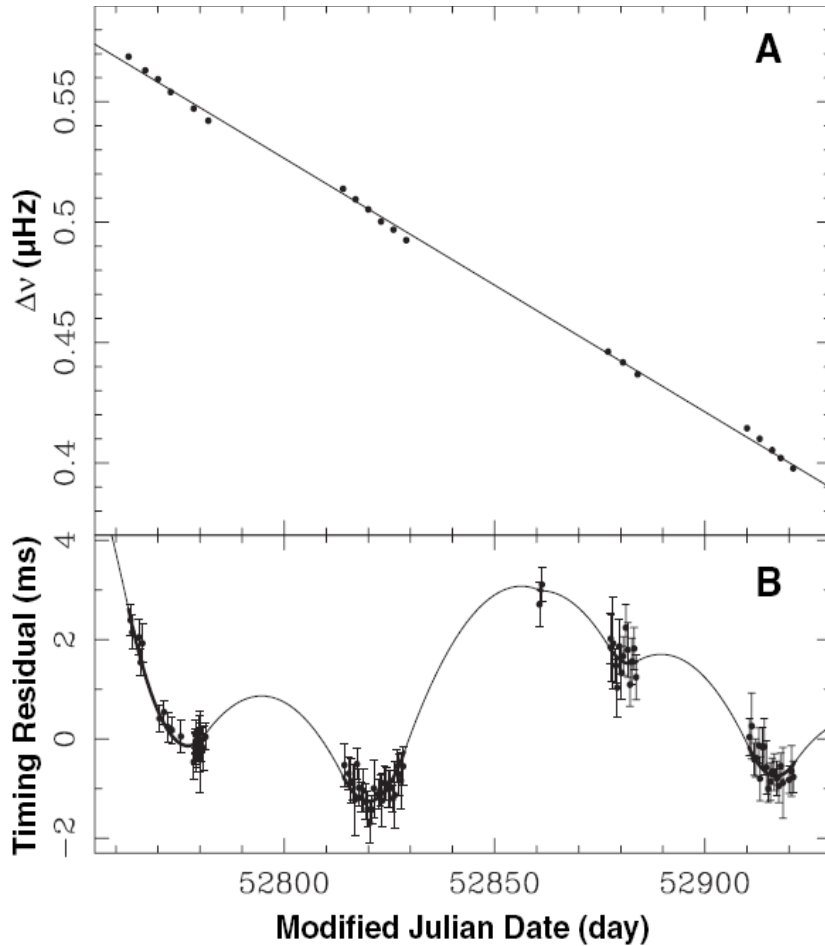


Figure 2.7: The rotational frequency (ν) evolution and timing residuals of PSR B1931+24 (figure taken from Kramer et al. (2006)). *Top panel:* The evolution of ν over a 160-day period of observations. Errors in ν are smaller than the size of the symbols. A gradual decrease in rotational frequency dominates the variation (i.e. the long-term spin-down). The line of best-fit is shown for the average frequency derivative $\dot{\nu} = -12.2 \times 10^{-15} \text{ s}^{-2}$. During active phases it is clear that the slope and, consequently, the magnitude of $\dot{\nu}$ is even greater. Therefore, suggesting a model in which $\dot{\nu}$ has different values during on and off phases. *Bottom panel:* Timing residual plot for B1931+24 with a model fitted to the data (solid line) for the same period of observations. It is apparent that there is significant variability in the spin-down behaviour over timescales of days to weeks.

two (or sometimes more) spin-down rates. As a result, Lyne et al. (2010) suggest that a multi-modal spin-down model, similar to that of PSR B1931+24, can be used to describe the timing noise in all pulsars. Furthermore, Lyne et al. (2010) found that six pulsars in the sample exhibit correlated changes between their average pulse shape and $\dot{\nu}$ (see Fig. 2.8), thus suggesting that these pulsars spend the majority of their time in

one extreme state or another. Moreover, the correlation between pulse shape changes and $\dot{\nu}$ variation suggests that the origins of the mode changing and nulling phenomena are indeed linked (c.f. Wang et al. 2007; see also §2.4), resulting from changing magnetospheric states (Lyne et al. 2010); as the radio emission from pulsars only accounts for a minute portion of the overall spin-down energy ($\sim 10^{-6} - 10^{-4}$; Kramer 2009), measurable alterations to the spin-down rate of a pulsar cannot solely be due to a variation in the radio emission, thus suggesting that mode changes and nulling events are linked with a global process which alters the spin-down rate of the pulsar.

In addition to these observational results, recent force-free simulations have provided evidence to suggest that a pulsar magnetosphere can transition between different configurations, each of which have a different spin-down and energy loss rate (see e.g. Contopoulos et al. 1999; Contopoulos 2005; Timokhin 2010; Li et al. 2012a,b). In particular, it was shown that stationary magnetospheric states can exist with different closed field line region sizes, along with different current density distributions in the open field line zone (Contopoulos 2005; Timokhin 2006, 2010). Therefore, one can infer that during the evolution of a pulsar its magnetosphere can undergo transitions between a set of such quasi-stable states. These transitions will appear as mode changing (in profile shape and perhaps drift rate; see van Leeuwen & Timokhin (2012) for a discussion on this topic), or nulls due to the unique current and plasma density distributions of each state; if the radio emission zone were to expand (contract) and/ or there were a redistribution of current, then there would be self-similar changes in the beam pattern and, hence, correlated changes in the mean pulse profile (perhaps dependent on the LOS) and spin-down rate (Timokhin 2010; Li et al. 2012a,b; see also Fig. 2.9).

Despite the breakthroughs of recent observations, and magnetospheric simulations, there is still a significant amount of work remaining to be addressed. In particular, we are yet to determine the actual mechanism responsible for magnetospheric reconfiguration. In the literature, there are a multitude of different models which attempt to explain this phenomenon e.g. non-radial oscillations (Rosen et al. 2011), asteroid belts (Cordes & Shannon 2008), precessional torques (Jones 2011), surface temperature variations in the polar gap region (Zhang et al. 1997) and magnetic field instabilities (Geppert et al. 2003; Urpin & Gil 2004; Rheinhardt et al. 2004; Wang et al. 2007; see also §2.5.1). However, none of these are conclusive, nor do they offer any insight into why variations alike those in PSR B1931+24 would have a given periodicity or fluctuation timescale. Therefore, continued observations of nulling and mode-changing pulsars are required to uncover how these global magnetospheric alterations arise, and whether they can be associated with the pulsar population as a whole.

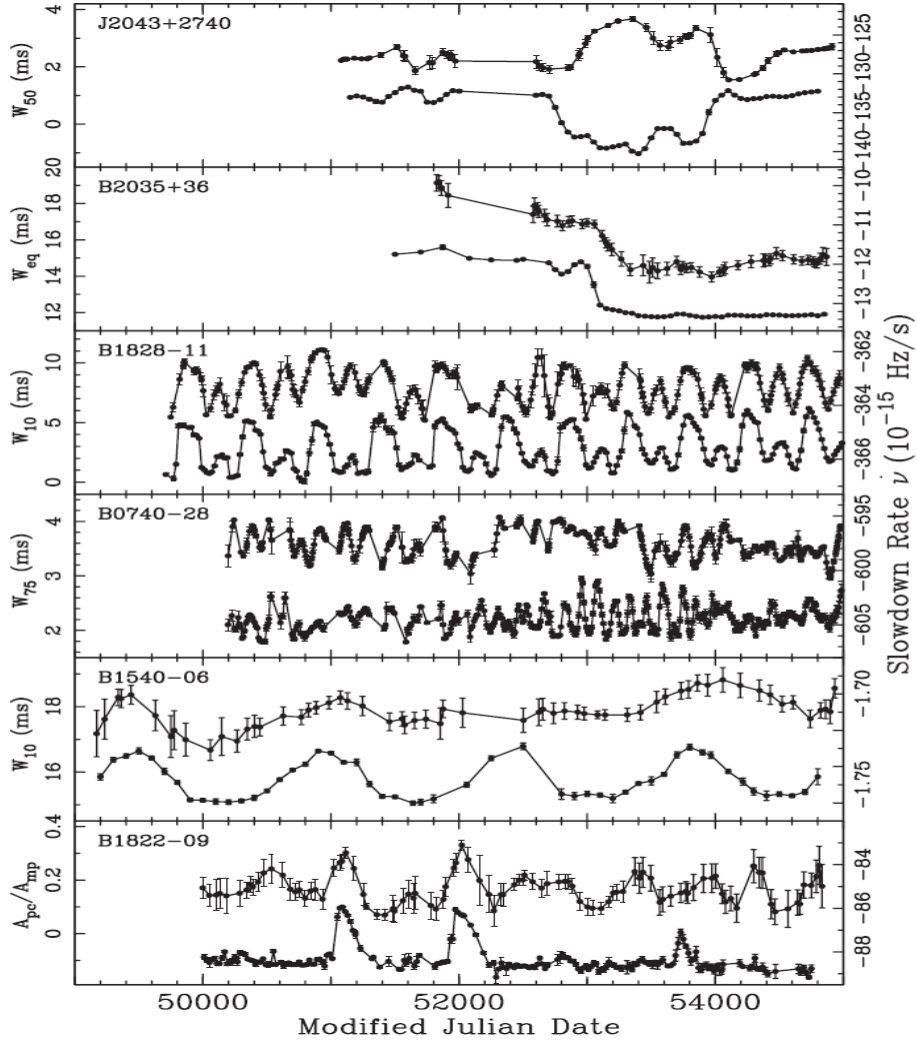


Figure 2.8: The variation of average pulse shape (upper trace) versus $\dot{\nu}$ state (lower trace) against time in six pulsars (figure taken from Lyne et al. (2010)). W_{10} , W_{50} and W_{75} are the full widths of the pulse profile at 10, 50 and 75 % of the peak pulse amplitude respectively. W_{eq} is the equivalent pulse width (ratio of the area under the pulse to the peak amplitude), and $A_{\text{pc}}/A_{\text{mp}}$ is the ratio of the amplitudes of the precursor and main pulse. The shape-parameter values are averaged over the same data-lengths of time as $\dot{\nu}$. Uncertainties in shape-parameters are derived from the standard deviation of individual values used to obtain the average.

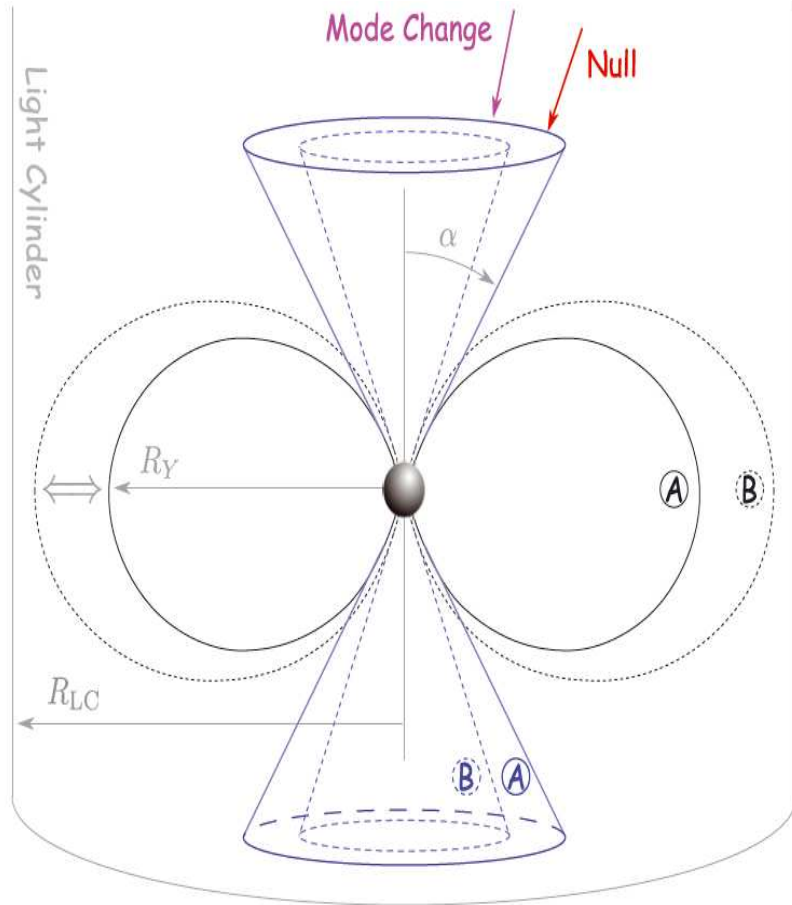


Figure 2.9: Schematic diagram of a pulsar magnetosphere whose closed field line zone varies in size (figure taken from Timokhin (2010)). The blue lines denote radio emission beams and the last closed field lines are shown by the black lines. The magenta line shows the LOS for which the pulsar will exhibit a mode change, whereas the red arrows show the LOS where a null is expected. See main text also for details.

2.5.3 Orbital Companions

In the case of PSR B1931+24, Rea et al. (2008) have proposed that a binary companion in a tight, eccentric orbit could modulate its radio emission and spin-down rate properties. In this scenario, the mass inflow rate from a low mass star ($< 0.1M_\odot$), or gaseous planet ($\sim 10^{-4}M_\odot$), is suggested to perturb the magnetosphere periodically during periastron and apastron. During apastron of the orbit, the mass inflow rate from the companion is proposed to be small. With this in mind, the pulsar radiation pressure is thought to overcome the ram pressure of the inflowing material and, hence, allow radio emission to escape from the magnetosphere (i.e. produce bursts of observable radio emission). Conceptually, quasi-periodicity in the radio-on phases of this object could

be attributed to fluctuation in the inflow rate over successive orbital periods.

During radio-off phases, that is during periastron, the mass inflow rate is expected to be much larger. This will cause the radiation pressure to be dominated by the ram pressure of inflowing material and, hence, cessation in the radio emission mechanism, as well as alteration to the spin-down behaviour of the pulsar (i.e. the *propeller regime*; Illarionov & Sunyaev 1975; Stella et al. 1986; Stella et al. 1994). It is not clear exactly how the pulsar spin-down would be affected in this scenario, but it is proposed that the inflowing material would impart extra rotational energy onto the pulsar, thereby decreasing the efficiency of the pulsar spin-down.

For the most favourable scenario, that is a gaseous planet at an inclination angle of 15° , there is only a 3.4 % chance of detecting the system via pulsar timing, which is not high but still possible. Indeed, optical and X-ray observations of PSR B1931+24 during the radio-on phase show that there is no evidence for a binary companion (Rea et al. 2008). This strikes doubt into a scenario which invokes the episodic accretion from a companion source. However, in the context of the propeller regime, it has been suggested that X-ray or optical emission would only be detectable during the radio-off phases (i.e. accretion phases; Rea et al. 2008). Therefore, further observation of PSR B1931+24, particularly in the infrared and X-rays, is clearly required to confirm or disprove the presence of circumstellar material (Malov 2007) or a binary companion (Rea et al. 2008). Detection of optical and X-ray emission, however, is ultimately thought to be unlikely due to the relatively large distance (~ 4.6 kpc, from the NE2001 model; Cordes & Lazio 2002) and the inherent emission intermittency of this system (Kramer et al. 2006).

For other objects, such as ‘normal’ nulling and RRAT-like pulsars, it is unlikely that their observed emission modulation can be explained under the context of this model. Ultimately, however, it would be of great interest to conduct a high-energy observing campaign for these objects to determine if (and how) they are modulated by companion objects.

2.5.4 Geometrical Models

‘Pseudo-nulls’

The measured rotational parameters of several nulling pulsars do not differ vastly from those of conventional radio pulsars (see Fig. 2.6). Therefore, one can suggest that many of these objects only appear differently due to the inherent geometry of the observed system (Zhang et al. 2007). As such, non-detections of pulsars, over short timescales (\ll minutes), could be a manifestation of non-preferential viewing geometry, where

our line-of-sight takes an unfavourable path through the beam pattern (Deshpande & Rankin 2001). If the beam of radio emission is only grazed by our LOS and some regions within it are not populated by e^\pm pairs, then we will not see any detectable emission (c.f. the carousel model; see §1.1.2). Indeed, this effect is suggested to account for the nulling behaviour of several objects, where the timescales and (or) periodicities of *pseudo-nulls* have been attributed to the carousel rotation time (e.g. Redman et al. 2005; Rankin & Wright 2007, 2008; Force & Rankin 2010; Kloumann & Rankin 2010). Clearly, however, this model cannot be applied to all nulling pulsars, especially RRATs and intermittent pulsars, where long-term modulation in radio emission requires explanation (as well as spin-down rate variation in intermittent pulsars). Therefore, this model only serves to explain the observations of pulsars with small nulling fractions and (or) emission modulation timescales.

Reversals of Radio Emission

It has also been suggested that the nulling behaviour of pulsars may be explained by radio emission reversals in the magnetosphere (Dyks et al. 2005; Melikidze & Gil 2006). In this model, which is based on observations of mode changes in PSR B1822–09, our LOS crosses the emission beams of both the traditional outward and non-traditional inward-directed emission during the reversal phase (Dyks et al. 2005), thereby accounting for mode changes and even nulls when a particular beam pattern is sampled by the observer. In this model, it is predicted that X-ray emission will be produced by the returning particle flow (i.e. emission reversals) whose (non-)detection could be used as a possible model discriminator (e.g. Zhang et al. 2005; Gil et al. 2006; Zhang et al. 2007). In the context of intermittent pulsars, this model is subject to the same caveat as several others, where changes in spin-down rate cannot be reconciled. At least for intermittent pulsars, therefore, this model can be discounted.

Chapter 3

The Emission Modulation Properties of PSR B0823+26

PSR B0823+26 was one the first pulsars discovered (Craft et al. 1968) and, as such, has been observed for over 40 years, allowing its emission properties to be studied in some detail (Hesse & Wielebinski 1974; Ritchings 1976; Clegg et al. 1993; Rathnasree & Rankin 1995; Bhat et al. 1999a; Everett & Weisberg 2001; Wang et al. 2005; Becker et al. 2004). This source is known to exhibit nulls typical of other nulling pulsars (Ritchings 1976; Rathnasree & Rankin 1995). However, we have recently also found evidence for longer term variation in its radio emission, which is described here. We present the analysis of approximately 153 days of unprecedented, high-cadence observations of PSR B0823+26. Using this data, we characterise the pulse intensity modulation of the source. We also investigate its spin-down behaviour to determine whether it displays any evidence for magnetospheric-state changing as seen in Lyne et al. (2010) and, ultimately, what relationship it has with the intermittent class of pulsars (Kramer et al. 2006). We find that this pulsar exhibits a continuum of nulling timescales (i.e. minutes up to several hours) which, subsequently, could link its behaviour to several other objects. The observed prevalence of nulls towards shorter timescales ($\lesssim 6$ minutes) suggests that the radio emission from PSR B0823+26 is highly variable. We place a limit on the spin-down rate variation of this source to be $\lesssim 6\%$. We conclude that single-pulse observations are required to probe the behaviour of this pulsar in more detail, and confirm whether longer null durations are absent of sporadic emission.

3.1 Background

Despite the normal appearance of PSR B0823+26, in relation to its spin and characteristic properties as shown in Table 3.1¹, this pulsar is by no means ordinary. It possesses an inter-pulse (IP) and post-cursor (PC) component (Backer et al. 1973), which are both typically a few percent of the main-pulse (MP) peak intensity. This instantly places the source in a subset of approximately 3 % of the normal population of pulsars that display an IP component of emission (Maciesiak & Gil 2011). Its scintillation properties are also found to be unusual. At an observing frequency of 1400 MHz, Clegg et al. (1993) determined that the pulsar undergoes diffractive scintillation over periods of 10 – 30 minutes² (15 minutes on average) across a bandwidth at least as great as 40 MHz, which is seemingly normal for such a close source. However, they also found that this object displays sharp changes in its diffractive scintillation pattern over timescales \lesssim 2 minutes, which are thought to be a result of multiple-imaging effects from refractive scintillation. A study by Rathnasree & Rankin (1995), over three observing runs, also showed that the pulsar has a nulling fraction $NF \sim 6.4 \pm 0.8\%$. Furthermore, they found that PSR B0823+26 shows unusual time varying polarisation behaviour with corresponding profile shape changes, which are indicative of mode-changing.

Table 3.1: Observed and derived properties of PSR B0823+26, with standard 1- σ errors. The distance was obtained from parallax measurements of the object (Gwinn et al. 1986).

Parameter	Value
Right Ascension (J2000)	08 ^h 26 ^m 51 ^s .383(2)
Declination (J2000)	+26° 37' 23".79(7)
Epoch of frequency (modified Julian day)	46450.00
Rotational frequency ν (Hz)	1.88444396743(9)
Rotational frequency derivative $\dot{\nu}$ (s^{-2})	-6.0700(3) $\times 10^{-15}$
Flux density at 1400 MHz S_{1400} (mJy)	10(2)
Dispersion measure DM (cm^{-3} pc)	19.454(4)
Characteristic age τ (Myr)	4.92
Surface magnetic field strength B (G)	0.96×10^{12}
Spin-down luminosity \dot{E} (erg s^{-1})	4.50×10^{32}
Distance (kpc)	~ 0.36

¹The properties of PSR B0823+26 are taken from the ATNF pulsar catalog (Manchester et al. 2005), which is available at <http://www.atnf.csiro.au/research/pulsar/psrcat>.

²The fluctuation in the scintillation timescale is attributed to refractive interstellar scintillation, which manifests as a result of large-scale inhomogeneities in the interstellar electron density (Wang et al. 2005; see also §2.1).

In addition to these unique emission properties, PSR B0823+26 is also found to exhibit pulsed soft X-ray emission (Becker et al. 2004), which makes it only one out of nine old pulsars ($1 \text{ Myr} < \tau < 20 \text{ Myr}$) that produce high-energy emission (Becker et al. 2004; Tepedelenlioğlu & Ögelman 2005; Zhang et al. 2005; Becker et al. 2006; Kargaltsev et al. 2006; Hui & Becker 2007; Gil et al. 2008; Li et al. 2008). Its energy spectrum is indicative of non-thermal X-ray emission and its luminosity is consistent with the source being powered solely by rotation (Becker et al. 2004). Consequently, the high-energy emission is thought to be magnetospheric in origin, being produced either through synchrotron emission in the outer gap (Cheng et al. 1998) or via Inverse Compton scattering in the polar gap region (Zhang & Harding 2000).

PSR B0823+26 has been monitored with the Lovell Telescope at Jodrell Bank since February 1969. In recent high-cadence observations it was noted that the pulsar exhibits longer than previously recorded nulls, making it appear similar to PSR B1931+24. Stimulated by these findings, and the knowledge that PSR B1931+24 displays emission correlated changes in spin-down rate (Kramer et al. 2006), high-cadence observations were carried out over ~ 153 days in an effort to gain insight into the mechanism(s) which regulate such emission modulation. These data represent the most comprehensive study of the intermittent behaviour of this pulsar thus allowing direct comparison with PSR B1931+24 and conventional nulling pulsars.

3.2 Observations

The observations of PSR B0823+26 were obtained with the Lovell Telescope over a period of approximately 153 days (1 January 2009 to 3 June 2009). These data were obtained using the Analogue Filter Bank (AFB) and Digital Filter Bank (DFB)³ back-ends using a 1400 MHz receiver, with an approximate cadence of 4 observations per day (see Table 3.2 for details).

In addition to this typical daily monitoring, we performed three observations with the AFB which spanned the entire time the source is above the horizon at Jodrell Bank (see Table 3.3 for details). These data were obtained to compare the long-term variation with possible short timescale modulation. As a result, there are significantly more observations with this back-end compared with the DFB. Despite the deficit in the number of observations, the data obtained with the DFB is complementary to the emission modulation study due to better sensitivity and availability of greater bandwidth.

³The DFB was commissioned approximately 20 days after the start of the AFB observations.

Table 3.2: System characteristics of the observations of PSR B0823+26 described here. The values quoted for the DFB back-end are with respect to times prior to and post MJD ~ 54922 respectively.

System Property	AFB	DFB _{pre}	DFB _{post}
Time span of observations	153.3 days	77.3 days	60.9 days
Total number of observations	1274	284	281
Typical observation duration	6 mins	6 mins	6 mins
Average observation cadence	8.3 days ⁻¹	3.7 days ⁻¹	4.6 days ⁻¹
Typical sky frequency	1402 MHz	1381.5 MHz	1373.875 MHz
Typical observing bandwidth	32 MHz	112.75 MHz	128 MHz
Typical channel bandwidth	1 MHz	0.25 MHz	0.25 MHz

Table 3.3: The observation properties for the three continuous observing intervals during January 2009. Each continuous observing run has a length T_{obs} , for which there are N_{obs} separate observations.

Start Epoch (MJD)	T_{obs} (days)	N_{obs}
54837.7215	0.6390	152
54854.6844	0.6623	155
54857.7146	0.6067	145

3.3 Emission Modulation

The denser coverage provided by the AFB observations meant that they were used for characterising the overall emission modulation properties of PSR B0823+26. To determine whether the pulsar was radio-on or -off, we used the average profiles formed over the entire bandwidth for each approximately 6 minute long observation. This was done by visual inspection and resulted in a times-series of one-bit data corresponding to the ‘radio activity’ of the pulsar; that is, 1’s for observations with detectable emission (integrated pulses representative of the pulsar, with a signal-to-noise ratio $\text{SNR} \gtrsim 1$) and 0’s for observations with non-detectable emission (integrated pulses dominated by receiver noise or radio frequency interference). To complement the visual inspection, we also made use of the timing model to confirm detections. A time-of-arrival (TOA) was calculated for each observation and was compared to the known timing model. Those in good agreement, i.e. without large time offsets (\sim second) and measurement uncertainties, were confirmed as detections.

Figure 3.1 shows an example of an observation where the pulsar is observed to transition between the radio-on and radio-off phases. The transition timescales between the emission phases for this pulsar are similar to those seen in PSR B1931+24 (i.e. of the order of seconds). Such sharp discontinuities in pulse intensity are inconsistent

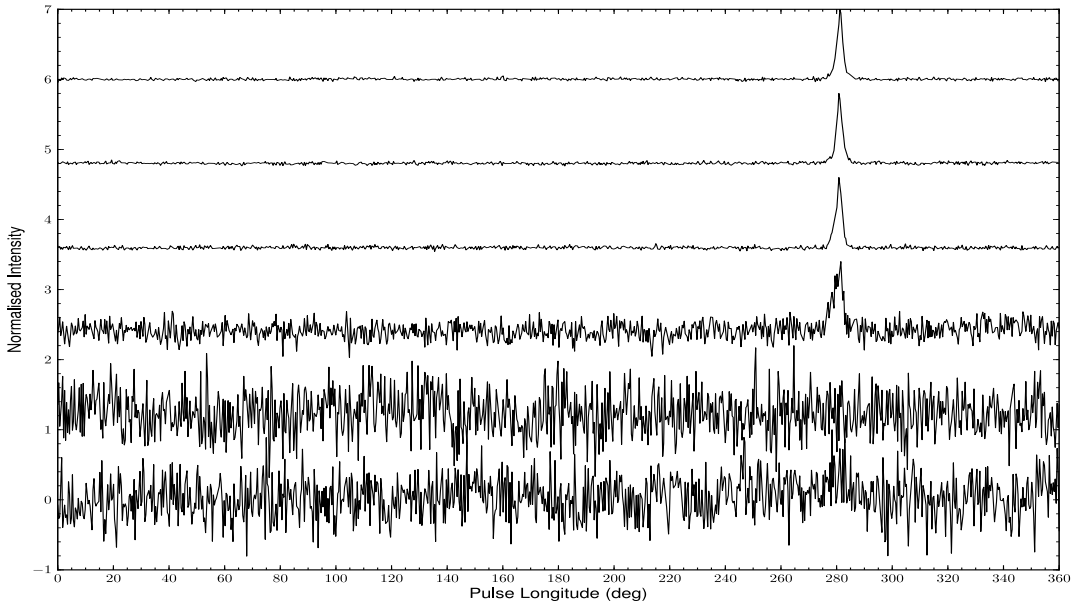


Figure 3.1: Consecutive pulse profile sub-integrations for PSR B0823+26 (*from top to bottom*) which were obtained in one observation on 10 May 2009. The pulse intensity of each sub-integration is normalised to one and is offset from the next profile for clarity. The pulsar is detectable in the first four sub-integrations (~ 60 seconds each), after which it abruptly ‘switches off’. This transition occurs sometime during the fourth sub-integration over a timescale of less than one minute.

with interstellar scintillation (see §2.1). Therefore, these transitions between emission phases are considered to be intrinsic to the pulsar.

Due to the greater sensitivity, we used the DFB data to provide limits on the average pulse flux density during the separate phases of emission. Considering a period-averaged observation of length T , with an equivalent pulse width W_{eq} and signal-to-noise ratio SNR, the mean flux density can be calculated by the modified radiometer equation (Lorimer & Kramer 2005):

$$S \sim \frac{\beta \text{SNR} T_{\text{sys}}}{G \sqrt{n_p B T}} \sqrt{\frac{W_{\text{eq}}}{P - W_{\text{eq}}}}. \quad (3.1)$$

Here, $\beta \sim 1$ is the digitisation factor, $G \sim 1 \text{ K Jy}^{-1}$ is the telescope gain, $T_{\text{sys}} \sim 35 \text{ K}$ is the system temperature, $n_p = 2$ is the number of polarisations, $B = 128 \text{ MHz}$ is the observing bandwidth, $P = 531 \text{ ms}$ is the pulsar period and $W_{\text{eq}} = 10 \text{ ms}$. We averaged a total of 202 radio-on and 6 radio-off observations, which correspond to total integration times of $T \sim 1174.2$ minutes and ~ 33.6 minutes for the radio-on and -off

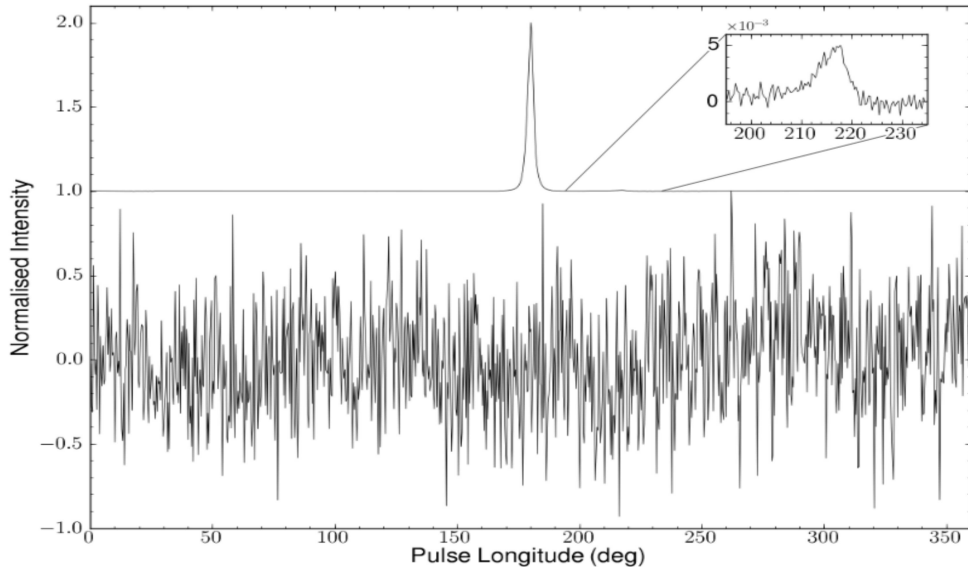


Figure 3.2: Time averaged pulse profiles of PSR B0823+26 for the radio-on (*top*) and radio-off (*bottom*) observations respectively, which are offset for clarity. The maximum pulse intensities are normalised to one. The inset plot shows a zoom-in of the PC emission in the radio-on profile (see §6 for more details), using the same axes units as the main plot. Note that the y-axis of the inset plot represents the intensity offset from one.

phases respectively. The resultant time-averaged profiles are shown in Fig. 3.2. We place a limit on the mean flux density in a radio-off phase $S_{\text{off}} \lesssim 0.022$ mJy (SNR ~ 3), which is approximately 100 times fainter than that of the radio-on phase $S_{\text{on}} \sim 2.18$ mJy (SNR ~ 1900). Converting these parameters into pseudo-luminosities, using (Lorimer & Kramer 2005)

$$L_{1400} \equiv S_{1400} d^2, \quad (3.2)$$

we find $L_{1400,\text{off}} \lesssim 2.9 \mu\text{Jy kpc}^2$ and $L_{1400,\text{on}} \sim 0.29$ mJy kpc 2 . We note that the pseudo-luminosity of PSR B0823+26 in the radio-off phase is approximately six times fainter than the weakest known radio pulsar PSR J2144–3933 ($L_{1400} \sim 20 \mu\text{Jy kpc}^2$; Lorimer 1994). Therefore, we conclude that the radio-off phases are consistent with emission cessation.

In Fig. 3.3, we show an ‘activity plot’ which indicates when the pulsar was observed and whether it was radio-on or -off. The radio emission in PSR B0823+26 is clearly seen to undergo modulation over variable timescales, which are much shorter than that typically observed in PSR B1931+24 (see §4).

The short-term emission modulation of PSR B0823+26 was probed using the data intervals of continuous observations, which are detailed in Table 3.3. These three data

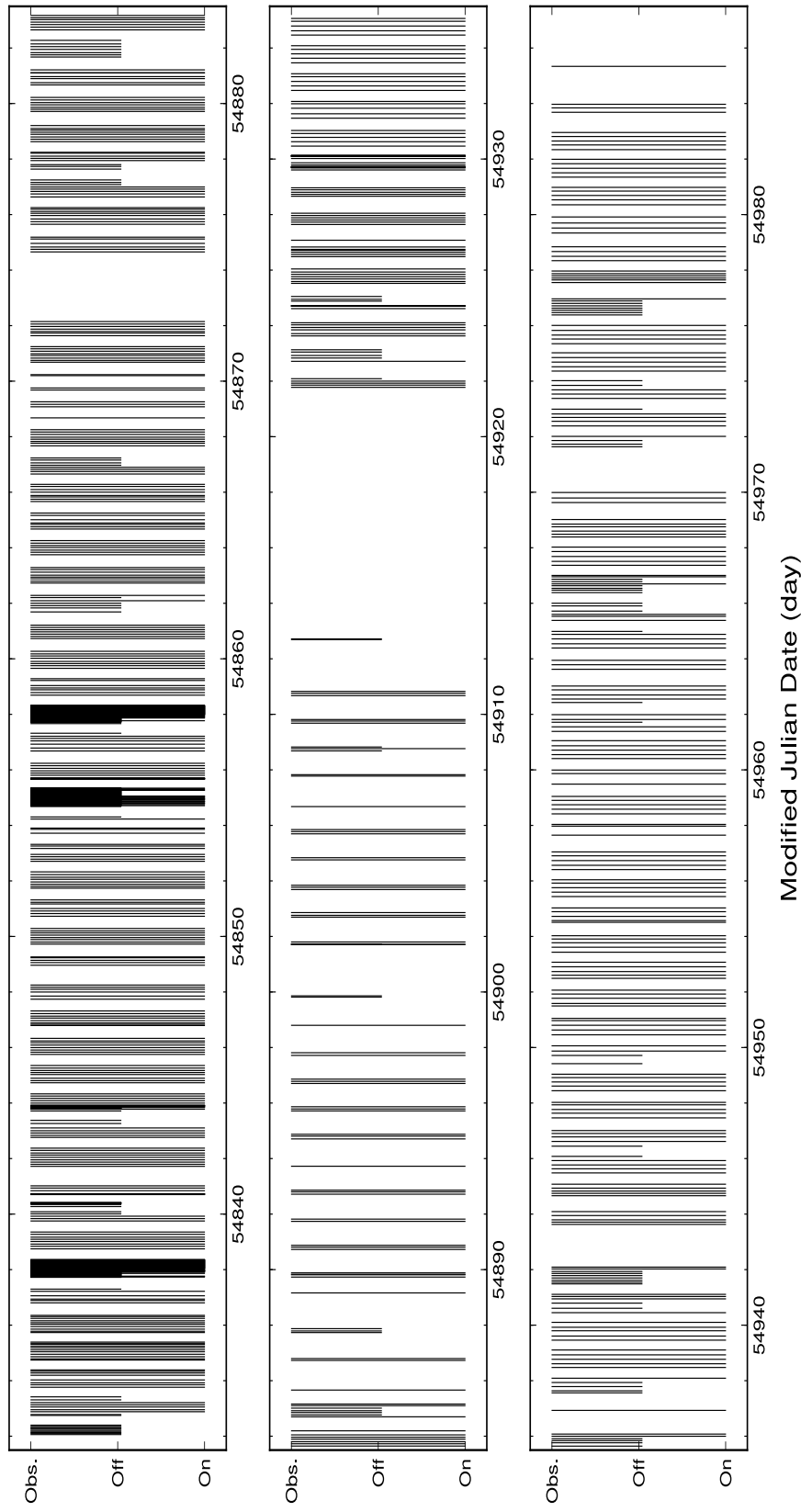


Figure 3.3: The sequence of observations of PSR B0823+26 carried out over the 153-day period, denoted by the black lines. The data are separated into three continuous $N \sim 54$ day panels. The times of observation and the times when PSR B0823+26 was radio-on (full-amplitude) and -off (half-amplitude) are shown by the extent of the black lines. The times of more intensive observing sessions are shown at MJD $\sim 54838, 54855$ and 54858 .

sets, shown in Fig. 3.4, display evidence for ‘emission flickering’, that is the radio emission from this pulsar can be observed to modulate strongly before a constant emission phase is assumed. During these ‘flicker’ phases, the radio emission sporadically changes in detectability. However, the flicker phase pulses do not appear to have unique properties; the radio-on pulses exhibit the same scintillation behaviour and can appear as strong as those in the constant radio-on phases. This behaviour is, therefore, not that dissimilar to pulse nulling typically seen in other sources, as there is a distinct separation between emission modes. From these observations, it may be inferred that intermittent pulsars undergo a radio emission ignition phase before attaining the necessary criteria for stable emission. However, this behaviour could just be specific to PSR B0823+26 and, therefore, requires the study of other intermittent candidates to associate it to the population class as a whole.

The start and end points of each emission phase were defined as the mid-points between radio-on and -off transitions i.e. the times exactly half-way between consecutive observations, when the pulsar changes from radio-on to -off and vice versa. Emission phase durations were subsequently calculated from the difference of these two values (see Fig. 3.5). The average time that the pulsar exhibited detectable radio emission was 1.4 ± 0.3 days. Whereas, the average radio-off timescale was 0.26 ± 0.04 days. The activity duty cycle (ADC), the percentage of time in the radio-on phase, was calculated from the ratio of the total radio-on duration to the total observation time. The uncertainty in this value was calculated from the ratio of the standard error in the radio-off time to the mean radio-off time. Subsequently, the pulsar is found to be radio-on for $80 \pm 10\%$ of the time.

It is clear that this pulsar possesses two distinct distributions of emission phase durations (or switching timescales) corresponding to the separate emission states. Overall, however, it appears that there is a bias towards short ($\lesssim 0.2$ days) emission phase durations, which is quite the opposite of PSR B1931+24 (i.e. days to weeks; see §4).

We were also interested in studying the flux density evolution of the pulsar following the work of Lyne & Ashworth (1983); van Leeuwen et al. (2002). In particular, van Leeuwen et al. (2002) performed an in-depth investigation into the nature of the mode changes observed in PSR B0809+74, and found that they were correlated with almost all nulls. In two sequences of observations they discovered that the drift rate remarkably decreased by $\sim 50\%$ after nulls, compared with the normal drift rate, after which it returned to the normal mode typically after several pulses. In addition, it was observed that the first pulse after a null was brighter than the average, which is the opposite of what is expected assuming a finite decay (rise) time in the emission around a null. The last pulse before a null, however, was indeed observed to be relatively less bright than

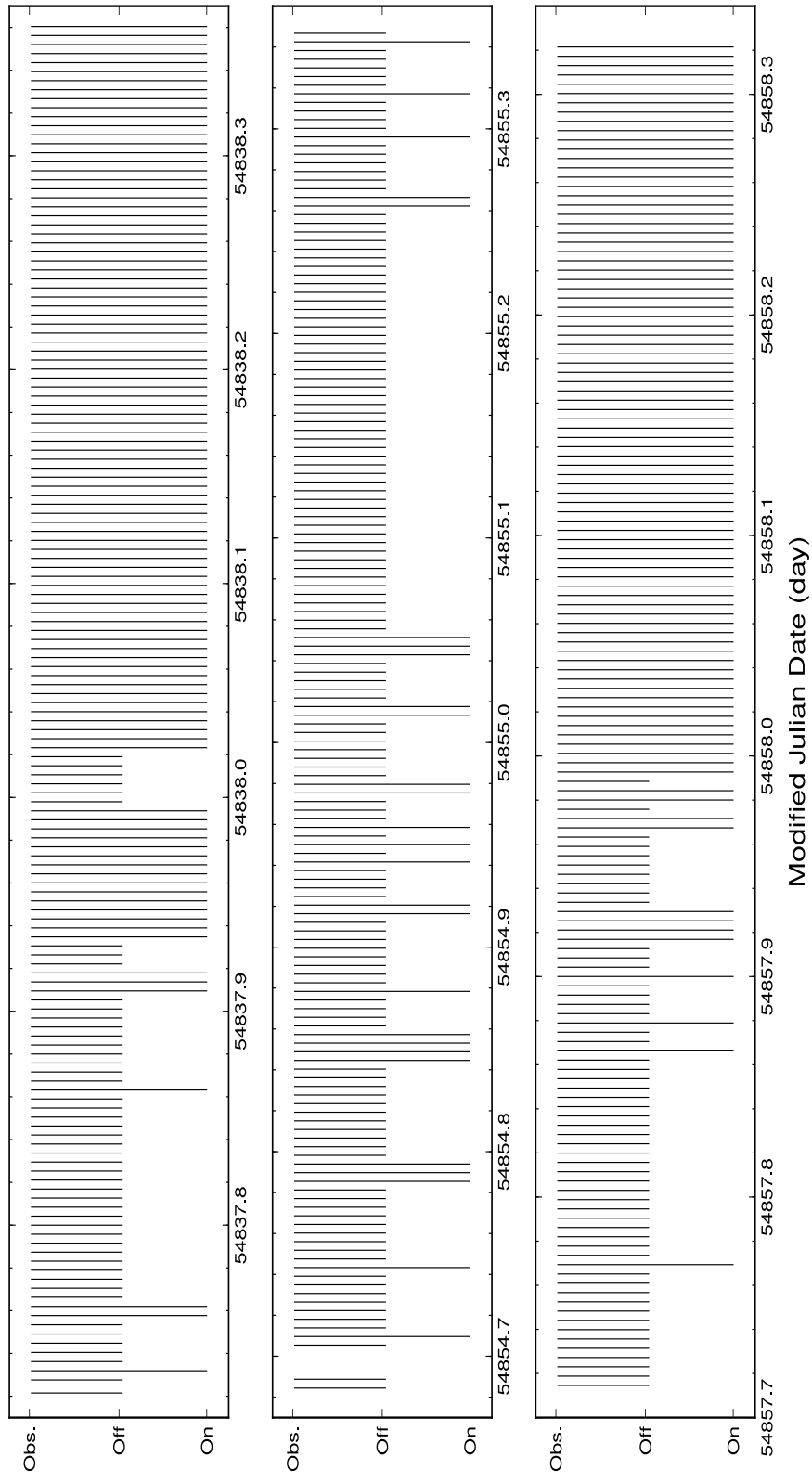


Figure 3.4: Three sequences of continuous observations of PSR B0823+26 during January 2009. The times when the pulsar was radio-on and -off are shown by the extent of the black lines.

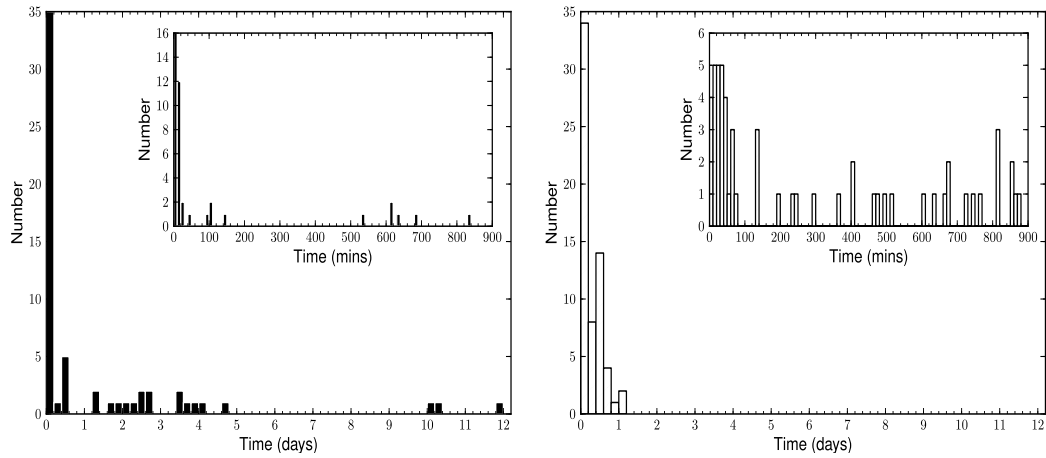


Figure 3.5: Histograms of the emission phase durations of PSR B0823+26, radio-on (*left*) and radio-off (*right*), with inset plots of the radio emission activity for timescales up to 15 hours.

the average, with a decay time less than 5 % of the pulse period. The positions of the first post null pulses were also found to be offset in pulse-longitude compared with the average and last active pulses, which is consistent with the jump in subpulses over the null.

Unfortunately, for the case of our current study of PSR B0823+26, single-pulse profile data were not available (see §6). Therefore, we were limited to using the integrated pulse profiles to discern any brightness pattern in the emission phases. Given that the observations were not flux calibrated, the observation system was assumed to remain approximately constant over the observing period. We then used a modified form of Eqn. 3.1 to determine the pulse intensity evolution of PSR B0823+26:

$$S_{\text{rel}} \sim \frac{\text{SNR}}{\sqrt{BT}}. \quad (3.3)$$

We determined the ‘relative’ flux density for all the radio-on observations across the entire data set. We also computed the average value attributed to each radio-on phase. To determine whether there existed any significant changes in pulse intensity, we calculated the difference between the individual values of S_{rel} and the respective averages for each emission phase using the AFB data. The result of this work is shown in Fig. 3.6.

We were particularly interested in determining whether there existed a discrepancy between the average pulse intensity and that of the first observation preceding (following) a radio-off phase, i.e. to determine the viability of a finite rise (decay) time in pulse intensity after (prior to) a null. We computed the averages of the relative flux densi-

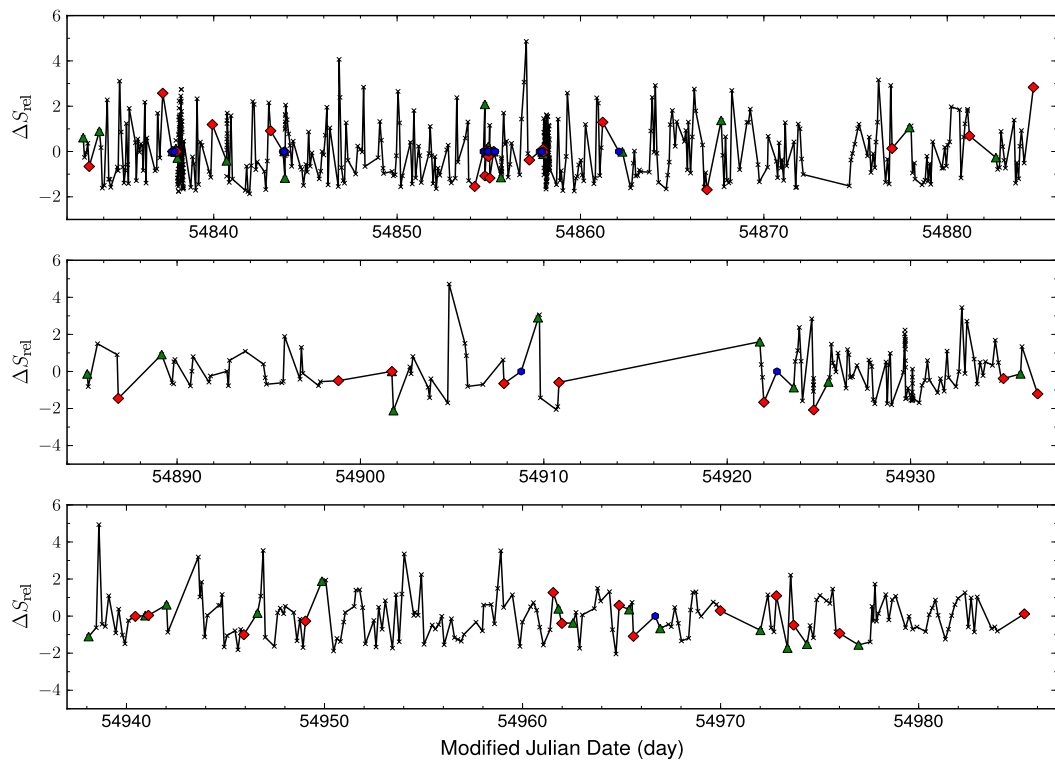


Figure 3.6: The evolution of the pulse flux density (after subtraction of the mean) across each radio-on phase for PSR B0823+26. The initial and final flux densities for each radio-on phase are denoted by the green triangles and red diamonds respectively. Emission phases where there was only one radio-on observation are shown by the blue hexagons and are zero by definition. The evolution of the pulse brightness in these observations suggests that there is no correlation with the ‘post’ or ‘pre-null’ state.

ties for the first and last observations of the radio-on phases. We also performed this analysis for the differences between these quantities and the averages of each emission phase. However, we find no evidence to suggest a systematic trend in the pulse flux density with respect to the pulse number preceding (following) a radio-off phase. We also performed linear regression on the data, to compare the relationship between pulse intensity and the length of a given active phase of emission. Using this analysis, we again find no evidence to suggest a significant trend in the pulse flux density evolution of PSR B0823+26. Table 3.4 shows the main results of this analysis. It is apparent that the variations in the relative flux densities of these observations are not significantly correlated with the ‘post-null’ or ‘pre-null’ state. Rather, the variation is random which is indicative of brightness variation due to scintillation or intrinsic behaviour.

Table 3.4: Results obtained from the relative flux density analysis of the AFB observations. The units here are arbitrary due to the assumptions made in the parameter calculations.

Statistic	S_{rel}	ΔS_{rel}	$\Delta S_{\text{first on}}$	$\Delta S_{\text{last on}}$
Mean	1.72	-1.91×10^{-16}	0.00309	-0.135
Median	1.57	-0.0631	0.0142	-0.0219
Standard Deviation	1.27	1.15	0.971	0.992

3.4 Periodicity Analysis

Periodicity analysis of astrophysical sources allows insight into the mechanisms which regulate their behaviour. In the case of PSR B1931+24, we have seen that the pulsar undergoes quasi-periodic radio emission modulation which is linked to its spin-down variation (Kramer et al. 2006). It has been suggested that this behaviour is due to dramatic reconfigurations in the pulsar magnetosphere (Contopoulos 2005; Kramer et al. 2006; Lyne et al. 2010; Hobbs et al. 2010; Timokhin 2010; Li et al. 2012a,b; see also §2.5.2). However, even in the most up-to-date simulations (Li et al. 2012a), there is no explanation to suggest why such changes would be (quasi-)periodic, or why they would occur over certain timescales. In order to elucidate such emission cessation behaviour, therefore, we have performed periodicity analysis on the modulation behaviour of PSR B0823+26. We initially consider periodogram analysis to understand the basic characteristics of the data, and then proceed to use WWZ analysis to obtain more detailed information.

3.4.1 Periodogram Analysis

In order to ascertain information about the emission cessation timescales of this pulsar, we performed Welch modified-periodogram analysis on the one-bit time-series data (see §B.2.1 for a detailed overview of the method). Firstly, this entailed computing the auto-correlation function (ACF) of the data with 0.1-day time lags. The ACF data was then separated into $N = 512$ data point segments, which overlapped by 50 %, and were windowed (tapered) using a Bartlett window function (Eqn. B.9). We then fast fourier transformed these data and averaged the spectra to obtain the averaged periodogram for all the data segments. Through performing this analysis, we were able to reduce the noise signature in the estimated power spectrum (periodogram), at the cost of compromising on frequency resolution. Figure 3.7 shows the result of this analysis.

The periodogram indicates the presence of multiple periodicities in the one-bit time-

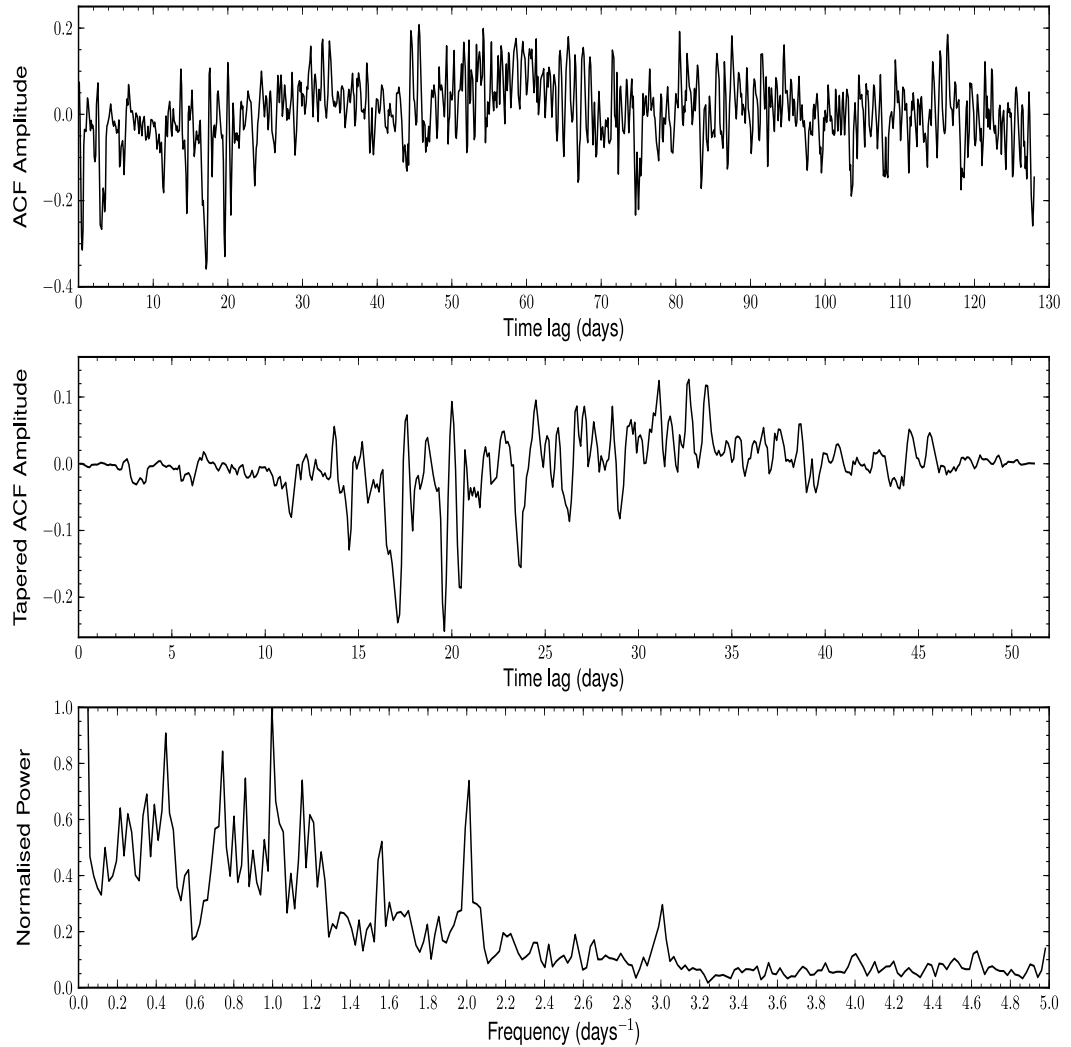


Figure 3.7: Welch periodogram analysis of the radio emission activity of PSR B0823+26 for observations spanning from 1 January 2009 to 6 March 2009. *Top:* ACF of the activity data, binned into 0.1-day time lags. *Middle:* The first tapered ACF segment used in the computation of the Welch periodogram (the segment length $N = 512$). *Bottom:* Normalised Welch periodogram of the ACF data, showing multiple features. Due to the number of peaks in the estimated power spectrum, it is difficult to discern the true fluctuation frequency of the source.

series data. However, it is unclear whether these features are intrinsic to the behaviour of the source; the emission activity of PSR B0823+26 may be highly irregular or, alternatively, there might be significant spectral leakage in the periodogram due to aliasing (i.e. sampling effects). The most prominent spectral features are present at $\sim 0.425 \text{ days}^{-1}$, $\sim 0.75 \text{ days}^{-1}$, $\sim 1 \text{ days}^{-1}$ and $\sim 2 \text{ days}^{-1}$ (corresponding to $\sim 2.4 \text{ days}$, $\sim 1.3 \text{ days}$, $\sim 1 \text{ day}$ and $\sim 0.5 \text{ days}$ respectively). We note that these features do not appear to be particularly significant, due to the degree of noise variations in the periodogram. The periodicity of 0.5 days is also coincident with the length of time the source is visible during a given day. Furthermore, due to the distribution of power in this periodogram - most likely because of the random nature of PSR B0823+26's radio emission activity - it is also possible that the latter spectral components could be attributed to harmonics of the lower frequency component around 0.425 days^{-1} .

3.4.2 WWZ Analysis

To determine whether the periodicities obtained in the periodogram analysis were significant, and whether they evolved with time, we also computed the weighted wavelet Z-transform (WWZ) of the one-bit time-series data (see §B.2.2 for a detailed overview of this method). The resultant 2-D transform showing the evolution of the peak fluctuation frequency (period) at successive epochs (time lags) is displayed in Fig. 3.8.

The WWZ of the PSR B0823+26 one-bit time-series data exhibits very sporadic structure. This is believed to be a result of data sampling on the local matching of the WWZ wavelet function. During the first ~ 40 days of the data-set, the observation sampling is at its greatest, with no gaps and $\sim 5 - 10$ observations per day (or more). The three continuous observing intervals are also included in this date range. Consequently, the data obtained over this period of time accounts for $\sim 62\%$ of the total. We find that the data sampling in this observing period is sufficient for the matched wavelet function to return power at several fluctuation frequencies. The most prominent of these features is at approximately $\sim 0.44 - 0.36 \text{ days}^{-1}$ ($\sim 2 - 3$ days). As the data sampling worsens with time, becoming more irregular (roughly a few observations per day) with occasional gaps (one is more than 10 days), there comes a point at which the prominent fluctuation frequencies of the system are no longer resolved.

In order to clarify the significance of these variations, we simulated several data-sets using the observed data sampling. We created model data-sets with single periodicities, ranging from 0.25 days to 10 days, and analysed them with the WWZ. We also performed WWZ analysis on a random model data-set. For the random data, we do not recover any dominant periodicities. For the data with an intrinsic periodicity, however,

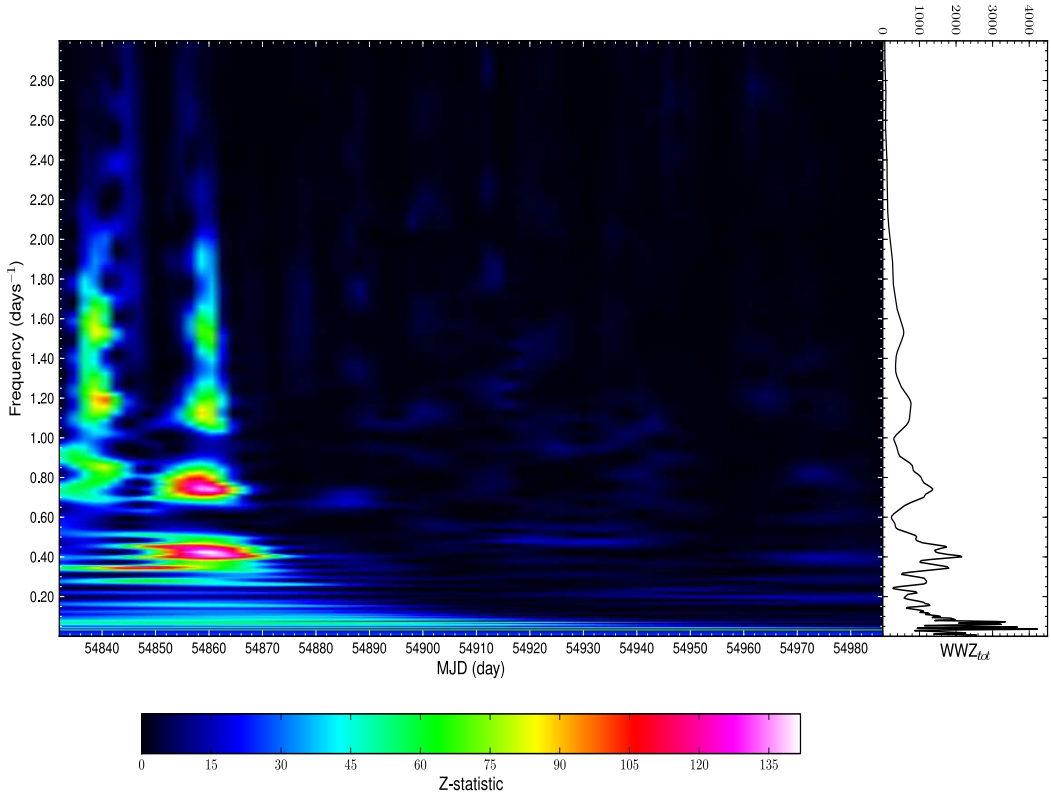


Figure 3.8: WWZ transform of the 153-day PSR B0823+26 radio emission activity data-set (*left*) and the corresponding integrated power spectrum (*right*). During the initial ~ 40 days of the data-set, the observation sampling is sufficient to resolve several prominent features. These spectral components are also accompanied by a broad distribution of power towards higher frequencies, which are most likely attributed to Fourier harmonics. At later times ($MJD \gtrsim 54872$), the reduced data sampling does not allow insight into the dominant fluctuation frequencies.

we find that the fundamental frequency is resolved at virtually all epochs⁴. However, the fundamental spectral component is also accompanied by a broad distribution of power and is substantially less significant after the first 40 days⁵. For periods of the order of a day, we note that the distribution of power is similar to that observed in the real data, thus indicating that our results are modulated by data-windowing effects. We note that the higher period components in the observed data ($\sim 10 - 30$ days) are most probably not related with the physical system. This is because the full-width of the wavelet window used in this analysis is approximately 10 cycles which, consequently, will not provide meaningful results for a data-set whose length is of the order

⁴Around $MJD \approx 54913 - 54922$ there is a gap in the observations, which often results in a substantial decrease in the WWZ power.

⁵The power relating to a time-frequency component in the WWZ signifies its significance (Bedding et al. 1998).

of the width of the wavelet (see §B.2.2). We conclude that there may be a number of fluctuation frequencies present in the data, analogous to more irregular radio emission behaviour, and that they are only resolved during the periods of time where there is the most frequent observation sampling.

As shown in §B.3, it is extremely difficult to derive analytic estimates for errors in the WWZ. Therefore, we rely upon more pragmatic methods to derive confidence estimates on the periodicities within the data. Following Templeton et al. (2005) (see also §B.3.1), we used the *confusion limit* method to estimate the peak fluctuation frequencies (periods) and their maximum $1-\sigma$ uncertainties. The result of this analysis is shown in Fig. 3.9. The average error in the fluctuation frequency (period) from the confusion limit estimation method is $\sim 11\%$. The variation in the dominant periodicity, within the first 40 days, is above the error limit. However, we are uncertain as to whether this is truly intrinsic to the source. It is more likely that the pulsar possesses a multitude of periodicities in its radio emission behaviour, with a dominant component of $\sim 2 - 3$ days, or that the system is highly irregular.

We also split the transform data into 14-day segments, in order to compute a measure of the modulation in the peak frequency and period. Table 3.5 shows the results of the data windowing method outlined in §B.3.2. The median peak fluctuation frequencies (periods) for the first three segments of the transform data are $\sim 0.42 - 0.35 \text{ days}^{-1}$ ($\sim 2 - 3$ days). We estimated the significance of periodicities within the WWZ data using a bootstrapping approach (e.g. Zoubir, A.M. & Iskander, D.R. 2004; see also §B.3.3). We determined the average standard deviation of the transform data from successive resamples and assumed a $5\sigma \approx 80$ WWZ power level as a confident signal detection. Consequently, we find that the median-peak WWZ values of the windowed data are significant for $\text{MJD} \lesssim 54872$. Whereas, those afterwards do not meet the cut-off criteria.

In order to elucidate the effect of the observation sampling on the data, and confirm the significance of periodicities, we applied the delete-d jackknife resampling method (e.g. Shao, J. & Tu, D. 1995; Politis, D.N. et al. 1999; see also §B.3.3) to the WWZ analysis. Here we define a resample size or percentage $f = d/n$, where d is the proportion of data which is randomly ‘deleted’ i.e. removed from the time-series data of size n . We computed the WWZ for the one-bit time-series data using several trial resample sizes. The central concept of the optimisation procedure is that the combined standard deviation of the upper and lower confidence interval end-points (a.k.a. *volatility index*) of the transform are calculated and compared for each successive resample size. The resample size which subsequently has the smallest volatility index is determined to be the optimum. Unfortunately, however, we find that this method cannot be applied

Table 3.5: Median-peak WWZ values and fluctuation frequencies (periods) for consecutive 14-day segments of transform data for PSR B0823+26. Uncertainties are quoted as $1-\sigma$ values.

MJD range	WWZ _{max}	$\Delta(\text{WWZ}_{\text{max}})$	ν_{fluc} (days $^{-1}$)	$\Delta(\nu_{\text{fluc}})$ (days $^{-1}$)	P_{fluc} (days)	$\Delta(P_{\text{fluc}})$ (days)
54832–54846	94	25	0.35	0.39	2.9	1.0
54846–54860	125	9	0.42	0.05	2.4	0.3
54860–54874	113	32	0.40	0.12	2.5	4.0
54874–54888	63.9	0.2	0.0728	0.0001	13.79	0.02
54888–54902	62	1	0.0728	0.0001	13.75	0.02
54902–54916	57	1	0.04	0.02	28.0	7.4
54916–54930	57.4	0.3	0.0357	0.0000	28.0	0.0
54930–54944	58.0	0.1	0.0357	0.0000	28.0	0.0
54944–54958	58.1	0.1	0.03570	0.00004	28.01	0.03
54958–54972	57.5	0.3	0.0356	0.0000	28.09	0.00
54972–54986	56.3	0.5	0.0356	0.0000	28.09	0.00

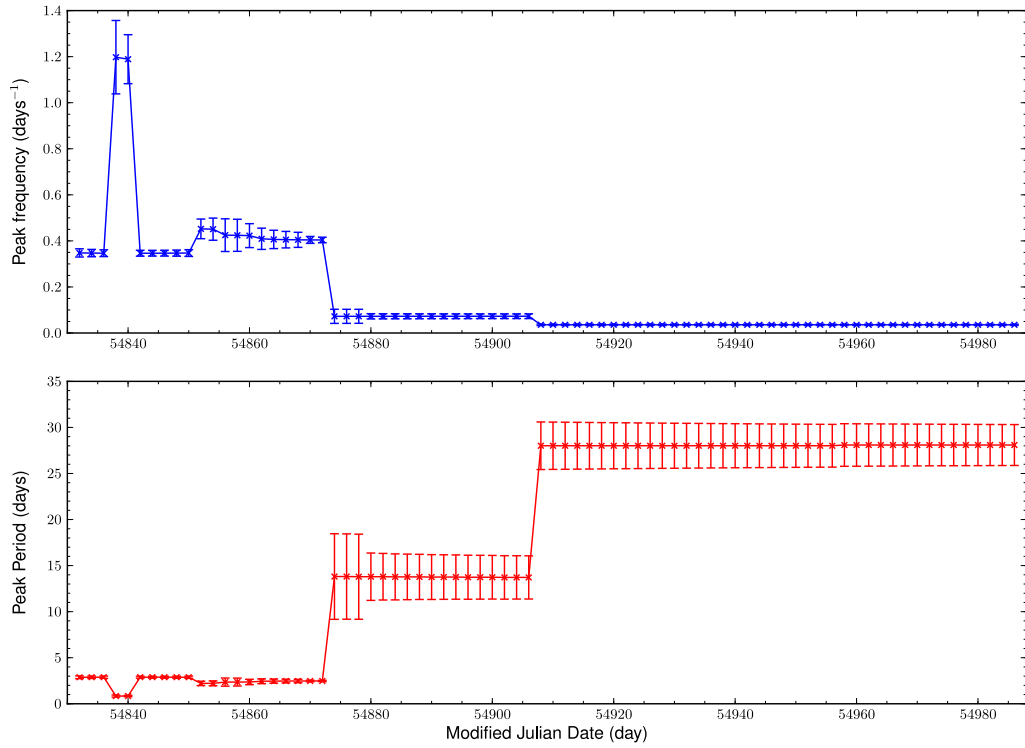


Figure 3.9: The peak fluctuation frequencies (*top*) and periods (*bottom*) from the weighted wavelet Z-transform data. Error bars are $1-\sigma$ values computed using the confusion limit estimation method (uncertainties for individual epochs). The average error in the peak fluctuation frequency (period) is $\sim 11\%$. For the first 40 days, the peak fluctuation period is typically $\sim 2-3$ days apart from at a couple of epochs (~ 0.8 days), which may represent a variation in the intrinsic periodicity. After $MJD \gtrsim 54872$, the data sampling becomes poorer, and more irregular, which favours the smaller (non-physical) peak fluctuation frequencies.

effectively to the WWZ error analysis of these data. This is because the confidence intervals of the WWZ data, based on the mean, do not constrain a region of values even if a conservative 68 % (i.e. $\pm 1\sigma$) interval is assumed; for the observed WWZ data, $\langle \text{WWZ} \rangle \sim 7$ and $\sigma(\text{WWZ}) \sim 15$. Therefore, we conclude that the bootstrap resampling method (e.g. Zoubir, A.M. & Iskander, D.R. 2004; see also §B.3.3) is a more favourable method of determining constraints on the significance of WWZ values.

3.5 Timing Behaviour

Intermittent pulsars are expected to show indications of (quasi-)periodic behaviour in their timing residuals, which appear as cubic structure due to mode-changing between a given set of spin-down rates (Kramer et al. 2006; Hobbs et al. 2010; Lyne et al. 2010; see also §2.5.2). To determine whether PSR B0823+26 conforms to this model, we analysed the timing measurements obtained from the 153-day AFB data-set. We obtained the topocentric times-of-arrival (TOAs) using PSRPROF⁶ and analysed them using the TEMPO2⁷ package (Hobbs et al. 2006). The resulting residuals from a best-fit timing model (Table 3.6) are shown in Fig. 3.10.

Table 3.6: The properties of PSR B0823+26 obtained from timing measurements presented here. The standard $1-\sigma$ errors are provided in the parentheses after the values, in units of the least significant digit.

Parameter	Value
Right Ascension (J2000)	$08^h 26^m 51\overset{.}{s}489$
Declination (J2000)	$+26^\circ 37' 23\overset{.}{s}706$
Epoch of frequency (modified Julian day)	54909.0
Rotational frequency ν (Hz)	1.884439516337(1)
Rotational frequency derivative $\dot{\nu}$ (s^{-2})	-5.997(1) $\times 10^{-15}$
Dispersion Measure DM (cm^{-3} pc)	19.464

We find that there is no significant evidence for quasi-periodicity in the 153-day AFB timing residuals. However, this is not that surprising considering the short timescales of emission variation. Even if the pulsar experiences the same fractional change in spin-down rate as PSR B1931+24, $\frac{\Delta\dot{\nu}}{\langle\dot{\nu}\rangle} = 45\%$, the source would only exhibit a change in rotational frequency ($\sim 10^{-10}$ Hz) that is approximately 10^3 times smaller than the measurement accuracy over the timescale of a day. Therefore, it is possible that the object alternates between spin-down rates, consistent with the magnetospheric-state changing scenario (Lyne et al. 2010), but we are not sensitive to the variations in the timing residuals. This idea will be explored in much more detail in the following section.

⁶<http://www.jb.man.ac.uk/pulsar/observing/progs/psrprof.html>

⁷<http://www.atnf.csiro.au/research/pulsar/tempo2/>

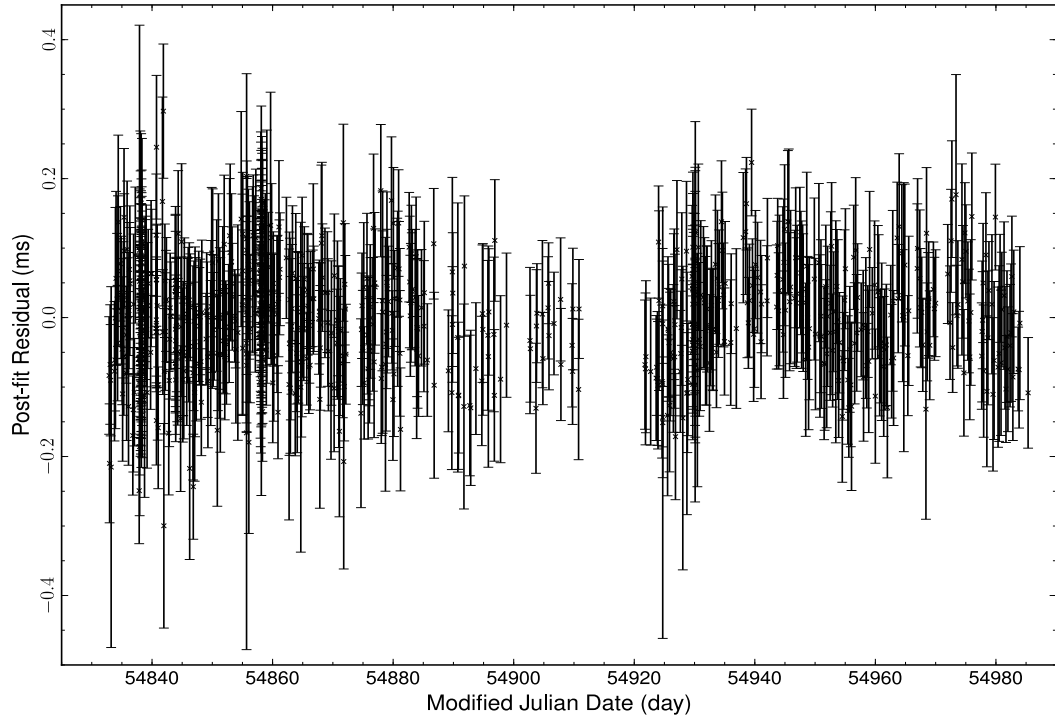


Figure 3.10: Post-fit timing residuals for PSR B0823+26 from the 153-day AFB dataset, after fitting for ν and $\dot{\nu}$. There is no apparent cubic structure in the timing residuals.

3.6 Simulations

3.6.1 Overview

To determine whether the timing measurements of PSR B0823+26 could be consistent with a variable spin-down model, we developed a simulation tool to reproduce the timing behaviour of intermittent pulsars. This tool is based on Monte-Carlo method experimentation, whereby we define a parameter space of trial radio-on and -off spin-down rates ($\dot{\nu}_{\text{on}}$ and $\dot{\nu}_{\text{off}}$) to produce simulated timing residuals that are compared with the observed. In addition to the radio-on and -off spin-down rates, the tool relies upon an initial rotational frequency, ν_0 , and average fitted rotational frequency derivative, $\dot{\nu}_{\text{av}}$, to simulate the timing noise of an object. These additional parameters are determined from fitting the pulsar's rotational and orbital parameters from the observed data using TEMPO2. The source's emission activity is represented by distributions which model the observed radio-on and -off emission phase durations, and are randomly sampled for each simulation trial (i.e. we produce pseudo-random generated number distributions,

PRGN). Consequently, the timing residuals of each trial represent one possible outcome, for a given pair of spin-down rates, considering a pulsar which exhibits variable emission activity.

As the spin-down rate of the model pulsar alternates between consecutive emission phases, the rotational frequency is updated at each integer step in pulse number:

$$\text{TOA} = \frac{n}{\nu} + t_{\text{ref}} . \quad (3.4)$$

The reference time t_{ref} corresponds to the total time elapsed at the last step and n is the number of pulses in each emission mode. The rotational frequency ν is updated using

$$\nu = \nu_{\text{ref}} + (\dot{\nu}_{\text{phase}} \times \Delta t) , \quad (3.5)$$

where ν_{ref} at the last step, $\dot{\nu}_{\text{phase}}$ is the spin-derivative in the corresponding emission phase and Δt is the duration of the emission mode.

These simulated TOAs are those that would be measured at the Solar System Barycentre (Barycentre reference frame) and are inclusive of additive white Gaussian noise (AWGN)⁸. For each simulated TOA, this noise signature is calculated from a randomly selected error bar from the observed data; a random number is generated from a Gaussian distribution with a full-width at half-maximum (FWHM) that is twice the size of the error bar. To track pulsar rotation in time, TOAs for radio-on and radio-off phases are calculated. The radio-off phase TOAs are the theoretical TOAs which an observer would measure if the pulsar was detectable.

Before the data is analysed, the rotational frequency has to be corrected. For each combination of $\dot{\nu}_{\text{on}} - \dot{\nu}_{\text{off}}$, the value for ν_0 is different due to their contributions, and results in a systematic offset in the data. Considering only the radio-on phase TOAs, to accurately simulate the observations, an average ν is fitted to the data using TEMPO2 to remove this effect. The simulated TOAs for each $\dot{\nu}_{\text{on}} - \dot{\nu}_{\text{off}}$ trial combination are then analysed using TEMPO2 to provide post- ν -fit root-mean-square (RMS) values. These RMS values serve as the minimisation criteria for the simulation, whereby the comparison of simulated values with the observed allows insight into the possible spin-down rate variation of the pulsar.

3.6.2 Analysis

To calibrate the simulation tool, and test its functionality, it was applied to the prototype intermittent pulsar PSR B1931+24. Kramer et al. (2006) show that there is clear

⁸AWGN offsets are used to simulate instrumental noise.

quasi-periodic, cubic structure in the timing residuals of this pulsar and fit the data to obtain $\dot{\nu}_{\text{on}} = -16.3 \pm 0.4 \times 10^{-15} \text{ s}^{-2}$ and $\dot{\nu}_{\text{off}} = -10.8 \pm 0.2 \times 10^{-15} \text{ s}^{-2}$. As a consistency check, we analysed the same data-set using a number of trial spin-down rates within the stated uncertainties. TOAs obtained between 4 May 2003 and 9 October 2003 with the Lovell telescope were analysed using TEMPO2 to determine ν_0 and $\dot{\nu}_{\text{av}}$, and to create a corrected ephemeris, to perform the analysis. We find that the simulation tool reproduces the timing behaviour of PSR B1931+24 well, as shown in Fig. 3.11, for $\dot{\nu}_{\text{on}} = -16.1 \times 10^{-15} \text{ s}^{-2}$ and $\dot{\nu}_{\text{off}} = -10.8 \times 10^{-15} \text{ s}^{-2}$.

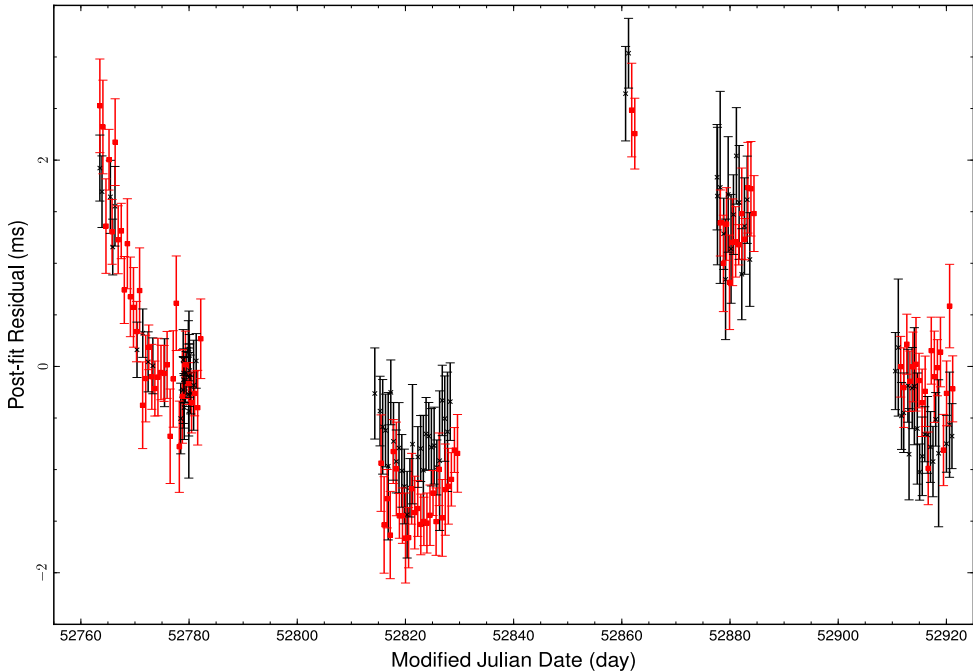


Figure 3.11: Observed (*black crosses*) and simulated (*red squares*) timing residuals of PSR B1931+24, using the same data as that in Kramer et al. (2006) but with slightly different spin parameters. The results of the simulation are consistent with the timing behaviour of the source.

We used the same approach to obtain ν_0 and $\dot{\nu}_{\text{av}}$ for the PSR B0823+26. Constraints on the $\dot{\nu}_{\text{on}} - \dot{\nu}_{\text{off}}$ combinations for this pulsar are derived from its ADC and fitted $\dot{\nu}_{\text{av}}$. By definition, the average fitted rotational frequency derivative is

$$\dot{\nu}_{\text{av}} = (t_{\text{on}} \times \dot{\nu}_{\text{on}}) + (t_{\text{off}} \times \dot{\nu}_{\text{off}}), \quad (3.6)$$

where t_{on} and t_{off} are the fractional times that the pulsar is in the radio-on and -off emission phases respectively. Thus, the parameter space of spin-derivatives to test was defined as $-6.06 \leq \dot{\nu}_{\text{on}} (10^{-15} \text{ s}^{-2}) \leq -5.99$ and $-6.0 \leq \dot{\nu}_{\text{off}} (10^{-15} \text{ s}^{-2}) \leq -5.6$

(assuming a small variation in the spin-down rate between emission phases). The spin-derivatives are inherently constrained by $\dot{\nu}_{\text{av}} \sim -5.997 \times 10^{-15} \text{ s}^{-2}$, so that neither $\dot{\nu}_{\text{on}}$ or $\dot{\nu}_{\text{off}}$ can physically cross this boundary. For each combination of input parameters, the post- ν -fit RMS was calculated for 2000 iterations of the simulation tool using a resolution of $2 \times 10^{-18} \text{ s}^{-2}$. These data were then averaged to obtain a residual RMS contour map, as seen in Fig. 3.12. The parameter space of $\dot{\nu}_{\text{on}} - \dot{\nu}_{\text{off}}$ where the RMS converges on the observed value is seen to be distributed (within observational errors) towards the central diagonal portion of the plot.

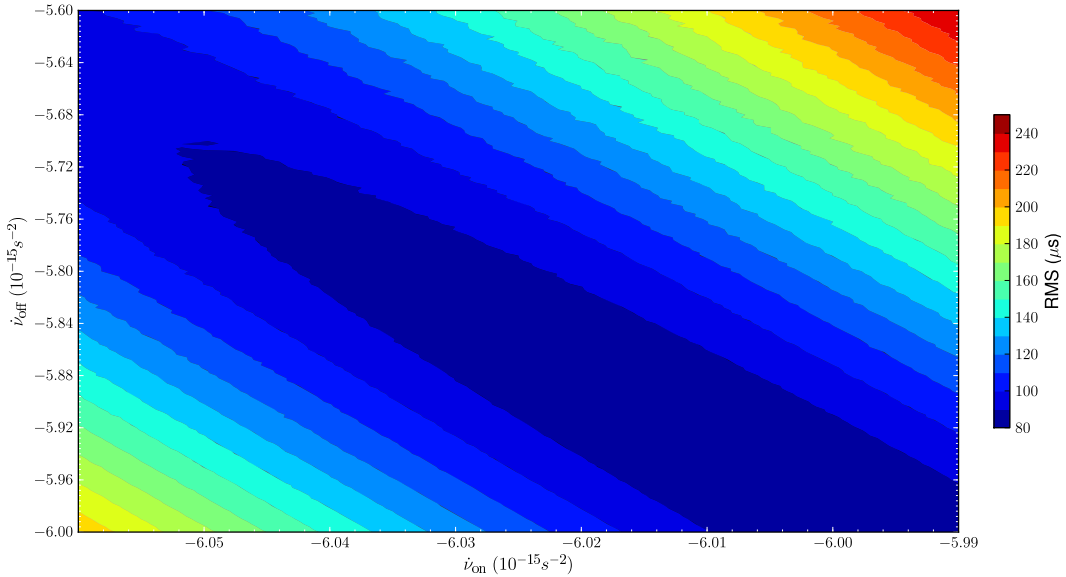


Figure 3.12: Residual contour map obtained from simulations of the timing behaviour of PSR B0823+26, for given combinations of rotational frequency derivatives. The plot shows the distribution of post- ν -fit RMS for the specified range of $\dot{\nu}_{\text{on},\text{off}}$, with the contours denoting RMS levels for the given parameters. The diagonal region in the middle of the plot shows the area of acceptable $\dot{\nu}$ combinations. The observed timing RMS is $80 \pm 10 \mu\text{s}$.

The constraints on the post- ν -fit RMS in the simulations are obtained from the measured uncertainty of this value in the real data. This was calculated using TEMPO2 to fit the observed data across individual segments. The average and standard deviation of the sample population of RMS values were computed, and then used to obtain the fractional error and measured uncertainty in the post- ν -fit RMS. Assuming a 3σ error in the RMS, the constraints on the simulated results are $\text{RMS} = 80 \pm 10 \mu\text{s}$. Consequently, we find that the maximum increase from $\dot{\nu}_{\text{off}}$ to $\dot{\nu}_{\text{on}}$ ($\Delta\dot{\nu}_{\text{max}}$) which satisfies the criteria is approximately 6 %.

As the emission phase durations are sampled randomly from the model distribu-

tions, there exists a variance in the computed average RMS for each combination of input parameters. The statistical uncertainties in these values are taken as the fraction of the standard deviations of the sample populations over the averages. Consequently, we find that the results of the simulation tool are less variable for $\dot{\nu}$ values which are closer to the observed average; the variance in the results from the simulated residuals has to be smaller for the simulation to be consistent with the observations. Despite the fact that the simulation tool can be applied to any intermittent pulsar, it is ideally suited to modelling those with small $\Delta\dot{\nu}$ as least-squares fitting methods, such as the method implemented by Kramer et al. (2006), will be more efficient for larger $\Delta\dot{\nu}$; the simulation tool can provide an upper limit to $\Delta\dot{\nu}$, which is independent of curve-fitting analyses that may falter when analysing timing signatures with little cubic structure.

3.6.3 Switching Timescale Dependency

Further to the analysis of the simulated data, the effects of altering the emission phase durations and ADC were investigated. We were interested in determining whether our results were subject to systematic effects and how they were affected by modelling the emission behaviour differently.

Firstly, we investigated the effect of over or under-estimating the observed emission phase durations. We added systematic errors to the observed durations, t_{obs} , from $\pm 0\%$ to $\pm 100\%$ of t_{obs} in steps of 5% (to make 21 realisations in total), with the polarity of the error being determined by a random number generator. We noted that as the percentage error was increased, so did the average post- ν -fit RMS. This is attributed to an increasing variance in the emission phase durations, that causes greater fluctuations in the timing residuals; the model pulsar assumes a spin-down rate for longer or less than observed, which results in larger scale variations in the timing residuals. We find that the tolerance of the post- ν -fit RMS to systematic errors increases towards smaller variations in the spin-down rate. This is particularly true for the combinations of spin-parameters which were comparable with the average spin-down rate; the results of the simulation remained consistent with the observed even for an error of $\pm 100\%$ in the emission phase durations. We also performed a simulation trial assuming the maximum change in spin-down rate, $\Delta\dot{\nu}_{\text{max}} \sim 6\%$, using the observed switching times without any systematic errors. This produced a post- ν -fit RMS which is greater than that observed. However, this result is only derived from one trial and, as such, is not expected to be as consistent as averaging over many simulated results. In addition, the value quoted for the maximum change in spin-down rate inherently serves as an upper limit. It is possible that the pulsar may undergo more modest variations

in its spin-down; simulations incorporating these spin-parameters produce results that are more consistent with observations. However, it is evident that systematic errors in the observed emission durations would have a significant effect on the results. As such, timing studies of intermittent pulsars will be more conclusive for better sampled data-sets.

We also tested our assumption that the emission activity of PSR B0823+26 can be modelled by randomly sampling two distributions of emission phase durations. We performed trials using randomly ordered emission phase durations from the observed distributions and compared them with the results of the randomly sampled model data, as well as the original observed data. We find that the average post- ν -fit RMS values from these trials are all consistent. Therefore, we conclude that the assumptions of our simulation tool are valid.

In addition, we examined the dependency of the results on the activity duty cycle assumed. We randomised all the observed emission phase durations together, so that the ADC no longer coincided with the observed value (i.e. $\sim 50\%$). A number of $\dot{\nu}$ combinations were used in this analysis, from $\Delta\dot{\nu}_{\min}$ to $\Delta\dot{\nu}_{\max}$. However, no post- ν -fit RMS values within the observed constraints could be obtained (except for $\dot{\nu}_{\text{on}} \sim \dot{\nu}_{\text{off}}$). This indicates that the form of the distribution which is used to model the emission phase durations is fundamental to the simulation procedure.

To investigate this further, and to determine how sensitive the $\Delta\nu_{\max}$ solution was, the pseudo-random generated number distributions were also directly altered. Here, simulations were carried out where the PRGN distributions were modified to obtain two test cases, for $\sim 5\%$ decrease and increase in the ADC; we conservatively assumed a 5% uncertainty in the ADC. These simulations returned $\dot{\nu}$ matches that corresponded best with the ADC. For approximately a 5% decrease in the ADC, the maximum change in the spin-down rate was reduced, and vice versa. For a lower percentage radio-on time, $\Delta\dot{\nu}$ is required to be smaller to obtain $\dot{\nu}_{\text{av}}$, and the opposite for a higher percentage. As a result, we obtain limits on the maximum change in spin-down rate $4.5\% \lesssim \Delta\dot{\nu}_{\max} \lesssim 7.6\%$, if we assume a maximum error of $\sim 5\%$ in the modelling of the PRGN distributions. Consequently, we see that alteration to the ADC has a significant effect on the results; if the initial parameters used are wrong, the simulation tool will not converge on an optimum combination of spin-down rates. Despite the incorporation of a 5% uncertainty in the ADC, it is apparent that the upper limits on the spin-down rate variation are still small compared with that of PSR B1931+24 ($\sim 50\%$; Kramer et al. 2006).

3.7 Discussion

From the analysis of the emission cessation behaviour of PSR B0823+26, over both short and long-timescales, we infer that the determination of the timescales of emission is quite strongly affected by the observation sampling. We suspect that the periodicity analysis of the one-bit time-series data is subject to subsequent effects, due to the spurious nature of the WWZ power during times of increased observation sampling⁹. Consequently, we believe that the emission cessation of this source is better represented by the three continuous observing runs due to their increased time resolution; it is possible that the sparser sampling of the long-term observations may have resulted in missing numerous radio-on and -off states. Over the course of each continuously sampled observing period, the pulsar is observed to undergo emission modulation over timescales of minutes to hours. We infer that these are the typical modulation timescales of the source, but do not rule out the possibility of longer radio-off phases; it could be perhaps that PSR B0823+26 exhibits a distribution of radio-off timescales. In order to confirm the longer-term emission cessation behaviour, and to determine an accurate nulling fraction, long duration single-pulse observing runs are required (we refer to §6 for more on this work). Nevertheless, we find that the emission cessation behaviour of PSR B0823+26 is inconsistent with typical nulling pulsars¹⁰. We note that this pulsar may represent a bridge between normal nulling and intermittent pulsars such as PSR B1931+24; the object may be located inbetween these source types on a nulling continuum scale (Keane 2010).

We note that the determination of errors in the WWZ data is by no means trivial. We applied three techniques to investigate the significance of time-frequency components in the WWZ data. We find that the confusion limit estimation performs well at determining uncertainties in peak fluctuation frequencies. However, it does not lend itself to the determination of confidence estimation. We find that the data-windowing and bootstrap methods complement this analysis by providing significance estimates. We conclude that the delete-d jackknife resampling method is not effective for the purposes of this work. We believe that this method is best suited to less complicated analysis of time-series data i.e. non-spectral estimation based work. This is because there appears to be an arbitrary nature to the application of this method; no constraint on the choice of resample size f could be obtained.

⁹Observation sampling can cause data-windowing effects, which result in inaccurate representation of periodicities within a signal. For our data, this likely occurs as a result of the wavelet waveform instantaneously matching several frequencies analogous to the harmonics of a Fourier transform.

¹⁰Although null durations can vary significantly, between one or two pulses to days (Wang et al. 2007), they are most commonly observed over 1 – 10 pulse periods in normal pulsars.

For the first time, we have presented a simulation tool which can model the timing behaviour of an ‘intermittent pulsar’ and obtain an upper limit on its spin-down rate variation. Through simulating the rotational behaviour of PSR B0823+26, we find evidence for $\Delta\dot{\nu}_{\max} \sim 6\%$ between emission phases, leading to $\dot{\nu}_{\text{on}} = -6.05 \times 10^{-15} \text{ s}^{-2}$ and $\dot{\nu}_{\text{off}} = -5.702 \times 10^{-15} \text{ s}^{-2}$. Using numerical arguments, however, we cannot discount a scenario where there is no variation in spin-down rate between the different radio emission phases. Keeping this in mind, the maximum plasma charge density (ρ_{plasma}) associated with a particle wind emerging from this pulsar, using Eqn. A.7, is estimated to be $\sim 0.002384 \text{ C m}^{-3}$. Comparing this with the charge-density associated with the electromagnetic dipole radiation (ρ_{GJ} ; Eqn. A.8), we find that that only a small amount ($\sim 12\%$) of the total available charge from rotation can be associated with the particle wind.

For PSR B1931+24 it is suggested that the radio emission cessation results from re-configuration of the global magnetospheric charge distribution, and that the spin-down rate variation is a signature of this phenomenon (Kramer et al. 2006; Timokhin 2010; Lyne et al. 2010; Li et al. 2012a,b; see also §2.5.2). Certainly, in several other pulsars we see evidence to support this theory¹¹. However, it is not entirely clear what manner of pulse shape variation will arise due to a variable spin-down rate; in the study performed by Lyne et al. (2010), pulsars with similar changes in spin-down rate were observed to undergo different magnitudes of variation in their pulse shape. It is interesting, therefore, to find that PSR B0823+26 exhibits the same break down in radio emission production (or detectability) as PSR B1931+24 without the need for a large change in the magnetospheric currents. This implies that the mechanism which produces radio emission is highly sensitive to even the smallest changes in the magnetosphere and that mode-changing, nulling and intermittency are closely related. From this, we infer that there could be a significant number of pulsars that exhibit regulated changes in their spin-down rate and emission, which contribute to ‘timing noise’, and that we are not yet aware of them due to small fractional changes in $\dot{\nu}$ or short timescale variations.

As the variation in spin-down rate in PSR B0823+26 is not definitive, it is unclear whether the object can be taken under the umbrella of the intermittent pulsar class. Clearly, more observations of similar objects are required before a consensus is reached on the properties unique to this class, if these sources are truly separate from the rest of the pulsar population, and how PSR B0823+26 fits into this framework. It is apparent, however, that this pulsar exhibits emission cessation over timescales that are

¹¹Lyne et al. (2010) show clear evidence for correlation between pulse shape and spin-down variation in six pulsars.

not consistent with conventional ‘pseudo-nulling’ (i.e. due to time-varying distributions of e^\pm in subbeams; see §2.5.4); PSR B0823+26 is undetectable for periods \gg minutes, which far exceed the estimated carousel rotation times in several other pulsars (c.f. $\lesssim 10^2 P$; Redman et al. 2005; Rankin & Wright 2007, 2008; Force & Rankin 2010). It is also unlikely that the nulls in this object are observed due to emission beam reversals (see §2.5.4); the pulsar is an orthogonal rotator ($\alpha \sim 86^\circ$; fitting for the main pulse and post-cursor component) with a very small beam inclination from our LOS (i.e. an impact angle of $\sim -3^\circ$) (Everett & Weisberg 2001). Therefore, the most natural explanation is that the pulsar undergoes mode changes between radio-on and radio-off, or extremely weak, phases of radio emission due to some unknown magnetospheric process. As such, simultaneous, multi-frequency (e.g. radio and X-ray) observations of this source should be carried out to determine the mechanism(s) responsible for its emission behaviour.

3.8 Conclusions

We have found evidence to suggest that PSR B0823+26 exhibits a broad distribution of nulling timescales i.e. \lesssim minutes up to several hours or more. Although longer duration nulls (\sim day) have been observed in our data, we cannot rule out the presence of short-term variations \lesssim minutes in the radio-off phases which we are insensitive to; radio emission flickering, which was observed in the continuous observing runs, could have occurred during times of low observation cadence and, hence, been missed. As such, long (\sim hours), single-pulse observations of this pulsar are required to confirm its emission intermittency timescales and, therefore, its periodicity, that is if the source does not exhibit random emission fluctuations (see §6 for a more in-depth discussion). Although we find evidence for a maximum variation in spin-down rate of approximately 6 %, we cannot rule out a scenario where the pulsar retains a constant, single $\dot{\nu}$. Therefore, the connection between PSR B0823+26 and intermittent pulsars remains elusive. Further study of this source, and others like it, however, should reveal significant information about the nature of ‘normal’ nulling pulsars, RRATs and intermittent pulsars. This should also help to determine how all these objects are related (if they are), what their typical characteristics are and what mechanism is governing their irregular behaviour.

Chapter 4

Further Investigation into the Emission Modulation Characteristics of PSR B1931+24

PSR B1931+24 is a well known pulsar, with intermittent emission and rotational properties which are so extraordinary that the source is the prototype for its own behavioural class. Despite the work of several authors, the mechanism responsible for its intermittent behaviour remains elusive (Kramer et al. 2006; Zhang et al. 2007; Rea et al. 2008; Timokhin 2010). Further to the work of Kramer et al. (2006), we present an analysis of approximately 13 years of observations of PSR B1931+24. Using this extensive data span, we analyse the timescales of emission modulation to determine whether they evolve over time. We also investigate the time evolution of the spin-down rates to see if they vary, and to possibly obtain a value for the braking index of the source which is unaffected by the torques associated with emission. Following the work of Lyne et al. (2010), we look for pulse-shape variations to determine whether any shorter term emission modulation exists, which might link the behaviour of this object to phenomena such as nulling or moding. We find that PSR B1931+24 exhibits an average modulation timescale of approximately 36 days, which is remarkably stable over many years. We also find evidence to suggest that the pulsar retains a very high degree of memory; the object appears to retain the same spin-down rate values, attributed to each emission mode, over the 13-year observation span. Subsequently, we confirm that the source undergoes $\sim 50\%$ change in spin-down rate, when transitioning between its different emission modes. In addition, no evidence is found to suggest that the pulsar exhibits any sporadic emission during the radio-off emission states.

4.1 Background

Kramer et al. (2006) showed that PSR B1931+24 is an intermittent pulsar; it undergoes long duration, quasi-periodic quiescent phases (i.e. radio-off phases) over timescales $\sim 25 - 35$ days, with active phases (i.e. radio-on phases) of emission lasting approximately $\sim 5 - 10$ days. Its emission cessation behaviour is observed to be broadband and is found to be correlated with the spin-down rate of the pulsar. During radio-on phases, the radio emission from this source appears very similar to that of a normal isolated pulsar. However, in these phases the source has a spin-down rate which is $\sim 50\%$ greater than that in the radio-off phases (Kramer et al. 2006). The properties of this pulsar are summarised in Table 4.1.

Table 4.1: The properties of PSR B1931+24 from Kramer et al. (2006). The standard ($1-\sigma$) errors are provided in the parentheses after the values, in units of the least significant digit. The distance is derived from the NE2001 model (Cordes & Lazio 2002).

Parameter	Value
Right Ascension (J2000)	$19^h 33^m 37.832(14)$
Declination (J2000)	$+24^\circ 36' 39.6(4)$
Epoch of frequency (modified Julian day)	50629.0
Rotational frequency ν (Hz)	1.2289688061(1)
Rotational frequency derivative $\dot{\nu}$ (s^{-2})	$-12.2488(10) \times 10^{-15}$
Rotational frequency derivative on $\dot{\nu}_{\text{on}}$ (s^{-2})	$-16.3(4) \times 10^{-15}$
Rotational frequency derivative off $\dot{\nu}_{\text{off}}$ (s^{-2})	$-10.8(2) \times 10^{-15}$
Spin-down rate variation $\Delta\dot{\nu}/\dot{\nu}_{\text{off}}$ (%)	51(2)
Dispersion measure DM ($\text{cm}^{-3} \text{ pc}$)	106.03(6)
Activity duty cycle (%)	19(5)
Characteristic age τ (Myr)	1.6
Surface magnetic field strength B (G)	2.6×10^{12}
Spin-down luminosity \dot{E} (erg s^{-1})	5.9×10^{32}
Distance (kpc)	~ 4.6

PSR B1931+24 is particularly interesting because no theory currently exists which can fully explain its radio emission. Although it does not reside in the hypothetical ‘death valley’ region of the $P - \dot{P}$ diagram (see Fig. 2.6), the source appears to cease emitting radio emission¹ on quasi-periodic timescales. As the transitions between emission phases are punctuated by changes in spin-down rate, and the fact that the radio-off phases are approximately 10^3 times longer than typical null lengths (i.e. 1 – 10 pulse

¹To the limit of our instrument sensitivity, no discernible emission is observed from the pulsar.

periods), it is highly unlikely that the cessation of emission is simply due to empty sight-line traversals of the emission beam (c.f. PSR J1819+1305 and PSR B1944+17 Rankin & Wright 2008; Kloumann & Rankin 2010; see also §2.5.4).

It is thought that the interaction of a stellar wind, or mass accretion inflow, with a pulsar magnetosphere could interfere with the emission mechanism, and result in behaviour similar to that seen in PSR B1931+24 (Stella et al. 1986; Stella et al. 1994; Cordes & Shannon 2008). However, the high-energy emission expected to be associated with such mechanisms have not been seen (Rea et al. 2008). Therefore, the cessation of the pulsed emission cannot be explained by an orbital companion, nor is it likely that the source emission is modulated by accretion from a remnant circumstellar disk. In addition, the timescales of modulation are inconsistent with those of interstellar scintillation² i.e. minutes to hours (Wang et al. 2005). Precessional scenarios are also disfavoured due to the fast transitions between states (Kramer et al. 2006; Lyne et al. 2010) and the inability of long-period precessional oscillations to be sustained over long timescales (Sedrakian et al. 1999; Frescura & Flanagan 2003; Link 2006). Therefore, it is most likely that the cessation of emission is of a magnetospheric origin (see also §2.5).

One of the most widely accepted scenarios is that there exists a multiplicity of magnetospheric states, between which the pulsar switches (e.g. Bartel et al. 1982; Contopoulos 2005; Kramer et al. 2006; Timokhin 2010; Li et al. 2012a; see also §2.5.2). These global re-distributions of current are thought to be responsible for causing alterations to the morphology of the emitting region, as well as fluctuations in the spin-down rate via associated changes in the magnetic field configuration. However, it is not clear how these alterations occur.

Recently, Jones (2011) attempted to reconcile pulsar precession with this state-switching scenario by proposing that the magnetospheric state of a pulsar is dependent on its precessional phase (see also §2.5.2). However, they were unsuccessful in incorporating PSR B1931+24 into their model. Several authors have also suggested that (thermo-)magnetic instabilities, such as small-scale multipolar magnetic field configurations, may develop through Hall-drift and (or) dynamo action (e.g. Goldreich & Reisenegger 1992; Thorsett & Dewey 1993). These instabilities are proposed to amplify localised field structures which would lead to intricate emission processes that may be intermittent in nature (e.g. Geppert et al. 2003; Urpin & Gil 2004; see also §2.5 for an overview). However, significant work is required to confirm the timescales and processes involved before a consensus can be reached.

²From the NE2001 model (Cordes & Lazio 2002), the scintillation timescale for PSR B1931+24 is approximately 4 minutes, with an associated bandwidth of ~ 1.3 MHz at an observation frequency of 1400 MHz.

4.2 Why look at PSR B1931+24 Again?

Kramer et al. (2006) provide conclusive evidence for correlated changes in spin-down rate and emission in PSR B1931+24. However, their results are based upon relatively few transitions (approximately 25 radio-on and -off states) with data sampling of approximately one observation per day and occasional gaps between emission modes. In order to characterise the behaviour of this object in more detail, we initiated a series of more intense observations with the intention of constraining emission phase transitions with greater accuracy. Through analysing this new data in combination with the previously published data-sets, we hoped to expand upon the findings of Kramer et al. (2006) and provide insight into a possible driving mechanism for the observed modulation.

In particular, we sought to take advantage of the longer observation baseline to confirm the (quasi-)periodic nature of the emission phase transitions and characterise any time-dependent variation in the spin-down rate. Through measurement of the variation in the spin-down rate in the radio-off emission phase, we hoped to obtain an accurate value for the braking index of the object that was unaffected by the torque due to emission and, hence, gain insight into the mechanism responsible for such modulation; such a measurement could provide greater insight into the dipole nature and geometry of the pulsar magnetosphere, through offering constraints on the inclination angle, magnetic field strength and energy loss of the object.

4.3 Observations

The observations of PSR B1931+24 presented here were made over the course of approximately 13 years (29 April 1998 to 19 May 2011), predominantly with the 76-m Lovell telescope and the 28×25-m Mark II telescope at Jodrell Bank. From 2006 onwards, we initiated a series of more intense observations, i.e. approximately twice-daily monitoring, in order to accurately constrain the emission phase transition times. Data was also obtained with the 94-m Nançay telescope in France so as to bridge a gap in observations during a period of extended telescope maintenance³. Two back-ends were used to acquire the Lovell observations: the Analog Filter Bank (AFB; up to May 2010) and Digital Filter Bank (DFB; since January 2009). Table 4.2 shows the typical observing characteristics for these instruments and the Nançay data.

³Between 20 October 2004 and 2 February 2005, the Lovell telescope was unable to observe PSR B1931+24 due to the discovery and replacement of a cracked tire. The Mark II telescope was used for continued timing measurements of other sources during this time.

Table 4.2: System characteristics for observations of PSR B1931+24 from 29 April 1998 to 19 May 2011.

System Property	AFB	DFB	Mark II	Nançay
Time span of observations	4403 days	856 days	3661 days	243 days
Total number of observations	3996	1168	636	78
Typical observation duration	12 mins	12 mins	42 mins	13 mins
Average observation cadence	0.90 days ⁻¹	1.37 days ⁻¹	0.17 days ⁻¹	0.32 days ⁻¹
Typical sky frequency	1402 MHz	1520 MHz	1396 MHz	1368 MHz
Typical observing bandwidth	32 MHz	384 MHz	32 MHz	64 MHz
Typical channel bandwidth	1 MHz	0.5 MHz	1 MHz	4 MHz

4.4 Emission Modulation

To quantify the timescales of emission variation, and the durations of the radio-on and -off phases attributed to PSR B1931+24, we again used the activity duty cycle (ADC) method introduced in §3.3. The one-bit data based on this analysis is shown in Fig. 4.1. In this approximately 13-year data-set, some of the observations which define the timescales of emission are separated by several days (particularly at earlier epochs). Therefore, a number of the emission phases in the data do not accurately represent the behaviour of the pulsar. Consequently, we only consider emission phases which have gaps $\lesssim 5$ days between consecutive observations, so that we can pinpoint transition times as accurately as possible. To complement this work, the one-bit time-series data was also visually inspected, to confirm the results and reject emission phases which contain failed observations; that is due to radio frequency interference (RFI). After applying these criteria we are left with only the highest confidence emission phase durations. These data were used to form the radio-on and -off phase duration histograms shown in Fig. 4.2. The average times in each emission phase are 7.8 ± 0.4 days and 22.2 ± 0.9 days for the radio-on and -off phases respectively. The average radio-on timescale is similar to that observed in Kramer et al. (2006) of ~ 6.3 days. However, the average radio-off timescale is somewhat shorter (c.f. ~ 28.4 days). We also note that the radio-on and -off timescales have a wider range of values than previously thought. These discrepancies are most likely due to the increased data span and observation cadence in our observations.

4: FURTHER INVESTIGATION INTO THE EMISSION MODULATION
CHARACTERISTICS OF PSR B1931+24

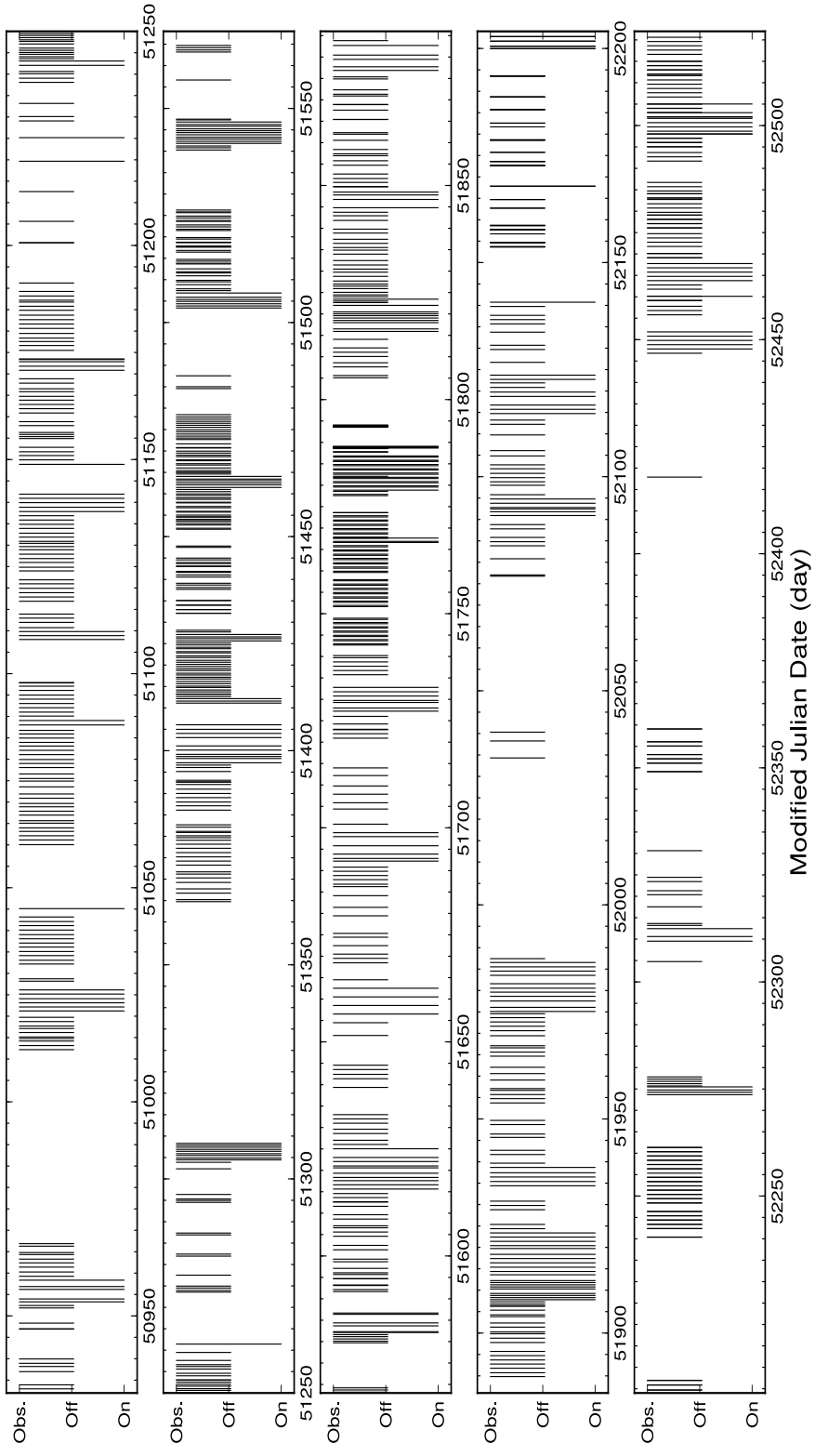


Figure 4.1: Sequence of observations, denoted by the black lines, carried out over the 13 year period. The data is separated into 15 contiguous 318-day panels. The times of observation and the times when PSR B1931+24 was radio-on (full height) and -off (half height) are shown by the extent of these lines.

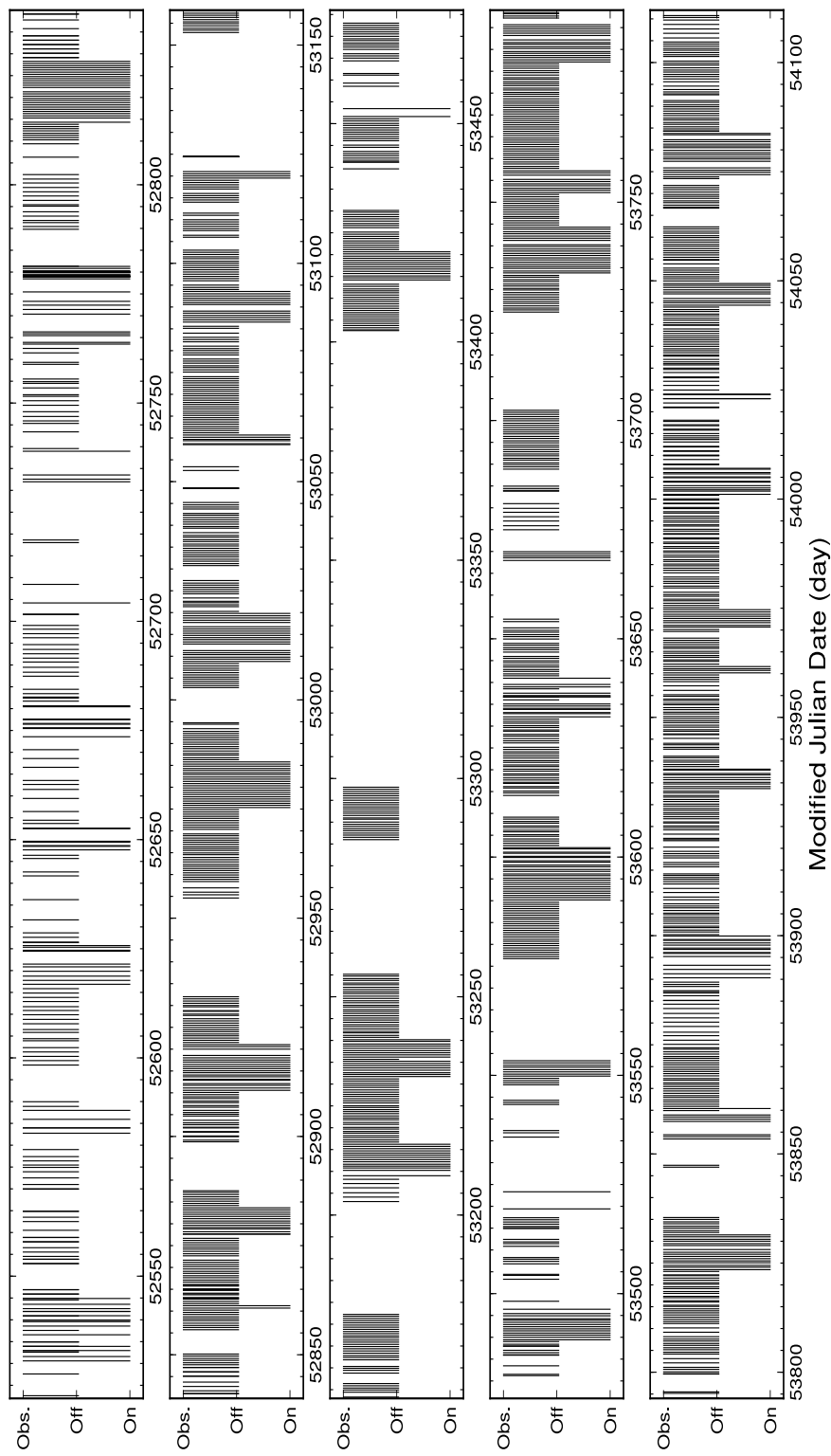


Figure 4.1: —continued. Emission modulation of PSR B1931+24.

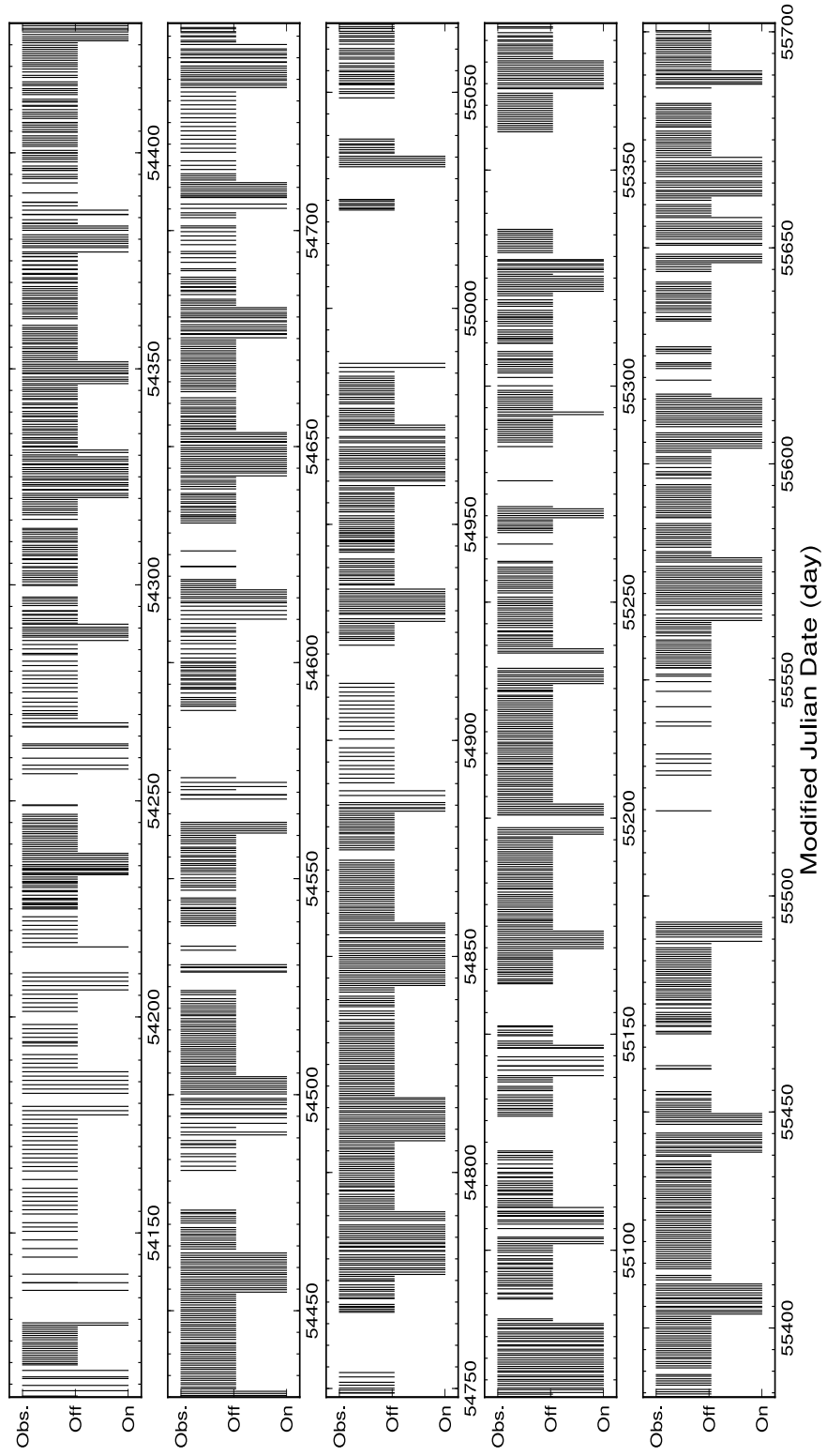


Figure 4.1: — *continued*. Emission modulation of PSR B1931+24.

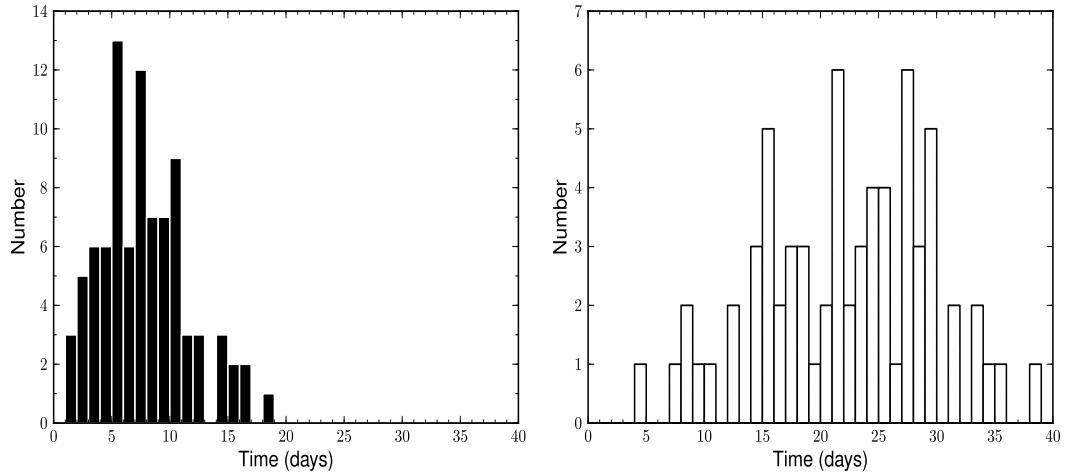


Figure 4.2: Histograms showing the durations when PSR B1931+24 is observed to be in a particular emission phase, radio-on (*left*) and radio-off (*right*).

We used the same high-confidence emission phase durations to calculate the ADC of the pulsar. Given that there are gaps between consecutive emission phases, and that there is a disparity between the number of suitable radio-on and -off phases, we determine the average total time spent in the radio-on and -off phases through bootstrapping the observed distributions of the emission phase durations⁴ (see §B.3.3 for an overview of the method). These values are used to calculate the average ADC over the entire data-set. The error in the ADC was calculated from the uncertainty in the total time spent in the radio-on phase, which was obtained from bootstrapping the observed uncertainties. This results in an $\text{ADC} = 26 \pm 6\%$ which is consistent with Kramer et al. (2006) i.e. $19 \pm 5\%$.

Having determined that the average ADC is the same as in Kramer et al. (2006) and yet the range of radio-on and -off durations is wider, we wanted to ascertain if there was any temporal evolution in these properties. Following the stride fitting method of Lyne et al. (2010), we determined the ADC over segments of length $T = 100$ days⁵, offset by intervals of $T/4 = 25$ days across the data set. We initially estimate ΔADC for each interval using the sum of the errors in the transition times between consecutive emission phase durations. Due to the irregular time sampling, however, there are also gaps between consecutive observations during emission phases. As the minimum time

⁴The data was sampled with replacement, to obtain 10^6 resamples for each distribution of emission phases.

⁵The interval length T was chosen to provide a compromise between resolution in the ADC and our sensitivity to short-term noise variations (i.e. short-term fluctuations which do not reflect the typical behaviour of the object).

4: FURTHER INVESTIGATION INTO THE EMISSION MODULATION CHARACTERISTICS OF PSR B1931+24

spent in a consecutive radio-on and -off phase is approximately 10 days, we assume that any gap between a neighbouring observation which exceeds this duration should contribute to the total uncertainty in the ADC. In order to compromise between data accuracy and volume, we apply cut-offs to the uncertainties in the data; we do not consider intervals which contain observations separated by more than 25 days or whose error in the ADC is greater than 40 %. The resultant ADC as a function of time is shown in Fig. 4.3.

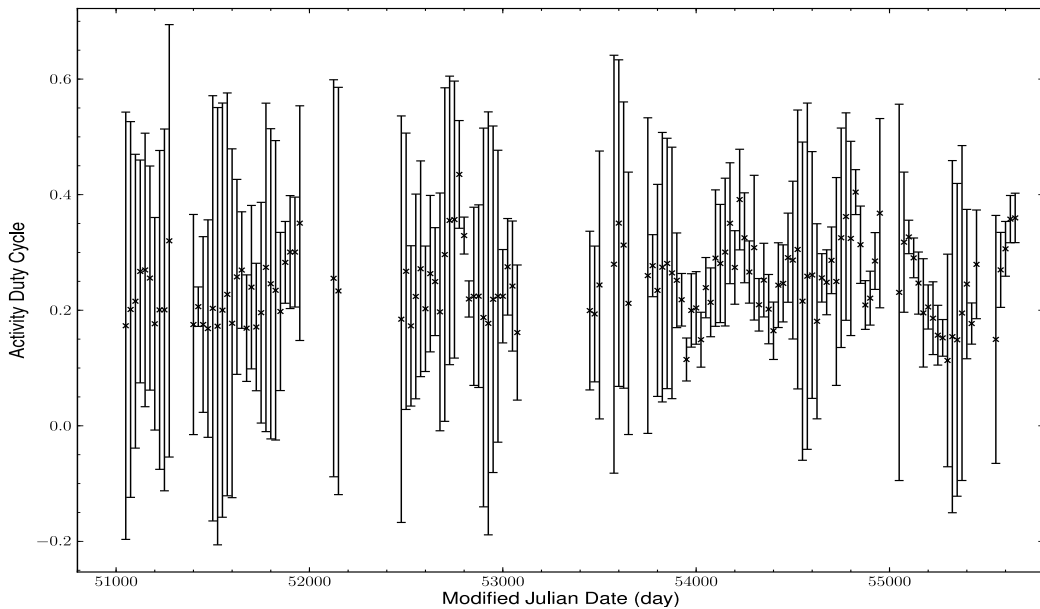


Figure 4.3: The evolution of the activity duty cycle of PSR B1931+24 over approximately 13 years of data.

We average these values (Fig. 4.3) to obtain $\langle \text{ADC} \rangle = 25 \pm 1\%$, which is consistent with that obtained by bootstrapping the emission durations. We use an Anderson-Darling test⁶ (Press et al. 1992) to determine if the ADC values are consistent with coming from a normal distribution. We find that the distribution of ADC values is consistent with a normal distribution, assuming Gaussian error bars, and that there is no compelling evidence for significant variation in the ADC of PSR B1931+24.

We also sought to determine whether there were any interdependencies in the characteristics of the pulsar emission. In particular, we were interested in discovering whether there is a correlation between the length of successive radio-on and -off phases. For this analysis, we selected nine data intervals from the entire data-set which had the highest observation cadence and, thus, the highest confidence in emission phase

⁶This test is adapted from the Kolmogorov-Smirnov test to have greater sensitivity towards the tails of a distribution (Press et al. 1992), which make it better suited to testing for normality.

durations. The properties of these data intervals are listed in Table 4.3. We correlated the durations of successive radio-on and -off emission phases, for each of these data intervals, to determine whether there was any connection between the length of consecutive emission phases (see Fig 4.4).

Table 4.3: Observation properties of the nine selected, well-sampled data intervals described here. The start and finish times of each data interval, of length T , are denoted by $\text{MJD}_{\text{start}}$ and $\text{MJD}_{\text{finish}}$ respectively. The number of emission phases which are radio-on and -off are given by N_{on} and N_{off} respectively. The average total time spent in a radio-on and -off phase are \bar{t}_{on} and \bar{t}_{off} , and the activity duty cycle of the pulsar for each data interval is denoted by ADC.

$\text{MJD}_{\text{start}}$	$\text{MJD}_{\text{finish}}$	T (days)	N_{on}	N_{off}	\bar{t}_{on} (days)	\bar{t}_{off} (days)	ADC (%)
51814.07	51924.38	110.31	4	3	7 ± 1	24 ± 2	22 ± 8
52762.52	52921.53	159.01	5	4	10 ± 4	27 ± 4	28 ± 2
53733.23	53832.01	98.78	4	3	7 ± 2	22 ± 7	29 ± 5
53889.35	54084.26	194.91	8	7	5 ± 1	21 ± 3	19 ± 5
54176.30	54504.73	328.43	11	10	9 ± 1	23 ± 2	27 ± 5
54609.06	54743.66	134.60	5	4	8 ± 1	23 ± 1	26 ± 4
54775.96	54973.34	197.38	6	5	11 ± 2	26 ± 4	30 ± 4
55066.68	55489.50	422.82	12	12	7 ± 1	28 ± 2	21 ± 3
55563.29	55688.01	124.72	4	4	12 ± 1	19 ± 6	38 ± 3

We find that there is no significant correlation between the length of time in a given emission phase and that of the opposing mode consecutive to it ($R = 0.07$ and $p = 0.6$ from linear regression). This suggests that the pulsar does not retain a memory of its previous magnetospheric-state after a transition. We also computed the ADC for each data interval to determine whether the results of the previous analysis may have been biased by observation cadence (see Table 4.3). We again find that there is no significant evidence for variation in the ADC over time.

Observations of PSR B1931+24 by Kramer et al. (2006) suggest that it exhibits enhanced particle flow during its radio-on phases. We were interested in seeing whether other, less severe, changes in particle flow occurred which might also be attributed to the mechanism which determines its emission behaviour. One way to test whether the emission in these phases was consistent with a ‘steady-state’ particle flow (c.f. Crab enhanced emission, see Shearer et al. 2003), was to determine whether the pulsar exhibited any regulated pulse intensity fluctuations during radio-on phases. In particular, we were interested in ascertaining whether there existed a typical rise (decay) time in pulse intensity after (before) a radio-off phase akin to PSR B0809+74 (Lyne & Ashworth 1983; van Leeuwen et al. 2002; see also §3.3). We employed the same methodology as in §3.3 to probe the variation in the ‘relative’ flux density of the pulsar in the first eight data intervals described in Table 4.3. These data intervals were chosen so as to

4: FURTHER INVESTIGATION INTO THE EMISSION MODULATION CHARACTERISTICS OF PSR B1931+24

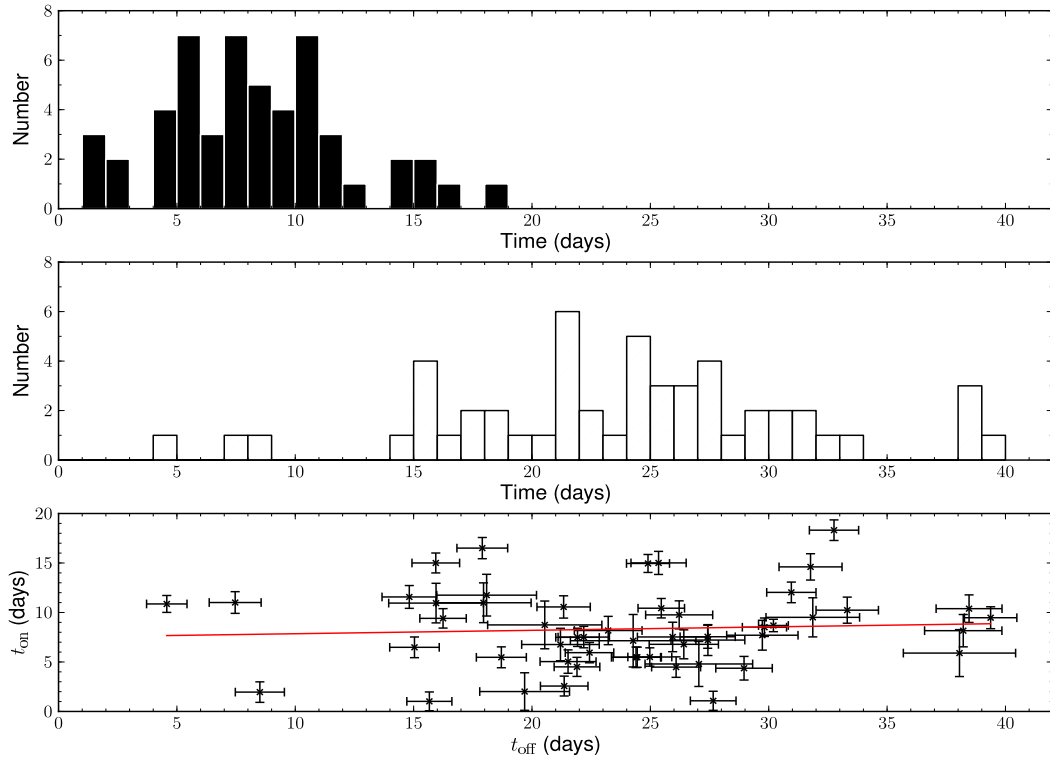


Figure 4.4: Emission duration histograms for all the radio-on (*top panel*) and radio-off (*middle panel*) phases from the observation periods defined in Table 4.3 respectively, as well as the linear regression of the two parameters (*bottom panel*). There is no evidence for a correlation between consecutive radio-on and radio-off interval lengths.

provide a consistent measure of S_{rel} with the AFB observations. The deviations from the average of each radio-emitting phase ΔS_{rel} for these intervals are shown in Fig. 4.5. Through performing a linear regression analysis on this data, we find that there is no significant correlation between the pulse intensity prior to, or after, a radio-off phase as the two-sided p-values for these statistics are always greater than 0.01. We also find that there is no significant modulation in the emission during a given radio-on phase i.e. variation in the pulse intensity was dominated by random fluctuations. This suggests that the particle flow in the magnetosphere of PSR B1931+24 is consistent throughout different radio-emitting phases, to the limit of our measurement sensitivity and the intrinsic flux variation of the source⁷.

In PSR B0823+26 we saw sporadic nulling (or ‘flickering’) behaviour over short timescales (i.e. \lesssim minutes), which implies there may be some ignition requirement to be satisfied before a stable, radio-on emission phase is resumed (see §3.3 for further

⁷Random noise fluctuations in pulse intensity may be caused by changes in radiometer noise, scintillation and (or) intrinsic pulse intensity variations.

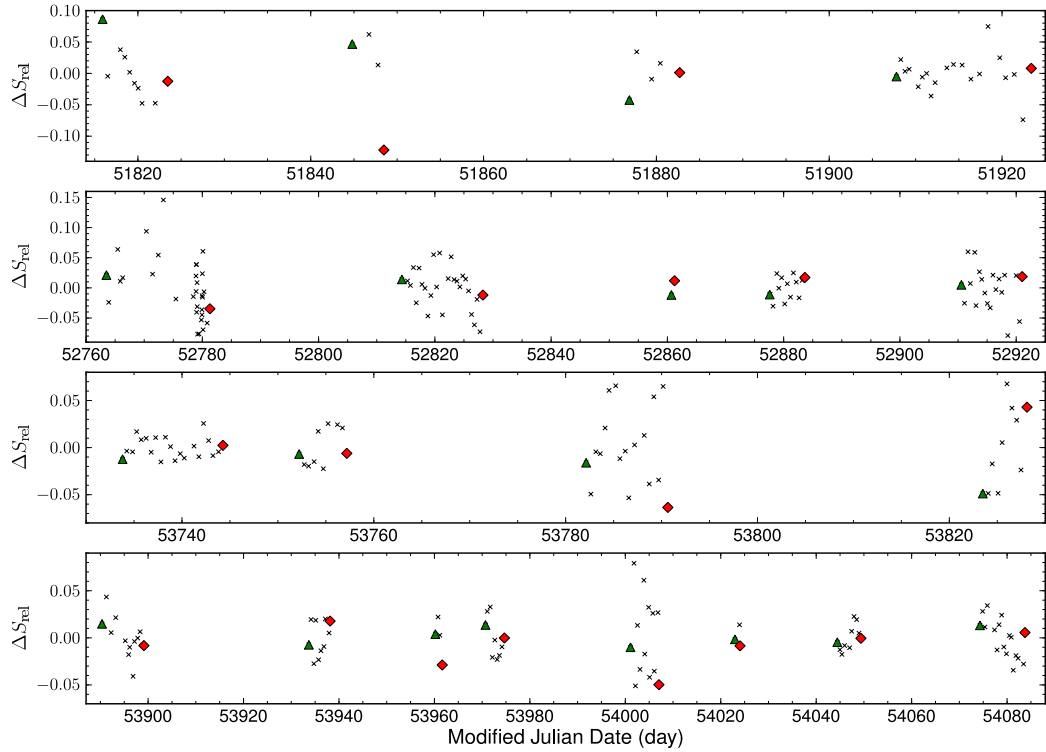


Figure 4.5: The evolution of the peak flux density (after subtraction of the mean for each radio-on phase) of PSR B1931+24 over eight data intervals. The initial and final flux densities for each radio-on phase are denoted by the green triangles and red diamonds respectively. The evolution of the pulse brightness in this data suggests that there is no correlation in the emission following or preceding a radio-off state.

details). Following this work, we sought to determine whether similar pulse intensity fluctuations existed in the emission of PSR B1931+24, which would infer a departure from steady-state emission. After sifting through every sub-integration (~ 1 minute) of the DFB data set, no evidence was found to suggest that PSR B1931+24 ‘flickers’ during radio-on or -off phases; once the pulsar has assumed an emission state, it remains in that state until an abrupt transition.

We were also interested in comparing the average flux densities of the pulsar attributed to the different phases of emission. For this analysis, we averaged 211 radio-on and 106 radio-off DFB observations of this object respectively (see Fig. 4.6), which correspond to total integration times of approximately 40 hours and 19.6 hours respectively. Following §3.3, we used Eqn. 3.1 to estimate the mean flux densities. For these observations the system characteristics are: digitisation factor $\beta \sim 1$, system temperature $T_{\text{sys}} \sim 35$ K and telescope gain $G \sim 1$ K Jy $^{-1}$. The pulsar has a period $P \sim 814$ ms and pulse-width $W_{\text{eq}} \sim 14$ ms. Consequently, we place a limit on the

4: FURTHER INVESTIGATION INTO THE EMISSION MODULATION CHARACTERISTICS OF PSR B1931+24

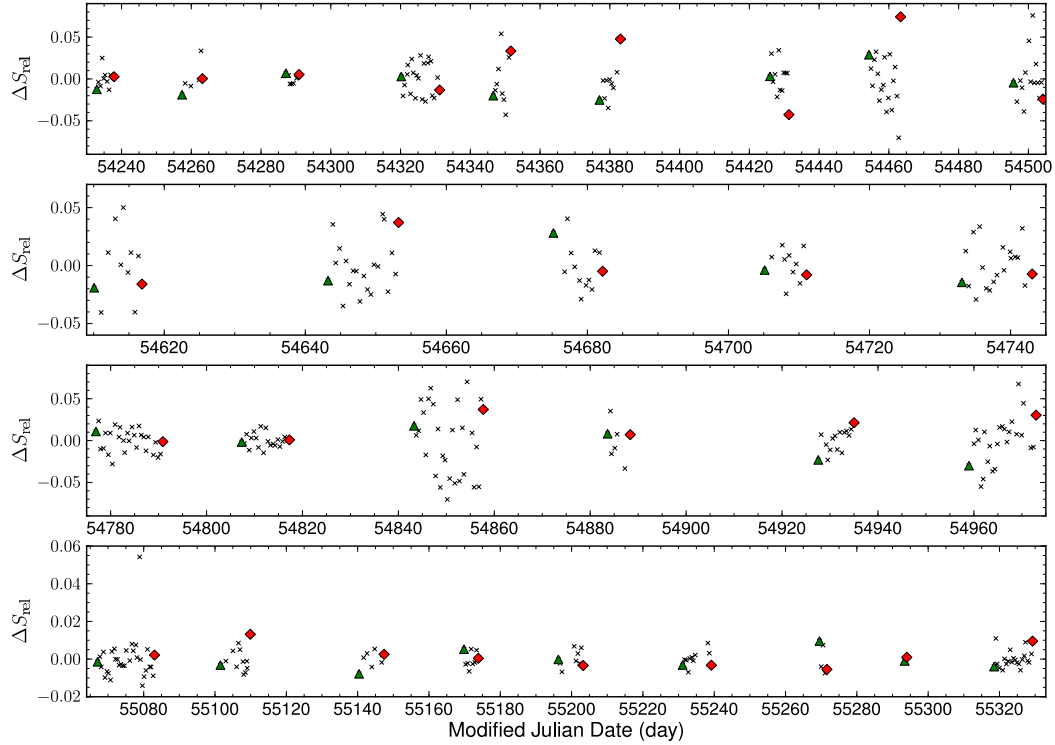


Figure 4.5: —continued. Evolution of ΔS_{rel} over numerous radio-on phases of PSR B1931+24.

mean flux density in the radio-off phase $S_{\text{off}} \lesssim 2.2 \mu\text{Jy}$ ($\text{SNR} \sim 4$). For the radio-on phase, we obtain a mean flux density $S_{\text{on}} \sim 39.8 \mu\text{Jy}$ ($\text{SNR} \sim 90$), which is approximately 20 times brighter than that in the radio-off phase. These values correspond to pseudo-luminosities $L_{1400,\text{off}} \lesssim 0.047 \text{ mJy kpc}^2$ and $L_{1400,\text{on}} \sim 0.84 \text{ mJy kpc}^2$ (see Eqn. 3.2). We note that the upper limit on the pseudo-luminosity of PSR B1931+24 in the radio-off phase is barely brighter than the two weakest known radio pulsars i.e. PSR J0030+0451 and J2144–3933 ($L_{1400} \sim 0.04 \text{ mJy kpc}^2$ (Lommen et al. 2000) and $L_{1400} \sim 0.02 \text{ mJy kpc}^2$ (Lorimer 1994) respectively). This implies that the radio-off phases are consistent with emission cessation. We note, however, that it may also be possible for the radio-off emission state to exhibit extremely weak, underlying emission which is far below our detection threshold; PSR B0823+26, another intermittent radio source, exhibits a factor of 100 difference in intensity between its separate emission modes (see §3.3; c.f. Esamdin et al. 2005).

To check whether there were any pulse shape changes during the radio-on phases, we examined the variation in the ratio of the first to second component peak intensities over time. This variation was investigated by aligning the DFB profiles with an analytic

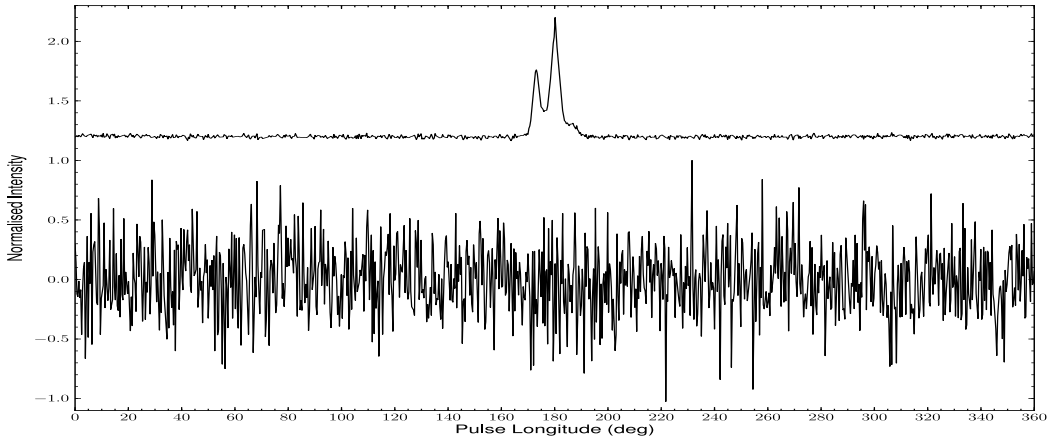


Figure 4.6: Time-averaged pulse profiles of PSR B1931+24 for the radio-on (*top*) and radio-off (*bottom*) observations respectively. The peak pulse intensities are normalised to one for each emission mode profile. The radio-on profile is offset in intensity from the radio-off profile for clarity.

template⁸ and quantifying the component peak intensities, using χ^2 minimisation to match the pulse-longitudes of the peak bins. To ensure a correct representation of the peak-to-peak ratios, we only performed this analysis on the highest SNR observations (SNR > 10). Figure 4.7 shows the distribution of peak ratios for the data discussed here. We note that the average peak ratio $\bar{R} = 0.69 \pm 0.09$ is consistent with that of the analytic template $R_{\text{temp}} \sim 0.70$.

In order to confirm whether the peak ratio variations were significant, we performed an Anderson-Darling test (Press et al. 1992) on the distribution of values. We find no evidence to suggest the data departs from a normal distribution, assuming Gaussian error bars. As a consistency check, we also implemented a χ^2 test to quantify the fluctuations in the pulse shape and compare them with normal Gaussian noise contributions, as defined by

$$\chi^2 = \frac{1}{\nu} \sum_{i=1}^N \left(\frac{R_i - \bar{R}}{\sigma_i} \right)^2, \quad (4.1)$$

where ν is the number of degrees of freedom, R is the ratio of the first peak to the second peak intensity and σ is the uncertainty in R . For pure noise variation in a profile, this quantity should be close to 1. For these observations we obtain $\chi^2 \sim 0.92$, which is consistent with random noise dominating the profile variation.

Periodicity analysis was also performed on this data, to complement this analysis

⁸This template was produced with the paas program, which was used to fit von-Mises functions to the highest SNR observation. For an overview see <http://psrchive.sourceforge.net/changes/v5.0/>.

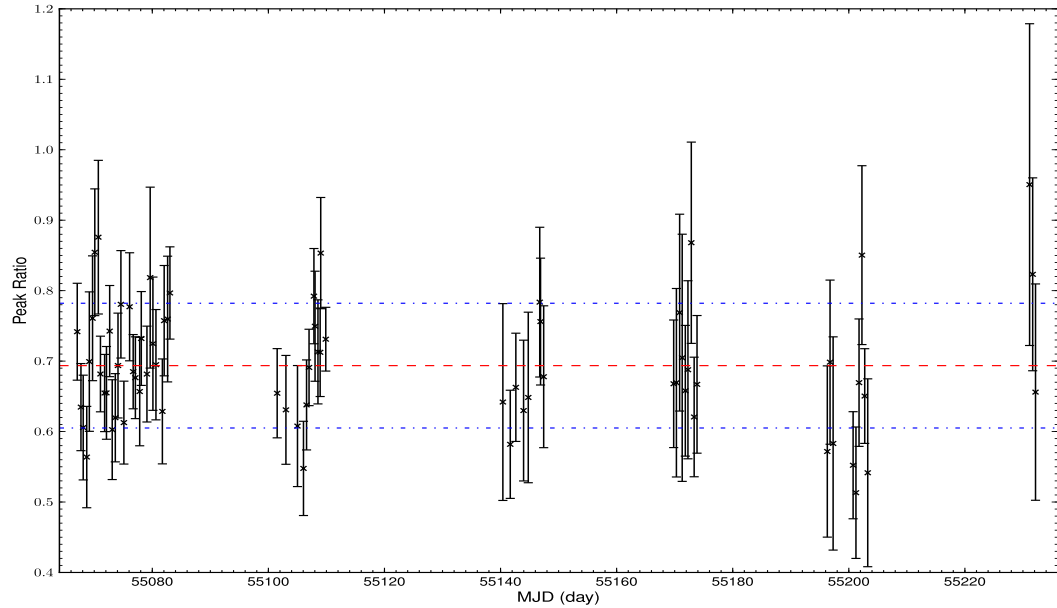


Figure 4.7: The evolution in the ratio of the first peak to second peak intensities of PSR B1931+24, over ~ 165 days of DFB observations. The average and $\pm 1\sigma$ values are denoted by the red (*dashed*) and blue (*dot-dashed*) lines respectively. The fluctuation in the peak ratio values does not appear to be significant with respect to the average.

and, to ascertain whether there is any regularity in the peak ratio fluctuations i.e. to determine whether the variations are truly random. However, this analysis is fundamentally limited by the amount of data in a radio-on phase, and inherently by the emission cessation timescales. Consequently, we find no evidence to suggest a departure from random pulse shape modulation, thus supporting the result of the previous analysis.

4.5 Periodicity Analysis

Following the procedure of §3.4, we performed a periodicity analysis on the first 12 years⁹ of the one-bit time-series data to accurately quantify any regulation in the modulation behaviour of PSR B1931+24.

4.5.1 Periodogram Analysis

We initially probed the emission fluctuation timescales using the Welch modified-periodogram method which was implemented in §3.4.1 (see §B.2.1 for a detailed de-

⁹A further year of observations was obtained after this analysis was carried out.

scription of this analysis method). We applied this analysis to the 12-year observation span, as well as consecutive 4-year segments. The periodograms spanning these shorter durations were subsequently used to probe the time evolution of periodicities within the data.

The periodogram of the 12-year observation span is shown in Fig. 4.8. The dominant periodicity within the data is best represented by the mid-point between the two peaks of the broad, central component i.e. ~ 0.03 days $^{-1}$, which corresponds to a ~ 33 -day period. There is also a broad component after the main peak centred around ~ 0.055 days $^{-1}$ (~ 18 days). However, this is probably a harmonic of the dominant periodicity.

Figures 4.9–4.11 show the long-term evolution of these spectral components at subsequent 4-year intervals (with 82, 92 and 102 emission phases in each interval respectively). Initially, the data sampling for PSR B1931+24 is quite poor compared to later times (after MJD ~ 52810 , i.e. 20 June 2003) where there are typically shorter intervals between successive observations, which is apparent when comparing the noise baselines. The main spectral features, therefore, become better resolved with time and have greater significance due to the reduced noise.

The periodogram of the first 4-year segment (Fig. 4.9) shows a dominant spectral feature at ~ 0.031 days $^{-1}$ (~ 32 days) which has a full-width at half-maximum (FWHM) equivalent to that of the 12-year data-set. It is also accompanied by other possible features at ~ 0.01 days $^{-1}$ and ~ 0.045 days $^{-1}$ (corresponding to ~ 100 days and ~ 22 days respectively). However, the component at ~ 100 days is most likely due to the observation sampling as this is seen to diminish considerably in the subsequent periodograms.

In the second 4-year data-set (Fig. 4.10), we find a dominant frequency of approximately 0.024 days $^{-1}$ (~ 42 -day periodicity), as well as other features at ~ 0.05 days $^{-1}$ and ~ 0.068 days $^{-1}$ (corresponding to ~ 20 days and ~ 15 days respectively). Interestingly, the FWHM of the main component is approximately 10 % larger than those of the previous periodograms, which suggests a lower degree of periodicity in the data. We note, however, that the ~ 20 -day and ~ 15 -day periods could be harmonics of the main spectral feature.

The periodogram of the final 4-year segment (Fig. 4.11) clearly indicates the advantages of greater observation sampling; the noise baseline in the periodogram is significantly reduced compared to the previous data intervals and allows confident identification of dominant features. The main periodicity in this periodogram is clearly centred at ~ 0.03 days $^{-1}$ (~ 33 days) with possible features at ~ 0.017 days $^{-1}$ and ~ 0.045 days $^{-1}$ (corresponding to ~ 59 days and ~ 22 days respectively). We find that

4: FURTHER INVESTIGATION INTO THE EMISSION MODULATION
CHARACTERISTICS OF PSR B1931+24

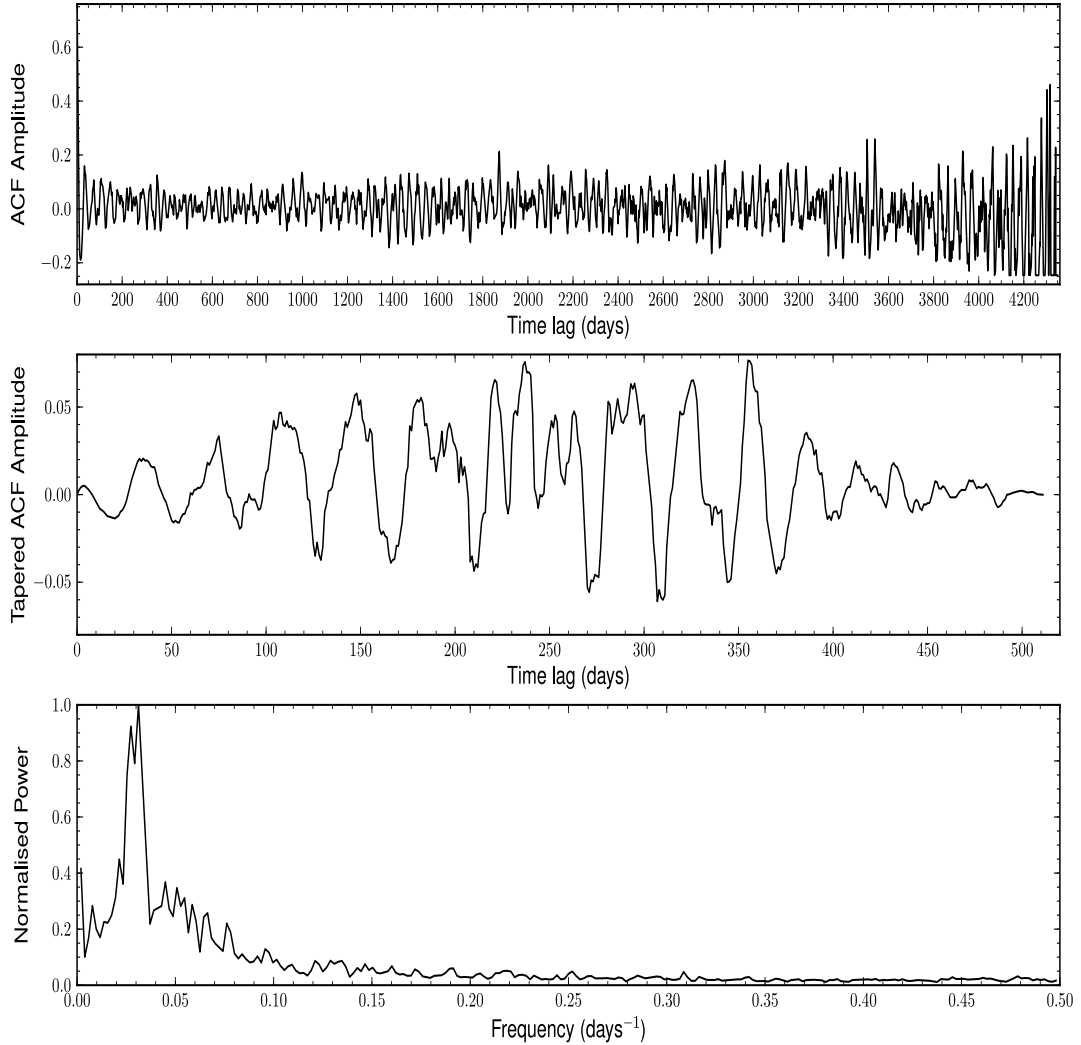


Figure 4.8: Welch periodogram analysis of the radio emission activity of PSR B1931+24 spanning from late April 1998 to late May 2010. *Top*: ACF of the activity data, binned into one-day time lags. *Middle*: The first tapered ACF segment used in the computation of the Welch periodogram (segment length $N = 512$). *Bottom*: Normalised Welch periodogram of the tapered ACF data, showing the prominent feature centred at $\sim 0.03 \text{ days}^{-1}$ (~ 33 days).

the FWHM of the main component is approximately 20% smaller than those of the 12-year and first 4-year periodograms, which again suggests some modulation in the periodicity of the source. We cannot rule out, however, the influence of data sampling on the FWHM.

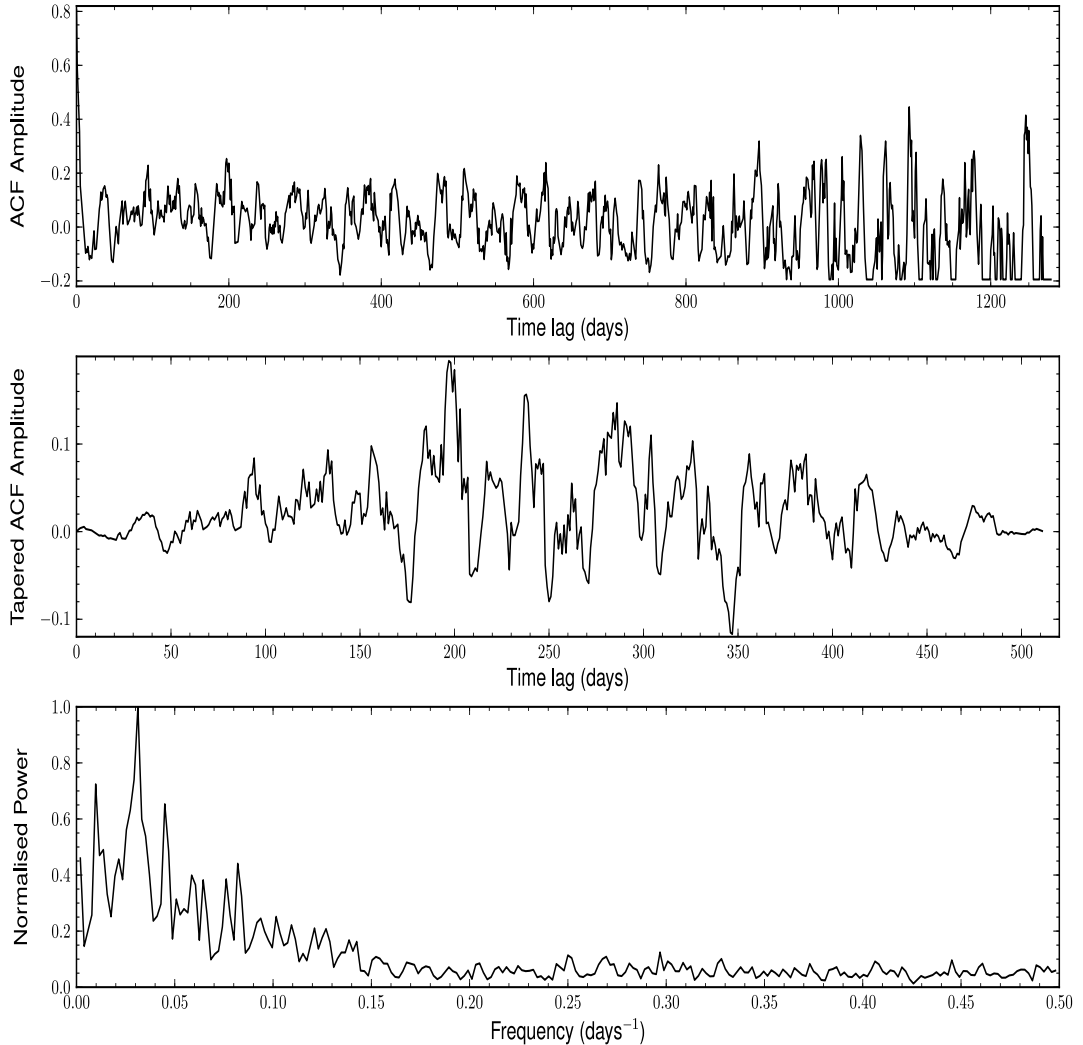


Figure 4.9: The same as Fig. 4.8, but for observations ranging from late April 1998 to late March 2002. The dominant spectral feature is centred at $\sim 0.031 \text{ days}^{-1}$ (~ 32 days) and is accompanied by other possible features at $\sim 0.01 \text{ days}^{-1}$ and $\sim 0.045 \text{ days}^{-1}$ (corresponding to ~ 100 days and ~ 22 days respectively).

4: FURTHER INVESTIGATION INTO THE EMISSION MODULATION
CHARACTERISTICS OF PSR B1931+24

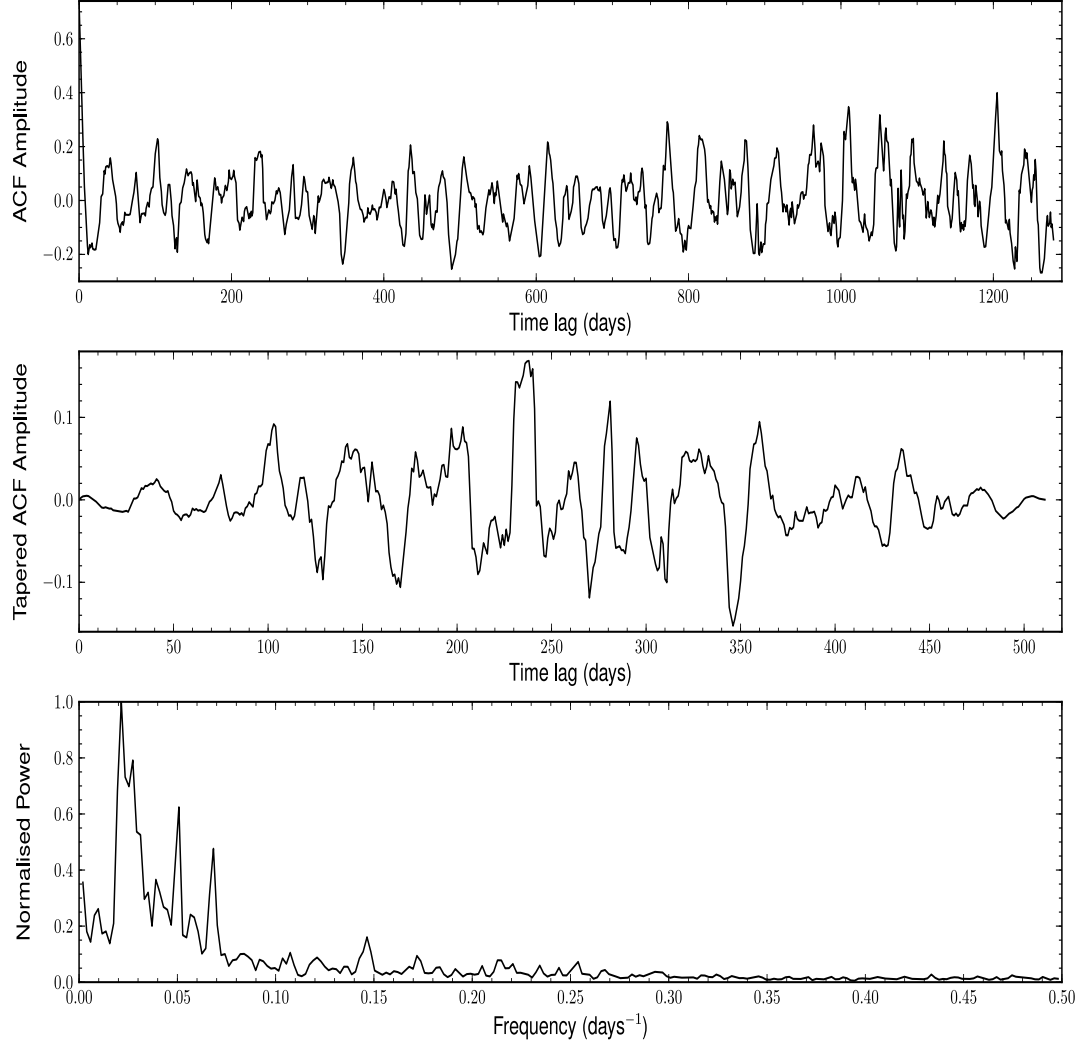


Figure 4.10: The same as Fig. 4.8, but for observations spanning late May 2002 to mid May 2006. The prominent component can be seen at $\sim 0.024 \text{ days}^{-1}$ (~ 42 days). There are also other significant features at $\sim 0.05 \text{ days}^{-1}$ and $\sim 0.068 \text{ days}^{-1}$ (corresponding to ~ 20 days and ~ 15 days respectively).

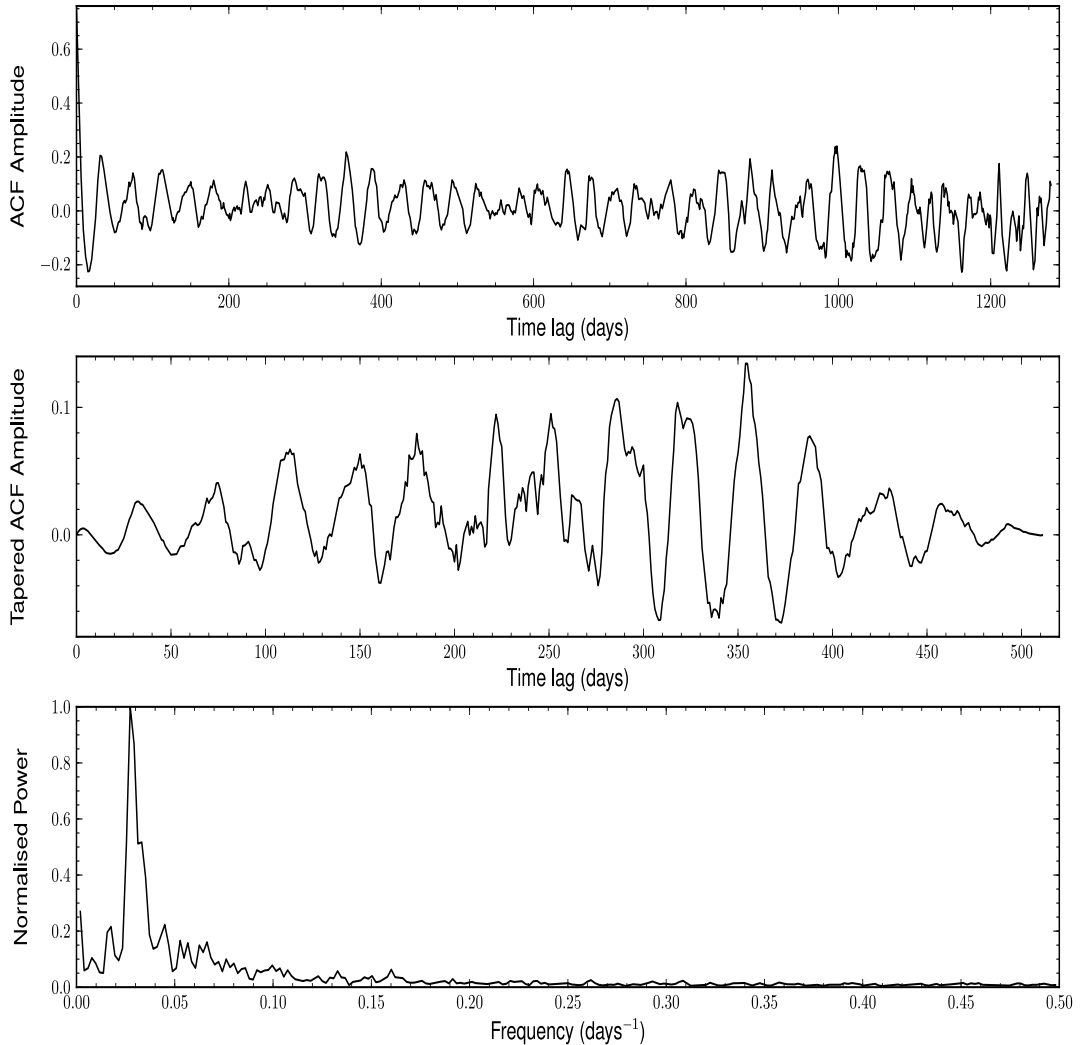


Figure 4.11: The same as Fig. 4.8, except for an observation coverage of mid May 2006 to late May 2010. The main periodicity in this periodogram is centred at $\sim 0.03 \text{ days}^{-1}$ ($\sim 33 \text{ days}$) with possible features at $\sim 0.017 \text{ days}^{-1}$ and $\sim 0.045 \text{ days}^{-1}$ (corresponding to $\sim 59 \text{ days}$ and $\sim 22 \text{ days}$ respectively).

4.5.2 WWZ Analysis

In order to elucidate the evolution of periodicities within the data, we also performed a modified wavelet analysis, i.e. WWZ analysis (see §B.2.2), on the 12-year one-bit time-series. Figure 4.12 shows the distribution of WWZ power at successive epochs (*left panel*) as well as the total integrated over all epochs (*right panel*). In the 2-D plot, we note that the peak frequencies, i.e. WWZ frequency maxima, modulate over time which gives rise to several features in the integrated spectrum. The broad prominent peak in the integrated spectrum shows that the WWZ power is preferentially distributed around $\sim 0.031 - 0.024 \text{ days}^{-1}$ ($\sim 32 - 42$ days), which corresponds well with the results of the periodogram analysis. We also note the presence of other features in the transform plane at $\sim 0.021 \text{ days}^{-1}$ (~ 48 days), $\sim 0.035 \text{ days}^{-1}$ (~ 29 days), approximately 0.042 days^{-1} (~ 24 days) and $\sim 0.052 \text{ days}^{-1}$ (~ 19 days) over small time intervals. However, they generally have much lower spectral power which suggest low significance. We find that the features centred on $\sim 0.042 \text{ days}^{-1}$ and $\sim 0.052 \text{ days}^{-1}$ are most likely spurious due to their proximity to a long, approximately 100-day gap in the data¹⁰. We note that the better observation sampling towards later times (after MJD ~ 52810) results in better resolution of the intrinsic variation of the source i.e. the fluctuation periods are generally represented by greater WWZ power towards later times.

To estimate the significance of spectral features, we implemented a number of methods which were introduced in §B.3 and § 3.4. Firstly, we sought to determine how significant WWZ features were with respect to the ‘noise background’. Here we computed the standard deviation of the WWZ data by bootstrapping over several hundred realisations, from which we assume a $5\sigma \approx 60$ WWZ power limit for significant features. We also determined the peak fluctuation frequencies and periods for each epoch, with $1-\sigma$ error bars calculated using the confusion limit estimation method (see §B.3.1), as shown in Fig. 4.13. We note that the peak period spans $\sim 20 - 50$ days over time, with a few epochs showing periodicities of ~ 100 days. However, the features in the wavelet transform attributed to this longer period are only represented by low WWZ power, and are over an interval of time which has a number of gaps between successive epochs (MJD $\sim 51987 - 52034$, $\sim 52040 - 52077$ and $\sim 52207 - 52240$). Therefore, we are hesitant to suggest that the longer fluctuation period is intrinsic to the source.

We performed an Anderson-Darling test (Press et al. 1992) on the peak fluctuation period data to determine whether the variations were significant. From the results of this test, we find that the short-term modulation in the source’s periodicity is not consistent with random variation and is most likely due to the quasi-periodic nature of

¹⁰Nothing meaningful can be obtained for a fluctuation period which is shorter than the length of a gap between data.

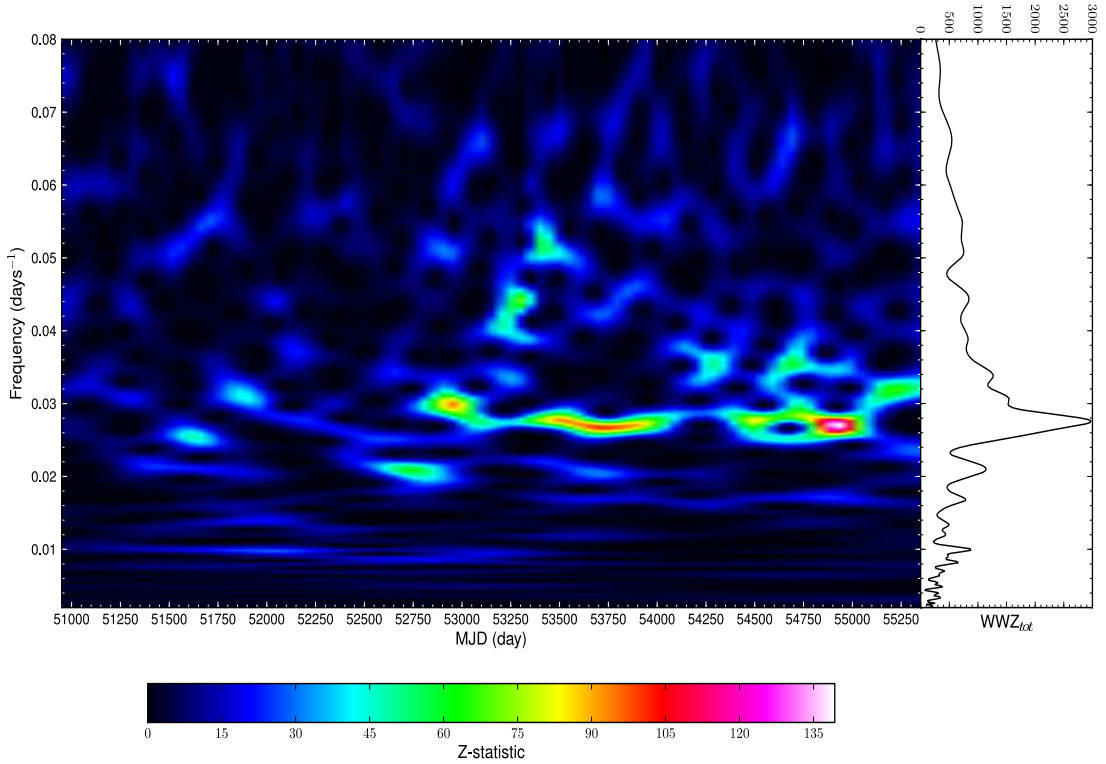


Figure 4.12: WWZ transform of the 12 year PSR B1931+24 radio emission activity data-set (*left*) and the corresponding integrated power spectrum (*right*). The integrated power spectrum reaches a maximum at $\sim 0.028 \text{ days}^{-1}$ ($\sim 36 \text{ days}$), which correlates well with the periodogram analysis. Throughout the transform plane the peak frequency modulates over time, typically ranging $\sim 0.024 - 0.032 \text{ days}^{-1}$ ($\sim 31 - 42 \text{ days}$). The bootstrap 5σ significance level corresponds to $WWZ \approx 60$ for this data-set.

the object.

As a consistency check, we also used the data-windowing method (outlined in §B.3.2) to compute a measure of the modulation in the peak frequency and period. We split the WWZ data into 400-day segments and, for each of these segments, determined the median fluctuation frequency and corresponding period (see Table 4.4). We find that the first four data segments do not have median peak WWZ values greater than the $5\sigma \approx 60$ significance level derived from bootstrapping. However, the rest of the segments (excluding the data spanning $MJD = 54150 - 54550$) have values greater or equal to this cut-off, which indicate that the periodicities within these data intervals are intrinsic to the source. We note that the uncertainty in the peak fluctuation frequency (period) becomes consistently smaller at later epochs, which again indicates the effect of data sampling on the WWZ transform data. From this analysis, we obtain

4: FURTHER INVESTIGATION INTO THE EMISSION MODULATION CHARACTERISTICS OF PSR B1931+24

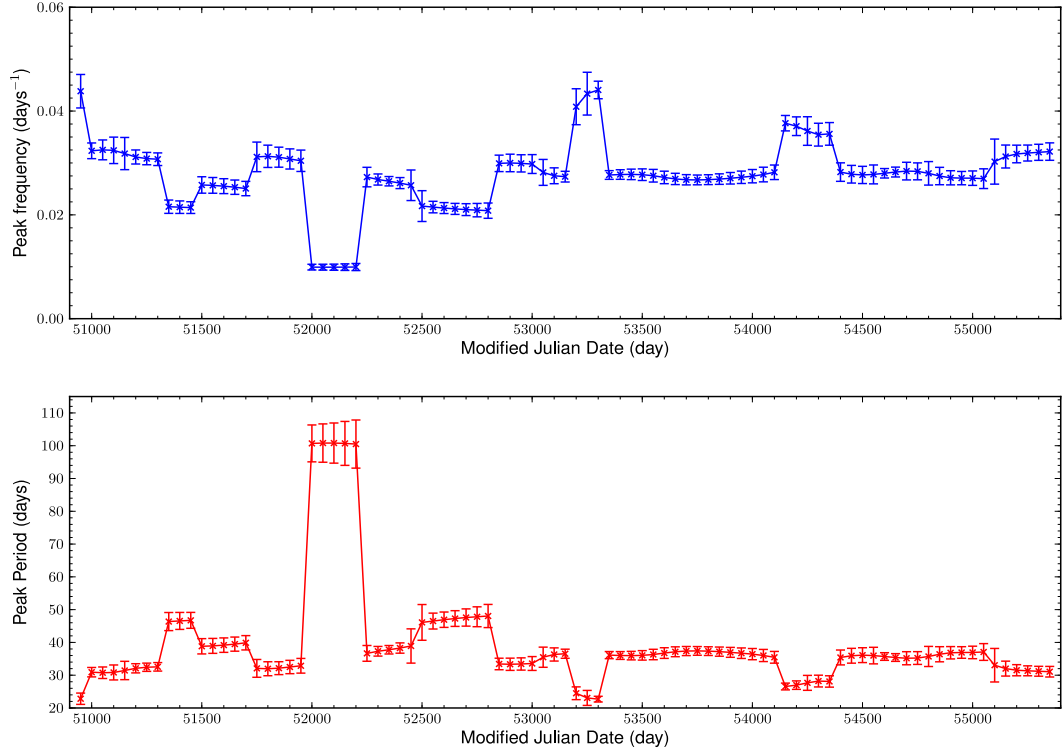


Figure 4.13: Peak WWZ fluctuation frequencies (*top*) and periods (*bottom*) for the 12-year PSR B1931+24 radio emission activity data. Error bars are $1-\sigma$ values computed using the confusion limit estimation method. The average error in $\nu_{\text{fluc}}(\tau)$ (or $P_{\text{fluc}}(\tau)$) is approximately 6 %. The peak fluctuation period spans $\sim 20 - 50$ days apart from at a few epochs where the data sampling is likely to have affected the local matching.

median peak fluctuation frequencies $\sim 0.035 - 0.021 \text{ days}^{-1}$ ($\sim 28 - 47$ days), which are largely consistent with the previous analysis; the periodograms display prominent spectral peaks at $\sim 0.031 - 0.024 \text{ days}^{-1}$ ($\sim 31 - 42$ days). Through performing another Anderson-Darling test, we find that the variations in the long-term periodicity of the source, i.e. over several years, are not significant.

Table 4.4: Median peak WWZ values and fluctuation frequencies (periods) for consecutive 400-day segments of transform data for PSR B1931+24 (12 year data-set). The standard $1-\sigma$ uncertainties are quoted in the parentheses and are in units of the least significant digit.

MJD range	WWZ _{median}	$\nu_{\text{fluc}}(10^{-2} \text{ days}^{-1})$	$P_{\text{fluc}}(\text{days})$
50950–51350	17(3)	3.2(6)	31(6)
51350–51750	30(10)	2.5(3)	40(5)
51750–52150	28(7)	3(1)	30(40)
52150–52550	23(4)	2.6(7)	40(30)
52550–52950	60(20)	2.1(4)	47(7)
52950–53350	60(20)	3.0(7)	34(6)
53350–53750	90(10)	2.75(4)	36(1)
53750–54150	80(30)	2.7(3)	37(3)
54150–54550	50(20)	3.5(5)	28(4)
54550–54950	80(30)	2.80(5)	36(1)
54950–55350	70(30)	3.1(2)	32(3)

4.6 Residual Fitting and Measurement of the Braking Index

To gain context on the emission modulation of PSR B1931+24, we studied its rotational behaviour. We were particularly interested in determining whether the object experiences any temporal evolution in the spin-down rates associated with the different phases of emission. We also sought to ascertain the braking index n of the pulsar through measurement of the rate of change in spin-down rate in the radio-off phase $\dot{\nu}_{\text{off}}$, which would enable us to derive information about how the pulsar undergoes its energy loss and, ultimately, provide us insight into the electrodynamics (see §1.1.3).

In order to quantify the spin-down rate variation in PSR B1931+24, we were required to take a different approach compared with conventional phase-coherent timing analysis (see e.g. Lyne et al. 1996); PSR B1931+24 does not exhibit detectable emission for sustained periods of time and also possesses two spin-down rates which, subsequently, does not allow conventional fitting methods to be employed for this analysis. Kramer et al. (2006) demonstrated the success of using a dual- $\dot{\nu}$, least-squares fitting method to derive the spin-parameters for this pulsar over a short span of data and, hence, the spin-down rates corresponding to each emission phase. We have expanded upon this initial analysis by applying the same fitting procedure to eight well-sampled data sets (including the one presented in Kramer et al. 2006). The procedure entails minimising the timing residuals of PSR B1931+24 by fitting for the change in rotational

phase, period and period derivative ($\Delta\phi^{11}$, ΔP and $\Delta \dot{P}$ respectively) with respect to the separate emission phases. The values of $\dot{P}_{\text{on/off}}$, and hence $\dot{\nu}_{\text{on/off}}$, were derived from the difference between the average spin-down rate (\dot{P}_{av}) and $\Delta \dot{P}$ associated with these modes. The total offset in $\Delta\phi$, ΔP and $\Delta \dot{P}$, which were required to obtain a phase-coherent solution, were modelled via:

$$t_{\text{res}} = \Delta\phi + \frac{\Delta P}{P} \times (t - t_i) + \frac{\Delta \dot{P}_i}{2P} \times (t - t_i)^2, \quad (4.2)$$

where t_{res} and t_i are the residual ($t_{\text{obs}} - t_{\text{pred}}$) and reference times respectively, and $\Delta \dot{P}_i$ is the change in spin-down rate in each emission phase (i.e. $\pm \Delta \dot{P}$). An example of this fitting process is shown in Fig. 4.14. The rotational behaviour of the pulsar is clearly characterised well by the model.

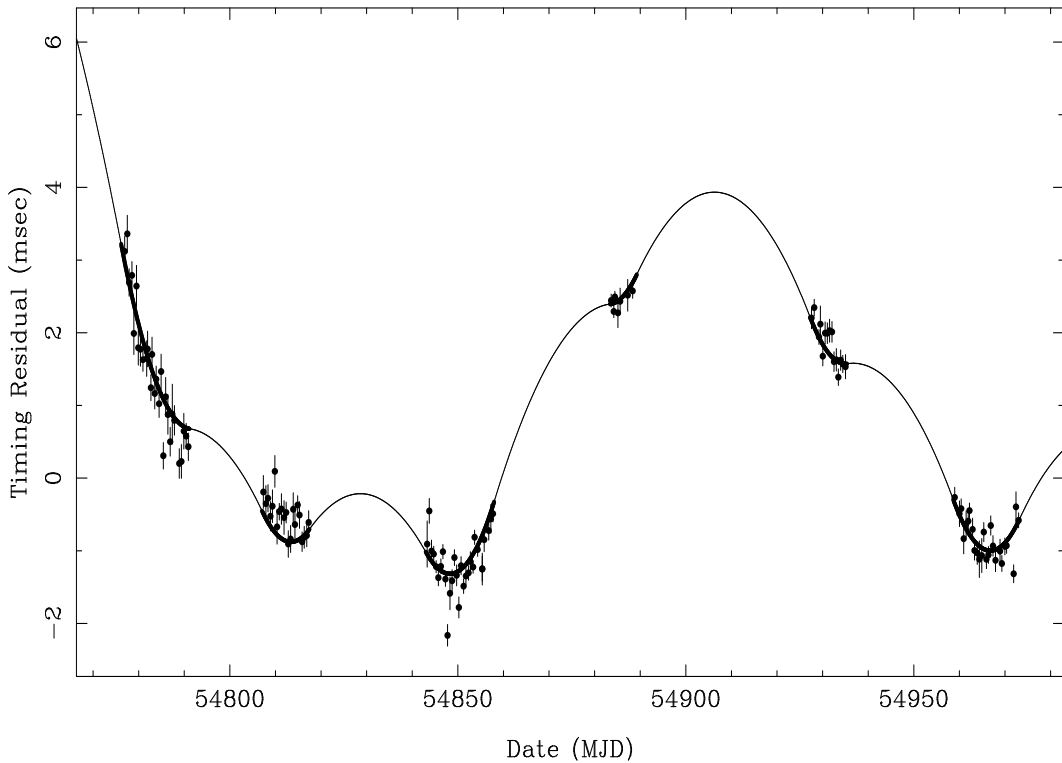


Figure 4.14: Least-squares, weighted fit to timing residuals of PSR B1931+24 for observations ranging MJD $\sim 54777 - 54973$. The fitted model is represented by the continuous line which overlays the data points.

We note that the total contribution of $\dot{\nu}_{\text{on/off}}$ to the average is determined from the total time spent in a given emission phase, which is inherently dependent on the

¹¹The change in rotational phase is the offset required to obtain a phase-coherent timing solution, given an original set of fit parameters.

transition times between phases. Typically, we can only constrain transition times to within about a day and, as such, imparts systematic errors into this analysis. To propagate the effects of such errors, therefore, we performed a Monte-Carlo simulation on the data. For each data interval, we performed 10^5 fits using transition times which are randomly distributed between the last radio-on and first radio-off phase observations. As a result, we were able to obtain a distribution of radio-on and -off spin-down rates for each data interval, from which we determined estimates for their averages and associated uncertainties. Table 4.5 shows the spin-down parameters obtained from this analysis, as well as the derived Goldreich-Julian (ρ_{GJ}) and plasma (ρ_{plasma}) charge densities associated with them (see §A for a definition of these parameters). The average values for $\dot{\nu}_{\text{on}} \sim 16.3 \pm 0.5 \times 10^{-15} \text{ s}^{-2}$ and $\dot{\nu}_{\text{off}} \sim 10.8 \pm 0.2 \times 10^{-15} \text{ s}^{-2}$ are found to be consistent with Kramer et al. (2006) (see Table 4.1).

In the radio-off phase, the rotational slow-down $\dot{\nu}_{\text{off}}$ is thought to be indicative of the torque produced by magneto-dipole radiation (Kramer et al. 2006). Consequently, the rate of change in the spin-down rate in the radio-off phase $\ddot{\nu}_{\text{off}}$ should provide a measure of the braking index associated with this radiation, which is not contaminated by the additional electromagnetic torque of the plasma current flow; that is, assuming that the additional torque completely disappears in the radio-off phase. We fitted the derived values for $\dot{\nu}_{\text{on}}$ and $\dot{\nu}_{\text{off}}$ for a number of epochs to determine if significant second order variations could be measured (Fig. 4.15). Unfortunately, however, we could not obtain a significant value for $\ddot{\nu}_{\text{off}}$ using data even with the greatest observation density (see §4.8 for a discussion on this). As a result, we could not obtain an accurate measure of the braking index of the source (see Table 4.6).

Consequently, we sought to determine a value for braking index using another method. Using the timing software developed by Weltevrede et al. (2011), we also modelled the variation in spin-down rate in PSR B1931+24, by fitting changes in rotational phase (using the first three terms of Eqn. 7; Weltevrede et al. 2011), analogous to glitches i.e. sudden changes in the spin-down rate, to the time-of-arrivals (TOAs) of emission. Each emission phase has a unique spin-down rate, which we assumed is acquired directly after (or before) the last (or first) radio-on observation of each active emission phase. Through fitting the observed TOAs for changes in spin-down rate only, we find that this method produces results consistent with Table 4.5. However, when the emission phase transition times are also taken as a fit parameter we obtain very large errors in the fit parameters. We applied maximum and minimum time constraints to the ‘glitch epochs’ but, due to the absence of data bounding a given transition into (or out of) a radio-on phase, the fitting process could not converge on a minimum; a global solution could not be achieved when fitting for the transition times, as we were

Table 4.5: Results from the residual fitting of PSR B1931+24 observations. The period epoch of each fit is denoted by P_{epoch} , T is the length of each fit interval and $\dot{\nu}_{\text{on}}$, $\dot{\nu}_{\text{off}}$, $\dot{\nu}_{\text{av}}$ are the radio-on, radio-off and average spin-down rates respectively. The change in spin-down rate (i.e. $\dot{\nu}_{\text{on}} - \dot{\nu}_{\text{off}}$) is represented by $\Delta\dot{\nu}$. Definitions for ρ_{GJ} and ρ_{plasma} can be found in §A. Standard (1- σ) errors are provided in the parentheses after the parameters, and represent the least significant digit.

P_{epoch}	T (d)	$\dot{\nu}_{\text{av}}$ (10^{-15} s^{-2})	$\dot{\nu}_{\text{on}}$ (10^{-15} s^{-2})	$\dot{\nu}_{\text{off}}$ (10^{-15} s^{-2})	$\Delta\dot{\nu}/\dot{\nu}_{\text{av}}$ (%)	ρ_{GJ} (10^{-2} Cm^{-3})	ρ_{plasma} (10^{-2} Cm^{-3})	$\rho_{\text{plasma}}/\rho_{\text{GJ}}$ (%)
51869.7	107.5	-12.01 (3)	-15.2 (2)	-11.13 (9)	36.6 (6)	3.38 (3)	2.45 (5)	72.20 (3)
52842.3*	157.5	-12.04 (1)	-16.0 (2)	-10.78 (7)	48.4 (7)	3.35 (2)	3.21 (5)	96.27 (3)
53782.6	97.7	-12.28 (2)	-17.6 (5)	-10.4 (2)	69 (2)	3.28 (7)	4.5 (2)	136.3 (3)
53987.1	193.4	-11.722 (8)	-18.7 (10)	-10.2 (2)	83 (5)	3.25 (7)	5.4 (3)	166.3 (7)
54340.7	326.8	-12.140 (6)	-16.2 (4)	-10.7 (1)	51 (1)	3.32 (4)	3.39 (9)	102.03 (9)
54676.6	133.0	-12.16 (1)	-17.1 (8)	-10.3 (3)	66 (4)	3.3 (1)	4.3 (3)	132.1 (6)
54875.0	196.0	-12.35 (1)	-15.8 (2)	-11.07 (8)	42.7 (6)	3.38 (2)	2.90 (4)	85.94 (2)
55198.2	262.2	-11.991 (5)	-14.3 (1)	-11.40 (3)	25.4 (2)	3.43 (9)	1.72 (1)	50.180 (4)

*Epoch of data used to derive spin-parameters in Kramer et al. (2006).

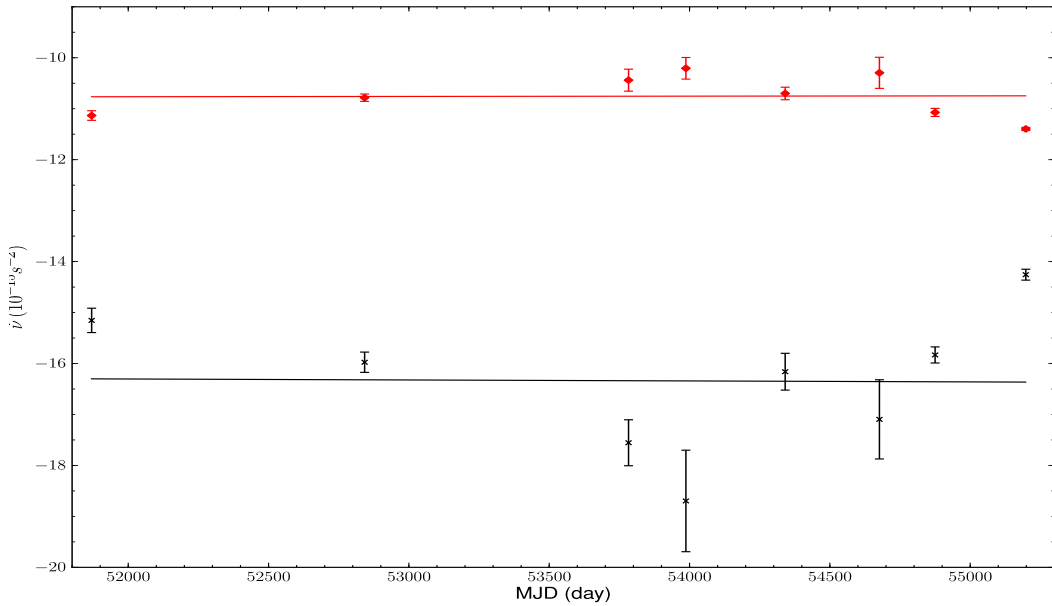


Figure 4.15: Linear regression fits of $\dot{\nu}_{\text{off}}$ (top trace) and $\dot{\nu}_{\text{on}}$ (bottom trace) for PSR B1931+24. Note the large gaps in the data around $\text{MJD} \sim 51870 - 52842$ and $\text{MJD} \sim 52842 - 53987$.

Table 4.6: The results of the linear regression analysis of the spin-down rate data, with least significant uncertainties in the parantheses. The length of each fitted data-set is denoted by T . The correlation coefficient and two-sided probability value for each fit are given by R and p respectively. The rate of change in the spin-down rate in the radio-off phase and braking index are represented by $\dot{\nu}_{\text{off}}$ and n respectively. The braking index calculated using the Johnston & Galloway (1999) method is given by n_{JG99} .

T (d)	R	p	$\dot{\nu}_{\text{off}}$ (10^{-19} s^{-3})	n (10^7)	n_{JG99} (10^7)
3328.5	0.01	0.97	0.05 (156)	5(164)	-78.6(9)
2355.9	-0.42	0.35	-2 (2)	-200(300)	-263(3)
1415.5	-0.78	0.06	-7 (3)	-800(300)	-730(20)

limited to only the radio-on phase data

4.7 Long-term Evolution in Spin-down Rate

From the residual fitting in §4.6, we were unable to determine a significant value for $\dot{\nu}_{\text{off}}$ or the braking index of the pulsar. This is most likely due to the transition time errors, between emission phases, which introduce an anti-correlation between $\dot{\nu}_{\text{on}}$ and $\dot{\nu}_{\text{off}}$ (a linear fit to these data obtains a correlation coefficient $R = -0.9$ and two-sided p-value

$p = 0.0003$; see also Fig. 4.15); systematic over and underestimation of the transition times, which are not fitted for, will cause $\dot{\nu}_{\text{on}}$ and $\dot{\nu}_{\text{off}}$ to become anti-correlated which, in turn, will increase the noise contribution to $\ddot{\nu}_{\text{off}}$.

To complement this analysis, therefore, we decided to examine the long-term evolution in the spin-down rates over the entire 13-year data-set. For this analysis, we used timing measurements of PSR B1931+24 to estimate the contribution of $\dot{\nu}_{\text{on}}$ to the rotational frequency ν over neighbouring radio-on phases. We assumed that the change in rotational frequency $\Delta\nu$, resulting from variation between $\dot{\nu}_{\text{on}}$ and $\dot{\nu}_{\text{off}}$, can be obtained from fitting the residuals of three successive radio-on phases in separate pairs (see Fig. 4.16). In order to separate the effects of the different spin-down rates in these fits, we set the average $\dot{\nu} = \dot{\nu}_{\text{off}}$ (using the average determined from residual fitting, i.e. $\langle \dot{\nu}_{\text{off}} \rangle = -10.8 \pm 0.2 \times 10^{-15} \text{ s}^{-2}$). We fitted the timing residuals of the latter and first halves of a given pair of radio-on phases, using PSRTIME¹², to estimate a value for the rotational frequency which is governed by the radio-off spin-down rate. We assumed that the contribution of $\dot{\nu}_{\text{on}}$ to these residuals was negligible due to the short length of time the on phases cover (w.r.t. the radio-off phases). By obtaining values for ν , for the first and second pair of radio-on phases, we were able to estimate the total change in rotational frequency due to the difference in spin-down rate $\Delta\dot{\nu}$ over the central radio-on phase. Given that $\dot{\nu}_{\text{on}}$ should only affect the residuals over this period, we obtain the relation

$$\Delta\nu = \nu_{23} - \nu_{12} = \Delta\dot{\nu} \times t_{\text{on}}, \quad (4.3)$$

where $\Delta\dot{\nu}$ represents $\dot{\nu}_{\text{on}} - \dot{\nu}_{\text{off}}$ and t_{on} is the total time spent in the central radio-on phase. The spin-frequencies for the first and second fit intervals are ν_{12} and ν_{23} respectively, as shown in Fig. 4.16.

To increase the number of measurements, we analysed the data using a stride-fitting method similar to that used by Lyne et al. (2010); we analysed groups of radio-on phase data in steps of single emission phases. We only included data windows which had three well defined radio-on phases i.e. containing gaps no greater than 10 days between observations¹³, with uncertainties in the emission phase transitions less than 4 days (less than 2 days for the longest data-set; see Table 4.7). We corrected for the long-term spin-down behaviour of the source by subtracting the average spin-down rate from the frequency data using the vfit program¹⁴.

¹²<http://www.jb.man.ac.uk/pulsar/observing/progs/psrtime.html>

¹³The minimum total time spent in a consecutive radio-on and -off phase is 10 days. A gap between residuals of this timescale would cause a large uncertainty in the contribution of $\dot{\nu}$ to $\Delta\nu$, due to possible unmodelled rotational behaviour.

¹⁴<http://www.jb.man.ac.uk/pulsar/observing/progs/vfit.html>

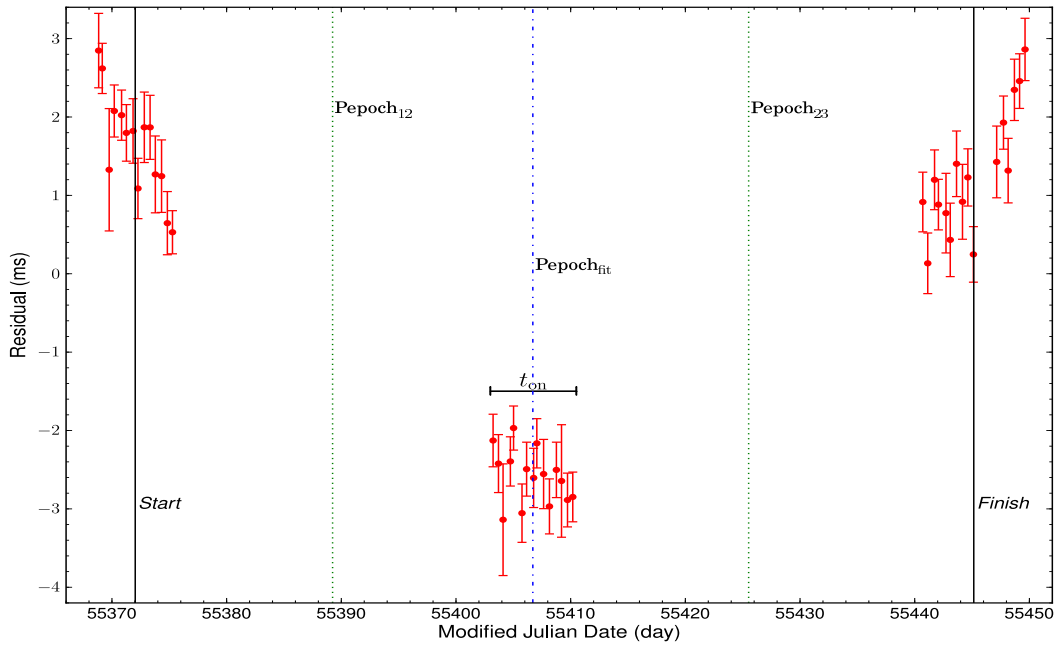


Figure 4.16: Timing residuals of PSR B1931+24, over approximately 80 days of data, depicting the $\Delta\nu$ fitting process. The epochs where ν was calculated are represented by P_{epoch}_{12} and P_{epoch}_{23} for the first and second pair of radio-on phases respectively. The epoch at which $\Delta\nu$, hence $\Delta\dot{\nu}$, was measured is denoted by $P_{\text{epoch}}_{\text{fit}}$. The bounding regions of the fits are shown by the ‘start’ and ‘finish’ lines.

Noting that Eqn. 4.3 is analogous to the equation for a straight-line, with a gradient equal to $\Delta\dot{\nu}$ and zero intercept, we were able to fit $\Delta\nu$ vs t_{on} across numerous data intervals, as shown in Fig. 4.17 and Table 4.7.

Table 4.7: The linear fit parameters for the long-term spin-down rate study of PSR B1931+24. The total length of each data-set used in the fitting process is denoted by T and N represents the number of data points used in each fit. The linear correlation coefficient is denoted by R^2 . The change in spin-down rate obtained from the fitting procedure is represented by $\Delta\dot{\nu}$ and $\dot{\nu}_{\text{on}}$ is the corresponding radio-on spin-down rate.

Data-set	T (d)	N	R^2	$\Delta\dot{\nu}$ (10^{-15} s^{-2})	$\dot{\nu}_{\text{on}}$ (10^{-15} s^{-2})
First Segment	1426	8	0.98	-5.6 (8)	-16 (1)
Second Segment	1451	9	0.89	-4 (1)	-16 (1)
Third Segment	1467	29	0.98	-5.2 (3)	-16.0 (5)
All data	4700	45	0.98	-5.2 (2)	-16.0 (4)

We find that these data are highly linearly correlated, which suggests that the spin-down rate assumed for the radio-off phase is indicative of the object. We find that

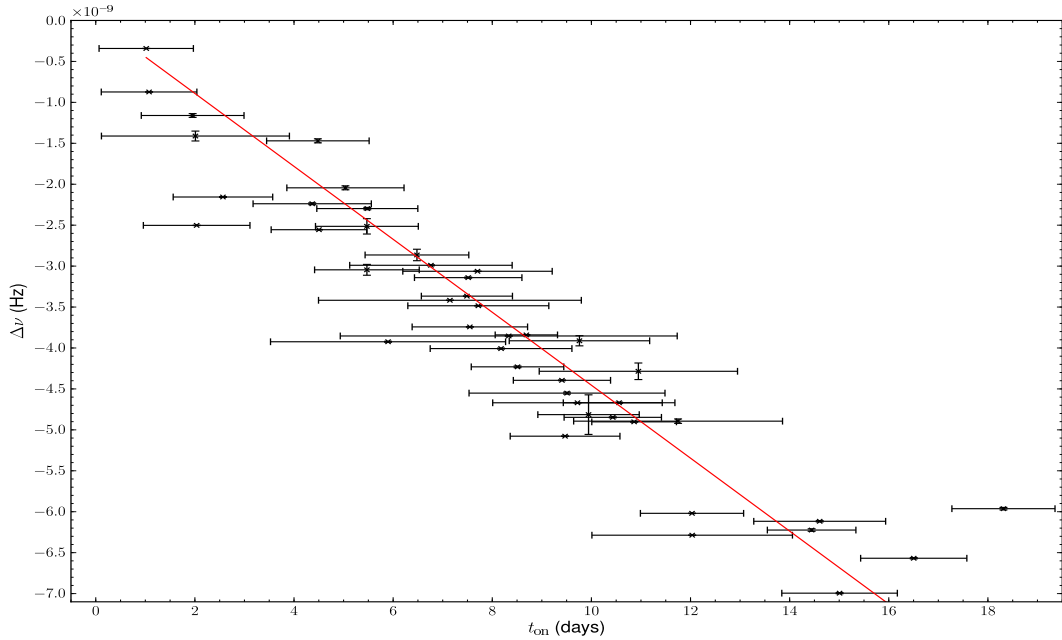


Figure 4.17: A linear fit to $\Delta\nu$ against t_{on} for approximately 13 years of observations of PSR B1931+24.

there is no evidence for variation in the spin-down rates associated with the different phases of emission within our measurement sensitivity.

4.8 Discussion

We have shown that PSR B1931+24 exhibits regulated emission modulation; to the limit of our measurements it maintains a constant activity duty cycle. To improve on these results, even more frequent sampling would be required. This would only be feasible with a large dedicated telescope, or new facilities such as LOFAR and the SKA¹⁵ which will have multi-beam capabilities and, hence, greater ability to dedicate observing time to individual sources. If we were to observe this source over hourly timescales, rather than daily, we would dramatically increase our chances of observing the pulsar transition between emission modes. As a result, we would possibly be able to uncover correlated changes in emission following (or preceding) radio-off phases which might give us insight into what causes the magnetospheric configuration to change so dramatically.

¹⁵Phase 1 science operations with the SKA are projected to commence in 2020, with full operation of the telescope proposed in 2024. See also <http://www.skatelescope.org/about/project/> for more details.

In this work, we also characterised the modulation timescales of the radio emission in PSR B1931+24. We find that the source exhibits a periodic modulation timescale of approximately 36 days on average. There do appear to be variations around this basic periodicity, but it remains remarkably stable over many years. This degree of stability provides a challenge for models of this process as it is significantly longer than the expected dynamic and plasma timescales.

In addition, we have quantified the variation in $\dot{\nu}_{\text{on}}$ and $\dot{\nu}_{\text{off}}$, over both short and long timescales, through fitting the residuals of PSR B1931+24. The variation in $\dot{\nu}$ between the radio-on and -off phases, as shown in Table 4.5, seems quite apparent when comparing the results from neighbouring data intervals. However, after performing an Anderson-Darling test on these data, we find that the distributions of $\dot{\nu}_{\text{on}}$ and $\dot{\nu}_{\text{off}}$ are consistent with coming from normal distributions; at no point does the test statistic A^2 exceed the ‘critical level’ for any significance level. Consequently, the variations in $\dot{\nu}_{\text{on}}$ and $\dot{\nu}_{\text{off}}$ are consistent with the measurement uncertainties. This result is supported by the long-term analysis (see §4.7), which provides additional evidence to suggest that we do not observe any significant changes in the spin-down rates attributed to each emission mode; that is, the pulsar appears to retain a constant $\Delta\dot{\nu} \sim 48 \pm 2\%$ between emission phases. This implies that the apparent changes in plasma flow in the radio-on phase are also not significant ($\langle \rho_{\text{plasma}} \rangle = 3.5 \pm 0.4 \times 10^{-2} \text{ Cm}^{-3}$; see Table 4.5), thus indicating a surprisingly high degree of stability in the apparently bi-modal system.

We do note, however, that there was an unavoidable systematic effect in the short-timescale fitting procedure. More specifically, the errors in the transition times between emission phases introduced uncertainty into the calculation of $\dot{\nu}_{\text{on}}$ and $\dot{\nu}_{\text{off}}$. This is highlighted by the results in Fig. 4.15, where the interdependency between the two spin parameters is made evident. We see that these quantities are in fact almost perfectly anti-correlated ($R = -0.9$ and $p = 0.0003$). In the model used, the transition times between phases of emission are not taken as a fit parameter. Therefore, the model converges around fixed times whose calculation is fundamentally dependent upon the observation cadence; observations spaced farther apart between two emission modes will have a higher uncertainty in the transition time compared with two spaced closer together. Furthermore, if the amount of time spent in a radio-on phase is overestimated, then the amount of time in a consecutive radio-off phase will be underestimated accordingly. Given that radio-on phases are much shorter than radio-off phases on average, it is evident that the effect on the error of $\dot{\nu}_{\text{on}}$ will be greater than that of $\dot{\nu}_{\text{off}}$. This naturally explains the observed anti-correlation between the two parameters and the larger error bars in $\dot{\nu}_{\text{on}}$. We conclude that it is quite possible that we did not see any significant variation in the spin-down rates as a result of this systematic effect. To

overcome this problem, we again would require greater observation cadence to provide better constraints on the transition times.

We also attempted to obtain a value for the braking index of PSR B1931+24 from $\ddot{\nu}_{\text{off}}$, in the hope of determining information about the energy loss of the object. However, as previously mentioned, our data is not sensitive enough to $\ddot{\nu}_{\text{off}}$ as it is dominated by systematic noise. Using Eqn. 1.10, we predicted the $\ddot{\nu}$ that would be required to obtain a braking index $n = 3$. Assuming the average parameters for ν and $\dot{\nu}_{\text{off}}$ from residual fitting, we would expect $\ddot{\nu} \sim 2.85 \pm 0.05 \times 10^{-28} \text{ s}^{-3}$ (i.e. $\sim 10^9$ less than that derived from fitting separate residual data-sets). Given the level of timing noise in this pulsar, and the $\ddot{\nu}$ quoted in Hobbs et al. (2010)¹⁶, it seems very improbable that any increase in data density would allow us to obtain a value for $\ddot{\nu}$ as low as that predicted from theory. The problem lies in decoupling the long-term contribution of $\dot{\nu}_{\text{on}}$ from the timing residuals; the value for $\ddot{\nu}$ from global fitting will always be contaminated by the modulation of $\dot{\nu}$. In the case of local fitting ($\dot{\nu}_{\text{on, off}}$), there will probably always be an uncertainty in the transition times which, again, means that it will be difficult to decouple $\dot{\nu}_{\text{on, off}}$ from $\dot{\nu}_{\text{av}}$.

4.9 Conclusions

Despite the depth of our study of PSR B1931+24, we unfortunately have not been able to determine the underlying mechanism which is responsible for its emission and rotational behaviour. Most importantly, it still remains unclear what drives the periodic oscillation and why its emission behaviour is uncommon among the pulsar population¹⁷. However, we have confirmed and expanded substantially upon the work of Kramer et al. (2006) which, in turn, has enabled us to provide further evidence for the magnetospheric state-switching scenario (e.g. Bartel et al. 1982; Lyne et al. 2010; Timokhin 2010). As with PSR B0823+26, dedicated infra-red and high-energy observations of this source would be required to determine a viable trigger mechanism for these switches (e.g. ‘circumpulsar asteroids’, Cordes & Shannon 2008).

If the spin-down rates attributed to each emission mode, and ADC, for this pulsar are truly constant over time, as suggested by our observations, this would be quite remarkable; as of yet, there is no clear reason to suggest why a pulsar should retain a memory of its previous magnetospheric state i.e. particle flow (c.f. Li et al. 2012a).

¹⁶Hobbs et al. (2010) obtain $\ddot{\nu} = 7.0 \pm 0.1 \times 10^{-25} \text{ s}^{-3}$ for a time span of ~ 13.7 years, which is 10^6 less than the value derived from this work. As they apply a global fit to the timing data, this lower limit is corrupted by the spin-down rate in the radio-on phase.

¹⁷Only two other pulsars have been observed to show similar behaviour i.e. PSR J1832+0029 (D. Lorimer, private communication) and PSR J1841–0500 (Camilo et al. 2012).

This raises a couple of important questions: 1) Is there charge or matter transfer in the magnetosphere which leads to these separate regulated states and, if so, how would this occur? 2) Why does the pulsar consistently assume the same rotational and emission characteristics? Unfortunately, we conclude that these questions are likely only to be answered based on future observations of this source and others like it. Fortunately, however, we already know a handful of pulsars which exhibit peculiar nulling behaviour and are most likely waiting to further confuse our theories of radio emission production¹⁸.

¹⁸Through characterising the emission and rotational properties of various transient pulsars, we will likely obtain information which will require the current models of radio emission production to be modified to reconcile their behaviour, along with that of PSR B1931+24.

*4: FURTHER INVESTIGATION INTO THE EMISSION MODULATION
CHARACTERISTICS OF PSR B1931+24*

Chapter 5

Radio Emission Moding and Nulling in PSR J1107-5907

PSR J1107–5907 is a recently discovered pulsar (Lorimer et al. 2006) which has very interesting radio emission properties. In the first and only previous study of its radio emission, O’Brien et al. (2006) found that the source undergoes mode changes between bright and weak emission states, as well as a quiescent state where no emission is detected. However, little is known about the timescales of these modulations, nor the possible cause of this behaviour. Here, we present an analysis of approximately 7.5 years of observations to address these questions. We characterise the emission in each mode and determine the nulling fraction of the pulsar. We also investigate a possible relationship between the emission modulation and rotational properties of the source, to determine its relation to the intermittent pulsar class. We find that the object most likely represents a bridge between rotating radio transients (RRATs) and normal nulling pulsars.

5.1 Background

PSR J1107-5907 was found in the Parkes 20-cm Multibeam Pulsar Survey of the Galactic plane (Lorimer et al. 2006), with nothing special initially noted about its behaviour or properties. However, this pulsar is by no means ordinary. Considering the spin-parameters of this source, as shown in Table 5.1, we find that it lies in an underpopulated region in $P - \dot{P}$ space, i.e. between the population of normal and recycled pulsars, which is home to only a small percentage ($\sim 5\%$) of the total population.

What is even more striking about this pulsar is its radio emission behaviour. Using Parkes observations, O’Brien et al. (2006) found that it exhibits 3 different modes of

Table 5.1: Observed and derived properties of PSR J1107–5907 from Lorimer et al. (2006), with standard 1σ errors. The distance was obtained from the NE2001 model (Cordes & Lazio 2002).

Parameter	Value
Right Ascension (J2000)	$11^h 07^m 34.46(4)$
Declination (J2000)	$-59^\circ 07' 18.7(3)$
Epoch of frequency (modified Julian day)	53089
Rotational frequency ν (Hz)	3.95611366927(8)
Rotational frequency derivative $\dot{\nu}$ (s^{-2})	$-1.4(2) \times 10^{-16}$
Dispersion measure DM (cm^{-3} pc)	40.2(11)
Characteristic age τ (Myr)	445
Surface magnetic field strength B (G)	4.8×10^{10}
Spin-down luminosity \dot{E} (erg s^{-1})	2.2×10^{31}
Distance (kpc)	~ 1.3

radio emission: a weak mode with a narrow profile, a strong mode ($S_{1400} \sim 1.1$ Jy, i.e. as bright as the strongest known pulsar: Vela) with a broad profile and, lastly, a quiescent (radio-off) state where no emission is detectable (see Fig. 5.1). In the strong mode, the main pulse is accompanied by extensive pre-cursor and post-cursor components of emission. During the weak mode, however, these emission components are far less pronounced or non-detectable.

O’Brien et al. (2006) noted that the emission behaviour of PSR J1107–5907 appears somewhat similar to that of the archetypal intermittent pulsar, PSR B1931+24; that is they discovered that the pulsar undergoes long periods of emission cessation atypical of normal nulling pulsars ($\gg 1$ –10 pulse periods). However, they were unable to determine the typical timescales of this modulation, most likely due to the sparsity of their data and lack of single-pulse observations.

On one of the days of study, they detected a transition from the weak mode to the strong mode in observations separated by less than thirty minutes (see Fig. 5.1). Within an hour afterwards, the pulsar was observed in its radio-off state and was not detected again until the next day. The shortest radio-off duration of PSR B1931+24 is approximately five times longer than this inferred cessation timescale (i.e. approximately 4.6 days). This implies that PSR J1107–5907 may represent an intermediate between PSR B1931+24 and normal nulling pulsars (similar to PSR B0823+26; see §3).

Since the initial analysis by O’Brien et al. (2006), ongoing observations of this source have been made using the Parkes 64-m telescope. With the increase in the number of observations, and availability of single-pulse data, a more detailed study of

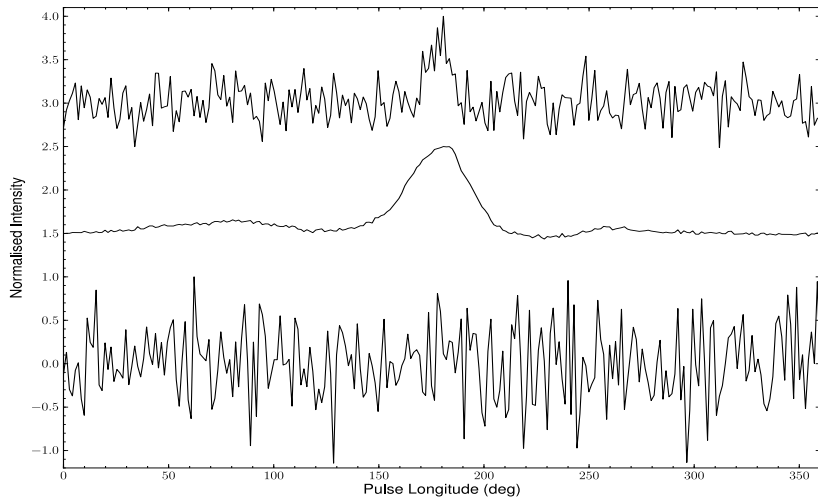


Figure 5.1: Three observations of PSR J1107–5907, showing the typical emission profiles for the weak (*top*), strong (*middle*) and radio-off (*bottom*) states of emission. The weak and strong observations were obtained on 25 May 2004, using 10-minute integrations, and are separated by approximately 28 minutes. The radio-off observation is from the following day using a 15-minute integration. The pulse intensities of each profile are normalised by their peak value and are offset for clarity.

the emission and rotational characteristics of PSR J1107–5907 has been made possible, which is presented in this work.

5.2 Observations

The observations of PSR J1107–5907 were made over the course of an approximately 7.5-year period (21 February 2003 to 24 August 2010) with the Parkes 64-m radio telescope in New South Wales, Australia. An analogue filterbank was used to record single-pulse data and ~ 59.3 s sub-integration data for each observation (apart from 10 observations for which single-pulse data was not obtained). Table 5.2 shows the typical observing properties.

For these observations, we were fortunate to obtain data which was subject to a small amount of radio frequency interference (RFI). However, we did note some strong RFI in a couple of the longest single-pulse observations. As the pulsar can emit across almost the entire pulse longitude range, automated RFI rejection was not feasible. Therefore, RFI was differentiated from emission intrinsic to the pulsar by checking the data for non-dispersed emission in the frequency band. Single-pulses which were identified as RFI were subsequently weighted to zero.

Table 5.2: Characteristics of the observations of PSR J1107–5907 described here.

Parameter	Value
Time span of observations	2741 days
Total number of observations	351
Typical observation duration	5 mins
Average observation cadence	0.13 days ⁻¹
Typical sky frequency	1374 MHz
Typical observing bandwidth	288 MHz
Typical channel bandwidth	3 MHz

Approximately 55 % of all the fully time-averaged data (i.e. averaged over the observation duration) exhibit detectable radio emission. Among these detections, the pulsar exhibits strong-mode emission in 17 out of a total of 351 observations ($\sim 5\%$ of the total or $\sim 9\%$ of the radio-on observations). The remaining detections show the pulsar in its weak emission state ($\sim 50\%$ of the total or $\sim 91\%$ of the radio-on observations). During the majority of the strong-mode observations, the pulsar is so bright that it saturated the one-bit analogue filterbank (see e.g. Fig. 5.7). We also note the presence of sporadic baseline variations in the data, during both strong and weak modes of emission. Unfortunately, however, it was not possible to mitigate these effects.

In total, 9 single-pulse observations were chosen for further study (see Table 5.3). Although a relatively small sample, this collection of observations contains the three longest single-pulse data sets (> 5 hours in duration), as well as 3 single-pulse observations of the pulsar which exhibit both strong and weak-mode emission in the same observation. Therefore, these data can be used to comprehensively study the emission modulation properties of PSR J1107–5907.

5.3 Emission Modulation

Following the work of previous chapters, we initially investigated the timescales of emission variation by applying the activity duty cycle (ADC) method (see §3.3) to the fully time-averaged data. Figure 5.2 shows a graphical representation of the one-bit data which results from this analysis. It is clear from this ‘activity plot’ that the observation cadence is quite low which, subsequently, limits our ability to characterise the typical modulation timescales. However, there are a number of emission phases which are well constrained in time and are able to provide useful information about the modulation properties of the source. The emission phase durations which are determined from

Table 5.3: Properties of the single-pulse observations of PSR J1107–5907 chosen for further study. The reference key for each observation is denoted by REF, MJD is the modified Julian date, ν is the centre frequency of each observation, $\Delta\nu$ is the bandwidth, SNR_{peak} is the peak signal-to-noise ratio, N is the total number of single-pulses and T is the observation length.

REF	MJD	ν (MHz)	$\Delta\nu$ (MHz)	SNR _{peak}	N	T (s)
PKS-S1	52894.037	1518	576	121.7	3556	899.1
PKS-S2	53150.457	1518	576	247.0	2365	598.0
PKS-S3	53801.686	1374	288	27.7	1173	297.0
PKS-S4	54440.958	1374	288	26.4	2826	714.8
PKS-S5	55291.635	1374	288	95.3	1174	297.0
PKS-S6	55291.639	1374	288	69.4	1174	297.0
PKS-L1	53150.168	1518	576	27.6	84648	21397.5
PKS-L2	53224.941	1518	576	2.6	75151	18997.2
PKS-L3	53241.940	1518	576	128.5	75152	18997.2

this data are shown in Fig. 5.3. Due to the sparsity of the observations, and the short timescale variability of PSR J1107–5907 (see Fig. 5.1), we only consider emission phase durations that have gaps ≤ 2 days between consecutive observations. This provides a compromise between time resolution and the number of available data points. We find that the average times spent in the radio-on and -off emission phases are 1.5 ± 0.2 days and 1.0 ± 0.1 days respectively. We also place upper limits on the maximum time spent in the radio-on and -off phases to be 4 ± 2 days and 3 ± 1 days respectively.

Using the same method as in §3.3, we obtain an ADC = $60 \pm 70\%$. The large uncertainty in this quantity is due to the short timescales of emission variation and large relative uncertainties in the emission phase durations. Therefore, we are very cautious to draw any conclusion from this result. In addition, we find no evidence for a significant periodicity in the emission modulation of the fully time-averaged data.

Motivated by the discovery of short-term ($\lesssim 1$ hour) emission variation (O’Brien et al. 2006), and in the hope of further constraining the timescales of modulation, we carried out a thorough inspection of the sub-integration data. It was quickly noted that the pulsar can switch between its separate modes of emission (i.e. strong, weak and radio-off) in less than one minute (see top panel of Fig. 5.4). In order to elucidate these variations, therefore, we also inspected the single-pulse data. Remarkably, we discovered that these transitions occur on a pulse-to-pulse basis (see bottom panel of Fig. 5.4), where the pulsar flux density varies from $\lesssim 45$ mJy up to approximately 453 mJy (see §5.3.1).

To further characterise the pulse intensity modulation of the source, we selected 9

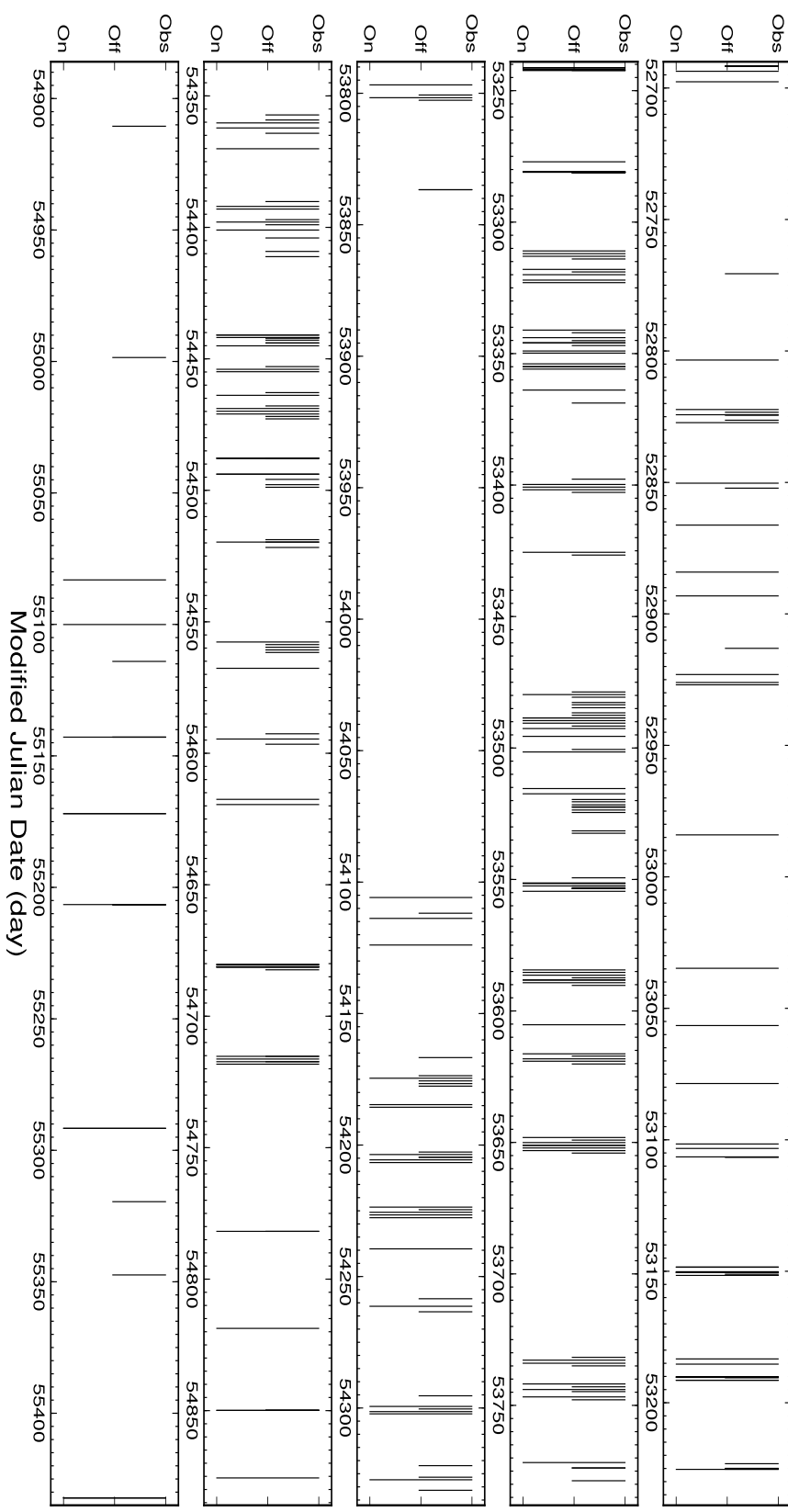


Figure 5.2: Radio activity of PSR J1107–5907 over the ~ 7.5 year period of study, denoted by the black lines. The data is separated into 5 contiguous 549-day segments. The times of observation and the times when PSR J1107–5907 was radio-on (full-height) and off (half-height) are shown by the extent of these lines.

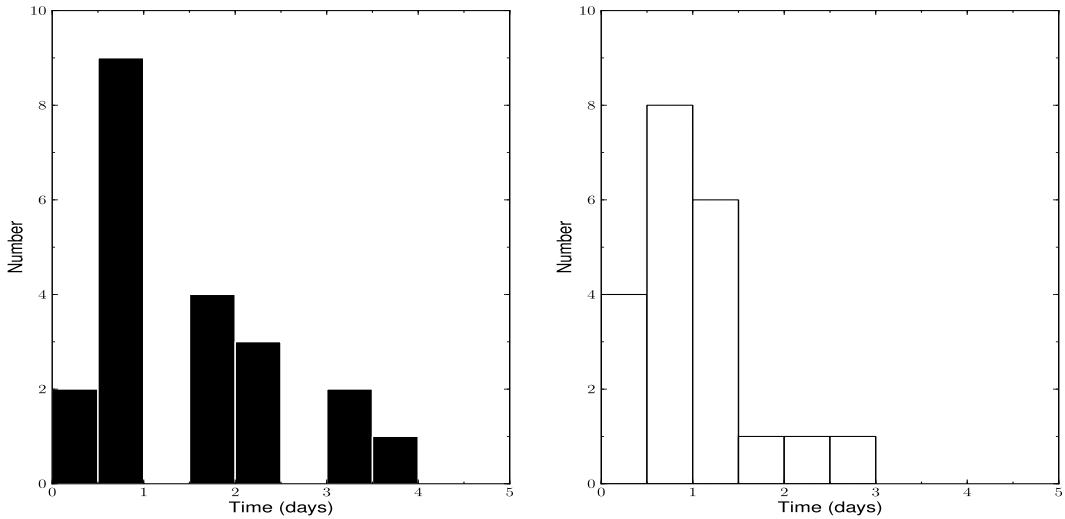


Figure 5.3: Histograms of the emission phase durations for the radio-on (*left*) and radio-off (*right*) modes respectively.

observations for detailed investigation (as discussed in §5.2). In each of these observations, it is apparent that the source does not emit any ‘steady-state’ emission; that is, the object behaves more like a nulling or RRAT-like pulsar than a source which undergoes intermittent radio-on phases (c.f. PSR B1931+24; Kramer et al. 2006). We find that the pulse intensity of the source’s radio emission constantly changes during a given mode. Furthermore, the pulsar exhibits a broad range of null lengths ($N_{\text{null}} \sim 1 - 10^4$ pulses) and does not exhibit any clear periodicity in its nulling behaviour; that is nulls can occur both during and after radio-on phases. Remarkably, in one single-pulse observation (PKS-L2), the pulsar does not exhibit any discernible emission during the entire ~ 5.3 -hour observing period ($\sim 7.5 \times 10^4$ pulses). Figure 5.5 shows a few examples of the emission variability in the source.

If the pulse intensity modulation of the object is a result of interstellar scintillation, we would expect the variations to occur over a gradual timescale i.e. consistent with the scintillation time $\Delta t_{\text{DISS}} \sim 259$ s at 1518 MHz (across an associated decorrelation bandwidth $\Delta\nu_{\text{DISS}} \sim 2$ MHz, using the NE2001 model; Cordes & Lazio 2002). To confirm whether this is true, we formed dynamic spectra for the three longest observations that exhibit strong emission; the strong mode of emission exhibits the highest density of consecutive pulses and, therefore, is better suited to the purpose of analysing the pulse intensity variations. Figure 5.6 shows the result of this analysis. The dynamic spectra show that the pulsar experiences scintillation over narrow, albeit somewhat wider than predicted, frequency bands ($\lesssim 20$ MHz). We also note that the scintillation

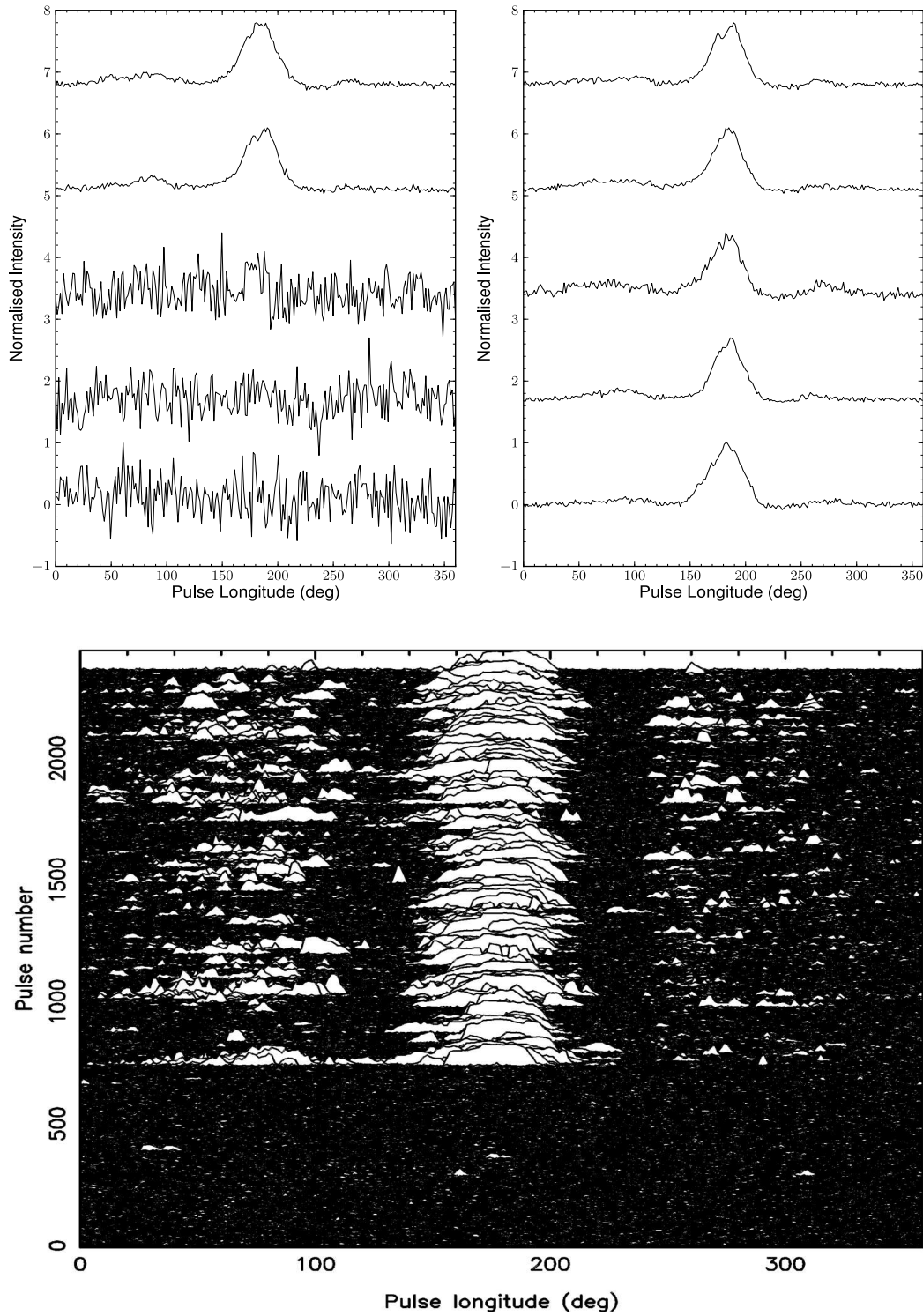


Figure 5.4: *Top panel:* Integrated pulse profiles for each 59.3 s sub-integration (approximately 235 pulses) of a single observation of PSR J1107–5907. The sub-integration data is separated into two columns, each of which display consecutive profiles along the vertical axis (from bottom to top and left to right). The pulsar clearly becomes active (and bright) in the fourth sub-integration. *Bottom panel:* Single-pulse data for the same 10-minute observation (PKS-S2), emphasising the pulse-to-pulse variability of the object.

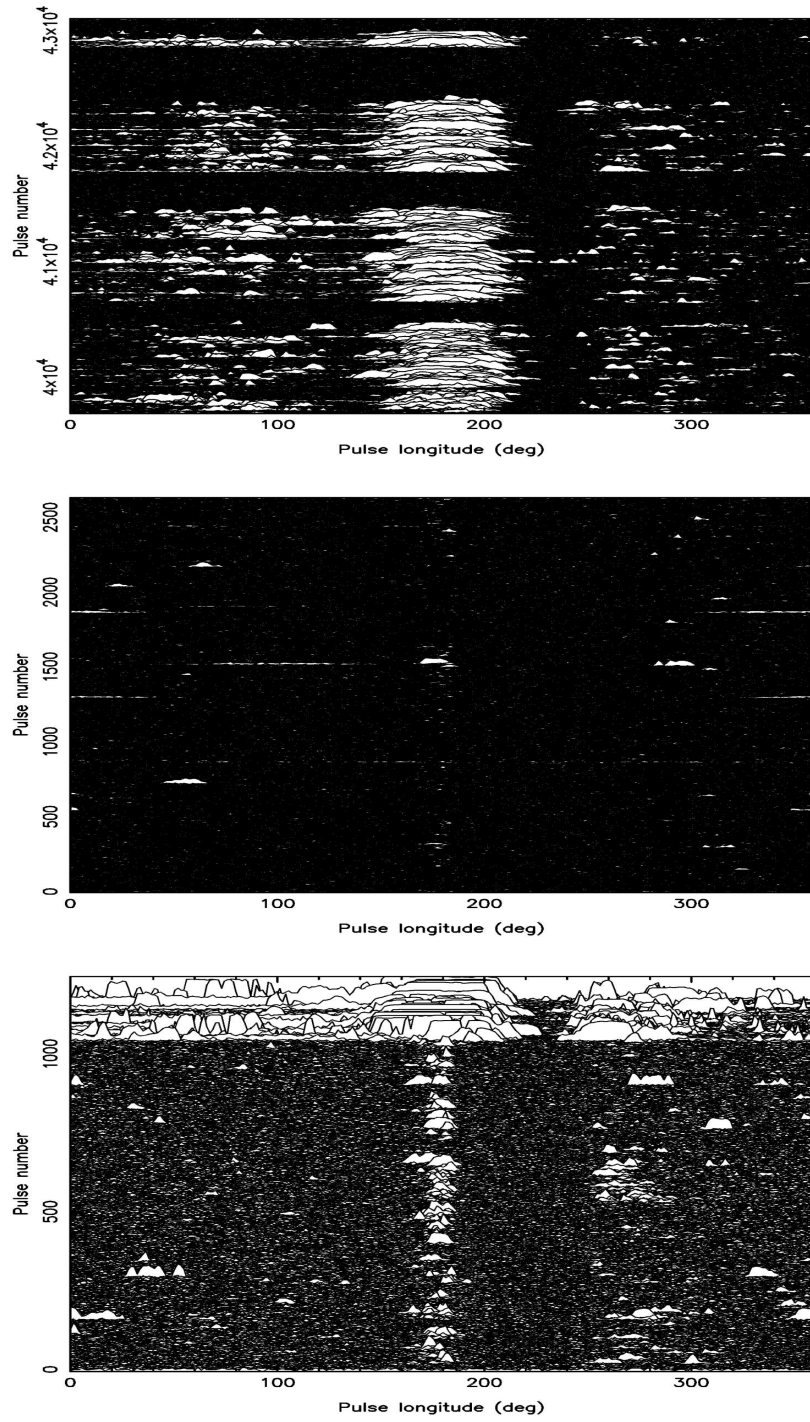


Figure 5.5: Examples of the emission modulation observed in PSR J1107–5907. *Top:* An extract from PKS-L3 (~ 13.5 minutes), where the pulsar is observed to switch between the strong and radio-off emission states numerous times. *Middle:* Single pulses from PKS-S4, demonstrating the typical properties of the weak-mode emission. *Bottom:* The pulse stack from PKS-S5, showing an example where the source emits uncharacteristically ‘steadily’ in its weak mode until a transition to the strong emission state.

behaviour of the source undergoes temporal variation between the different observations i.e. the frequency structure of scintles varies over long periods of time (of the order of days). From the observation of PKS-L3 in particular, we can see that the pulse intensity variations of PSR J1107–5907 are very irregular and occur over short timescales ($\lesssim 1$ minute). We also find that the total intensity minima correspond exceedingly well with the number of null pulses. Coupled with the very low scintillation bandwidth, this implies that the pulse intensity fluctuations of the source are not dominated by interstellar scintillation. Therefore, we can be confident that the emission modulation observed in this object is due to mode-changing and nulling.

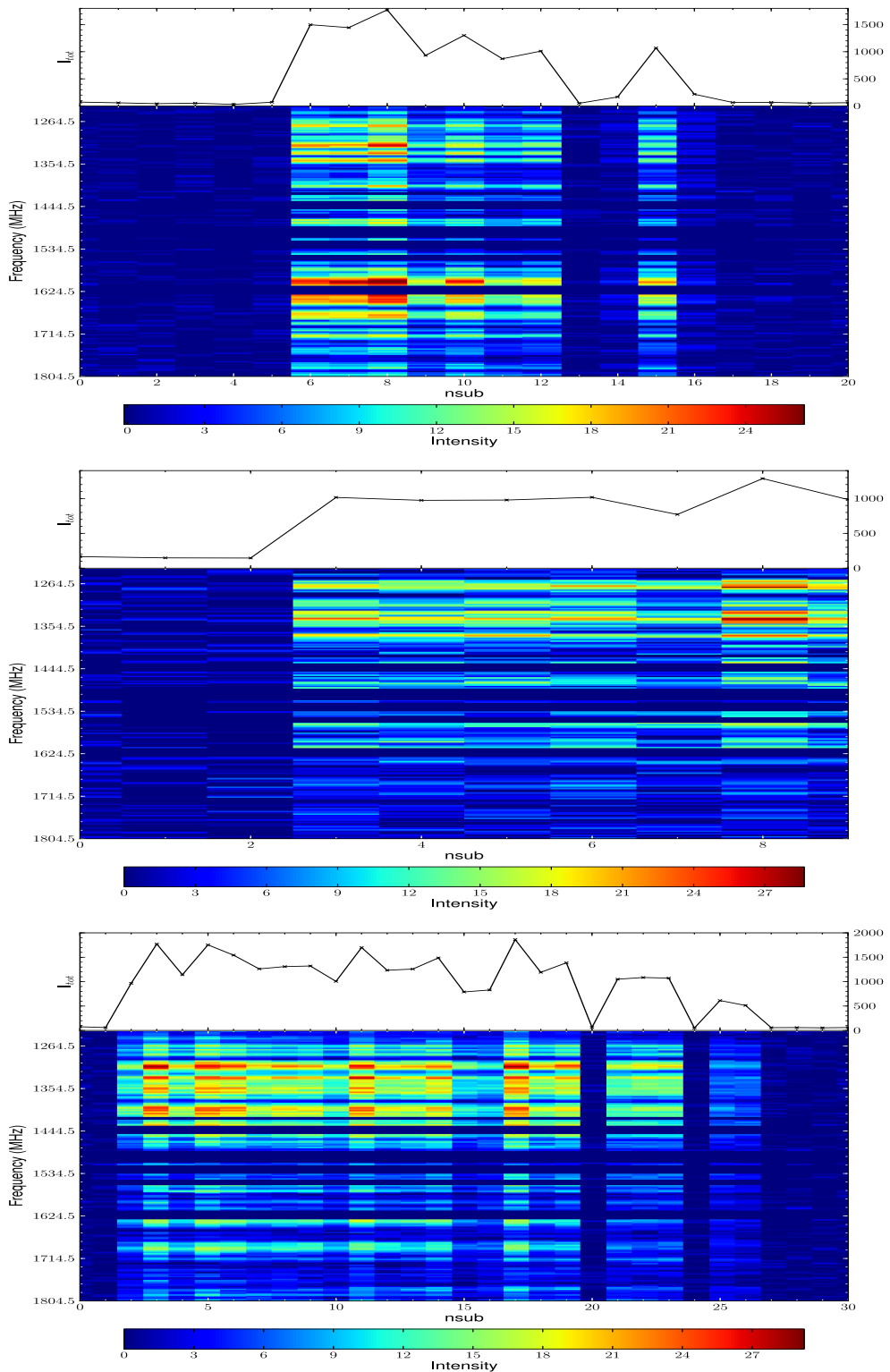


Figure 5.6: Dynamic spectra for three observations of PSR J1107–5907, which are separated into 59.9 s sub-integrations with 192 3-MHz frequency channels. These correspond to extracts from the single-pulse observations PKS-L1, PKS-S2 and PKS-L3 (*top to bottom*) respectively. For each observation, the time versus frequency pulse intensity data is shown in the *bottom panel*. The total intensity across the observed bandwidth is also shown in the *top panel*.

5.3.1 Single-pulse Emission Mode Characterisation

After discovering that the pulsar does not exhibit any steady-state emission, we sought to characterise the emission properties of the different modes based on the single-pulse data. In order to do this, we had to devise a method to accurately differentiate pulses attributed to each emission state. Due to the degree of pulse intensity variation, there is some ambiguity when drawing a distinction between the pulse properties of the radio-on modes. Although the strong-mode emission profile is generally much broader than that of the weak mode, we find that the best differentiator is the density of the number of consecutive radio-on pulses; pulsed emission in the weak mode is typically separated by a few hundred (or more) null pulses, which is in stark contrast to the strong-mode emission (strong pulses are bunched in ‘blocks’, over timescales of up to 20 minutes). Due to the irregularity of the weak radio-on pulses (with respect to intensity and density), and the pulse longitude range over which the pulsar emits, we decided to characterise the emission modes based on the density of high SNR (≥ 10) subpulses within the observations i.e. to locate the regions of strong emission. We analysed the fraction of pulses which meet this criteria over a given range (N_{block}) and, subsequently, find that the most robust identification results from using $N_{\text{block}} = 200$ and a fractional cut-off $f_{\text{crit}} = 0.2$ (i.e. $N_{\text{crit}} = 40$). Single-pulse data which has a fraction of strong pulses less than f_{crit} is defined as weak/off and that above this cut-off is called strong. These criteria are sensitive enough to detect short-term strong emission (i.e. down to a hundred pulses), but are also stringent enough to mitigate the number of false-positive detections. We also inspected the pulse stacks by eye to confirm our findings. Table 5.4 shows the result of this analysis.

Table 5.4: The single-pulse observation statistics of PSR J1107–5907. The observation reference key is denoted by REF, the number of strong, weak/off and total pulses in each observation are represented by N_{strong} , $N_{\text{weak, off}}$ and N_{total} respectively.

REF	N_{strong}	$N_{\text{weak, off}}$	N_{total}
PKS-S1	3556	0	3556
PKS-S2	1645	720	2365
PKS-S3	0	1173	1173
PKS-S4	2826	0	2826
PKS-S5	143	1031	1174
PKS-S6	280	896	1174
PKS-L1	2102	81425	83527
PKS-L2	0	75151	75151
PKS-L3	4904	70248	75152

In PSR B0656+14, it was noted that the pulse shape was energy¹ dependent. Such that the pulse profile became more irregular, compared with the average, towards higher flux density (Weltevrede et al. 2006). To determine whether there was a possible brightness dependent variation in the pulse properties of PSR J1107–5907, we formed pulse-energy separated profiles for two single-pulse observations (PKS-S1 and PKS-S5) using the method above. We averaged pulses within energy ranges $E > 10 \langle E \rangle$, $5 - 10 \langle E \rangle$, $2.5 - 5 \langle E \rangle$ and $0 - 2.5 \langle E \rangle$ (where $\langle E \rangle$ is the average pulse energy of an observation), as shown in Fig. 5.7.

As the pulse intensity increases in the strong-mode observations, the main pulse becomes increasingly broad and flat-topped i.e. more clearly saturated. The baseline also becomes more negative in the trailing edge of the main pulse component, corresponding to the degree of saturation. This is an instrumental effect introduced by the one-bit back-end², which unfortunately cannot be removed from the data. Therefore, the average profiles of the brightest strong-mode pulses ($E \gtrsim 2.5 \langle E \rangle$) are not indicative of the true pulse properties of the source. In the weak mode of emission, however, this is not an issue and we see that the pulse shape changes are quite modest. Namely, there does not appear to be a clear separation in pulse shape leading up to the strongest energies. We also determined the brightest pulse-energy sample for each pulse longitude bin, for both modes of emission (see Fig. 5.7). In the strong mode of emission, the brightest pulse-energy samples are preferentially distributed among the main-pulse and pre-cursor pulse longitude regions. However, it is clear that the pulsar emits across almost the entire pulse longitude range. By comparison, the weak-mode emission is slightly more constrained; the brightest pulse-energy samples are preferentially distributed over a smaller proportion of the pulse profile.

To ascertain whether the pulse shapes attributed to each mode of emission are truly different, i.e. indicative of mode-changing, we formed average profiles of the faintest strong-pulses ($0 - 2.5 \langle E \rangle$) and brightest weak-pulses ($E > 5 \langle E \rangle$) from PKS-S1 and PKS-S5 respectively (see Fig. 5.8). The strong-mode emission does not simply appear to be a scaled version of that attributed to the weak mode; the main-pulse component in the strong mode is intrinsically broader than that in the weak mode (i.e. has a greater duty cycle), regardless of any intensity scaling. This implies that the emission profiles are representative of two different modes of emission.

Similar to the work in the previous chapters, we also computed the flux densities associated with each mode of emission. As the pulsar undergoes extreme emission

¹Following the convention of Weltevrede et al. (2006), we define the ‘pulse energy’ to be interchangeable with pulse intensity.

²The gain of the analogue filterbank is reduced during saturation and, subsequently, results in a reduced baseline after recovery.

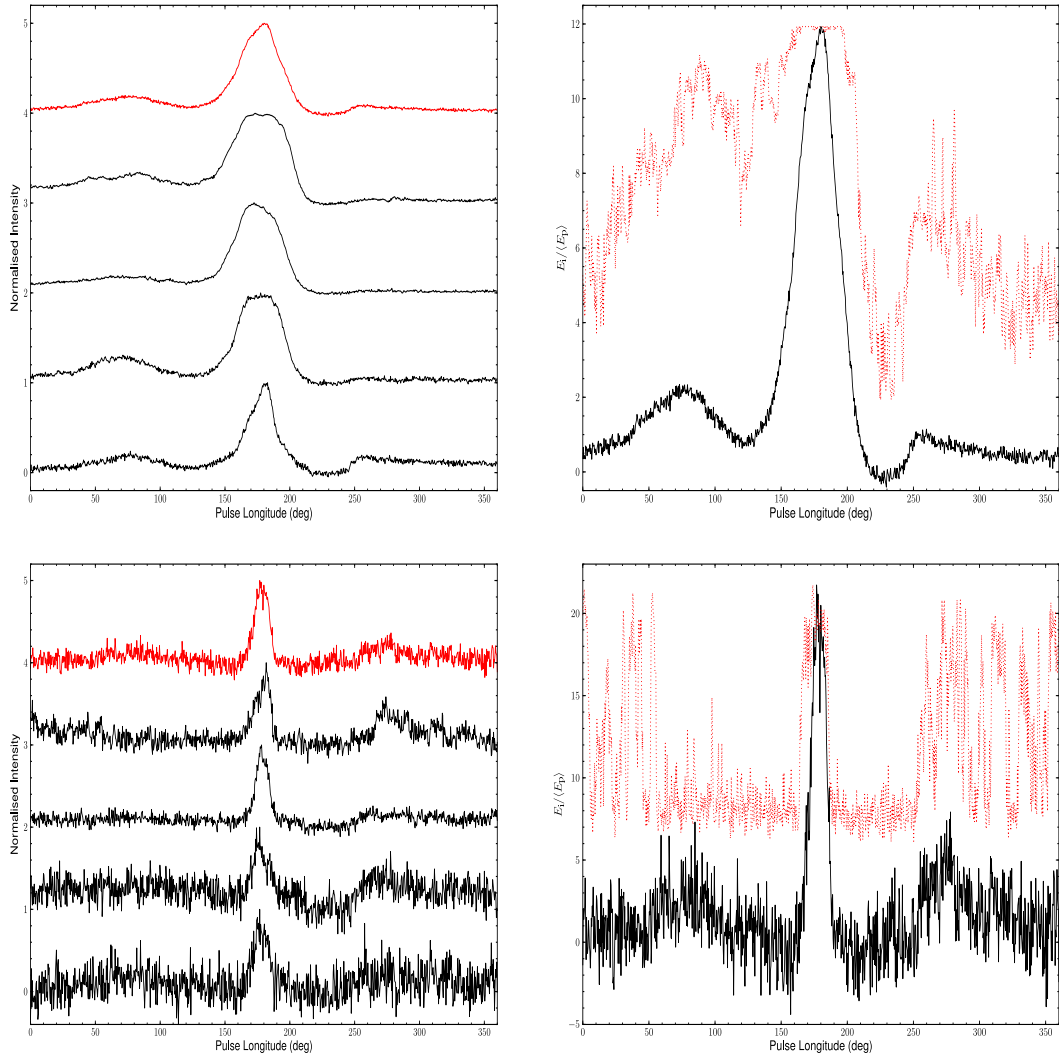


Figure 5.7: Pulse intensity fluctuation with respect to pulse longitude for PKS-S1 (top panels) and PKS-S5 (bottom panels) respectively. *Left:* The top thick line represents the average pulse profile, with successive lines (from top to bottom) denoting average profiles for pulses with $E > 10 \langle E \rangle$, $5 - 10 \langle E \rangle$, $2.5 - 5 \langle E \rangle$ and $0 - 2.5 \langle E \rangle$, and for PKS-S1 contain 65, 161, 178 and 2110 pulses respectively. For PKS-S5, these profiles contain 15, 96, 186 and 328 averaged pulses respectively. *Right:* Scaled average profile (solid line) and the brightest time sample for each pulse longitude bin (dotted line), compared with the average peak-energy of the profile $\langle E_p \rangle$ (at a pulse longitude of $\sim 180^\circ$).

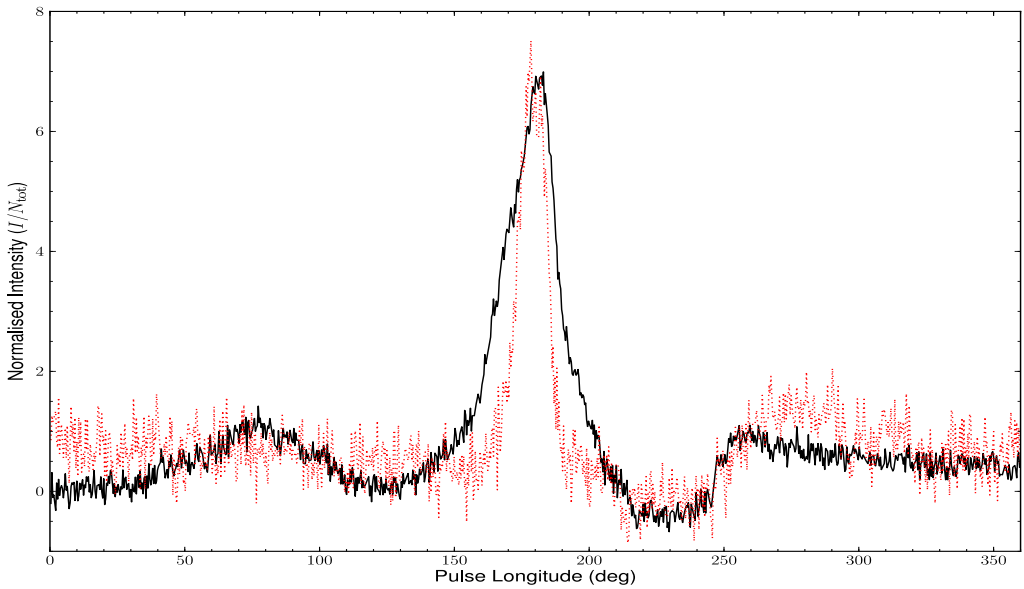


Figure 5.8: Mode-averaged profiles for PSR J1107–5907, made from the faintest strong-pulses of PKS-S1 ($0 - 2.5 \langle E \rangle$; *solid line*) and the brightest weak/off-pulses of PKS-S5 ($\langle E \rangle > 5 \langle E \rangle$; *dotted line*). The pulse intensities are normalised by the number of pulses used to form the average profiles. The pulse intensity of the average weak/off profile is scaled by a factor of 0.8 to enable direct comparison.

modulation over pulse-to-pulse timescales, however, it is not feasible to obtain flux density limits from the averages of multiple observations; the pulsar can exhibit all three modes of emission in a single observation which, ultimately, does not allow the calculation of a stable, average flux density. Instead, we searched the single-pulse data for the brightest (i.e. highest SNR) pulses of each mode to obtain upper limits on the strong, weak and radio-off mode emission. Following McLaughlin & Cordes (2003), these limits can be calculated via:

$$S = \frac{\text{SNR} T_{\text{sys}}}{G \sqrt{n_p B W_{\text{eq}}}}. \quad (5.1)$$

For the single-pulse observations chosen, the system temperature $T_{\text{sys}} \sim 23.5$ K, the telescope gain $G = 0.64$ K Jy $^{-1}$, the number of polarisations $n_p = 2$ and the observation bandwidth $B = 288$ MHz. The equivalent pulse widths (W_{eq}) are approximately 37.8 ms and 9.1 ms for the strong and weak modes respectively. We also assume $W_{\text{eq}} = 9.1$ ms for the radio-off mode emission. As such, we obtain a limit on the flux density in the radio-off state $S_{\text{off}} \lesssim 45$ mJy 3 (SNR ~ 3). For the strong mode

³This quantity reflects the single-pulse detection threshold for discernible emission.

we obtain $S_{\text{strong}} \gtrsim 453$ mJy (SNR ~ 58), which is 10 times brighter than that in the radio-off mode, and approximately 3 times brighter than that in the weak mode $S_{\text{weak}} \sim 165$ mJy (SNR ~ 10). Converting these quantities into pseudo-luminosities, using Eqn. 3.2), we obtain $L_{1400,\text{off}} \lesssim 77$ mJy kpc 2 , $L_{1400,\text{strong}} \gtrsim 766$ mJy kpc 2 and $L_{1400,\text{weak}} \sim 280$ mJy kpc 2 . Comparing these upper limits with the rest of the pulsar population, we find that the object likely resides with the strongest $\sim 6\%$ of sources⁴. Due to saturation, we note that the maximum pseudo-luminosity of the strong-mode emission is likely to be much higher than the value obtained; data clipping will artificially reduce the peak SNR of a pulse and, subsequently, will result in a reduction in L_{1400} . Therefore, it is likely that PSR J1107–5907 could be the highest luminosity pulsar known.

5.3.2 Pulse-energy Distributions

The single-pulse properties of the different modes of emission in PSR J1107–5907, i.e. characteristic pulse shapes and intensities, provide evidence for the existence of two separate pulse populations. To confirm this finding, and further characterise the emission in the different modes, we computed pulse-energy distributions (PEDs; see Weltevrede et al. (2006) for details on this method) for the longest two observations i.e. PKS-L1 and PKS-L3; as these observations contain the highest number of pulses in both emission modes, they are an obvious choice for the purpose of this analysis. To mitigate the effect of nulls on the average pulse energies, we only considered pulses with significant emission peaks; that is, we used a boxcar algorithm to find pulses which exhibit $\text{SNR}_{\text{peak}} \geq 5$ emission in the on-pulse regions. This resulted in a total of 1289 ‘strong’ and 19 736 ‘weak’ pulses for PKS-L1, and a total of 3185 ‘strong’ and 20 000 ‘weak’ pulses for PKS-L3. Figure 5.9 shows the integrated on-pulse and off-pulse energy distributions, separated by emission mode, from this analysis (c.f. Burke-Spolaor et al. 2012). Due to the discrepancy in the number of available on-pulse (N_{on}) to off-pulse (N_{off}) longitude bins, the off-pulse energies are scaled by $\sqrt{N_{\text{on}}/N_{\text{off}}}$.

In the strong emission state, the PEDs show a clear bias towards positive energies. Whereas, the weak-mode PEDs appear more Gaussian distributed (PKS-L1 in particular). This is the major distinction between the different emission-mode PEDs. However, this discrepancy is most likely due to a large number of null pulses still being present in the computation of the weak PEDs which, in turn, cause the average energies to fall close to zero energy. Weak emission from the pulsar is represented by

⁴Data taken from the ATNF pulsar catalog (Manchester et al. 2005) for all the pulsars with a pseudo-luminosity calculated.

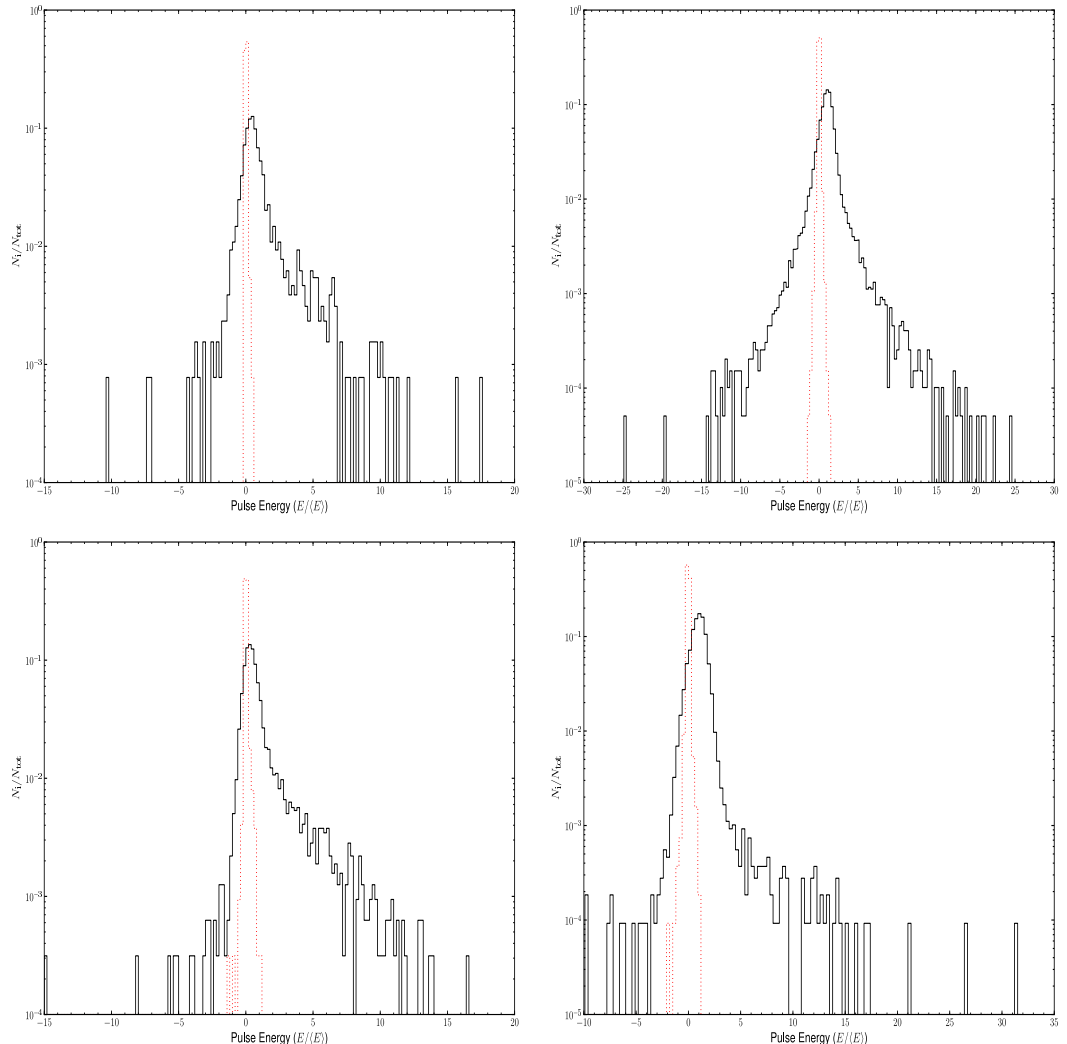


Figure 5.9: Integrated pulse-energy distributions for PKS-L1 (*top*) and PKS-L3 (*bottom*), for the strong and weak emission states (*left to right*) respectively, normalised by the average pulse energy $\langle E \rangle$ of each mode. The on-pulse and off-pulse energies are denoted by the *solid* and *dotted* lines respectively. The off-pulse energies are scaled according to the proportion of on to off-pulse longitude bins used. The maximum pulse energy observed in the strong mode is ~ 18 times the average. However, as these data are saturated, this maximum is likely to be underestimated. We note that the pulse energies of the weak-mode observations are most likely overestimated due to the inclusion of null pulses.

the positive tail in the distributions, which are dominated by the noise; that is, they appear to be convolved with broad, zero-centred Gaussian components. In both emission modes, it is clear that the scaled off-pulse distributions do not track the noise fluctuations well. This is most probably due to the lack of off-pulse bins available, as well as possible baseline variations in the on-pulse region which, subsequently, could cause misrepresentation of the noise signature.

Longitude-resolved Pulse-energy Distributions

To further investigate the relationship between pulse energy and pulse longitude, and a possible separation in pulse population, we computed longitude-resolved PEDs for those observations which showed a prevalence of a given mode of emission. We separated pulse profiles out into four pulse longitude regions for the off-pulse (region 0), pre-cursor (region 1), main-pulse (region 2) and post-cursor emission (region 3). Fig 5.10 shows the longitude-resolved PEDs, along with the average profiles for the mode-separated observations chosen.

The sharp cut-offs at the highest energies are an artifact of data clipping, caused by saturation of the one-bit back-end when the pulsar was in the strong emission mode. Due to this shortcoming, it is not possible to obtain the true form of the pulse-energy distributions for the strong-mode emission. However, we are able to determine that the brightest single-pulse emission in this mode is associated with the main-pulse component (region 2). In the strong-mode observations, we also note that the ‘off-pulse’ region (0) contains distinct excess emission, as shown by the tail of the PEDs. This excess is almost non-existent for the weak/off-mode observations, which implies that emission in this mode is most prominent over a smaller pulse longitude range. The emission in the pre-cursor (1) and post-cursor (3) regions is also typically less pronounced in the weak mode (except for PKS-S5 which was the strongest weak-mode observation). Furthermore, the shape of the weak/off-mode distributions is largely Gaussian, which suggests that these observations are mainly dominated by receiver noise. This in contrast to the strong-mode distributions, which display evidence for more frequent, high energy emission. Therefore, it is not surprising that the maximum longitude-resolved pulse energies in the weak/off observations are unrealistically high compared with the peak average. We also note that emission in the post-cursor region is typically less bright, and more infrequent, than that in the pre-cursor region when the pulsar is the strong mode (and vice versa for the weak mode).

To determine whether there is any correlation between the pulse energies of the on-pulse regions, we also performed longitude-resolved cross-correlation on several pulse profiles for both modes of emission. However, we do not find any evidence for such a

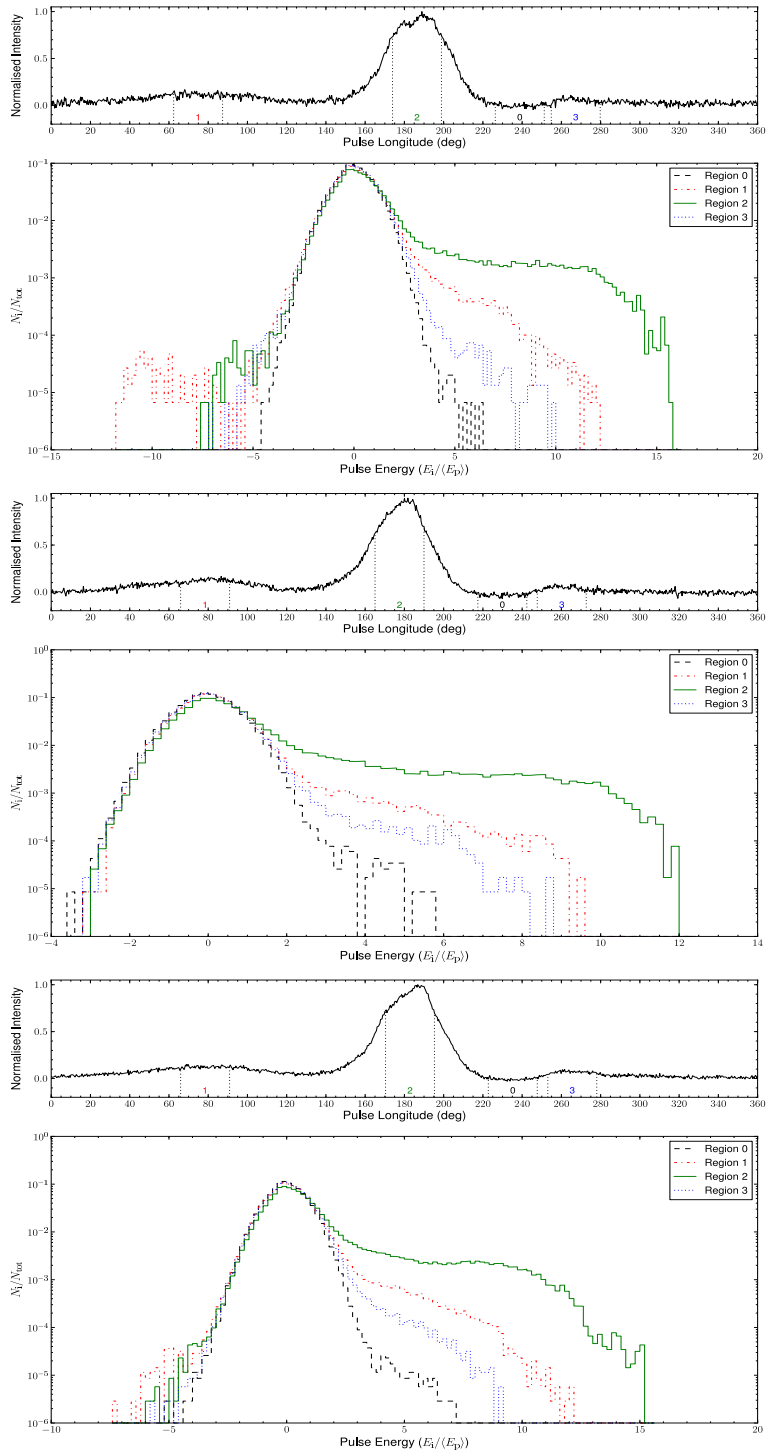


Figure 5.10: Longitude-resolved pulse-energy distributions for strong (*first three*) and weak (*last three*) mode-separated observations PKS-L1, PKS-S2, PKS-L3, PKS-S3, PKS-S4 and PKS-S5 (*from top to bottom*) respectively. The top panel for each of these plots shows the average profile for each observation, with the emission regions numbered. The pulse energies are normalised by the average peak-energy $\langle E_p \rangle$.

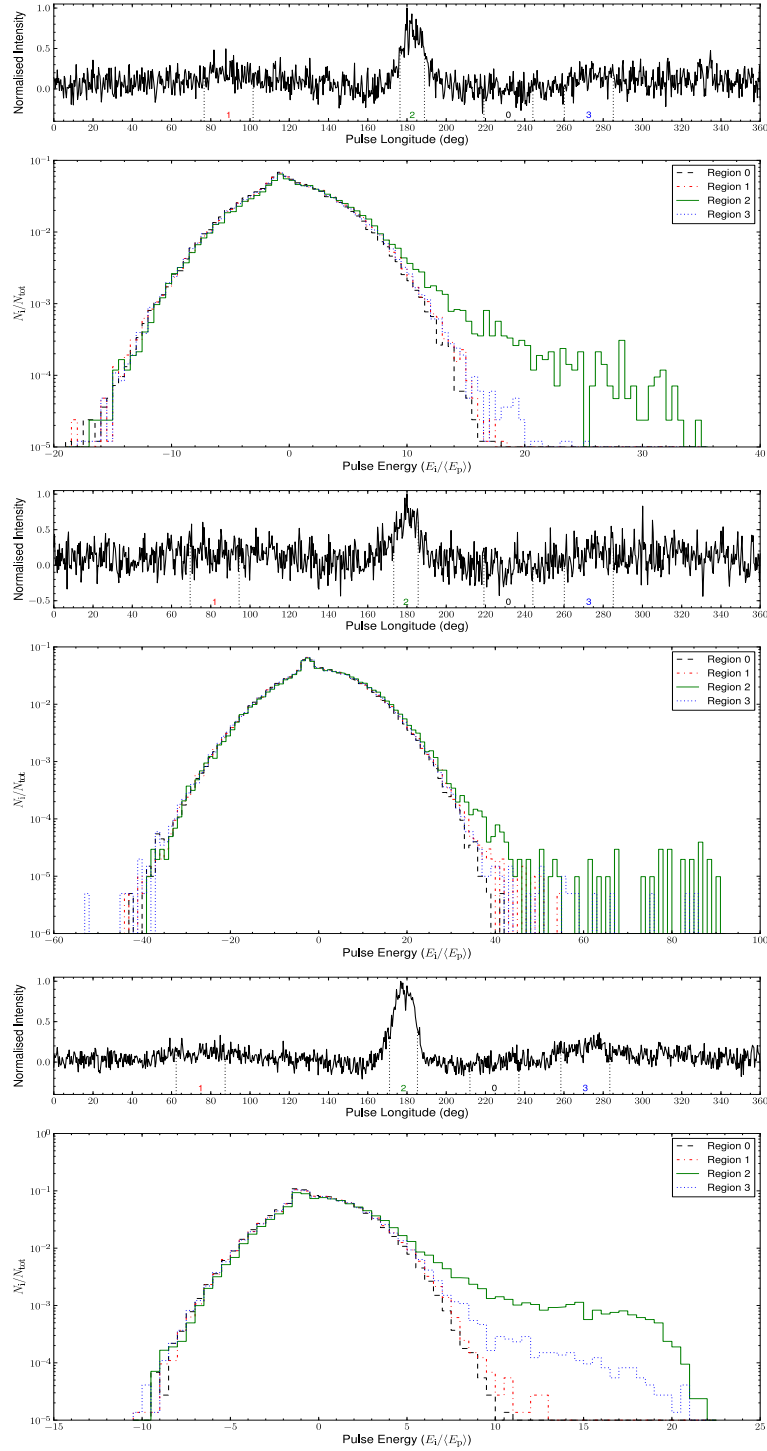


Figure 5.10: —continued. Mode-separated pulse-energy distributions of PSR J1107–5907.

relationship.

With the above in mind, it is clear that the pulse energy characteristics of the strong and weak/off modes are quite different, thus indicating that their emission might constitute two separate pulse populations. Furthermore, we can infer that emission, particularly at higher energies, is preferentially located in the main-pulse region.

Pulse-energy Distribution Fitting

To further characterise the distinction between the separate modes of emission, we modelled the longitude-integrated PEDs of PSR J1107–5907, using the same mode-separated observations as those in §5.3.2. We also sought to quantify the nulling fraction (NF) associated with each mode of emission. Following Weltevrede et al. (2006), we used lognormal and power law trial distributions to fit the integrated on-PEDs of both the strong⁵ and weak-mode emission:

$$P_{\text{powerlaw}}(E) \propto E^p, \quad (5.2)$$

$$P_{\text{lognormal}}(E) = \frac{\langle E \rangle}{\sqrt{2\pi}\sigma E} \exp \left[-\left(\ln \frac{E}{\langle E \rangle} - \mu \right)^2 / (2\sigma^2) \right]. \quad (5.3)$$

To improve the accuracy of the model, pulse energy cut-offs E_{\min} and E_{\max} (minimum and maximum pulse energies) were also applied in the fitting process, to constrain the range of pulse energies to those observed. Further to this, the model distributions were convolved with the noise signature of each observation to represent the contribution due to receiver noise. As the off-pulse profile range for each observation is particularly small compared with the on-pulse region, and the fact that the noise distribution deviates from a pure Gaussian distribution, we estimated the noise signature by producing a symmetric distribution from the negative on-pulse energies. This ‘mirrored’ distribution is probably an oversimplification of the true noise variation, but has the advantage of not introducing extra fit parameters and complexity to the model.

The presence of nulls were incorporated into the model by adding pulses with zero energy to the fitted distribution (before convolving this distribution with that of the noise), until the average energy $\langle E \rangle$ converged with the observed value. The parameters of each model distribution were optimised by minimising the χ^2 between that and the observed distribution, using the downhill simplex method (amoeba algorithm; Press

⁵The majority of pulses in the strong emission state represent the true emission properties of the source. However, a significant proportion of the total ($\sim 20\%$) do experience saturation. These saturated pulses are also the brightest and, as such, are required to represent the highest energies in the model fit. Therefore, the fits to the strong-mode data are likely to be somewhat affected by the degree of saturation.

et al. 1992).

We find that a power law (Eqn. 5.2), with E_{\min} and E_{\max} cut-offs, fits the PEDs with the highest confidence (compared to using a log-normal distribution), irrespective of the mode of emission. The results of this analysis are detailed in Table 5.5. Figure 5.11 shows the highest confidence fits of this analysis. The models fitted to these data clearly coincide well the observed on-pulse distributions. Here, we find tentative evidence to support the previous indication of a separation in pulse population. That is, there is a tendency towards greater NF and spectral index (p) in the weak/off-mode data. However, this result requires further investigation to determine whether this is a common property of the weak/off-mode pulses, and how the data may have been biased by saturation effects.

Table 5.5: The best-fit parameters to the pulse energy distributions of PSR J1107–5907. The reference key of each observation is denoted by REF, the type of pulses included in each fit is represented by ‘mode’ and the power law exponent is given by p . The number of nulls added to a distribution is denoted by N_{null} , the total number of pulses included in each fit is N_{pulses} . The nulling fraction NF, total χ^2 and significance probability $P(\chi^2)$ are also tabulated.

REF	Mode	p	N_{null}	N_{pulses}	NF (%)	χ^2	$P(\chi^2)$
PKS-S2	Combined	-1.31	62 304	1 062 234	5.9	38	0.09
PKS-L1	Combined	-1.63	12 943 663	13 943 663	92.8	10	0.71
PKS-L3	Combined	-1.46	12 183 307	13 183 307	92.4	20	0.64
PKS-S2	Strong	-1.44	356 129	1 356 129	26.3	27	0.07
PKS-L1	Strong	-1.58	1 037 502	2 037 502	50.9	14	0.72
PKS-L3	Strong	-1.53	1 009 126	2 009 126	50.2	21	0.10
PKS-S3	Weak	-3.03	2 989 435	3 989 435	74.9	24	0.30
PKS-S4	Weak	-5.98	4 373 059	5 373 059	81.8	4	0.74
PKS-S5	Weak	-1.66	1 556 741	2 556 741	60.9	18	0.98

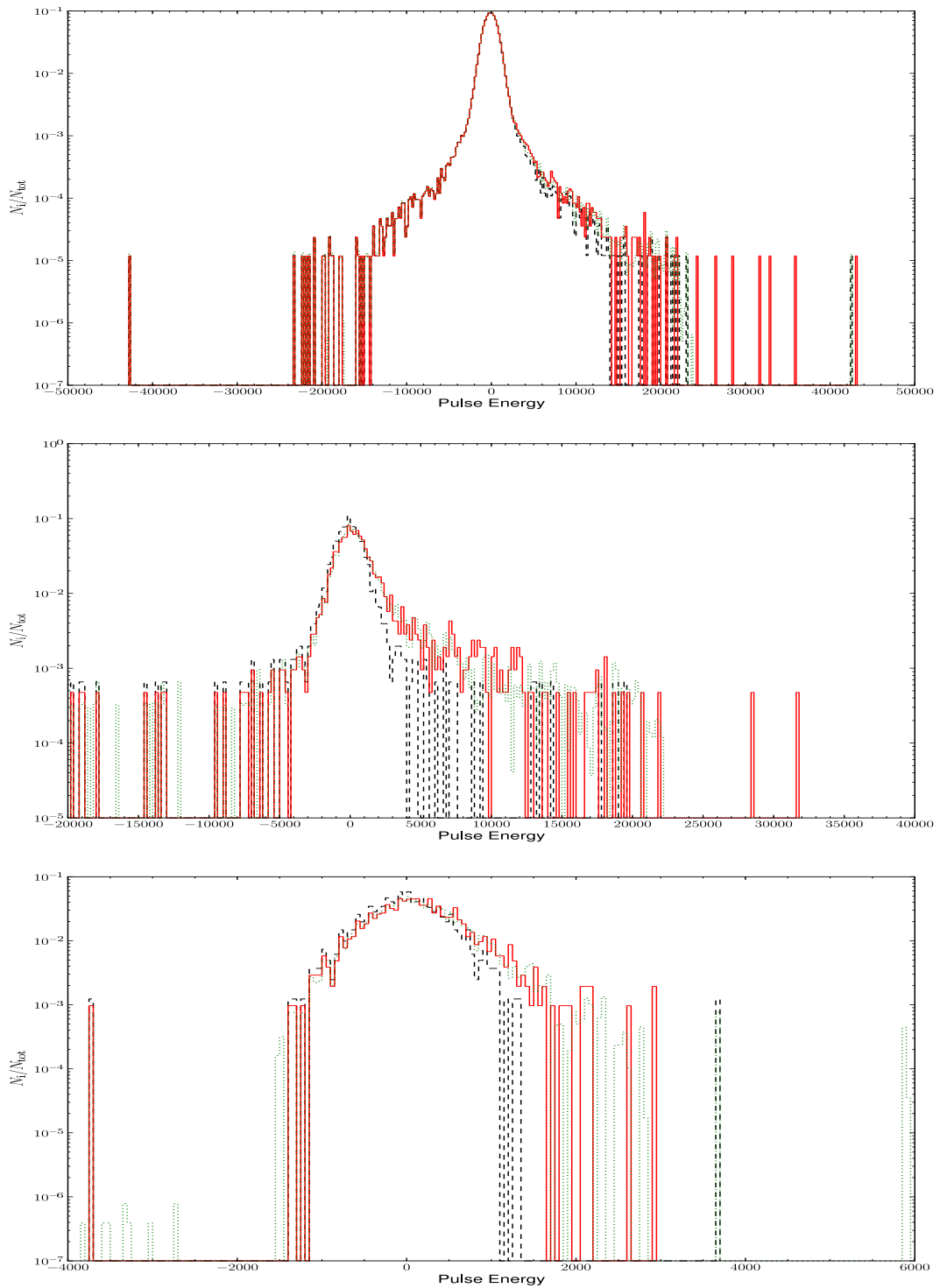


Figure 5.11: Best-fit model PEDs (dotted line) compared with the observed on-pulse (solid line) and off-pulse (dashed line) distributions. *Top:* PEDs from PKS-L1 using both strong- and weak/off-mode pulses. *Middle:* Strong mode PEDs from PKS-L1. *Bottom:* Weak/off-mode PEDs from PKS-S5.

Residual Histograms

To confirm the nulling fraction (NF) results of the previous analysis, we also computed ‘difference histograms’ from the on-pulse and off-pulse energy distributions and tested their goodness-of-fit for various trial (upper limit) NFs (we refer to Ritchings 1976; Wang et al. 2007 for a detailed overview of the method). In this analysis, the NF is simply the scale factor that is applied to the off-pulse histogram which, in turn, determines the proportion of histogram counts that are subtracted from the on-pulse histogram. Following Wang et al. (2007), we determine the goodness-of-fit from the proportion of the difference counts (i.e. on-pulse minus off-pulse counts) in bins with $E < 0$. For the best trial NF, the number of difference counts with $E < 0$ should be zero, with an uncertainty $\sqrt{N_{\text{null}}} / N_{\text{total}}$.

Before performing this analysis, single-pulse data is typically normalised by a running average energy to correct for pulse intensity variations due to scintillation. In the case of PSR J1107–5907, however, the intensity modulations are dominated by mode changing and nulling, rather than by interstellar scintillation. Coupled with this fact, and in order to be consistent with the previous PED analysis, we do not perform any pulse energy normalisation.

Using a method similar to that in §5.3.2, we sampled negative on-pulse energies to form the off-pulse distributions. Negative on-pulse energies were ‘mirrored’ to make a symmetric distribution as above. However, we also randomly sampled this data to fill any deficit in pulse number between the on-pulse and off-pulse histograms. Consequently, we quote NFs as the averages formed from successive samples of the ‘off-pulse’ distribution. Table 5.6 and Fig.5.12 shows the results of this analysis for the same observations as in §5.3.2.

Table 5.6: The best-fit trial nulling fractions for the observations discussed here. The reference key of each observation is denoted by REF, the type of pulses included in the analysis are represented by ‘mode’ and the nulling fraction is given by NF.

REF	Mode	NF (%)
PKS-S2	Combined	$\leq 54 \pm 2$
PKS-L1	Combined	$\leq 98.4 \pm 0.3$
PKS-L3	Combined	$\leq 97.4 \pm 0.4$
PKS-S2	Strong	$\leq 41 \pm 2$
PKS-L1	Strong	$\leq 72 \pm 2$
PKS-L3	Strong	$\leq 68 \pm 1$
PKS-S3	Weak	$\leq 82 \pm 3$
PKS-S4	Weak	$\leq 88 \pm 2$
PKS-S5	Weak	$\leq 78 \pm 3$

Due to the disparity in the results of the different methods of NF determination, we also inspected the pulse intensity modulation of the single-pulse data by eye. We find that the results of the ‘residual’ histogram method are far more consistent (within $\lesssim 3\sigma$) with the true nulling behaviour of the pulsar attributed to each observation. Therefore, it is apparent that the PEDs of the radio-on emission modes cannot be fully described by simple normal (lognormal) or giant pulse (power law) distribution functions (see e.g. Lundgren et al. (1995); Cairns (2004) for details on these pulse population properties). This is probably due to population mixing and the artificial cut-offs in the data.

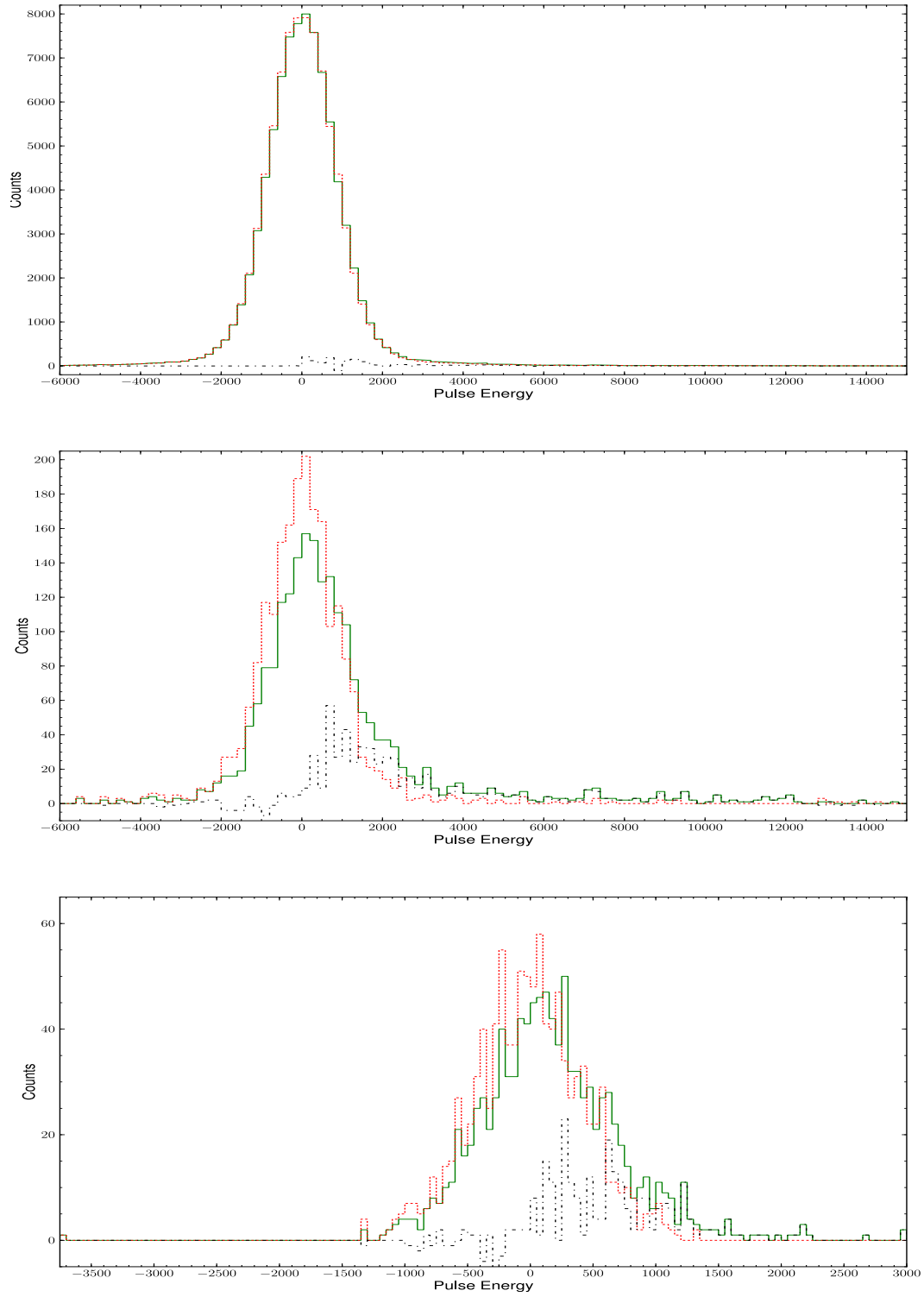


Figure 5.12: Histograms of on-pulse (green solid line), off-pulse (red dotted line) and residual (black dot-dashed line) pulse energies for the PKS-L1 (*combined and strong mode*) and PKS-S5 (*weak mode*) observations (from top to bottom) respectively.

5.3.3 Fluctuation Spectra

To further characterise the modulation properties of PSR J1107–5907, we computed longitude-resolved fluctuation spectra (LRFS; Backer 1970a), as well as two-dimensional fluctuation spectra (2DFS; Edwards & Stappers 2002) for several of the strong and weak single-pulse observations. We calculated the LRFS by taking Discrete Fourier Transforms (DFTs) along lines of constant pulse longitude, over successive blocks of 256 pulses, which were averaged and used to detect any periodic intensity fluctuation in the data. We also computed the longitude-resolved variance (σ_i^2) and modulation index ($m_i = \sigma_i/\mu_i$) profiles for the observations through vertical integration of the LRFS (μ_i is the average intensity at a given pulse longitude; see also Weltevrede et al. 2006 for more details). These parameters, in combination with the LRFS, were used to infer the presence of any intensity modulation and the degree of periodicity i.e. to determine whether any intensity variation was random or (quasi-)periodic. To differentiate between an intensity or phase modulation, DFTs along lines of different slopes (in pulse longitude) were also performed on separate pulse longitude regions within the LRFS to provide the 2DFS. The pulse longitude range was again separated into three on-pulse regions i.e. the pre-cursor, main-pulse and post-cursor emission regions. The results of this analysis are shown in Fig. 5.13 and Fig. 5.14 for the strong and weak observations respectively.

In each of these plots, the top panel shows the integrated profile (*solid line*) and the longitude-resolved modulation index profile⁶ (*solid line with error bars*), as well as the longitude-resolved standard deviation profile (*open circles*). Below these panels the LRFS is shown, with pulse longitude in degrees displayed on the horizontal axis. The subsequent panels show the 2DFS for the pre-cursor, main-pulse and post-cursor emission regions respectively. The power in each 2DFS is vertically integrated and is shown in the adjacent panels beneath, which are used to quantify the subpulse phase modulation (P_2). Both the LRFS and 2DFS are horizontally integrated, producing the side panels of the spectra and show the subpulse intensity modulation (P_3).

In the modulation index profiles of the strong observations, we clearly see that the most prominent intensity variation is associated with the pre-cursor emission component, as well as the shoulders of the main-pulse component (as shown by the distinctive U-shapes). In each observation (apart from PKS-L1), we also note significant intensity modulation in a small portion of the post-cursor pulse longitude range. From these observations, we infer that the source has a typical strong-mode modulation index

⁶The uncertainty in m_i is determined by bootstrapping σ_i ; that is, additional random off-pulse intensity samples are incorporated into the calculation of σ_i and, subsequently allow $\sigma(m_i)$ to be obtained.

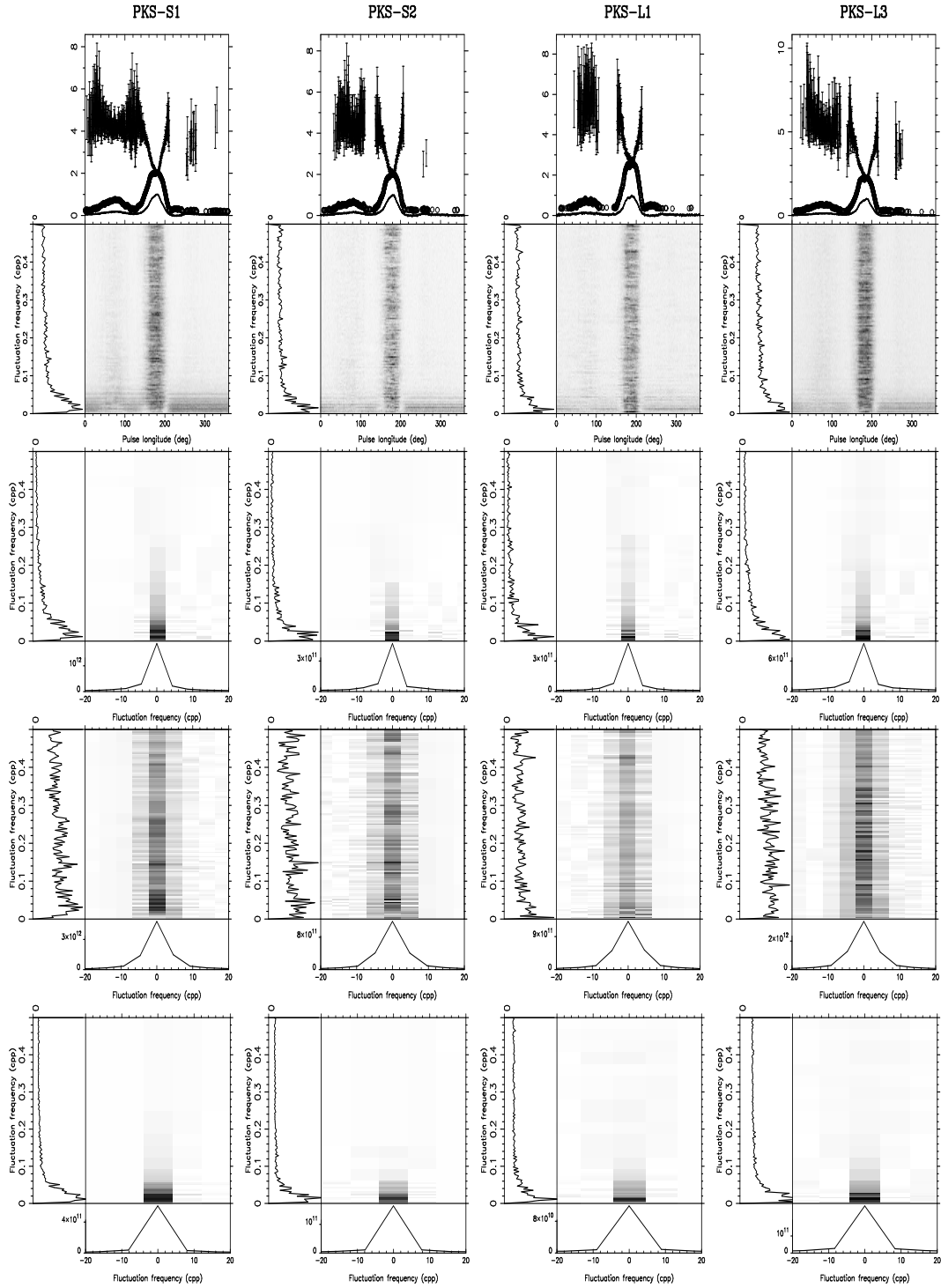


Figure 5.13: The modulation properties of PSR J1107–5907 in the strong emission mode for PKS-S1, PKS-S2, PKS-L1 and PKS-L3 respectively. The modulation index profile and LRFS of the observations are shown in the first and second panels respectively. The subsequent 2DFS of the pre-cursor, main-pulse and post-cursor components are shown by the bottom 3 plots, from top to bottom respectively. A description of these plots is given in the text.

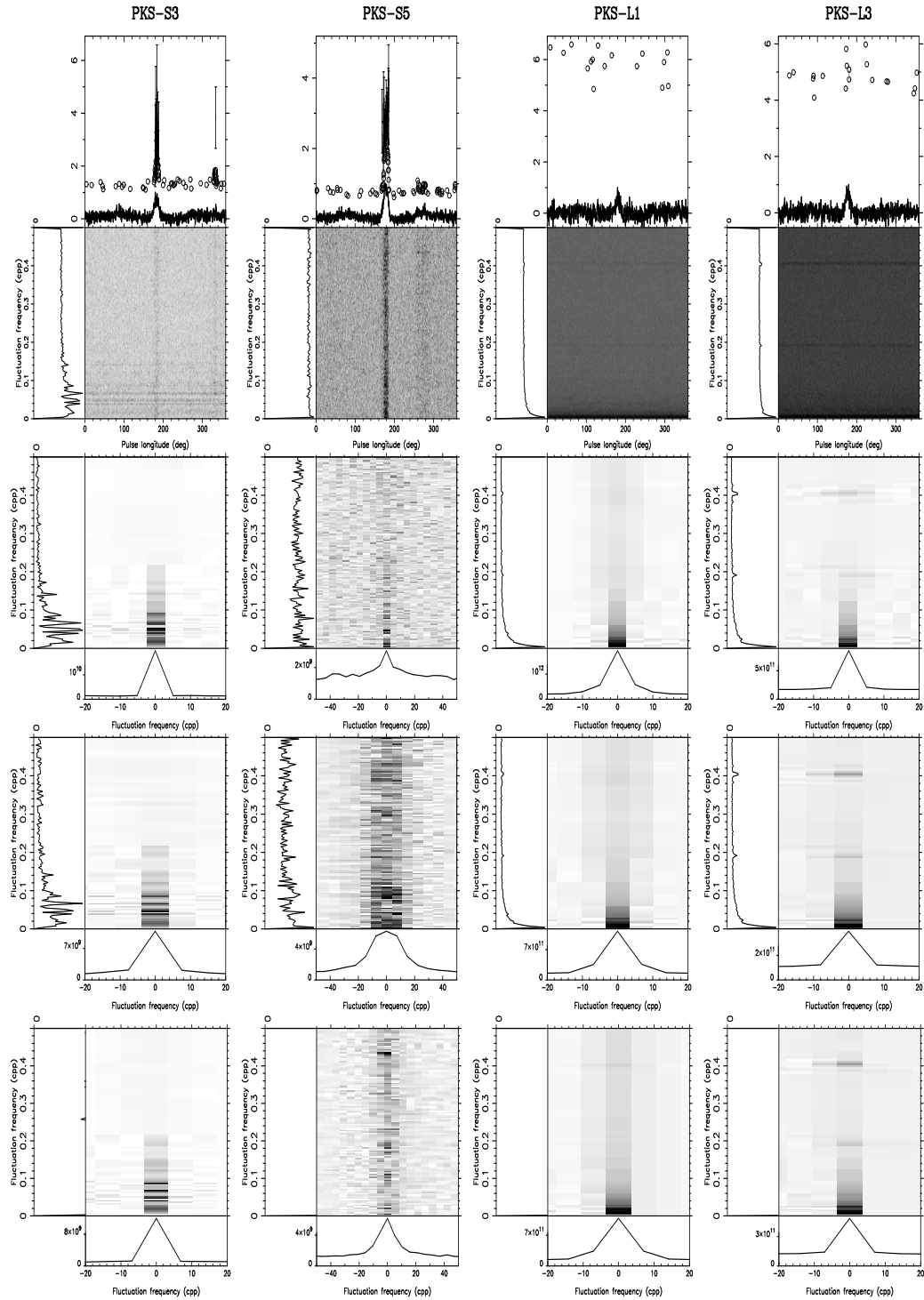


Figure 5.14: The modulation properties of PSR J1107–5907 in the weak emission mode for PKS-S3, PKS-S5, PKS-L1 and PKS-L3 respectively. See text for details.

($\langle m_i \rangle \sim 4$) which is far greater than that associated with normal pulsars (i.e. $m_i \sim 0.5$ Weltevrede et al. 2006). Furthermore, the typical modulation indices associated solely with the pre-cursor, and main-pulse shoulder regions ($m_i \sim 5$), are consistent with that of RRAT-like sources such as PSR B0656+14 (Weltevrede et al. 2006; Serylak et al. 2009; Weltevrede et al. 2011).

In the LRFS of the strong observations, there is a dominant broad feature centred around $P_3 \sim 100 P_0$. However, the power associated with this spectral component is distributed across the whole pulse longitude range. This implies that it is associated with baseline variations and (or) RFI in the data, rather than with any intrinsic intensity modulation of the source. Therefore, we are cautious to draw any conclusions from the subsequent 2DFS, which are also dominated by this spectral feature.

In the weak observations, the only significant intensity modulation is displayed in the shortest observations (PKS-S3 and PKS-S5) which exhibit the greatest density of pulses. The longitude-resolved modulation index profiles for these observations show that there is some strong intensity modulation associated with the main-pulse component. The modulation index ($\langle m_i \rangle \sim 3$) is slightly lower than that observed in the strong emission mode. However, it is still far more extreme than that observed in typical pulsars, thus confirming that the source undergoes extraordinary pulse intensity variation in both modes of emission. In the longest observations (PKS-L1 and PKS-L3), we note that there is an unusually large offset between the standard deviation and integrated pulse profiles. Furthermore, no significant longitude-resolved modulation indices were able to be obtained for these observations. This could be due to artificial effects (e.g. baseline variations) on the data, or perhaps a result of the intrinsic sparsity of the pulses.

In the LRFS of the weak observations, we again see that the power associated with the dominant features (except for PKS-S5, which has none) is distributed across the entire pulse longitude range. We note that the dominant periodicities in the subsequent 2DFS correspond with these instrumental features and, therefore, are unlikely to be associated with emission modulation intrinsic to the pulsar. In the case of the longest observations, however, it may be possible that the modulation features of the 2DFS are related to the nulling behaviour of the source; PSR J1107–5907 exhibits nulls which last several hundreds or even thousands of pulses, which would be represented by power in the lowest frequency bin ($P_3 = 256 P_0$).

5.4 Timing Analysis

In PSR B1931+24 (and perhaps PSR B0823+26) we see evidence for changes in pulse intensity which are associated with the timing behaviour of the object(s) (§3-4), which leads us to suggest that similar changes should occur in PSR J1107–5907 if it is governed by the same process(es). To investigate such a relation between pulse intensity and rotational stability, we calculated the timing residuals of PSR J1107–5907 for the entire data-set. As the radio-on observations contain a mixture of strong ($\sim 9\%$) and weak ($\sim 91\%$) emission profiles, TOAs were calculated using two profile templates. That is, we fitted analytic templates to the highest SNR strong- and weak-mode profiles, and used them to calculate the TOAs for the corresponding emission mode. We computed the timing residuals, i.e. the observed - predicted TOAs, using the TEMPO2⁷ package (Hobbs et al. 2006). We noted that the strong- and weak-mode residuals exhibited a systematic offset of $\sim 3 - 4$ ms, which can be attributed to the offset in the fiducial reference points of the different profile templates. We accounted for this effect by fitting a global ‘jump’ in the weak-mode residuals; that is, a global best-fitting offset was added to each weak-mode residual. This, in turn, reduced the root-mean-square of the residuals by a factor of 2. The result of this analysis is shown in Fig. 5.15. For these data, we obtain an average $\dot{\nu} = -1.403 \pm 0.001 \times 10^{-16}$ s $^{-2}$, which is significantly lower than that of PSR B1931+24 (i.e. $\dot{\nu}_{\text{av}} = -12.249 \pm 0.001 \times 10^{-15}$ s $^{-2}$; Kramer et al. 2006).

There is no clear distinction between the two sets of residuals (for the strong and weak mode), apart from the typical size of the error bars; that is, the strong-mode residuals have substantially (~ 3 times) smaller uncertainties than those of the weak mode on average. This can be attributed to the much greater SNR of the strong-mode observations, in general, compared with those of the weak mode.

Due to the sparsity of the data, it is not apparent whether the timing residuals show evidence for any (quasi-)periodicity (i.e. cubic structure), which would be indicative of magnetospheric changes; that is spin-down rate variation, as observed in PSR B1931+24 (Kramer et al. 2006; Hobbs et al. 2010; Lyne et al. 2010). As the timescales of emission modulation are particularly short, however, it is unlikely that we would be able to resolve the effect of a variable spin-down rate on such a low average $\dot{\nu}$. To test this hypothesis, we fitted the residuals of the weak and strong modes separately to obtain their associated spin-down rates. We find that the spin-down rate in the strong mode, $\dot{\nu}_{\text{strong}} = -1.392 \pm 0.004 \times 10^{-16}$ s $^{-2}$, is slightly less than that in the weak mode, i.e. $\dot{\nu}_{\text{weak}} = -1.404 \pm 0.002 \times 10^{-16}$ s $^{-2}$. However, the uncertainties

⁷<http://www.atnf.csiro.au/research/pulsar/tempo2/>

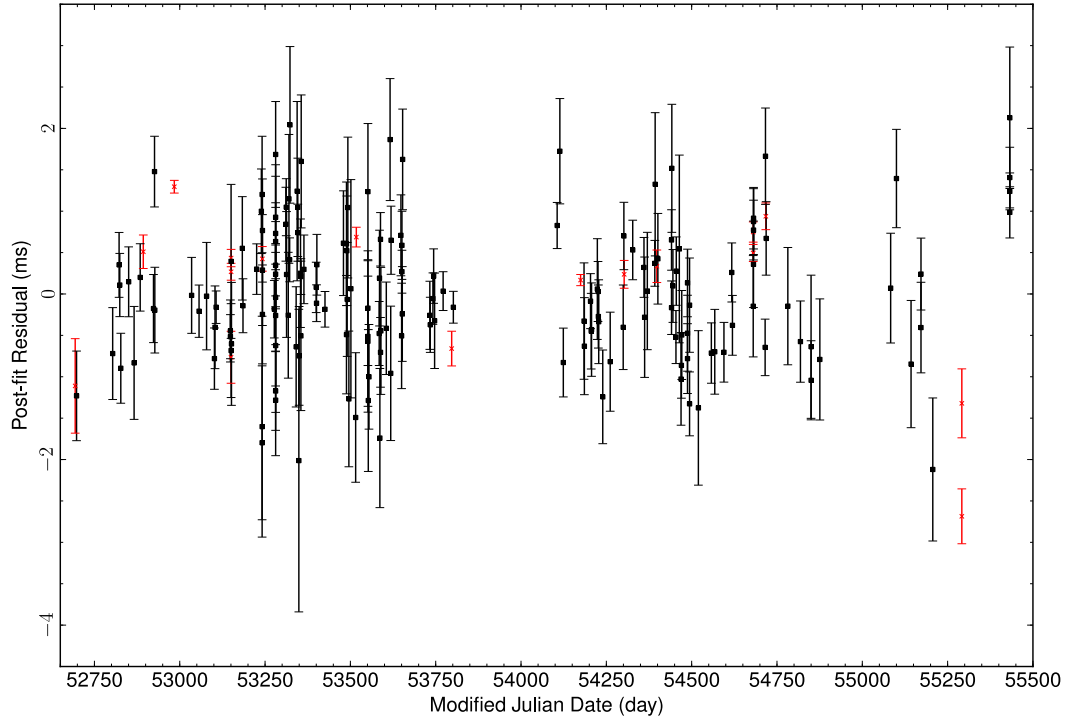


Figure 5.15: The timing residuals of PSR J1107–5907 over the ~ 7.5 -year period. Analytic templates, based on the strong- and weak-mode pulse shapes, were used to calculate the residuals using folded profile data. Here ν , $\dot{\nu}$ and DM have been fitted for. The strong-mode residuals are shown by the *red crosses* and the weak-mode residuals are indicated by the *black squares*.

on these parameters do not support any significant ($\gtrsim 3\sigma$) change in $\dot{\nu}$ between the different emission modes. Furthermore, we note that the folded profiles used to obtain the strong-mode residuals are often artificially broadened due to saturation, which may have influenced the fitting process somewhat; pulse broadening will introduce a time offset during the template matching process (see §1.2 for a detailed overview of the pulsar timing method) as the fiducial reference point will occur later relative to a non-broadened pulse which, in turn, could affect the timing solution obtained. Therefore, further observations of this source are required to confirm whether the spin-down rate variation is indeed significant.

5.5 Discussion

Through analysing the emission modulation characteristics of PSR J1107–5907 in detail, we have further indicated the importance of obtaining high time resolution data for

transient pulsar studies. Namely, it is clear that the nature in which the modulation behaviour of an object is interpreted is greatly affected by the available observation cadence; without single-pulse data we would not have discovered the true nature of the pulse intensity modulation in PSR J1107–5907 and, subsequently, assumed that it was somewhat similar to PSR B0823+26 (i.e. undergoes intermediate timescale radio-off phases; see §3).

Despite experiencing problems with data quality, due to saturation and sporadic baseline variations, we have been able to characterise the single-pulse properties of PSR J1107–5907 in some detail. We confirm that the pulsar exhibits three modes of emission i.e. a weak, strong and radio-off state of emission (see §5.3 for details). Intriguingly, the object only appears to emit strong pulses in high density (i.e. in blocks of several hundred or thousand pulses) compared with the weak mode whose emission is indicative of RRAT-like behaviour (weak pulses are separated by $1 - 10^4$ pulse periods, with an average rate of ~ 85 pulses per hour; see §5.5.1). In both of the radio-on modes, the emission is not constrained to any particular pulse longitude range, i.e. the pulsar emits across the whole range of longitude, which suggests that the sites of emission might be the same. This also implies that the underlying mechanism which determines the emission modulation should be similar for both radio-on modes of emission.

Due to data clipping, we obtain a maximum flux density which is substantially lower than that presented in O’Brien et al. (2006) ($S_{\text{strong}} \sim 453$ mJy at an observation frequency of 1400 MHz, c.f. $S_{\text{Vela}} = 1.1$ Jy). Therefore, the value obtained represents a lower bound to the peak flux density of the object. As such, it is feasible that PSR J1107–5907 could be observed as bright as the Vela pulsar, thus potentially making PSR J1107–5907 one of the brightest radio pulsars known.

5.5.1 Nulling Statistics and Detection Probability

From the results of the longest observations (PKS-L1 and PKS-L3), it is evident that the pulsar is far less active than previously thought; that is $\text{NF} \lesssim 98.4 \pm 0.3\%$ and $\lesssim 97.4 \pm 0.4\%$ respectively (from the residual histogram analysis). In PKS-L2, the pulsar remarkably has a $\text{NF} = 100\%$ over the ~ 5 hr 16 min period of observation, which means that the pulsar has an average $\text{NF} \sim 98.6\%$. Over shorter timescales $\lesssim 15$ minutes, the pulsar exhibits a variable NF which is modulated by the probability of observing the pulsar during a radio-on mode of emission.

One of the main questions which arises is whether the long-term emission (nulling) behaviour observed in the object here is representative of its typical properties. This

can be sub-divided into three more specific questions: 1) Are the lengths of the strong modes typically the same? 2) Is the weak mode emission truly distributed randomly in time? 3) Does the pulsar exhibit a random distribution of null phases, with some lasting greater than a day, or is the nulling behaviour more periodic in nature? To provide an answer to the first two questions, we performed a consistency check on the observed detection statistics; that is, we estimated the number of observations which would exhibit a given mode of emission and compared these values with the actual quantities. For this analysis, we made a number of assumptions. Firstly, we assumed that we would have an identical observation sample; that is, the same number of observations and respective durations as in our data sample. Secondly, we speculated that a total of two strong emission modes occur in an entire transit period ($\sim 11 \text{ hr } 26 \text{ min } 56 \text{ s}$ i.e. $\sim 10^{5.2}$ pulses). Thirdly, we assumed an average strong-mode length $N_{\text{strong}} \sim 3500$ pulses, from the results of PKS-L1 and PKS-L3. Lastly, we inferred that the average number of randomly distributed weak pulses, during the entire transit period of the source, is $\langle N_{\text{weak}} \rangle \sim 1000$ (using the results from the residual histogram analysis of PKS-L1 and PKS-L3). Assuming that the above properties describe the typical behaviour of the source, we estimated the probability of detection in each mode using

$$P_{\text{strong}} = \frac{\text{Number of strong blocks}}{\text{Total number of blocks}} \quad (5.4)$$

$$P_{\text{weak}} = \frac{\text{Number of weak pulses}}{\text{Total number of pulses}}, \quad (5.5)$$

where P_{strong} and P_{weak} represent the probabilities of detecting a sequence of strong observations and a single weak-pulse respectively. For the strong mode, the number of data segments (blocks) which contain strong pulses in an observation is highly dependent on the integration time, and correspondingly affects the detection probability, as shown in Table 5.7. Following the above assumptions, we obtain a total number of 17 strong detections, which matches perfectly with the observations. This indicates that the pulsar exhibits a distribution of strong-mode lengths, with an average of approximately 15 minutes in total.

For the weak mode of emission, we obtain a detection probability of $\sim 6 \times 10^{-3} \%$ in the total number of pulses over a transit period which, subsequently, corresponds to an average rate of ~ 1 weak pulse every 332 rotations (or ~ 85 weak pulses per hour). Therefore, we would expect every observation that is longer than approximately 84 s to exhibit a weak detection, if the pulsar retains its average rate of weak-pulse emission. Clearly, this is not an appropriate assumption as all of our observations span longer than this hypothetical limit, but only 177 out of 351 of the fully-time averaged observations

Table 5.7: Predicted detection statistics for the strong mode of emission with respect to the length of a sample observation. The number of observations with a given integration time T is denoted by N_{obs} . The number of predicted strong-mode detections is denoted by $N_{\text{strong, obs}}$.

T (min)	N_{obs}	$P_{\text{strong}} (\%)$	$N_{\text{strong, obs}}$
2	13	0.044	0.6
3	4	0.044	0.2
4	8	0.047	0.4
5	232	0.044	10.2
10	12	0.044	0.5
15	74	0.044	3.2
20	2	0.059	0.1
300	3	0.667	2.0

exhibit a weak emission profile. Consequently, the pulsar is likely to emit weak pulses in non-sequential ‘bunches’; that is irregular groups of several pulses, which do not appear to be periodic. It might also be possible that some of the weak pulses from the object are too faint to be detected with our observational sensitivity. This potentially adds the complexity of a sensitivity threshold to the calculation of the weak-mode detection statistics.

5.5.2 A RRAT connection?

Giant Pulses and PSR B0656+14

It was noted that when the pulsar is in the strong mode, pulses can be $\gtrsim 18$ times as energetic as the average pulse (see Fig. 5.9). This far exceeds the energy threshold $10 \langle E \rangle$ for giant pulses (e.g. Cairns et al. 2001; see also §2.3). In addition, the pulse-energy distribution of the strong emission can be described well by a general power law, which is largely consistent with that of giant pulses⁸. However, a number of differences exist between the emission of PSR J1107–5907 and that typical of giant pulses (GPs) in other pulsars.

Giant pulses are classified by narrow pulse widths (e.g. ~ 0.4 ns – 120 μ s for the Crab pulsar; Knight 2007; Hankins & Eilek 2007; Karuppusamy et al. 2010) and, in some cases, the small pulse longitude envelopes over which they are constrained (e.g. Kuzmin & Ershov 2004; see also §2.3). In contrast, PSR J1107–5907 is found

⁸Although giant pulses follow power law statistics, they are observed at the extreme ends of PEDs (i.e. towards the highest energies) and, as such, take the form of an extended power law tail in the PEDs of pulsars (e.g. Argyle & Gower 1972; Lundgren et al. 1995; Karuppusamy et al. 2010).

to emit very strong pulses over a large fraction of the pulse longitude range. These pulses are also found to have broad widths $\sim 1 - 75$ ms and, hence, large duty cycles ($10^{-2.4} \lesssim \delta \lesssim 10^{-0.5}$, c.f. $10^{-7.9} \lesssim \delta \lesssim 10^{-2.4}$ for the Crab; Karuppusamy et al. 2010) that are atypical of classical giant pulses. Therefore, the strongest pulses attributed to PSR J1107–5907 cannot be considered as classical GPs. However, we do find a strong relation with the emission of PSR B0656+14; Weltevrede et al. (2006) noted that pulses from this object can intermittently exceed well above the giant pulse threshold $10 \langle E \rangle$ (up to $\sim 116 \langle E \rangle$ in fact), which also do not conform with other typical GP properties e.g. pulse width and longitude confinement. Coupled with the fact that the PED of this pulsar does not exhibit a break (i.e. it exhibits an extended tail towards very high energies), Weltevrede et al. (2006) suggest that PSR B0656+14 could be observed as a RRAT if it were situated farther away (see also Weltevrede et al. 2006). As such, we speculate that the same logic could be applied to PSR J1107–5907, given its large peak flux density ($S_{\text{peak}} \gtrsim 453$ mJy; see e.g. Weltevrede et al. 2006; Keane et al. 2010; Burke-Spoloar et al. 2011) and GP-like intermittency. To confirm this result, a more thorough investigation into the shape of the PED of PSR J1107–5907, through follow-up observations, would have to be conducted; that is, to characterise the tail of the PED using higher quality data.

Comparison with PSR J0941–39

Remarkably, PSR J1107–5907 is not the only pulsar to undergo highly irregular pulse intensity variation. In a recent study of archival Parkes survey data, Burke-Spoloar & Bailes (2010) discovered that PSR J0941–39 exhibits non-sequential RRAT-like ($\sim 95 - 110$ pulses per hour) emission, as well as 'bright' emission phases (~ 10 mJy) in which the pulsar is observed to have a broad three-component profile. During the 'bright mode', the pulsar experiences quasi-periodic nulling with a $\text{NF} < 10\%$, as well as complex subpulse drift, mode-changing and longitude dependent modulation. The presence of both nulling and RRAT-like behaviour in both of these objects suggests that they may be undergoing a transition between a pulsar mode and a RRAT mode (i.e. experiencing an evolutionary progression or step-rate in nulling activity), as suggested by Burke-Spoloar & Bailes (2010). This provides potential further evidence to suggest that RRATs are not a distinct class of objects. Rather, they consist of a mixed population of modulated pulsars with extended pulse-energy distributions (Weltevrede et al. 2006) and extreme nulling pulsars (Burke-Spoloar & Bailes 2010; Keane 2010).

Interestingly, PSR J1107–5907 has a large associated, characteristic age ($\tau \sim 445$ Myr) and is also located in the death valley region of the $P - \dot{P}$ diagram (see Fig. 2.6). This indicates that the object could provide direct insight into the processes

which govern the degradation of the radio emission mechanism, as well as a link between normal and transient (or non-emitting) radio pulsars. As yet, a timing solution (i.e. P , \dot{P} , \ddot{P} information) for PSR J0941–39 still remains to be acquired. Therefore, it will be interesting to see what characteristic age is associated with this pulsar and what its connection is to PSR J1107–5907. Given the similarities between these objects, as well as the selection effects against their detection and (or) characterisation⁹, one could easily suggest that several more sources that are similar in nature could exist, but have not yet been discovered or properly characterised.

5.5.3 What Is Driving PSR J1107–5907?

Magnetospheric State Changes

Recently, Lyne et al. (2010) provided evidence to suggest that magnetospheric state changes are responsible for mode changing and nulling, and that they appear as (quasi-)periodic timing signatures in residuals (see also §2.5.2). Such alterations to the magnetospheric configurations are currently suggested to be triggered, for example, by precessional torques (Jones 2011) or non-radial oscillations (Rosen et al. 2011). Unfortunately, we did not find evidence for a significant variation in spin-down rate between the separate radio-on emission modes, i.e. $\Delta\dot{\nu} = 0.012 \pm 0.006 \times 10^{-16} \text{ s}^{-2}$. Nor did we find evidence for any (quasi-)periodicity. However, this is not surprising. It is possible that the effect of a variable $\dot{\nu}$, on the timing residuals of this pulsar, is suppressed by the timescales of the variation. In this context, the average $\dot{\nu}$ could assume a value close to that in the radio-off phase, which is clearly more prevalent than the radio-on phases. If we assume the greatest confirmed $\Delta\dot{\nu}/\langle\dot{\nu}\rangle \sim 45\%$ (i.e. that of PSR B1931+24¹⁰) between the spin-down rates in the radio-on and -off states, we obtain $\dot{\nu}_{\text{on}} \sim -2.025 \times 10^{-16} \text{ s}^{-2}$ and $\dot{\nu}_{\text{off}} \sim -1.394 \times 10^{-16} \text{ s}^{-2}$. Assuming an extraordinarily long radio-on phase of 5 hours, and the above spin-down rates, the maximum variation between the observed and predicted frequency (for a single spin-down rate model) would be $\Delta\nu \sim 2 \times 10^{-12} \text{ Hz}$; that is, two times lower than our measurement accuracy over ~ 7.5 years. Therefore, it seems very unlikely that we would be able to measure such a change in rotational frequency at all; $\Delta\dot{\nu}$ would have to be uncharacteristically large in a radio-on phase, which lasts a maximum of ~ 20 minutes (for the strong-mode emission), compared with the average to be detected at all.

Nevertheless, we obtain a plasma charge density (ρ_{plasma} , using Eqn. A.7) associated

⁹Transient pulsars or pulsar phenomena are unlikely to be identified without particularly long survey pointings or follow-up observations.

¹⁰We note the discovery of $\Delta\dot{P} \sim 250\%$ in PSR J1841–0500 by Camilo et al. (2012). However, values for $\dot{\nu}_{\text{on}}$, $\dot{\nu}_{\text{off}}$ and $\langle\dot{\nu}\rangle$ are yet to be published.

with the onset of emission that is approximately 91 % of the Goldreich-Julian charge density (ρ_{GJ} , from Eqn. A.8) i.e. the total available charge from rotation. Therefore, the pulsar could be undergoing extreme magnetospheric changes without us having the ability to detect the signature in its timing residuals. Without dramatic improvements in instrument sensitivity, it is unlikely that such an effect on the timing behaviour of this object could be observed, even for the above extreme case of a $\sim 50\%$ change in spin-down rate between the separate modes of emission.

Accretion Scenarios

It is quite remarkable that PSR J1107–5907 can be as bright as Vela at 20-cm i.e. $S_{1400} \sim 1.1$ Jy (O’Brien et al. 2006). It is also interesting to note that the source is located in a peculiar transition region between normal and millisecond pulsars in the $P - \dot{P}$ diagram, which is populated by few active pulsars. As a result, one might seek an explanation for the behaviour of PSR J1107–5907 in an accretion scenario. Namely, the pulsar might accrete material from a companion star (planet) or via a remnant circumstellar disk (Illarionov & Sunyaev 1975; Stella et al. 1986; Stella et al. 1994; Cordes & Shannon 2008). In both of these scenarios, radio emission is expected to be produced in ‘bursts’ through the presence (absence) of charged material which is accreted into the light cylinder, and should be accompanied by changes in the spin-down rate.

To help determine the viability of an accretion scenario, we computed the radio luminosity of the object and compared it with the total energy available from rotation, i.e. the spin-down luminosity \dot{E} , via (Lorimer & Kramer 2005):

$$L = \frac{2\pi d^2}{\delta} (1 - \cos \rho) S_{\text{mean}}(f_0) \frac{f_0^{-\epsilon}}{\epsilon + 1} (f_2^{\epsilon+1} - f_1^{\epsilon+1}) \quad (5.6)$$

where d is the pulsar distance, $\delta = W_{eq}/P$ is the pulse duty cycle, $S_{\text{mean}}(f_0)$ is the mean radio flux density for a centre frequency f_0 , f_1 and f_2 are the lower and upper frequency bands of the observation respectively, ϵ is the spectral index and $\rho = 1.1 \times 4.9^\circ P^{-0.5}$ (Eqn. 15, Maciesiak & Gil 2011) is the opening angle of the beam. Assuming with our observing set-up (see Table 5.2) that PSR J1107–5907 is as bright as Vela ($S_{\text{mean}} \sim 1.1$ Jy) in its strong mode, and $\epsilon = -1.8$ (Maron et al. 2000), we obtain $L \sim 3.8 \times 10^{28}$ erg s $^{-1}$ which is a factor of ~ 580 less than \dot{E} . Therefore, the radio emission from this pulsar can be explained without the need for the accretion of material.

Further to this, we find that the timescales of modulation (\lesssim mins) appear too short and irregular to be consistent with orbital periodicities. With this in mind, it is unlikely that an orbital companion is responsible for the emission modulation in

PSR J1107–5907. Despite this, it still remains possible that material from a ‘debris disk’ could perturb the outer magnetosphere of the pulsar and, subsequently, stimulate (suppress) radio emission over a range of timescales (i.e. seconds to months; Cordes & Shannon 2008). However, it is unclear how the presence of such a disk could account for the moding seen in PSR J1107–5907. Why would the injection of asteroid material cause RRAT-like emission and exceptionally strong emission on two different timescales? Is it possible that the pulsar normally behaves like a RRAT, but then exhibits enhanced emission via the accretion of material?

For both of the accretion scenarios presented, we would expect high energy emission to be produced, either through direct accretion onto the neutron star surface (Stella et al. 1986) or through the activation of the outer gaps (Cordes & Shannon 2008). Therefore, the best confirmation of either of these scenarios would be the detection of optical, X-ray or γ -ray emission coincident with the pulsar.

Other Theories

The period and surface magnetic field strength of PSR J1107–5907 suggest that it should be experiencing some degradation in the radio emission mechanism (which is consistent with our observations); PSR J1107–5907 is located past the central dipole ‘death-line’ (see Fig. 2.6), which implies that the source might only temporarily satisfy (dissatisfy) the criteria for radio emission production (Chen & Ruderman 1993; see also §2.5.1). Several authors suggest that sporadic reactivation of the radio emission mechanism could occur through (thermo-)magnetic instabilities (e.g. Geppert et al. 2003; Urpin & Gil 2004; see also §2.5.1), which should be coincident with non-thermal X-ray emission and polar-cap heating (Zhang et al. 2007). However, it could also be possible that the nulling behaviour of PSR J1107–5907 can be described by radio emission beam reversals (Melikidze & Gil 2006; see also §2.5.4).

5.5.4 Future Prospects

Due to the multitude of possible driving mechanisms in PSR J1107–5907, we note that future observations would greatly benefit our understanding of this source, as well as the mechanisms responsible for its emission modulation. Ideally, follow-up radio observations would be multi-frequency, high time resolution (i.e. single-pulse data), high bit-rate, long duration (i.e. over the entire transit time of the source), high cadence (i.e. over multiple consecutive days) and polarisation calibrated. The long observing runs and multiple frequencies of observation would allow confirmation of the broad-band nature of the nulling phenomenon, and the high bit-rate would ensure accurate

representation of the pulse energy during the strong modes, which, in turn, would enable the accurate characterisation of the pulse-energy distributions. The multitude of observations would also facilitate the discovery of a possible periodicity between the different modes of emission. Most importantly, the polarisation data might enable the accurate determination of the geometry of the system; the rotating vector model (Radhakrishnan et al. 1969) could be used to fit the polarisation angle swing of the different emission regions and, subsequently, allow the determination of the emission heights of the different components of each phase. As a follow-up to this work, it would also be advantageous to perform dedicated observations of this source in the high-energy and infra-red regimes to verify the different driving mechanisms discussed here.

5.6 Conclusions

We have found that PSR J1107–5907 exhibits a RRAT-like weak emission mode, as well as a strong emission mode ($\langle t_{\text{strong}} \rangle \sim 15$ minutes) which undergoes extreme pulse intensity modulation and nulling behaviour. Due to the similarity between the emission from this object and RRATs (see §5.5.2), it is tempting to suggest that the source could represent an evolutionary connection between normal pulsars, RRATs and old non-emitting neutron stars (c.f. PSR J0941–39; Burke-Spolaor & Bailes 2010). As a result of the short timescales of emission modulation in this source (\lesssim minutes), and poor observation cadence, it is impossible to determine whether PSR J1107–5907 resembles an intermittent pulsar; we could not verify whether the source undergoes spin-down rate variation from our timing analysis, which is due to instrument sensitivity over such short timescales. In order to better characterise the emission behaviour of PSR J1107–5907, further long duration radio observations are required. These observations would be complemented by dedicated multi-frequency observations in the high-energy and infra-red regimes which, ultimately, should provide clues to the mechanism(s) responsible for the emission modulation behaviour in this object.

Chapter 6

The Single-pulse Characteristics of PSR B0823+26

PSR B0823+26 is a highly erratic pulsar, which exhibits both short and long-term nulling (i.e. seconds to hours, or longer) that does not appear to be periodic in nature (see §3). In order to elucidate the radio emission behaviour of this source, and to investigate a possible connection with RRAT-like pulsars (see e.g. §5), a series of single-pulse observations have been carried out. We find that the object possesses two discrete nulling timescales, i.e. $1-3 P$ and $\gtrsim 10^2 P$, which may be explained by a combination of “pseudo-nulls” and long-term nulling behaviour. The post-cursor emission component is found to be highly erratic and, as such, is comparable to RRAT-like emission. We find that follow-up observations are required to characterise the long-term nulling behaviour of this object and, hence, the mechanism(s) responsible for its emission variability.

6.1 Observations

In total, 18 single-pulse observations of PSR B0823+26 were carried out on days in the period between 27 May 2011 and 10 November 2011, using the Lovell Telescope at Jodrell Bank. The data was obtained with the Reconfigurable Open Architecture Hardware (ROACH) digital backend. The majority of the single-pulse observations (17 out of the total of 18) were approximately 6 minutes in duration, as they were performed commensally with the usual timing observations of this source. Recognising the need for a longer continuous observation, however, an approximately 1-hour single-pulse observation was also obtained.

Although the data is generally of good quality, some pulses were affected by radio

frequency interference (RFI). As such, we used a combination of interactive (PSRZAP¹) and automated (PAZ²) software to mitigate the effect of interference (see also Hotan et al. 2004). Table 6.1 shows the properties of the single-pulse observations which were of sufficient quality for further study.

Table 6.1: Properties of the single-pulse observations of PSR B0823+26 chosen for further study. The reference key for each observation is denoted by REF, MJD is the modified Julian Date, ν is the central observation frequency, $\Delta\nu$ is the observation bandwidth, T is the total length of each observation and N is the corresponding total number of pulses. The ‘status’ describes whether or not any pulsed emission was detected in an observation (i.e. radio-on (‘on’) or radio-off (‘off’)), whose integrated, main-pulse peak signal-to-noise ratio is represented by SNR_{peak} . PC denotes whether or not the post-cursor emission component was detected.

REF	MJD	ν (MHz)	$\Delta\nu$ (MHz)	T (s)	N	Status	SNR_{peak}	PC
JBO-S1	55708.78	1532	400	359.8	678	On	149.9	No
JBO-S2	55728.77	1532	400	359.3	677	On	209.1	No
JBO-S3	55734.69	1532	400	359.3	677	On	309.6	Yes
JBO-S4	55735.45	1532	400	359.3	677	Off	3.1	No
JBO-S5	55751.46	1532	400	359.8	678	Off	4.0	No
JBO-S6	55777.71	1532	400	358.2	675	On	207.5	No
JBO-S7	55784.23	1532	400	359.8	678	Off	3.2	No
JBO-S8	55786.26	1532	400	359.2	677	On	92.1	No
JBO-S9	55805.15	1532	400	359.8	678	On	26.0	No
JBO-S10	55829.13	1532	400	359.2	677	On	188.7	No
JBO-S11	55840.16	1532	400	358.2	675	On	525.2	Yes
JBO-S12	55848.16	1532	400	366.1	690	On	73.8	No
JBO-L1	55875.96	1532	400	3653.3	6885	On	731.2	Yes

6.2 Single-pulse Modulation Properties

Following the work in §3, we sought to characterise the single-pulse emission characteristics of PSR B0823+26 over timescales of seconds to hours, that is to confirm the nulling behaviour of the object and investigate a relationship with RRAT-like sources. With this in mind, we studied the pulse properties of each observation by eye, to determine which contained discernible radio emission and, hence, assigned an ‘activity status’ to each (see Table 6.1). We find that the pulsar is clearly detected in all but three observations (i.e. JBO-S4, JBO-S5 and JBO-S7). Examples of detections and non-detections are shown in Fig. 6.1.

Through closer inspection of the radio-on observations, we find that the pulsar typically undergoes bursts of a few dozen active pulses, that are separated by nulls

¹<http://psrchive.sourceforge.net/manuals/psrzap>

²<http://psrchive.sourceforge.net/manuals/paz>

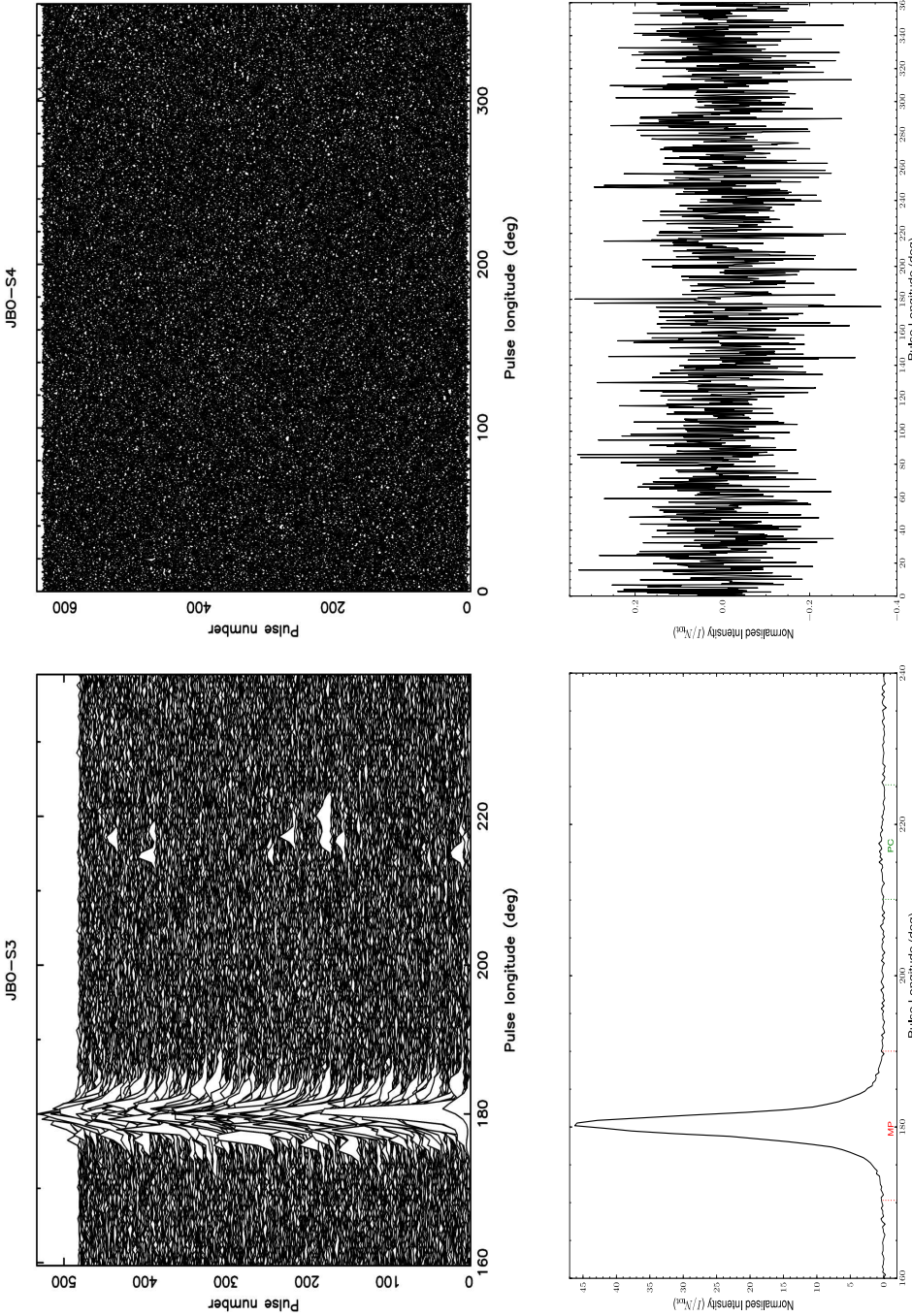


Figure 6.1: Two single-pulse observations of PSR B0823+26, demonstrating the pulse intensity variation of the source. *Top:* The pulse stacks of JBO-S3 and JBO-S4 (from left to right). *Bottom:* The corresponding integrated profiles (with the components indicated for JBO-S3). In JBO-S3, the main-pulse (MP) component of the pulsar is visible across the entire pulse range. Whereas, there is no discernible radio emission in JBO-S4. Note also the irregularity of the post-cursor (PC) component in JBO-S3.

of 1 – 3 pulse periods in length. In the longest observation, i.e. JBO-L1, we hoped to find evidence for longer nulls. However, the bursting and nulling behaviour of PSR B0823+26 in this observation is consistent with that of the short observations (i.e. 6-minute observations). As a result, we conclude that JBO-L1 was obtained during one of the longer radio-on phases attributed to the source (i.e. \gtrsim hours; see §3.3). During this observation, we note that the pulsar undergoes strong modulation over both pulse-to-pulse and more gradual (i.e. longer) timescales, which will be discussed in the following sections.

6.2.1 Scintillation Effects

In order to elucidate the brightness variations due to interstellar scintillation, and hence the effects on the modulation properties, we formed a dynamic spectrum for the longest observation JBO-L1 (see Fig. 6.2). At 1-hour duration, this observation is longer than the scintillation timescale at 1532 MHz (i.e. $\Delta t_{\text{DISS}} \sim 13.5$ minutes³). It is clear that the integrated pulse intensity (top panel) undergoes a strong, gradual variation which is consistent with interstellar scintillation (see the scintle pattern in the bottom panel). The scintillation bandwidth ($\Delta\nu_{\text{DISS}} \sim 150$ MHz) and duration ($\Delta t_{\text{DISS}} \sim 25$ minutes) of this observation are found to be in agreement with the range of values in Wang et al. (2005) at 1540 MHz. On top of the gradual intensity fluctuations, there are also strong pulse-to-pulse variations which are observed at all times.

In the scintillation minima, it is apparent that the range of pulse flux densities that can be sampled is reduced. This means that distinguishing nulls from weaker pulses becomes very difficult (see e.g. the left panel Fig. 6.3). In contrast, in the scintillation maxima, where the flux density can be up to $\sim 4 - 5$ times brighter, it is easier to distinguish nulls (see e.g. the right panel of Fig. 6.3). Therefore, we conclude that the short-term (i.e. pulse-to-pulse) nulling behaviour of the source is best studied using the brightest observations (i.e. $\text{SNR}_{\text{peak}} \gtrsim 200$) which allow accurate determination of the nulling and bursting behaviour.

³The scintillation timescale was obtained assuming a Kolmogorov spectrum and $\Delta t_{\text{DISS}} \sim 13.6$ minutes at 1540 MHz (Wang et al. 2005).

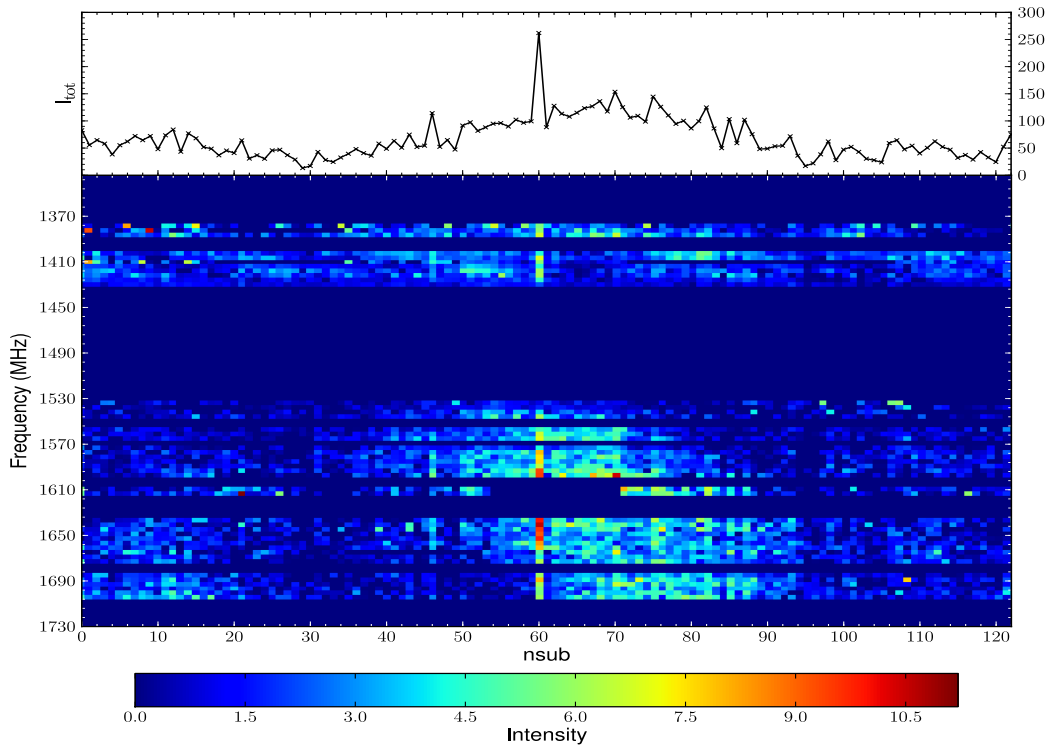


Figure 6.2: The scintillation properties of PSR B0823+26. *Bottom:* The dynamic spectrum for JBO-L1, showing the time-evolution of pulse intensity with respect to frequency. The data is averaged into sub-integrations (n_{sub}) of length 29.7 seconds. The pulse intensities associated with flagged RFI frequencies are set to zero. *Top:* Integrated pulse intensity using the whole observing bandwidth.

6.2.2 Nulling Fraction Estimation

Following the work in §3.3, we sought to characterise the effect of scintillation on the nulling fraction estimation of the source; observations obtained with the AFB have a frequency coverage which is less than the scintillation bandwidth ($\Delta\nu = 32$ MHz, compared with $\Delta\nu_{\text{DISS}} \gtrsim 40$ MHz at 1400 MHz; Clegg et al. 1993) and, hence, may have been subject to strong intensity modulation that could have resulted in an overestimation of the NF. For this analysis, we considered all the integrated, main-pulse component ($\phi \sim 173^\circ - 187^\circ$) pulse energies of the radio-on pulses, as well as those of the brightest radio-on pulses only; that is, pulses from observations with $\text{SNR}_{\text{peak}} \geq 200$ and pulses $N = 2600 - 4599$ for JBO-L1. In total, we obtain 11860 and 4230 radio-on and bright radio-on pulses respectively. Instead of normalising the pulse energies with respect to a running mean, which would result in broadening of the off-pulse ($\phi \sim 35^\circ - 49^\circ$) energy

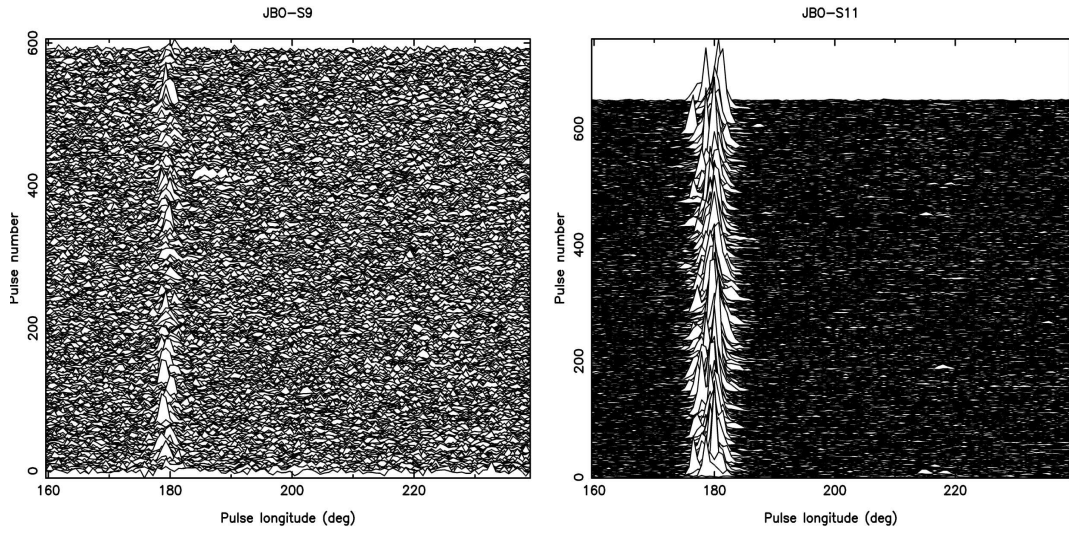


Figure 6.3: The pulse stacks of JBO-S9 (*left panel*) and JBO-S11 (*right panel*), demonstrating the variation in the brightness and detectability of the source. In JBO-S9 (i.e. the weakest radio-on observation; likely obtained during a scintillation minimum), the emission from the pulsar appears, for the most part, just above the receiver noise level. This suggests the weakest pulses may be below the instrumental sensitivity, resulting in ‘nulls’ which are not related to pulses which are truly radio-off. By comparison, the source is clearly detected above the receiver noise throughout JBO-S11, which likely corresponds to a scintillation maximum, and is even found to exhibit PC emission in a few pulses (at a pulse longitude $\phi \sim 215^\circ$).

distribution⁴, we compared them with the average pulse energy ($\langle E \rangle$) for each data-set. While this normalisation method will result in losing the absolute values of the pulse energies, the shapes of the PEDs will be preserved, thus allowing a good measurement of the NF for the on observations. The PEDs of the radio-on pulses are shown to be significantly broader than those of the brightest radio-on pulses only (see Fig. 6.4). This can be explained by the effect of scintillation on $\langle E \rangle$, which will be influenced by the inclusion of pulses which are heavily weakened or amplified.

We see that the on-pulse energy distributions do not appear to be distinctly bimodal; that is, they do not clearly indicate the presence of nulls. To confirm the presence of nulls, and characterise the effect of scintillation on the ‘apparent’ nulling behaviour, we used the residual histogram and pulse-energy fitting analyses outlined in §5.3.2. We fitted the on-pulse energy distributions of the all the radio-on, and brightest radio-on pulses only, using lognormal distributions (Eqn. 5.3). We find that both on-PEDs can be described well by these distributions, as shown in Fig. 6.5. The results of this

⁴Interstellar scintillation will result in broadening of the off-pulse energy distribution when the off-pulse energies are expressed in units of the variable running average on-pulse energy (Weltevrede et al. 2006).

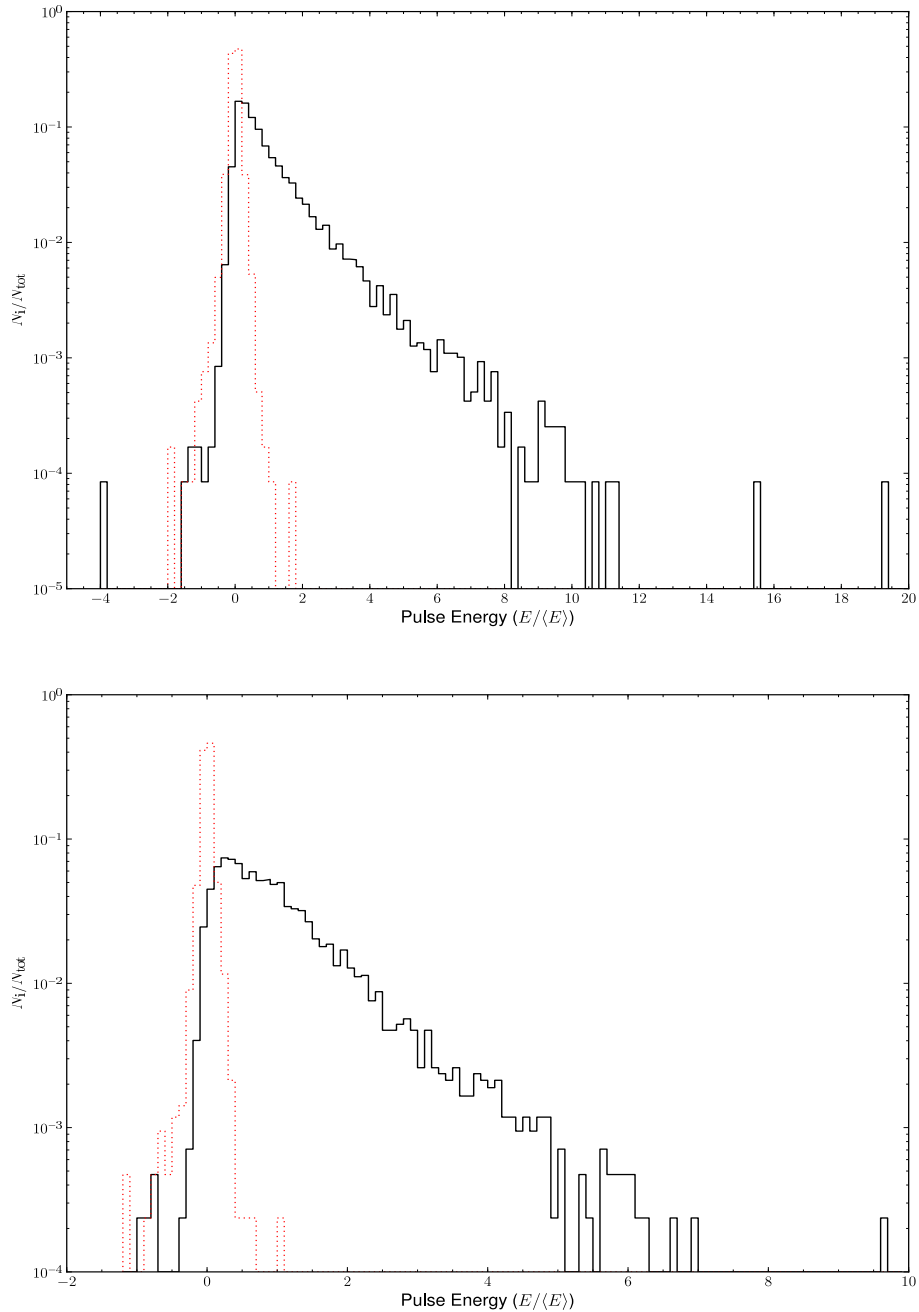


Figure 6.4: Pulse-longitude integrated PEDs for the off-pulse (dotted line) and on-pulse (solid line) emission regions, for the radio-on and brightest radio-on pulses respectively (*from bottom to top*). The pulse energies are normalised by the average on-pulse value for each data-set ($\langle E \rangle$). Note that the PEDs of the combined on pulses are significantly broader than those of the brightest on-pulses. In both cases, the on-pulse distribution does not appear to be distinctly bimodal.

analysis, as well as those of the residual histogram method are summarised in Table 6.2. Through comparing the NF estimates of the two data-sets, we confirm that some nulls during scintillation minima result from false-positive detections. Using the result from the brightest on-pulses, we find that the $\text{NF} \leq 6.5 \pm 0.4\%$. This is supported by the work of Rathnasree & Rankin (1995), who obtained a NF which is consistent with our own (i.e. $\text{NF} = 6.4 \pm 0.8\%$ ⁵). Therefore, we conclude that the short-term ($1 - 3 P$) nulling behaviour observed in our data is intrinsic to the pulsar.

Table 6.2: The single-pulse nulling properties of PSR B0823+26. The pulses used in the nulling fraction analyses are indicated by the ‘pulse type’. The NFs from the PED fitting and residual histogram methods are denoted by NF_{fit} and NF_{res} respectively.

Pulse Type	$\text{NF}_{\text{fit}} (\%)$	$\text{NF}_{\text{res}} (\%)$
All on	10.1	$\leq 11.1 \pm 0.3$
Brightest on	6.3	$\leq 6.5 \pm 0.4$

Unfortunately, however, we were not able to further characterise the long-term (i.e. $\gtrsim 10^2 P$) nulling behaviour of the source, which was discussed in §3.3. This is because we did not obtain radio-off observations of sufficient length; our radio-off observations were shorter than the scintillation timescale and, as such, could not effectively probe the ‘flickering’ behaviour of the source. However, we believe that these long-term nulls are intrinsic to the source; even when the pulse intensities are dramatically weakened i.e. during scintillation minima, we always see evidence for pulsed emission which, subsequently, implies that entirely radio-off observations represent true cessation in the pulsar emission mechanism. Nevertheless, several longer (i.e. $\gtrsim 1$ hour) single-pulse observations of PSR B0823+26 in the radio-off phase would prove invaluable when characterising the timescales of the longer nulls.

6.2.3 Main-pulse and Post-cursor Component Variability

In addition to the clear radio-on and -off phases, we find that there is strong pulse intensity modulation on pulse-to-pulse timescales. Namely, the pulsar exhibits a high degree of variation in its main-pulse (MP) emission⁶, and an even greater degree of variation in its post-cursor (PC) emission; PC emission is only detected in a handful of pulses in three of the radio-on observations (see e.g. Fig. 6.6).

⁵The Arecibo Telescope, which was used to obtain this result, is currently the world’s most sensitive at L-Band i.e. 1 – 2 GHz. This indicates that the pulsar does indeed undergo nulls when in the radio-on phase.

⁶This confirms the result of Weltevrede et al. (2006), who obtain a modulation index ($m \sim 1$) for the MP component of PSR B0823+26, which is twice the average value of other pulsars in their sample (i.e. $\langle m \rangle \sim 0.5$).

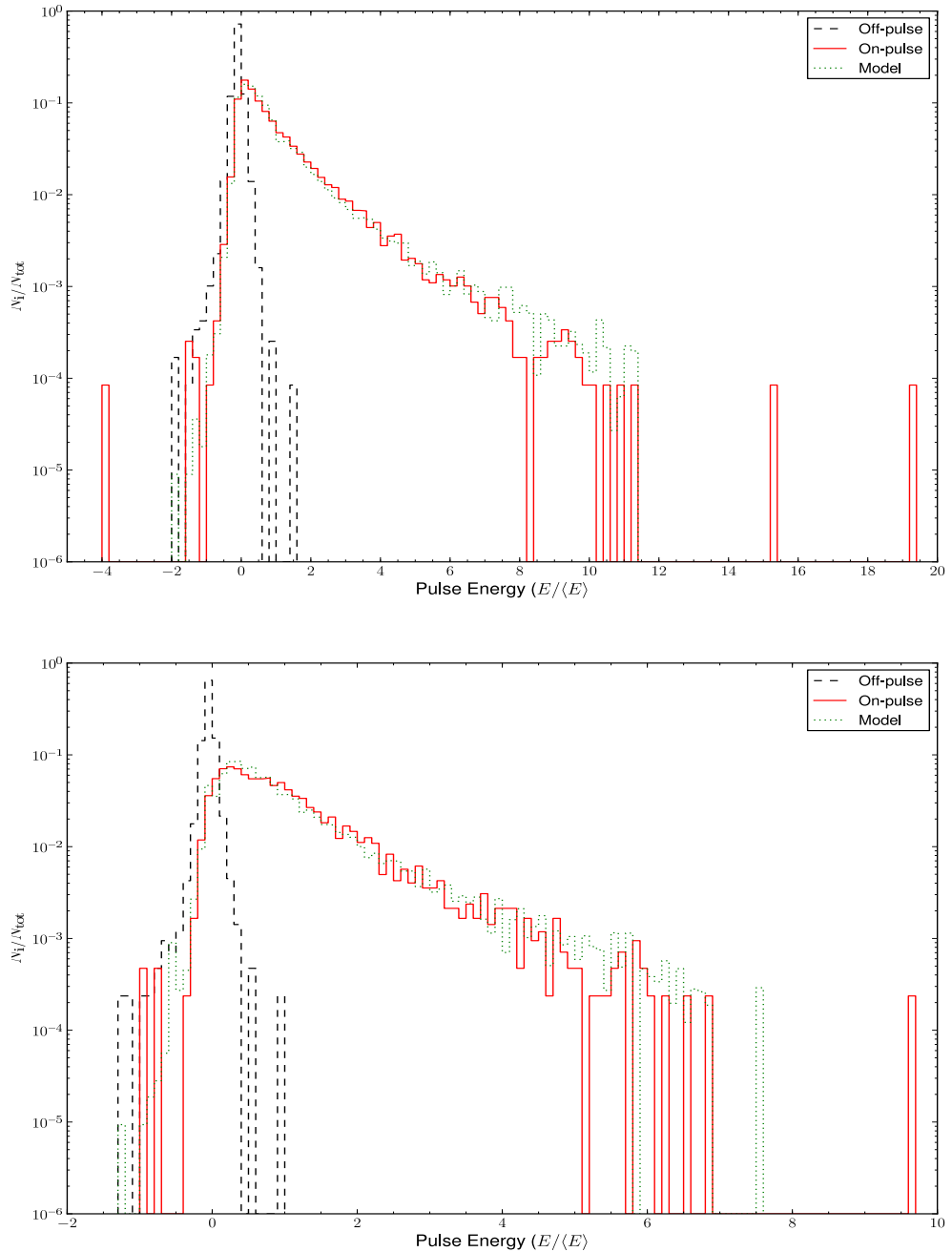


Figure 6.5: Integrated pulse-energy distributions for PSR B0823+26, formed from all the radio-on pulses (*top panel*), as well as the brightest pulses only (*bottom panel*). The off-pulse, on-pulse and NF model PEDs are shown by the dashed, solid and dotted lines respectively. The pulse energies are normalised by the average on-pulse value for each data-set ($\langle E \rangle$).

With the above points in mind, we set out to quantify the modulation of the PC component in relation to that of the MP. In the longest observation (JBO-L1), we clearly see that the PC emission is most readily visible during the scintillation maximum, as shown in Fig. 6.6. This result is consistent with the two other 6-minute observations, which show evidence for the PC component when the main-pulse $\text{SNR}_{\text{peak}} \gtrsim 300$ (see Table 6.1), during extreme maxima at 1532 MHz.

Given the obvious PC variability, we wanted to study the variability of the entire pulse profile with respect to pulse intensity. We corrected for scintillation by comparing the pulse energies of JBO-L1 with the running average of 500 pulses⁷, after which we formed pulse-energy separated average profiles for JBO-L1 (see the left panel of Fig. 6.7). We find that there is no significant variation in the main-pulse shape with respect to pulse energy. We also note that the PC component does not contribute a significant amount to the average profile shape. Looking at the single pulses, however, we can clearly distinguish the presence of this emission component on numerous occasions (see e.g. Fig. 6.6). Subsequently, we sought to determine the magnitude of brightness variations in the MP and PC components. For this analysis, we computed the brightest pulse energies for each pulse-longitude bin and compared them with the average profile (see the right panel of Fig. 6.7). We find that the brightest energies are most readily found in the leading edge of the MP component. Remarkably, we find that the PC component can be approximately twice as bright as the average peak-intensity of the MP pulses.

To further characterise the pulse intensity variation of the PC component, we located pulses which exhibited significant PC emission in JBO-L1. This was achieved by using a boxcar algorithm to search for significant peaks in the pulse longitude range $\phi \sim 210^\circ - 225^\circ$. We formed average profiles for pulses with $\geq 3\sigma$, $\geq 5\sigma$, $\geq 7\sigma$ and $\geq 10\sigma$ PC peaks, as shown in Fig. 6.8. To confirm the PC peak detections, we visually inspected these data and, subsequently, discovered that approximately 75 pulses (or $\sim 1\%$ of the total) in JBO-L1 exhibit significant PC emission. Further to this, we find that the PC component constitutes $\lesssim 5\%$ of the average peak-intensity of the MP for the least significant pulses (i.e. $\geq 3\sigma$ PC detections)⁸, and up to approximately 25 % for the most significant (i.e. $\geq 10\sigma$ PC detections). We do note, however, that there are increasingly fewer pulses towards greater peak significance. As such, the PC emission does not contribute substantially to the average pulse shape (see also Fig. 6.3 and Fig. 6.7). We find that only a handful of the most significant pulses (i.e. $\geq 7\sigma$

⁷This timescale was chosen to smoothly track the scintillation behaviour of the source.

⁸We note that several pulses with the lowest detection threshold (i.e. $\geq 3\sigma$ and $\geq 5\sigma$) are contaminated by false-positive detections due to RFI and/or baseline variations.

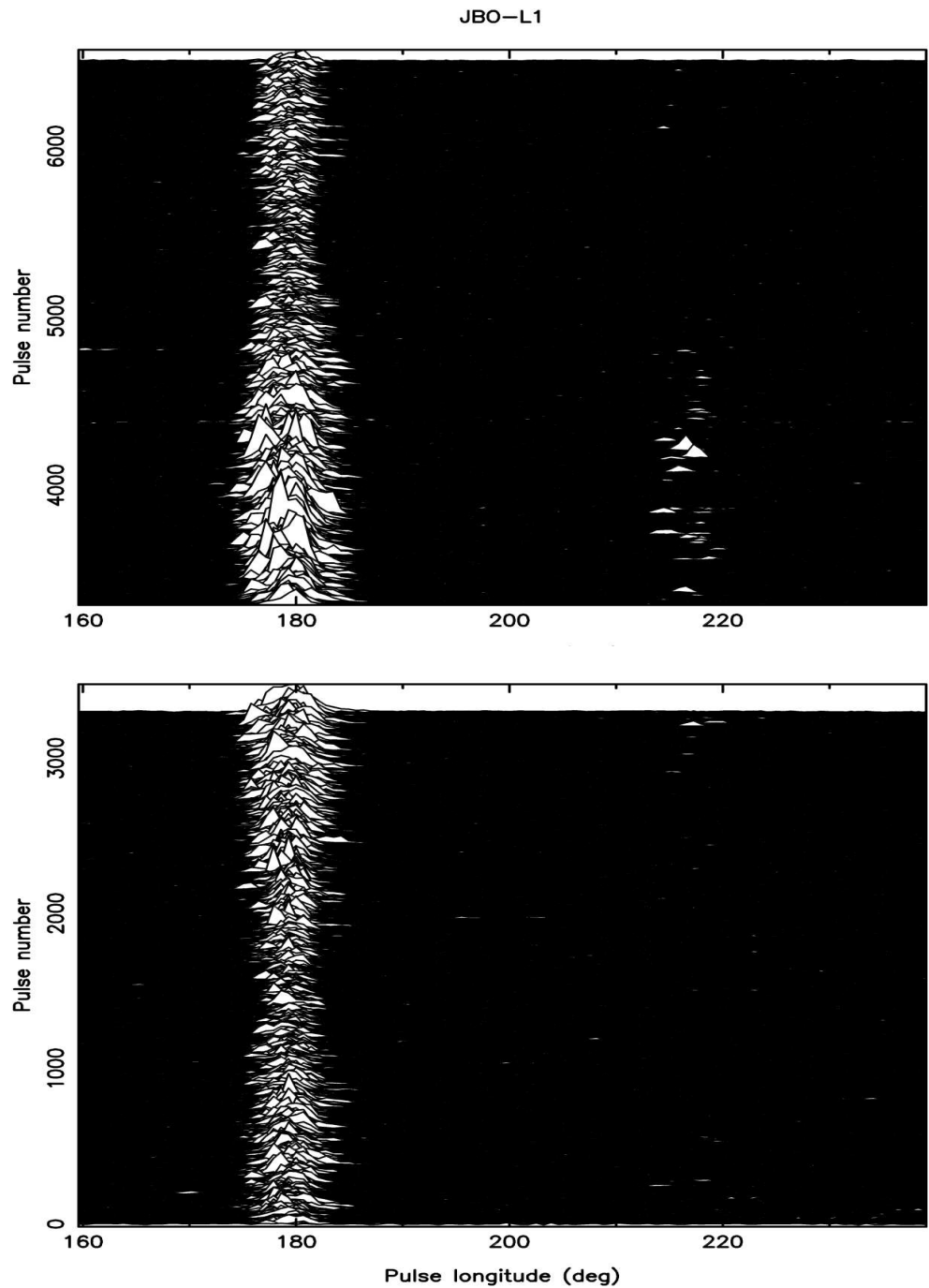


Figure 6.6: Pulse stacks of the 1-hour, single-pulse observation of PSR B0823+26 at 1532 MHz, which are separated to maintain high image resolution. *Bottom panel:* Pulses 0-3299. *Top panel:* Pulses 3300-6506. Note that the PC intensity varies substantially during the scintillation maximum (i.e. $N \sim 2600 - 4800$, in the pulse longitude range $\phi \sim 210^\circ - 230^\circ$).

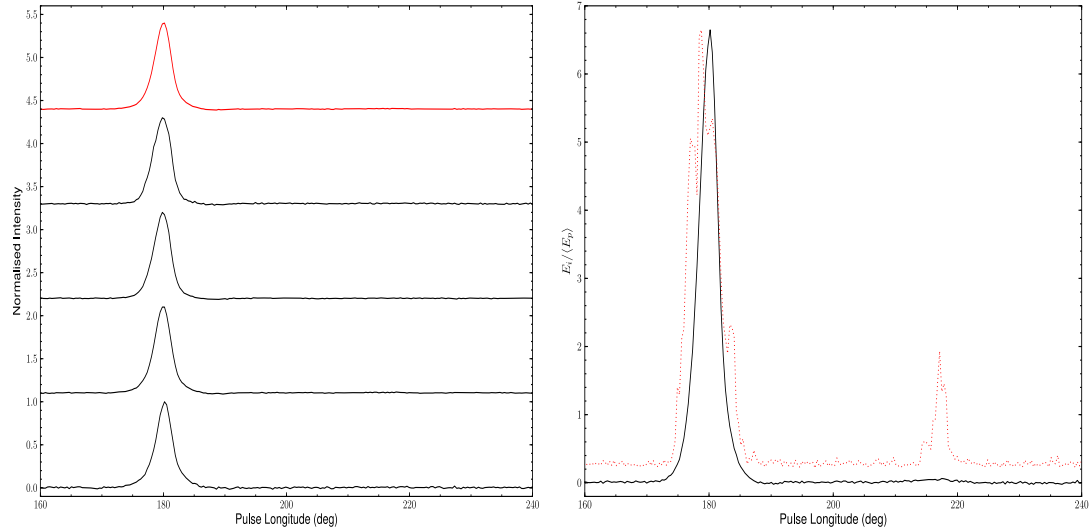


Figure 6.7: The pulse intensity variation of PSR B0823+26 for JBO-L1. *Left:* The average pulse-profile (top trace), as well as the average profiles (from top to bottom) for integrated pulse energies of $E > 3 \langle E \rangle$, $E = 2 - 3 \langle E \rangle$, $E = 1 - 2 \langle E \rangle$ and $E < 1 \langle E \rangle$, containing 97, 525, 1731 and 2951 pulses respectively (where $\langle E \rangle$ is the average pulse energy). The profiles are offset from one another and are normalised to a maximum intensity of one for clarity. *Right:* The scaled, average profile (solid line) and the brightest time-sample for each pulse-longitude bin (dotted line), compared with the average peak-energy $\langle E_p \rangle$ for pulses which were the least affected by RFI i.e. $N = 2600 - 4599$.

PC detections) display PC emission that has a peak intensity which is comparable to, or greater than, that of the MP. On no occasion do we find evidence for significant PC emission without the MP present.

In order to elucidate the fraction of pulses which exhibit particularly strong PC emission, we also computed longitude-resolved pulse-energy distributions (PEDs; see Weltevrede et al. (2006) for a detailed description) for the brightest pulses in JBO-L1 (i.e. $N = 2600 - 4699$), for the MP, PC and off-pulse emission (see Fig. 6.9). These pulses were selected so as to mitigate the possible misrepresentation of pulse energies due to scintillation. We confirm our earlier finding that although the PC component is infrequent, it can be quite bright compared with the MP emission (i.e. up to 2 times the average peak-intensity of the MP). We also note that the off-pulse and PC energy distributions tail off towards greater negative energies, compared with that of the MP component. This is most likely due to baseline variations and RFI in the aforementioned emission regions.

Following the work in §5.3.3, we also computed fluctuation spectra for the MP and PC emission in the longest observation (JBO-L1) so that we could characterise the sig-

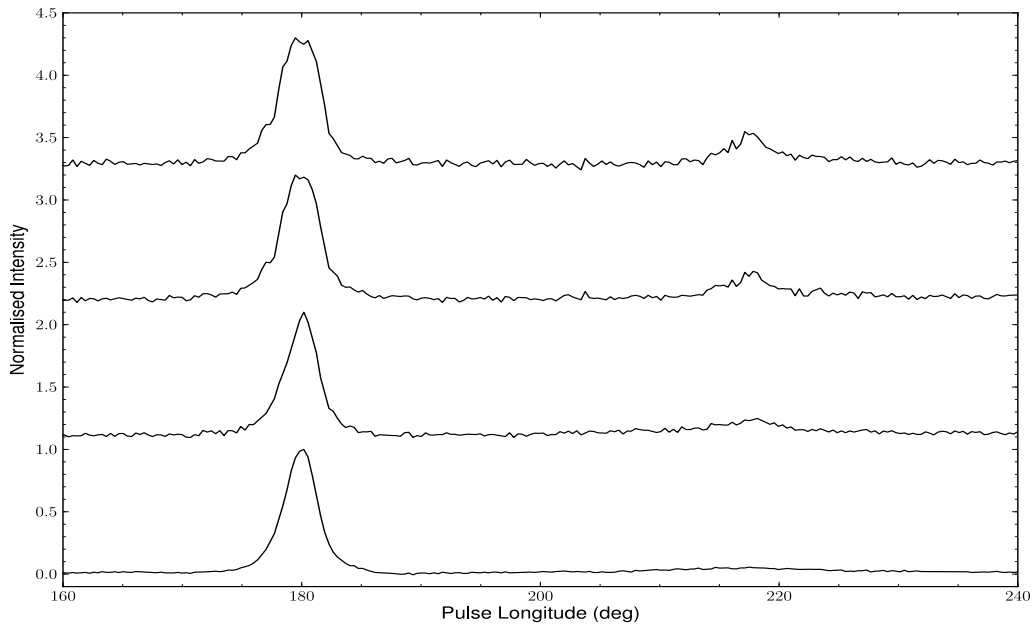


Figure 6.8: The average pulse shape of the MP and PC component for increasing post-cursor peak SNR (*from bottom to top*). The profiles contain 1537, 101, 35 and 19 pulses for the $\geq 3\sigma$, $\geq 5\sigma$, $\geq 7\sigma$ and $\geq 10\sigma$ averages respectively. Note that the broad PC component in the average profile of the least significant pulses (i.e. $\geq 3\sigma$ profile) is due to the presence of false-positive detections.

nificance, and degree of periodicity, in the pulse intensity modulation. We selected this observation based on its duration and high SNR, so that we could accurately represent the subpulse modulation. For the calculation of the longitude-resolved fluctuation spectrum (LRFS; Backer 1970a), and two-dimensional fluctuation spectra (2DFS; Edwards & Stappers 2002), we used an FFT length of 256 pulses. We computed the 2DFS for both the MP and PC pulse-longitude ranges of the observation. However, we find that the PC emission is too infrequent to obtain any significant information in the 2DFS. Figure 6.10 shows the result of this analysis.

From the modulation index profile, we conclude that both the leading and trailing parts of the MP profile component exhibit significant subpulse intensity modulation. We note that the PC emission undergoes the greatest modulation ($m \sim 5$), which is comparable to RRAT-like sources (e.g. Weltevrede et al. 2006; Serylak et al. 2009; Weltevrede et al. 2011; see also §5.3.3). We find that the pulsar exhibits a dominant subpulse modulation periodicity ($P_3 = 5.46 \pm 0.03 P_0$), with a clear preference in drift direction ($P_2 = 40 \pm 10^\circ$) in the leading part of the MP component (i.e. corresponding to the broad spectral component in the 2DFS), which is consistent with the findings of Weltevrede et al. (2006, 2007). We suspect that the other features in the LRFS

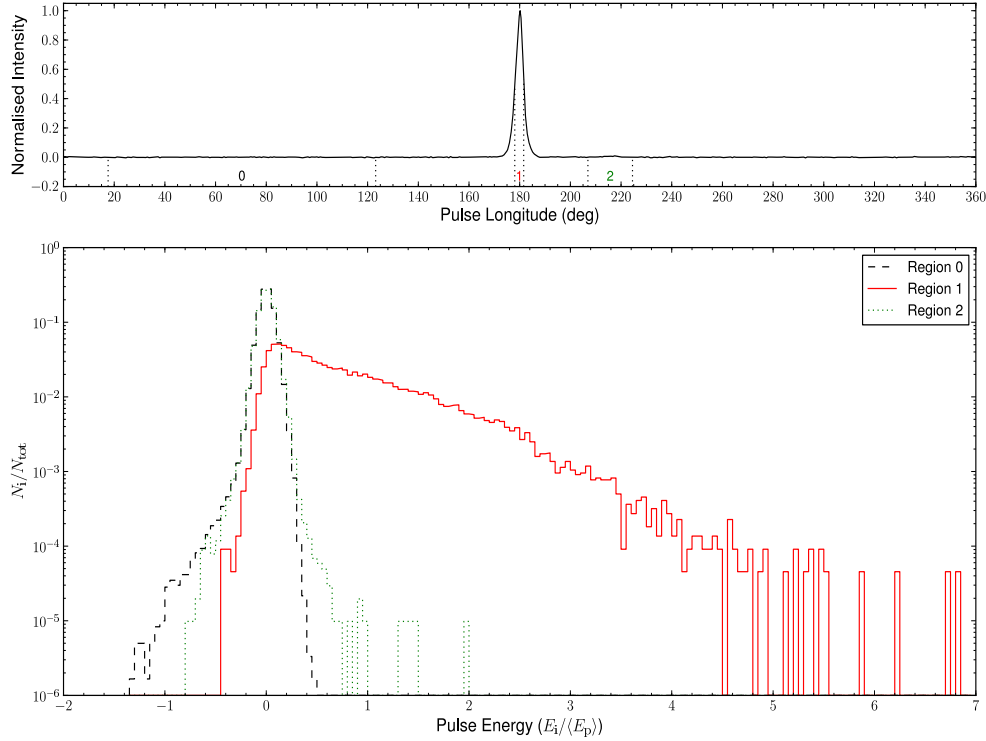


Figure 6.9: *Bottom:* Longitude-resolved PEDs for JBO-L1, which are corrected for scintillation and normalised with respect to the average peak-energy of the profile $\langle E_p \rangle$. *Top:* The average profile of the 2000 pulses selected (i.e. $N = 2600 - 4599$), with the different emission regions numbered i.e. off-pulse (0), main-pulse (1) and post-cursor (2) components.

and 2DFS, towards lower frequency (i.e. at $P_3 = 10.0 \pm 0.1 P_0$, $P_3 = 15.8 \pm 0.2 P_0$ and $P_3 = 44 \pm 2 P_0$, with no significant subpulse drift), could be due to pulse nulling (i.e. longitude stationary modulation). However, they could equally be harmonics of the dominant subpulse modulation periodicity. We note that there is no significant modulation at other pulse longitudes in this observation.

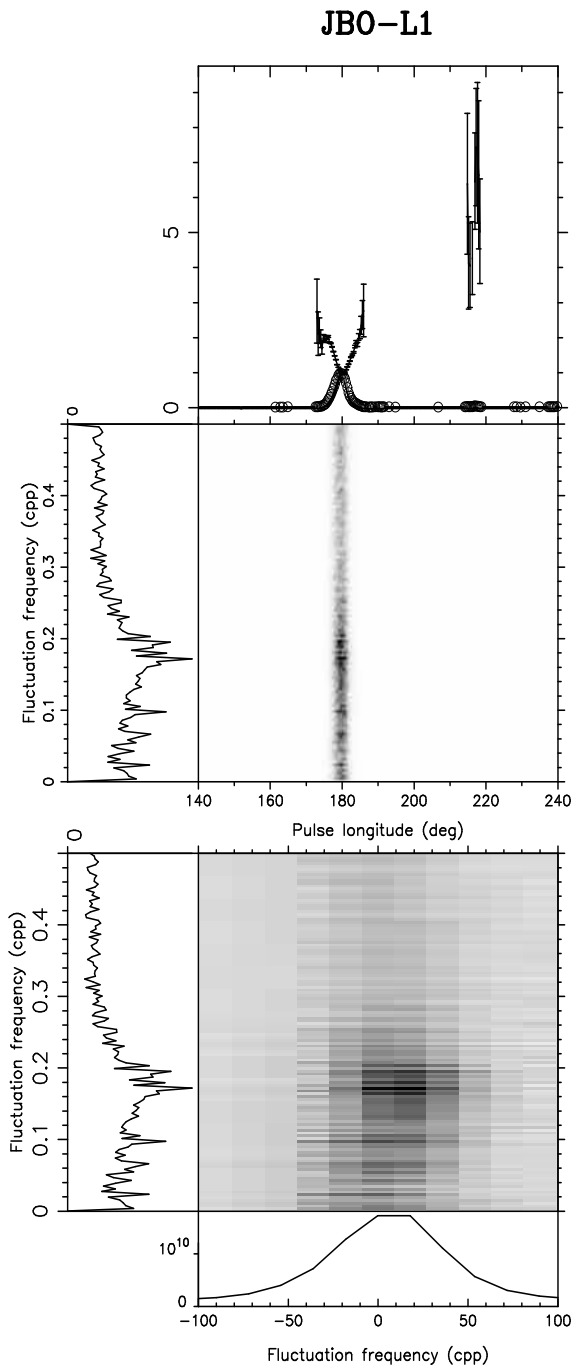


Figure 6.10: The subpulse modulation properties of PSR B0823+26. *Top:* The integrated profile (solid line), the longitude-resolved modulation index (solid line with error bars) and the longitude-resolved standard deviation (open circles) profiles. *Middle:* The LRFS (centre) and corresponding subpulse intensity modulation spectrum (P_3 ; side panel on the left). *Bottom:* The 2DFS of the main-pulse emission region (centre) and corresponding subpulse intensity (side panel on the left) and phase (P_2 ; bottom panel) modulation spectra. See also §5.3.3 for a description of how these plots are computed.

6.3 Discussion

In the single-pulse observations presented here, we have seen that PSR B0823+26 undergoes extreme pulse intensity modulation. Remarkably, this is not isolated to variation between distinct radio-on and -off phases. During the radio-on phases, the pulsar exhibits a very high degree of modulation; that is, the main-pulse emission component exhibits a modulation index which is twice that typical of other pulsars, and that of the post-cursor component is comparable to RRAT-like emission. In fact, the PC emission undergoes such a high degree of modulation that it can occasionally be observed as bright, or brighter, than the MP component (see §6.2.3).

With this in mind, it is interesting to consider the work of Rathnasree & Rankin (1995), who characterised the pulse shape properties of the MP and PC components in PSR B0823+26 based on their polarisation-angle (PA) ‘modes’⁹. They found that the MP of the pulsar is comprised of three emission components (i.e. a dominant central core component and a surrounding pair of conal components or ‘outriders’), whose strength, along with that of the PC, correlates with a given polarisation mode (see Figs. 4 – 5; Rathnasree & Rankin 1995); that is, the ‘primary-mode’ emission exhibits a core component and the PC, the ‘secondary-mode’ manifests as a dominant core component and two conal outriders, and the ‘residual-mode’ appears as a triple-peaked MP profile with enhanced PC emission¹⁰. Moreover, they found that the PC emission is correlated with the conal outriders. This indicates that the PC and conal outrider emission might originate in nearby regions in the light cylinder. Furthermore, this suggests that the pulsar may possess a multitude of different magnetospheric states (i.e. not just radio-on and -off, c.f. PSR B1822–09; Lyne et al. 2010), in which the MP emission components and PC emission are enhanced (diminished) accordingly. In this context, we could speculate that some pulses from this source might only contain weak, isolated PC (or outrider) emission and, subsequently, be attributed to an infrequent magnetospheric state. However, our existing observations seem to suggest that this is unlikely, considering that no isolated PC pulses have been observed.

In addition, we have provided further evidence to suggest that PSR B0823+26 undergoes nulls over two different timescales. Namely, short-term nulls which are typical of other pulsars (i.e. $1 - 3 P$) and longer nulls which are at least 6 minutes in duration (up to several hours; see §3.3). This suggests that the pulsar may undergo a combina-

⁹Rathnasree & Rankin (1995) defined pulses which had a linear polarisation above a noise threshold, and PAs which fell within $\pm 45^\circ$ of their model PA, to be ‘primary-mode’ (for PAs closest to the model) and ‘secondary-mode’ (for PAs in the opposite hemisphere) pulses. They called pulses which did not exceed the noise threshold ‘residual-mode’ pulses.

¹⁰The primary polarisation mode profile is $\gtrsim 3$ times stronger than those of the other modes and, as such, dominates the average profile shape (Rathnasree & Rankin 1995).

tion of ‘pseudo-nulls’ (e.g. Deshpande & Rankin 2001; see also §2.5.4) and long-term nulls corresponding to true emission cessation. From the brightest observations, we find that the short-term nulls have a nulling fraction upper limit $NF \leq 6.5 \pm 0.4\%$, which is consistent with the results of Rathnasree & Rankin (1995). Due to the length of the majority of the observations, however, we were unable to characterise the overall nulling fraction of the pulsar, i.e. due to the presence of long nulls ($\gtrsim 6$ minutes), nor were we able to investigate the ‘emission flickering’ phenomenon discussed in §3.3. Therefore, further, long-term (i.e. $\gtrsim 10^3$ seconds) single-pulse observations of this source are required to confirm our predictions and further characterise its emission behaviour which, ultimately, should provide us with a better understanding of nulling pulsars and, hence, the mechanism(s) responsible for pulsar radio emission.

6.4 Conclusions

We find that PSR B0823+26 possesses two distinct nulling timescales i.e. short-term ($1 - 3 P$) and long-term ($\gtrsim 600 P$) nulls. In addition to this ‘switching’ behaviour, the pulsar is also found to exhibit a very high degree of modulation in its post-cursor component, which is comparable to RRAT-like emission. We speculate that the object possesses a multitude of different magnetospheric states, in which the polarisation and emission properties of the source change significantly and, hence, lead to intermittent PC emission. Ultimately, we emphasise the need for further single-pulse observations of this source to elucidate the nature of its nulling behaviour. These observations would nominally be greater than a few hours in duration, and would also be polarisation calibrated, to characterise the pulse intensity modulation properties of the source accurately.

Chapter 7

Conclusions

We have conducted a detailed investigation into the emission and rotational properties of three extreme nulling pulsars (i.e. PSRs B0823+26, B1931+24 and J1107–5907) at L-band. This has enabled us to gain insight into the intermittent nature of these objects, as well as expand upon the current understanding of emission modulation and spin-down rate variation in pulsars. Here, we review the main results of these studies and how these objects can be interpreted in the context of other sources.

7.1 PSR B0823+26

PSR B0823+26 is found to exhibit very unusual emission properties, which indicate that it is significantly more variable than previously reported (e.g. Ritchings 1976; Rathnasree & Rankin 1995). In particular, the source is shown to undergo both short ($1 - 3$ pulse periods) and long-term ($\gtrsim 600 - 10^4$ pulse periods or more) nulls, which suggest that it follows a bimodal distribution of nulling timescales¹. Furthermore, we find that the object undergoes a ‘pre-ignition’ or ‘emission flickering’ phase before it assumes a long-term (i.e. \sim hours), relatively stable radio-on emission phase (§3.3). This suggests that other nulling pulsars may undergo a similar process before they attain the necessary conditions for stable radio emission. Remarkably, we also find that the object exhibits a high degree of variability in the radio-on phase, where it possesses three different pulse shapes (Rathnasree & Rankin 1995) and a large modulation index; this is particularly evident for the post-cursor emission component, which has a modulation index that is comparable to RRAT-like emission (§6). We conclude that the nulling fraction (NF) in the radio-on mode is $\leq 6.5 \pm 0.4\%$ (§6.2.2), which is in

¹Note that only a handful of other pulsars are known to exhibit long-term nulling timescales as extreme as this source.

7: CONCLUSIONS

contrast to the inferred, albeit likely overestimated, overall $\text{NF} = 20 \pm 10\%$ (§3.3).

Despite having very high-cadence observations of this object, we find no direct evidence to suggest that the pulsar exhibits any change in spin-down rate between the radio-on and -off (i.e. $\gtrsim 6$ minute null) emission modes; we place an upper limit on this variation to be $\lesssim 6\%$ from simulations (§3.6). Given the timescales of modulation, however, it is unlikely that this effect, if present, will be able to be detected until significant advances have been made in observational sensitivity and, hence, timing precision. With this in mind, PSR B0823+26 cannot readily be fitted into the framework of the ‘intermittent’ pulsar class. It is clear, however, that this source is an extreme nulling pulsar, which should provide clues to the mechanism(s) which govern radio emission modulation in similar objects.

7.2 PSR B1931+24

Through analysing the emission and rotational properties of PSR B1931+24, using approximately 13 years of data, we have expanded upon the work of Kramer et al. (2006)². We have confirmed that the object is an intermittent pulsar (§4); that is, the source is found to exhibit a detectable change in spin-down rate, which is correlated with the presence (absence) of radio emission. In addition, we have discovered that the pulsar possesses a high degree of magnetospheric memory: 1) the radio-on and -off phases in this object retain a remarkably stable periodicity of approximately 36 days on average throughout the data; 2) the change in spin-down rate between the radio-on and -off modes remains surprisingly constant throughout the observations ($\Delta\nu = 48 \pm 2\%$); and 3) the pulsar exhibits a stable, overall $\text{NF} = 74 \pm 6\%$. We also do not find evidence to suggest that the pulsar undergoes any emission flickering phases before assuming a stable, emission mode. However, we note that the flux density associated with the radio-on phase is only 20 times brighter than that in the radio-off phase (c.f. ~ 100 in PSR B0823+26). Therefore, it could be possible that this pulsar exhibits very weak, underlying emission in the radio-off mode (c.f. Esamdin et al. 2005). Regardless of the detectability of emission, it is very likely that this pulsar undergoes extreme magnetospheric changes, in order to account for its emission and rotational properties. Accordingly, this pulsar represents a particularly useful testbed against which to probe magnetospheric and radio emission models.

²In total, Kramer et al. (2006) used approximately 700 days of data to study the properties of PSR B1931+24. Due to the relatively short time-span of these data, no consideration to evolution in the spin-down rates or modulation timescales was provided.

7.3 PSR J1107–5907

PSR J1107–5907 is, arguably, the most unusual pulsar which has been studied in this work (§5). While it was originally suggested that this pulsar may resemble an intermittent pulsar (O’Brien et al. 2006; Kramer 2008), we show that it undergoes much shorter-term emission variation. We find that the pulsar not only exhibits two very different radio-on emission modes (strong and weak), but that it also possesses a null state which can span $\sim 1 - 10^4$ pulse periods (i.e. seconds to several hours or more). In the strong modes, we note that source emits during the entire rotational period (i.e. pulses exhibit extended pre-cursor, main-pulse and post-cursor emission), which can be as bright as that from the Vela pulsar (with a flux density at 1400 MHz $S_{1400} \sim 1.1$ Jy; O’Brien et al. 2006). We find that this emission is preferentially emitted in bursts of pulses, which last approximately 15 minutes on average. From the observations of this source, the NF in the strong mode is estimated to range between $\leq 41 \pm 2\%$ and $\leq 72 \pm 2\%$. We also note that if the pulsar were situated farther away, the strong-mode emission could be interpreted as coming from a RRAT; that is due to the large, peak flux density ($S_{\text{peak}} \gtrsim 453$ mJy) and irregularity of the brightest pulses (c.f. PSR B0656+14; Weltevrede et al. 2006; see also §5.3.2). By comparison, weak emission from the pulsar (i.e. emission with a narrow main-pulse and diminished outer components) is observed far more infrequently. So much so, in fact, that the emission in this mode is comparable to that of RRAT-like sources; weak pulses are detected with an average rate of approximately 85 per hour (§5.5.1). Overall, we find that the pulsar exhibits a NF $\sim 98.6\%$, which further supports an association with RRAT-like objects (e.g. Keane 2010; Burke-Spoloar et al. 2011).

Further to this, we note that PSR J1107–5907 lies in the pulsar ‘death valley’ and that it has a large characteristic age ($\tau \sim 445$ Myr). Coupled with its emission properties, this indicates that the object may be undergoing a transition between a pulsar mode and a RRAT mode; that is, the pulsar could be experiencing a step-change in NF over time (see also Burke-Spoloar & Bailes 2010). As such, this object could provide direct insight into the processes which govern the degradation of the radio emission mechanism, as well as a link between normal and transient (or non-emitting) radio pulsars. Given that similar behaviour has already been seen in one other source, PSR J0941–39 (Burke-Spoloar & Bailes 2010), it is likely that several more objects exist that are similar in nature.

Similar to PSR B0823+26, we could not find direct evidence for any change in spin-down rate between the emission modes in this pulsar. However, it is very unlikely that any such variation can ever be detected in PSR J1107–5907; the low, average spin-down

rate and short-term emission modulation in this source imposes a strong bias against such a detection (§5.4). Despite this, it is still possible that the different emission modes could be attributed to magnetospheric reconfiguration and that spin-down rate variation does occur, albeit below our instrument sensitivity.

7.4 Distinctions Between the Different Types of Nulling Pulsars

Due to the combination of an incomplete sample of nulling pulsars (i.e. across the $P - \dot{P}$ diagram and range of NFs), and an insufficient number of in-depth studies, no concrete theory has been developed which can explain and differentiate the transient nature of these objects. As such, there is some ambiguity as to how we can best classify nulling pulsars, based on their behaviour and/or properties (see §2.5). In this work, we have provided further evidence to suggest that the labels given to the presumably different types of nulling sources (i.e. ‘typical’ nulling pulsars, RRATs and ‘intermittent’ pulsars) are mainly associated with the nature of observations. Namely, we have seen that two of the pulsars in this study (PSRs B0823+26 and J1107–5907) exhibit prominent mode changes, that is extreme nulls and substantial pulse profile changes. However, they cannot be fitted into the framework of the intermittent pulsar class because they do not show discernible variations in spin-down rate. As such, we argue that intermittent pulsars may only be discerned from typical nulling pulsars and RRATs, based on the fact that they possess long enough modulation timescales to facilitate the detection of $\Delta\nu$; as of yet, the only distinguishing factors are the length of emission phases and the detection of $\Delta\nu$ which, subsequently, go hand-in-hand.

Further to the work of several authors (e.g. Weltevrede et al. 2006; Burke-Spolaor & Bailes 2010; Kaspi 2010; Keane 2010; Burke-Spolaor et al. 2011; Weltevrede et al. 2011), we provide additional evidence to suggest that the distinctions made between RRATs and typical nulling pulsars are predominantly governed by detection labels. For example, in the observations of PSR J1107–5907, we have seen that it is possible for a pulsar to exhibit both a RRAT-like mode and a more conventional nulling mode, over a wide range of timescales (c.f. PSR J0941–39; Burke-Spolaor & Bailes 2010). Therefore, the interpretation of a pulsar’s emission behaviour will be modulated by the length, sensitivity and cadence of observations; these factors will determine whether an object is observed in only one or more possible emission modes (including extended null phases), how well the modulation timescales of a source are characterised, and whether

a pulsar is most readily detected in single-pulse or periodicity searches³.

With the above points in mind, we speculate that conventional nulling pulsars, RRATs and intermittent pulsars all exhibit a similar underlying process (e.g. magnetospheric state changes; see §2.5.2) and might not need to be separated into different classes. We suspect that the different ‘types’ of nulling pulsars may just be objects which lie at a certain point on a ‘nulling continuum’ scale, as suggested by Keane (2010). However, continued observations of these sources are required to determine whether they are in fact distinct from one another (see below).

7.5 Future Prospects

In order to elucidate the principal properties of the various ‘types’ of nulling pulsars, and hence their transient nature, more observations and detailed studies are required. Ideally, they would be systematic (i.e. across the $P - \dot{P}$ diagram), with long observing spans (i.e. several hours) and high-time resolution (i.e. single-pulse data), and at multiple frequencies (at least in the radio regime). As such, they would provide the necessary time resolution and coverage, as well as frequency range, to determine whether the emission modulation in transient/nulling pulsars is generally a broadband effect, whether pulsars undergo ‘flicker’ phases before assuming a constant mode of emission, what the true distribution of nulling (modulation) timescales is and, hopefully, what mechanism(s) are responsible for their behaviour⁴. It would also be beneficial to incorporate polarimetry information into these studies, which would likely provide significant insight into the characteristics (e.g. emission heights) of the intermittent emission components observed in such pulsars, as well as tests of current magnetospheric models; for example, Li et al. (2012a) predict that there is a strong correlation between inclination angle (α) and $\Delta\nu$ in intermittent pulsars i.e. $\Delta\nu \sim 120\% - 290\%$ for $\alpha \sim 30^\circ - 90^\circ$ (with increasing $\Delta\nu$ towards lower α).

With the next generation of telescopes (e.g. LOFAR, FAST, ASKAP, MeerKAT and the SKA) coming online in the near future⁵, we anticipate a dramatic increase in the number of known transient pulsars⁶. Coupled with the continued observation of existing sources (e.g. PSRs B0823+26, J1107–5907, J1832+0029, J1841–0500 and B1931+24), characterisation of these objects should lead to an improved understanding

³RRATs could merely be extreme nulling pulsars ($NF \gtrsim 95\%$) that are more readily detected in single-pulse searches, compared with periodicity searches (Burke-Spolaor et al. 2011).

⁴Infra-red and high-energy (e.g. X-ray and γ -ray) observations would be particularly useful in this to discriminate between viable cessation (modulation) mechanisms (see §2.5).

⁵Although LOFAR is already collecting data, the complete array is yet to be fully built.

⁶Approximately 900 pulsars are predicted to be discovered with LOFAR (van Leeuwen & Stappers 2010), many of which will likely be transient objects.

7: CONCLUSIONS

of the general emission and rotational properties of pulsars which, ultimately, should facilitate the development of more realistic radio emission and magnetospheric models.

Appendix A

The Energy Loss Model of PSR B1931+24

PSR B1931+24 is the archetype of the intermittent class of pulsars i.e. neutrons stars which undergo active (radio-on) and quiescent (radio-off) phases of radio emission, with directly associated changes in spin-down rate ($\dot{\nu}$). Transitions between these emission phases are observed over very short timescales ($\lesssim 10$ s) and, subsequently, are thought to be associated with global reconfigurations in the charge-density structure of the pulsar magnetosphere. The central concept of this model relies upon the presence (absence) of an outflowing plasma whose current flow modifies the spin-down behaviour of pulsars like PSR B1931+24 in nature. As such, the open field lines above the magnetic pole are thought to become depleted of charged particles during the radio-off phases (Kramer et al. 2006), where the deceleration of the pulsar ($\dot{\nu}_{\text{off}}$) is a result of an electromagnetic torque that is dominated by magnetic dipole radiation (Pacini 1967; Gunn & Ostriker 1969; Harding et al. 1999). During the radio-on phases, an additional torque is suggested to be provided by the outflowing plasma of an activated pulsar wind which, subsequently, enhances the pulsar spin-down $\dot{\nu}_{\text{on}}$ (Kramer et al. 2006). This additional torque is described by (Eqn. 4; Harding et al. 1999)

$$T \sim \frac{2}{3c} I_{\text{pc}} B_s R_{\text{pc}}^2, \quad (\text{A.1})$$

where c is the speed of light, B_s is the dipole magnetic field strength at the neutron star surface, R_{pc} is the polar cap radius¹ and I_{pc} is the electric current along the field

¹From Lorimer & Kramer (2005), the polar cap radius can be related to the pulsar radius R by $R_{\text{pc}} = \sqrt{2\pi R^3 \nu/c}$.

lines crossing the polar cap (Eqn. 5; Harding et al. 1999)

$$I_{\text{pc}} \sim \pi R_{\text{pc}}^2 \rho_{\text{plasma}} c, \quad (\text{A.2})$$

where ρ_{plasma} is the plasma current charge density². We note that the simplified geometry of an aligned rotator is assumed (i.e. $\alpha = 0^\circ$), for a pulsar which is not in a vacuum (see Goldreich & Julian (1969) for basics on aligned rotators). It is also assumed that the neutron star magnetosphere is spontaneously charged in order to support the charges and electric currents (Contopoulos et al. 1999). In addition, electrons and positrons with a charge density ρ_{plasma} are only considered to flow outward from the polar cap at the speed of light. Subsequently, the value for the electric current above is only a crude estimate for the actual current flowing in the magnetosphere.

Following Kramer et al. (2006), ρ_{plasma} can be estimated from the difference in the loss of rotational energy, \dot{E} , between the radio-on and -off phases. The spin-down luminosity during the radio-off phases is assumed to be due to magnetic dipole braking only i.e. $\dot{E}_{\text{off}} = \dot{E}_{\text{dipole}}$. During the radio-on phases, however, the energy loss from the neutron star surface is greater due to the presence of the additional outflowing plasma current of the wind (\dot{E}_{wind}):

$$\dot{E}_{\text{on}} = \dot{E}_{\text{off}} + \dot{E}_{\text{wind}}. \quad (\text{A.3})$$

Rearranging this equation to find \dot{E}_{wind} , and utilising Eqn. 1.2, we find that

$$\dot{E}_{\text{wind}} = 4\pi^2 I \nu \dot{\nu}_{\text{off}} - 4\pi^2 I \nu \dot{\nu}_{\text{on}} = -4\pi^2 I \nu \Delta \dot{\nu}. \quad (\text{A.4})$$

Following Harding et al. (1999), the energy loss rate due to the wind is

$$\dot{E}_{\text{wind}} = T \Omega = 2\pi T \nu, \quad (\text{A.5})$$

where T is the total electromagnetic torque. Combining equations A.2 and A.1, and inserting T into \dot{E}_{wind} above, we obtain

$$\dot{E}_{\text{wind}} = \frac{4\pi^2}{3} R_{\text{pc}}^4 B_s \nu \rho_{\text{plasma}}. \quad (\text{A.6})$$

Relating this with Eqn. A.4, and using $B_s = 3.2 \times 10^{19} \sqrt{P \dot{P}}$ (Eqn. 1.7), the plasma

²Harding et al. (1999) assume that ρ_{plasma} is equal to the Goldreich-Julian charge density, which is in contrast to Kramer et al. (2006) who make no assumption about this quantity.

charge density can be estimated via

$$\rho_{\text{plasma}} \approx \frac{3Ic^2 \Delta \dot{P}}{1.26 \times 10^{21} R^6 P^{1/2} \dot{P}_{\text{off}}^{1/2}} \approx \frac{3Ic^2 \Delta \dot{\nu}}{1.26 \times 10^{21} R^6 \nu^{1/2} \dot{\nu}_{\text{off}}^{1/2}} [\text{statC}] . \quad (\text{A.7})$$

where $I = 10^{45}$ g cm² is the moment of inertia of the rotating neutron star and $R = 10^6$ cm. We note that the above equations for the plasma charge density are quoted in centimetre-gram-second units (statcoulombs). To convert this quantity into SI units (i.e. Cm⁻³), we incorporate an additional factor of $10^7 c^{-1}$ into the calculation.

Inserting the rotational parameters of PSR B1931+24 into Eqn. A.7, i.e. using the values quoted in Kramer et al. (2006), we find that the plasma current which is associated with the radio emission carries a charge density $\rho_{\text{plasma}} \sim 0.034$ Cm⁻³. Comparing this quantity with the Goldreich-Julian charge density (i.e. total charge density available from rotation) (Lorimer & Kramer 2005)

$$\rho_{\text{GJ}} = \frac{1 \times 10^7 B_s \nu}{c^2} \approx -\frac{3.2 \times 10^{26} \dot{\nu}_{\text{off}}^{1/2}}{\nu^{1/2} c^2} = 0.033 \text{ Cm}^{-3} , \quad (\text{A.8})$$

we obtain $\rho_{\text{plasma}}/\rho_{\text{GJ}} \sim 102\%$. Therefore, the plasma charge density of PSR B1931+24 is entirely sufficient to explain the changes in the neutron star's torque. It is uncertain, however, as to what mechanism is responsible for spontaneously altering the plasma flow in the pulsar's magnetosphere.

A: THE ENERGY LOSS MODEL OF PSR B1931+24

Appendix B

Periodicity Analysis of Astronomical Signals

Periodicity analysis of continuous data, which is evenly sampled, is relatively straightforward. However, due to the availability of observing instruments and visibility of sources in the sky, astronomical data are often plagued by having to deal with uneven data sampling. Furthermore, astronomical sources are often non-stationary (i.e. highly variable in frequency). As a result, traditional methods of periodicity analysis have to be modified to gain useful information from such data; both the mathematical validity and spectral noise susceptibility of traditional methods are heavily affected by uneven data sampling (see §B.2). Here, we review the basic concepts of periodicity analysis and present two modified Fourier methods, both of which have been implemented in this thesis to deal with uneven data sampling.

B.1 Periodicity Analysis Basics

Traditionally, time-frequency information of time-series data has preferentially been obtained using Fourier analysis techniques. Fourier theory enables a signal to be represented as a sum of a, possibly infinite, series of sines and cosines through Fourier expansion (e.g. Addison 2002; Smith 2003). The study of Fourier series within a signal $x(t)$, where t is a continuous variable, provides a representation of the frequency content of x and, therefore, enables an arbitrary periodic function within the signal (if it exists) to be decomposed into a set of simple terms or *harmonic frequencies* (e.g. Daubechies

1992). Following Addison (2002), the standard Fourier transform (FT) is defined as

$$\mathcal{F}(f) = \int_{-\infty}^{\infty} x(t) e^{-i2\pi ft} dt, \quad (\text{B.1})$$

where f is the signal frequency and $x(t)$ is the original signal.

Fourier analysis has great success with representing the frequency content of a stationary (i.e. non-variable) signal in time. However, complications arise when this technique is applied to highly variable, non-periodic signals which exhibit discrete and discontinuous changes with time; the standard Fourier transform only provides information about the overall frequency content of a signal, and not the times at which a specific frequency feature arises (i.e. it provides no information about the correlation of time and frequency in a signal). Therefore, a significant amount of work has been conducted on rectifying this issue, which will be discussed below.

B.1.1 Time-frequency Localisation

Time localisation was first introduced by Gabor in 1946, through his definition of elementary time-frequency ‘atoms’ as waveforms that have a minimal spread in a time-frequency plane. He proposed decomposing signals over these elementary atomic waveforms to measure time-frequency ‘information’ content (Mallat 1999). In this context, a Fourier transform can be modified to include the convolution of a window function with the signal which, in turn, allows the frequency content of a signal to be examined in time (via Fourier frequency decomposition of the signal at successive epochs; Addison 2002). This ‘windowed’ Fourier transform, is also known as the *short-time Fourier transform* (STFT). Specifically, the STFT employs a window function to localise the complex sinusoid function (i.e. the wavefunction) and is defined as (e.g. Addison 2002)

$$\mathcal{F}(f, d) = \int_{-\infty}^{\infty} x(t) h(t - d) e^{-i2\pi ft} dt, \quad (\text{B.2})$$

where $h(t - d)$ is the window function which confines the complex sinusoid $e^{-i2\pi ft}$ (d is the time offset applied to the window function). The combination of a window function and a complex sinusoid is referred to as a *windowed Fourier atom* or more generally as a *time-frequency atom* (Gabor 1946):

$$h_{f,d}(t) = h(t - d) e^{-i2\pi ft}. \quad (\text{B.3})$$

The down-fall of this analysis technique is that it lacks adaptivity (i.e. the STFT

cannot probe all frequencies with equal resolution) and is unsuitable for the analysis of sudden transient signatures and frequency evolution (e.g. Zhong & Yang 2007). This is primarily because each time-frequency atom has a constant width in the frequency domain and, hence, a fixed size in the time-frequency domain that is regardless of the internal frequency of the signal (Addison 2002). As such, the STFT fails to obtain high resolution time-frequency variations of spectral components (Mallat 1999)¹. Figure B.1 shows the basic principle of an STFT.

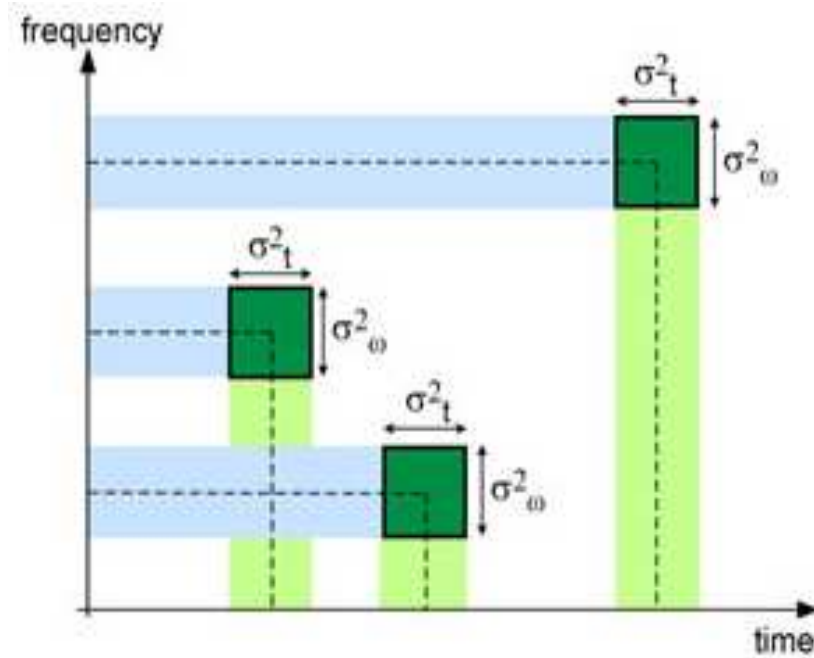


Figure B.1: A schematic diagram depicting the basic principle of a short-time Fourier transform (figure adapted from <http://nocios.webnode.com>). A signal is windowed at successive time intervals, with a fixed size in the time-frequency plane (i.e. σ_t^2 , σ_ω^2), and is FFTed to obtain local frequency information. Note that the window widths are limited by the Heisenberg uncertainty principle i.e. $\sigma_t^2 \cdot \sigma_\omega^2 = \text{constant}$.

B.1.2 The Wavelet Transform

The wavelet transform (WT) was developed as an alternative approach to Fourier analysis to overcome the inherent resolution problem described above. Wavelet analysis is analogous to the STFT, in that a window function is applied to the original signal before frequency decomposition is performed. In the case of the WT, however, the

¹For a comprehensive review of this topic, we refer to <http://users.rowan.edu/~polikar/WAVELETS/WTtutorial.html>.

choice of wavefunction that can be used is extensive. In fact, there are several families of local wavelike functions, known as *wavelets*, that are commonly used to construct wavefunctions for the purpose of this analysis (e.g. Daubechies 1992; Mallat 1999; Addison 2002; see also Fig. B.2). Wavelets can be thought of as a family of functions constructed from the *translation* and *dilation* of a single function Ψ , called the *mother wavelet* or *analysing wavelet*. From Daubechies (1992), wavelets are defined as

$$\Psi_{s,d}(t) = \frac{1}{\sqrt{|s|}} \Psi\left(\frac{t-d}{s}\right), \quad (\text{B.4})$$

where $s = 1/f$ is the scaling parameter, the measure of the degree of compression or scale (a.k.a. dilation) in the wavelet decomposition, d is the translation parameter which determines the time location of the mother wavelet, and $\Psi_{s,d}$ are the daughter wavelets generated by Ψ .

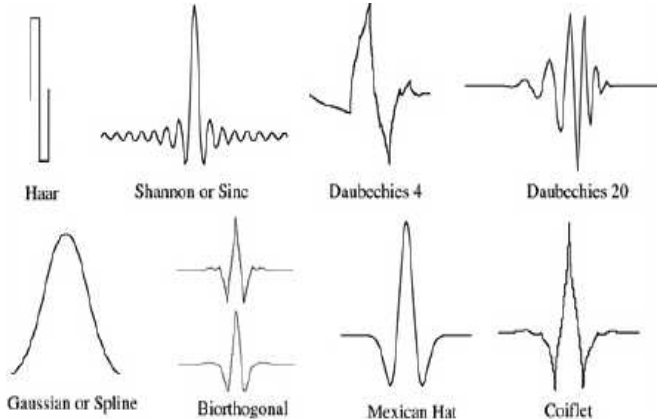


Figure B.2: Examples of the different types of wavelet functions used in wavelet analysis (figure adapted from <http://www.satmagazine.com>).

The continuous wavelet transform (CWT) of a signal $x(t)$ is defined as (e.g. Addison 2002)

$$T(s, d) = \int_{-\infty}^{\infty} x(t) \frac{1}{\sqrt{|s|}} \Psi^*\left(\frac{t-d}{s}\right) dt, \quad (\text{B.5})$$

Here, $T(s, d)$ are the wavelet transform coefficients, which represent the closeness of the signal to the wavelet for a specific scale and location. The result of a CWT is a synthesised version of $x(t)$ using Ψ to fit the function for best-fitting s and d values (e.g. (Mallat 1999; Addison 2002)). Figure B.3 shows the wavelet transform of a signal, which essentially quantifies the local matching of the wavelet with the signal (Addison 2002). If the wavelet function applied in the transform matches the shape

of the signal well at a specific scale and location, then a large transform coefficient is obtained. However, if the wavelet and signal do not correlate well, a low transform coefficient is obtained. The transform is calculated at numerous locations of the signal, and for numerous scales of the wavelet, thus allowing these coefficients to permeate a 2D transform plane (e.g. Addison 2002).

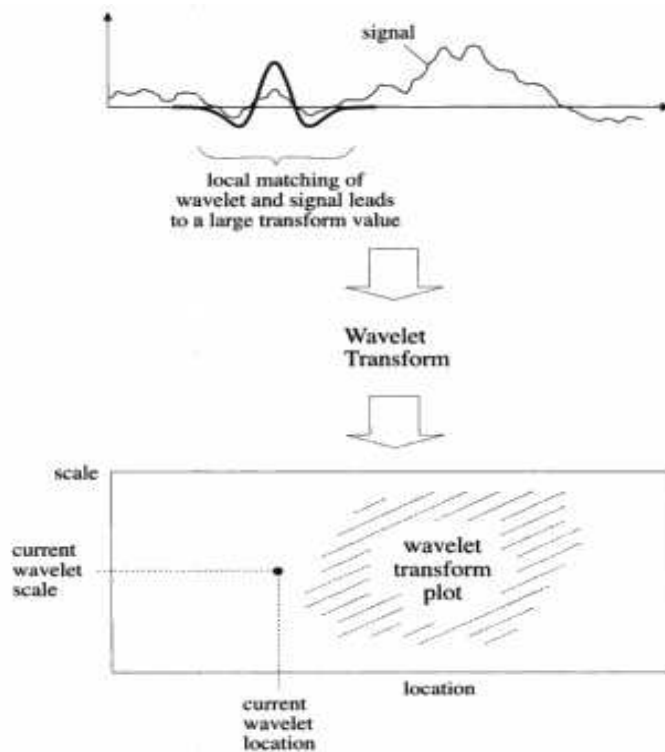


Figure B.3: The local matching of a wavelet function to a time-series signal (*top*), along with the corresponding transform plot (*bottom*) (figure taken from Addison (2002)). When the wavelet function matches the signal well at a specific location, for a specific scale (i.e. frequency), a large transform coefficient is obtained and vice versa. By convolving a wavelet with the signal at numerous locations, for different scales, a 2D time-frequency plane can be populated. This enables information about the frequency content of a signal, at a specific time, to be obtained.

As the time-frequency resolution of a signal is limited by the Heisenberg Uncertainty Principle (i.e. $\sigma_t^2 \cdot \sigma_\omega^2 = \text{constant}$), WTs apply an adaptive window function (which is altered in time and frequency coverage) to a signal in order to provide optimal spectral information²; for smaller scales, hence larger frequencies, the frequency coverage (i.e. window width, σ_ω^2) increases at the cost of decreasing the frequency resolution, but allows greater time resolution due to narrower time coverage and vice versa (e.g.

²This is an exclusive characteristic of wavelet transforms.

B: PERIODICITY ANALYSIS OF ASTRONOMICAL SIGNALS

Addison 2002; see also Fig. B.4)³. As such, wavelet analysis solves the inconsistent treatment of different frequencies adopted by FTs by decomposing a time-series into time-frequency space simultaneously, with different segments of the time-domain signal being computed separately (Mallat 1999; Addison 2002). This allows information to be obtained about the amplitude of periodic signals within the time-series, as well as their variation in time (Daubechies 1992). Like an STFT, a wavelet transform is able to measure the time-frequency variations of spectral components. In the case of a WT, however, its variable time-frequency resolution provides consideration to both the short-term and long-term variation of signals (Mallat 1999; Zhong & Yang 2007). Therefore, wavelet analysis is a rather ideal implementation of analysing time-frequency content of a signal.

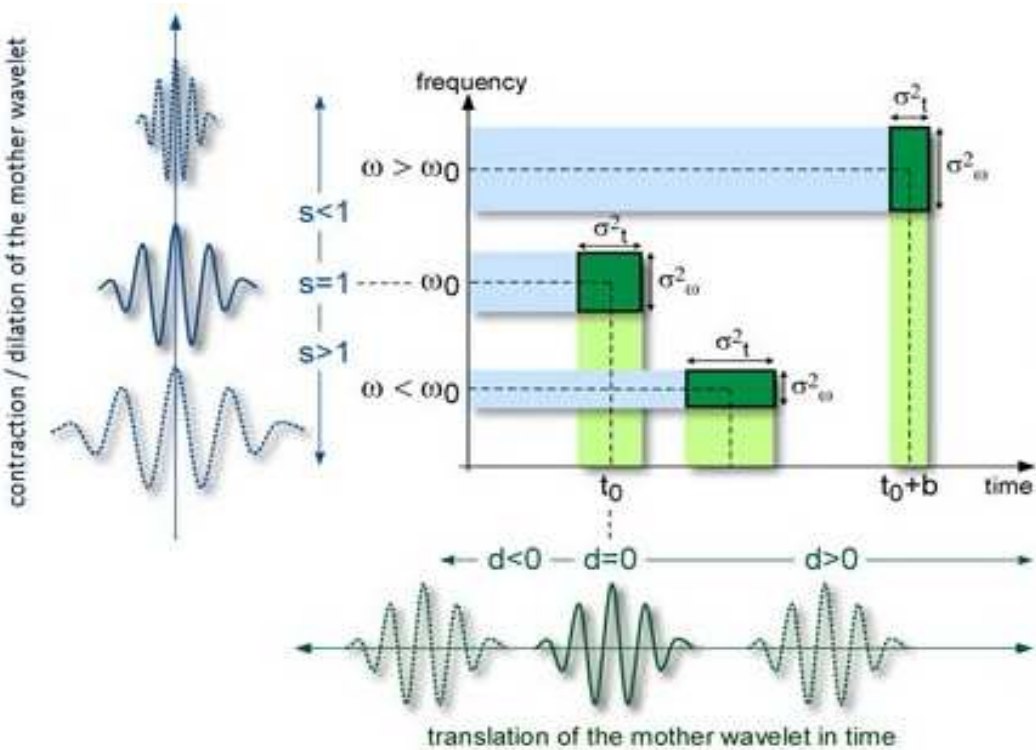


Figure B.4: An illustration showing the basic principles of wavelet analysis (figure adapted from <http://nocións.webnode.com>). Example wavelet functions, with appropriate scaling and translation, are shown towards the left and bottom respectively. When the scale s is decreased, for example, the time support of the wavelet function is reduced but the frequency spread increases. This provides coverage of an interval that is shifted towards higher frequencies and also allows multi-scale zooming within a signal, to detect transient signatures and quantify time-frequency evolution.

³See <http://www.wavelet.org> for several useful links and resources relating to this concept.

B.2 Periodicity Analysis of Unevenly Sampled Data

Unevenly sampled data does not lend itself to trivial periodicity analysis. This is because traditional Fourier methods are highly sensitive to data sampling consistency; the ‘true’ frequency content of a signal can often be masked by spectral noise and leakage due to irregularities in data sampling which, ultimately, may cause periodicities in the data sampling to dominate over those intrinsic to the signal itself (see e.g. Foster (1996)). As a result, a multitude of different modifications to traditional Fourier analysis, and alternative analysis methods, have been proposed in the literature (e.g. Högbom 1974; Scargle 1982; Buccheri et al. 1983; Foster 1996; Tagliaferri et al. 2001; Otazu et al. 2004). Here, we review two particular techniques which have been implemented in this thesis.

B.2.1 Autocorrelation and Welch Periodogram Method

The cross-correlation of a function with itself is called *autocorrelation*. This is where a signal is correlated with itself at successive time delays or *lags*, thus allowing the identification of periodic structure within a signal that was perhaps masked by noise. The mathematical operation of autocorrelation for a continuous real function $f(t)$ is defined as (Papoulis 1962)

$$R_f(\tau) \equiv \lim_{T \rightarrow \infty} \frac{1}{2T} \int_{-T}^T f(\tau) f(t + \tau) d\tau, \quad (\text{B.6})$$

where T is the total length of the signal and τ is the time lag at which the autocorrelation is calculated (see e.g. Box & Jenkins (1976) for more detail). Through application of this operation to unevenly sampled time-series data, one can bin the data into equally spaced time lags and, therefore, mitigate the effects of sampling by effectively interpolating the signal (e.g. Scargle 1982). This facilitates the application of traditional Fourier analysis, such as a Fast Fourier Transform (FFT), to estimate the power spectrum (periodogram) of a signal and, hence, decompose its frequency information.

To improve the statistical properties of periodogram estimates, Welch (1967) developed a modified version of the periodogram. By dividing the data into K , possibly overlapping, equal segments of length N , one can compute and average several periodograms to reduce the variance in the resultant average. Each data segment is tapered

using a suitable window function before being FFTed to mitigate noise and spectral leakage (Press et al. 1992). Through the use of non-overlapping segments, $D = 0$, one can reduce spectral variance by a factor of $2K$. This increases to a reduction of $18K/11$ if we overlap each segment by a half, i.e. $D = L/2$, and also gives equal weighting to data points on average (Welch 1967; Porat 1997). As such, this modification to the traditional periodogram is quite attractive. However, there is a trade-off with the frequency resolution of the averaged periodogram, due to the reduction in data length (c.f. $f_{\text{Nyquist}} = 1/2T = f_{\text{max}}/2$; Smith 2003), and the frequency content of the signal at different times is washed out. The mathematical operation of performing a Welch periodogram with a 50% overlap is defined as (Porat 1997)

$$P_x(f) = \frac{1}{K} \sum_{k=0}^{K-1} \left\{ \frac{1}{N} \left| \sum_{n=0}^{N-1} w[n] x[n + 0.5kN] e^{-i2\pi fn} \right|^2 \right\}, \quad (\text{B.7})$$

where x consists of the data samples within each segment, f is the frequency and $w[n]$ is the window function applied to each bin (n) of a data segment.

The choice of window function to apply to each data segment is very important, as its properties will determine the sidelobe structure and, hence, the leakage of power into frequency bins near the true values (e.g. Scargle 1982; Press et al. 1992; see also Fig. B.5):

$$(\text{leakage width in bins}) \approx \frac{N}{\text{window rise/fall time}}. \quad (\text{B.8})$$

Typically, ‘Bartlett’ and ‘Welch’ windows are used in conjunction with FFTs, which are defined as (Press et al. 1992)

$$w_j = 1 - \left| \frac{j - \frac{1}{2}N}{\frac{1}{2}N} \right| \equiv \text{‘Bartlett Window’}, \quad (\text{B.9})$$

$$w_j = 1 - \left(\frac{j - \frac{1}{2}N}{\frac{1}{2}N} \right)^2 \equiv \text{‘Welch Window’}. \quad (\text{B.10})$$

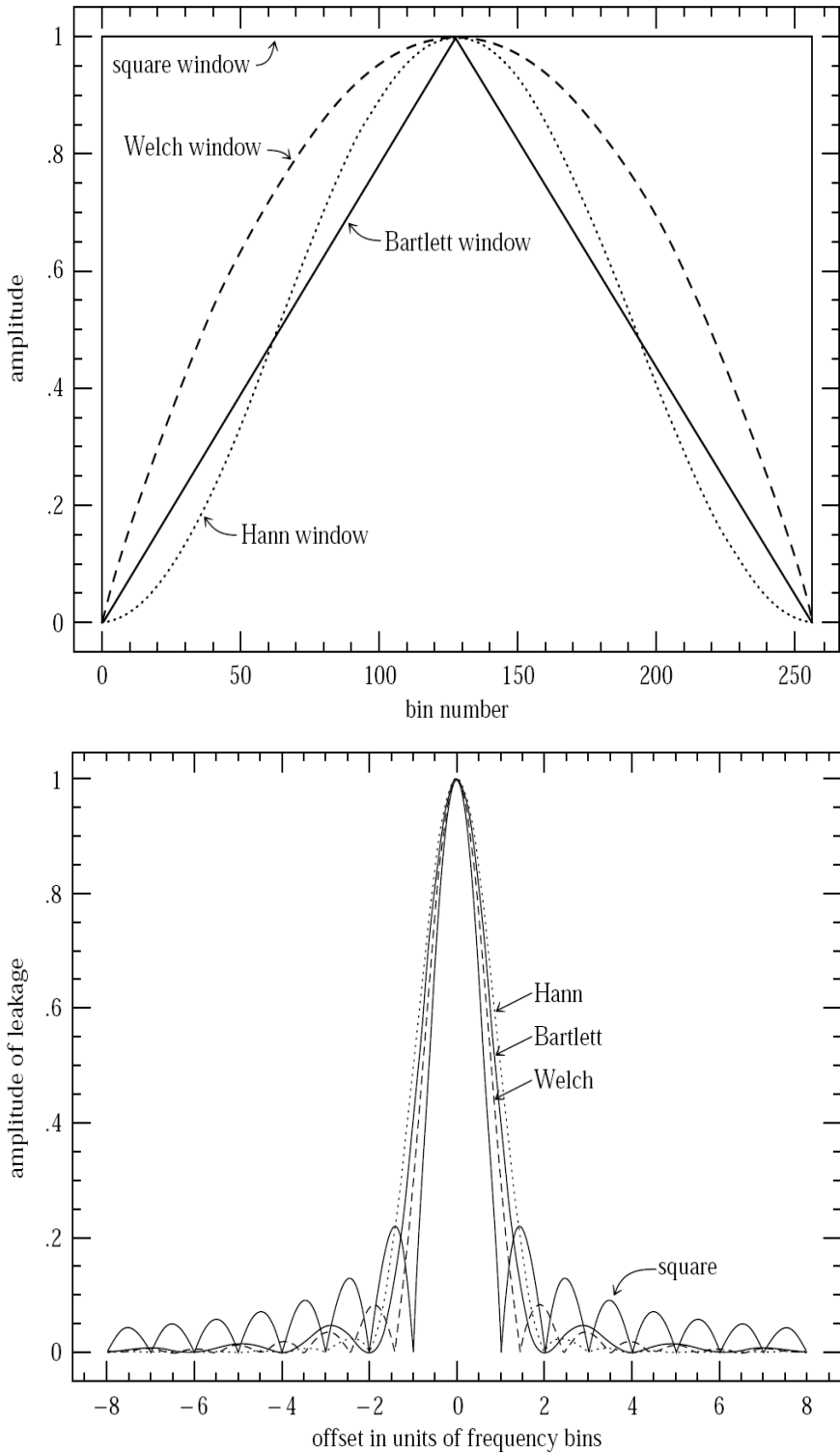


Figure B.5: *Top:* Common window functions used in FFT power spectral estimation (figure taken from Press et al. (1992)). Here, a data segment is divided into 256 bins and is multiplied by the window function, bin by bin, before an FFT is computed. *Bottom:* Spectral leakage functions for the window functions above (figure taken from Press et al. (1992)). The true frequency of the signal is located at zero offset. However, there is also leakage of power into neighbouring bins around the true frequency, which is dependent on the choice of window function.

B.2.2 Weighted Wavelet Z-Statistic

Traditional wavelet analysis of time-series data is very successful when applied to continuous, evenly sampled data. However, when applied to unevenly sampled time series, this is not the case; the response of the traditional wavelet transform is more sensitive to irregularities in the number and spacing of available data than on actual variations in a signal (Foster 1996). To overcome these shortcomings, Foster (1996) developed a weighted projection of the wavelet transform to form the *weighted wavelet Z-transform* (WWZ), which allows improved ability to detect and quantify (quasi-)periodic signals in unevenly sampled data.

The WWZ algorithm performs a wavelet transform (Eqn. B.5) by employing a wavelet function which includes both a periodic, sinusoidal test function of the form $e^{i\omega(t-\tau)}$ (by projecting the data onto a set of sine and cosine trial functions, i.e. the waveform) and a Gaussian window function (weighting function of the data) which is defined as (Foster 1996)

$$w_\alpha(\omega, \tau) = e^{-c\omega^2(t_\alpha - \tau)^2}, \quad (\text{B.11})$$

and is centred at τ , with a variable width defined by the frequency ω and tuning constant c (specified by the user)⁴.

As such, the WWZ uses a sinusoidal wavelet to fit the data and a sliding window function to weight the data points. As a result, data points towards the centre of the window in the fit are weighted the heaviest, and those near the edges of the window the least. The spectral content of the signal is then obtained at times corresponding to the centre of the window (Bedding et al. 1998; Templeton 2004; Templeton et al. 2005). As the size of the wavelet window is increased in the WWZ process, variations in the frequency centroid (peak frequency), or equivalently the period centroid (peak period), of a signal will become much less erratic as the time resolution is decreased and vice versa. Therefore, when implementing WWZ analysis of data, it is important to strike a balance between frequency and time resolution, which is altered by the choice in c . In addition, Templeton (2004) emphasise that this analysis should be performed on data of sufficient length, e.g. $\gtrsim 50$ times the mean period, to correctly determine the best-fitting fluctuation period of a source: 1) the length of a data-set will determine the maximum wavelet window width and, hence, the maximum time-frequency resolution that can be obtained for a signal under investigation; 2) consistent recovery of a fluctuation frequency (period) at several independent epochs in a WWZ indicate a physical significant periodicity i.e. a fluctuation frequency (period) which is intrinsic to the system.

⁴Note that w_α is the statistical weight given to a data point α .

B.3 WWZ Error Analysis

The determination of analytic errors in a WWZ is very difficult. This is primarily due to the complex nature of the weighted parametric projection implemented in its calculation. Error determination is also complicated by the assumptions made whilst devising the WWZ projection (see Foster (1996) for more details), which do not allow accurate representation of formally derived errors; the WWZ statistic naively assumes that time-series data is comprised of pure sinusoidal variations, which have constant frequency and amplitude, and a random noise contribution (Foster 1996). As such, we have implemented a number of quantitative methods to estimate the WWZ errors in this thesis, which we review below.

B.3.1 Confusion Limit Estimation

Templeton et al. (2005) suggest that a suitable approximation of the *maximum* error in a WWZ spectral feature is its confusion limit at a given epoch (τ), which is measured as the half-width at half-maximum (HWHM) of the WWZ-statistic ($Z(\omega, \tau)$). Using this method, a $1-\sigma$ uncertainty in the peak fluctuation frequency (ν_{fluc}) or period (P_{fluc}), at each epoch, can be estimated. It is important to note, however, that this method requires consideration of the nature of the spectral features in a transform. Namely, what we observe as a feature can have quite broad structure and, ultimately, will provide ambiguity in the location of dominant frequencies; if the location of the HWHM of a spectral peak is embedded in broad structure, the uncertainty in $\nu_{\text{fluc}}(\tau)$ or $P_{\text{fluc}}(\tau)$ will be quite significant. This method, therefore, is quite intuitive and relies upon the user to determine whether a local spectral feature is related to a more global (broader) one.

B.3.2 Data Windowing Method

Another method which can be used for the determination of errors in a WWZ transform is the use of standard deviation estimation of windowed data. Here, WWZ data is separated into segments of a specified length T , for which the standard deviation of all the $\nu_{\text{fluc}}(\tau)$ ($P_{\text{fluc}}(\tau)$) values is calculated. This provides an estimate of the uncertainty in the average or median $\nu_{\text{fluc}}(\tau)$ ($P_{\text{fluc}}(\tau)$) from the variation in the fluctuation frequency (period), i.e. the $1-\sigma$ value of that segment. It is important to note that WWZ power can be distributed towards lower fluctuation frequencies (higher periods) due to quasi-periodicity in a source, and the increase in the effective number of data points at those scales; there is an increased likelihood of local matching for wider wavelet windows, i.e. low scales, as more data is contained within them. As a result, features at high periods

will most likely correspond to characteristics of the initial data sampling or noise rather than spectral components intrinsic to the system. Therefore, it is crucial to set a ν_{fluc} (P_{fluc}) limit when using this windowing method, that is where we only compute σ for peak frequencies (periods) above a certain cut-off. Otherwise, we will be subject to very noisy data which will bias our results.

B.3.3 Resampling Methods

Resampling methods, namely the *bootstrap* and *delete-d jackknife*, have been developed by numerous authors (e.g. Tukey 1958; Efron 1979; Shao, J. & Wu, C.F. 1989) and have become powerful statistical analysis tools through the advent and accessibility of powerful computer processors. There is a large amount of literature pertaining to such resampling methods, describing their mathematical validity and statistical application. Consequently, we can confidently apply these tools to statistical work that is too complicated for realistic analytical treatment, such as the error analysis of WWZ transform data.

The basic premise of resampling methods is to gain information about the physics of a system by gathering more ‘experimental’ data by resampling the observed data. A test-statistic or estimator $\hat{\theta}$ is obtained for the observed data, providing information on the unspecified distribution of the data F . A distribution of $\hat{\theta}$ can be obtained through subsequent resamples of the parent sample, providing m values of replicated estimators, $\hat{\theta}^*$, from the observed system assuming a different sampling distribution (Zoubir, A.M. & Iskander, D.R. 2004). Resampling methods suggest that we resample a distribution close to F , which could be a subsample or empirical distribution \hat{F} (Zoubir, A.M. & Iskander, D.R. 2004). The difference between resampling methods is inherently the way in which such a distribution is constructed from the parent sample, and there is no shortage of subsampling methods available.

The principle of bootstrapping is demonstrated in Fig. B.6. In this example, $\chi = \{X_1, X_2, \dots, X_n\}$ is a sample drawn at random from the unknown distribution F . Therefore, each X_i is an *independent and identically distributed* (iid) random variable, obeying the distribution F i.e. each X_i is taken from the parent sample. As we do not know the exact nature of the system, we model the observed distribution F by randomly sampling with replacement from the parent sample (non-parametric bootstrapping) to obtain a bootstrap resample χ^* . Through repetition of this resampling process, we can approximate the distribution of $\hat{\theta}$ by the distribution of $\hat{\theta}^*$ (bootstrap replicates) and obtain an average $\hat{\theta}^*$. As a result, we can infer information about the

nature of the physical system⁵. A critical point to note about the bootstrap is that the bootstrap replicates we obtain will be determined by the way we model an observed distribution; for example, whether we resample data by including random measurement uncertainties or not. It is also important to note that there will be a repetition of values in the bootstrap resamples. Hopefully, our estimate will be close to the true (i.e. observed) distribution, but we cannot always be sure (e.g. Shao, J. & Wu, C.F. 1989; Shao, J. & Tu, D. 1995; Politis, D.N. et al. 1999; Zoubir, A.M. & Iskander, D.R. 2004)

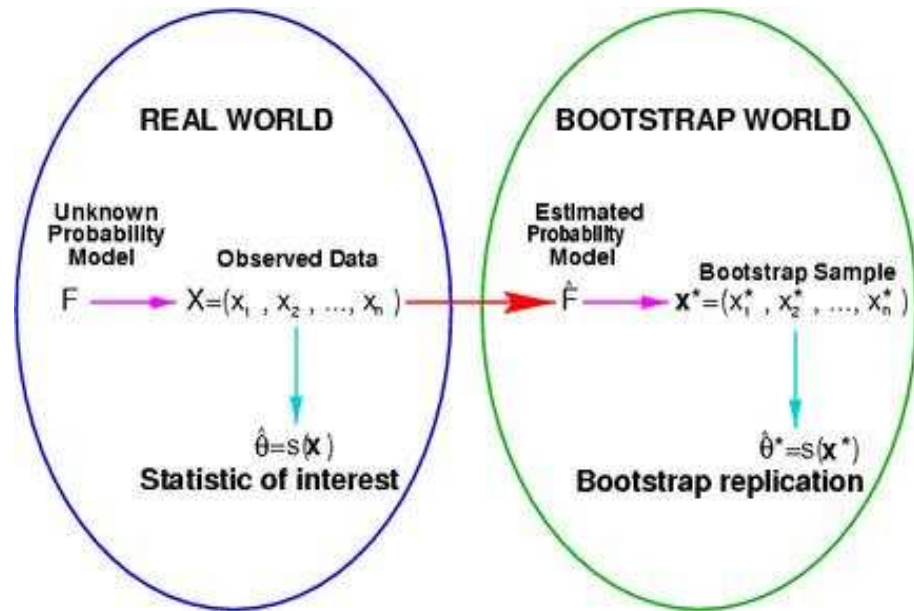


Figure B.6: The basic principles of the bootstrap method (figure taken from <http://www.spg.tu-darmstadt.de/>). Observational data is obtained for a physical (i.e. real) system and a statistic of interest is computed. This statistic, however, represents one possible outcome from a multitude of possible data samples. As such, the observed data can be resampled to replicate the outcome of an experiment, assuming a different sampling distribution is possible. Repetition of this process allows a distribution of bootstrap estimators to be obtained and, hence, an indication of the ‘true’ probability model of the real system. See main text also for details.

Such methods of estimator approximation are particularly attractive due to the inherent flexibility; practically any estimator $\hat{\theta}$ can be computed for the observed distribution, whose variance will approach the true value for the estimator under asymptotic conditions, to first order (e.g. Shao, J. & Tu, D. 1995; Politis, D.N. et al. 1999).

⁵For example, if we want to determine whether a die is loaded (i.e. biased) or not, we can roll it a large number of times and obtain a sample of outcomes. From the distribution of observed outcomes, or measurements, we can resample the data and simulate an almost infinite number of experiments, so that we can obtain a distribution of bootstrap replicates (e.g. numerous averages from ‘different’ experiments). If the standard deviation of these bootstrap replicates is small and the die consistently assumes a given average, then the die can be said to be biased.

Under mild assumptions, it is also known that \hat{F} will approach F as $n \rightarrow \infty$ (Hall 1992). Therefore, given enough resamples from observed data, we should have a reasonably accurate representation of the true parametric distribution pertaining to that physical system.

Another resampling method which has been very successful is the *delete-d jackknife*. Instead of constructing a probability model from which we obtain resamples, this method allows a more general approach to the computation of the distribution of $\hat{\theta}^*$; we draw m resamples *directly* from the parent sample using sampling without replacement i.e. we remove a random sample $\{X_i, i \in \mathbf{s}^c\}$ from the observed data-set (where \mathbf{s} is a subset of $\chi\{1, \dots, n\}$, the complement \mathbf{s}^c chosen from $\mathcal{S} = \{\mathbf{s}_1, \dots, \mathbf{s}_m\}$; Shao, J. & Tu, D. 1995; Politis, D.N. et al. 1999). It is clear that an approximation of the parent sampling distribution can be obtained based on a sample of size $r = n - d$ (where n is the total number of data points in the parent sample and $1 \leq d \leq n$) (Shao, J. & Tu, D. 1995; Politis, D.N. et al. 1999). Hence, the jackknife is more robust against model assumptions and employs a more systematic approach to taking resamples compared with the bootstrap. However, the convergence rate of the jackknife distribution estimator is not as good as that of the bootstrap (Shao, J. & Tu, D. 1995).

Furthermore, the consistency of the jackknife variance estimator is crucial to the application of the method, and is highly dependent on the ‘smoothness’ of the observed distribution i.e. data which is highly variable (contains more noise, i.e. measurement errors) is less smooth than one which pertains closely to its true distribution (contains negligible noise). The delete-d jackknife is adaptable to a given distribution, and will be consistent provided that $d \rightarrow \infty$ as $n \rightarrow \infty$ with a certain rate as

$$\frac{nr\sqrt{\text{var}(\theta_{r,s}^2)}}{d\sqrt{m}} \longrightarrow 0, \quad (\text{B.12})$$

where $\theta_{r,s}$ is the estimator obtained from a given resample (Shao, J. & Tu, D. 1995).

If these conditions are met, the delete-d jackknife variance estimator $\nu_{\text{SJACK-d}}$ will be consistent i.e. $\nu_{\text{SJACK-d}}/\sigma_n^2 \rightarrow_p 1$ (where σ_n^2 is the asymptotic variance of θ_n and \rightarrow_p denotes convergence in probability). The delete-d jackknife variance estimator is defined as

$$\nu_{\text{SJACK-d}} = \frac{r}{dm} \sum_{t=1}^m \left(\theta_{r,\mathbf{s}_t} - \frac{1}{m} \sum_{k=1}^m \theta_{r,\mathbf{s}_k} \right)^2, \quad (\text{B.13})$$

which is very similar to the bootstrap variance estimator, whose consistency is determined by its stability for a given m (Shao, J. & Tu, D. 1995)

$$\nu_{\text{BOOT}} = \frac{1}{m} \sum_{t=1}^m \left(\theta_{n,t}^* - \frac{1}{m} \sum_{k=1}^m \theta_{n,k}^* \right)^2. \quad (\text{B.14})$$

In the case of the bootstrap, the same number of data points are computed for each resample, thus allowing fairly general application. However, as bootstrapping randomly resamples data (i.e. results in unordered data and duplicates), this method can only be applied to WWZ transform data itself and not the initial time-series data; a time-series signal is not iid and, therefore, cannot be randomly sampled or re-ordered. The delete-d jackknife, on the other hand, can be employed to simulate different initial sampling distributions (which we could have observed) and allows computation of the WWZ transform for effectively different data-sets. However, a very important issue to tackle with the usage of delete-d jackknife resampling, and other such methods, is what choice of block size r is used in the resampling, as this will determine the distribution of $\hat{\theta}_{r,s}$. Intuitively, one would assume that bootstrap or jackknife estimators will be consistent (i.e. accurate) when their variances assume or converge towards the observed. However, this is not the case for WWZ transform data using the delete-d jackknife method; the more data we delete from the observed distribution, the lower the WWZ transform power will be at a given epoch due to the reduction in the effective number of data. This means that estimators such as the average, median and standard deviation of the WWZ transform will decrease as d increases, and there is no convergence for $\nu_{\text{SJACK}-d}$ towards the observed value. When applying this method analytically, it can be found to converge at a certain rate as $d \rightarrow \infty$ as $n \rightarrow \infty$ and is accurate to first order when Eqn. B.12 is satisfied. However, when this method is applied to physical data, it can be very difficult to justify the optimum value for d ; physical data has finite length, which means that these asymptotic conditions do not give much guidance towards the choice of d . In fact, Politis, D.N. et al. (1999) even state that the optimal choice for such a value depends on the “purpose for which subsampling is used”.

Politis, D.N. et al. (1999) suggest that the block size can be constrained by the *minimum volatility method*. This method is used to find the minimum standard deviation of confidence level intervals for an estimator (typically the mean) using a given d , i.e. ‘minimising confidence interval volatility’. If the number of data points removed d is too small, then the subsampling statistics $\hat{\theta}_{r,s_k}$ will be almost equal to the observed $\hat{\theta}_n$, and will result in under-coverage of subsampling confidence intervals. However, if d is too large then the intervals can undercover or overcover depending on the system. Consequently, there should be a region where we expect the ‘correct’ results with stable confidence intervals as a function of d . For each d , therefore, subsampling intervals for $\hat{\theta}_{r,s_k}$ can be computed, at a desired confidence level, with endpoints $I_{d,\text{low}}$ and $I_{d,\text{high}}$.

These endpoints are averaged over the number of *realisations* (or resamples) and their standard deviations are computed. The combined standard deviation of the low and high interval end-points, a.k.a. the *volatility index* VI_d , can also be computed in a neighbourhood of d (Politis, D.N. et al. 1999). The smallest, stable VI_d then corresponds to a so-called optimum choice in the number of data points to remove during the resampling process. This theoretically enables ‘optimal’ resamples of time-series data to be obtained, which can be used to represent the measurement uncertainty in a WWZ due to the possibility of alternative data sampling.

References

- Abdo A. A., Ackermann M., Ajello M., Allafort A., Antolini E., Atwood W. B., Axelsson M., Baldini L., Ballet J., Barbiellini G., et al. 2010, ApJS, 188, 405
- Abdo A. A., Ackermann M., Ajello M., Atwood W. B., Axelsson M., Baldini L., Ballet J., Barbiellini G., Baring M. G., Bastieri D., et al. 2010, ApJS, 187, 460
- Addison P. S., 2002, The Illustrated Wavelet Transform Handbook: Introductory Theory and Applications in Science, Engineering, Medicine and Finance. IoP, Bristol and Philadelphia
- Argyle E., Gower J. F. R., 1972, ApJ, 175, L89
- Arons J., 1983, ApJ, 266, 215
- Arons J., 1993, ApJ, 408, 160
- Arons J., 2000, in M. Kramer, N. Wex, & R. Wielebinski ed., IAU Colloq. 177: Pulsar Astronomy - 2000 and Beyond Vol. 202 of Astronomical Society of the Pacific Conference Series, Pulsar Death at an Advanced Age. pp 449–+
- Arons J., Scharlemann E. T., 1979, ApJ, 231, 854
- Arzoumanian Z., Nice D. J., Taylor J. H., Thorsett S. E., 1994, ApJ, 422, 671
- Asgekar A., Deshpande A. A., 2005, MNRAS, 357, 1105
- Ashworth M., 1988, MNRAS, 230, 87
- Asseo E., Khechinashvili D., 2002, MNRAS, 334, 743
- Baade W., Zwicky F., 1934, Proc. Nat. Acad. Sci., 20, 259
- Backer D. C., 1970a, Nature, 227, 692
- Backer D. C., 1970b, Nature, 228, 1297
- Backer D. C., 1970c, Nature, 228, 42
- Backer D. C., Boriakoff V., Manchester R. N., 1973, Nature, 243, 77
- Backer D. C., Hellings R. W., 1986, Ann. Rev. Astr. Ap., 24, 537
- Baring M. G., 2004, Advances in Space Research, 33, 552
- Bartel N., Morris D., Sieber W., Hankins T. H., 1982, ApJ, 258, 776
- Becker W., Kramer M., Jessner A., Taam R. E., Jia J. J., Cheng K. S., Mignani R., Pellizzoni A., de Luca A., Słowikowska A., Caraveo P. A., 2006, ApJ, 645,

1421

- Becker W., Swartz D. A., Pavlov G. G., Elsner R. F., Grindlay J., Mignani R., Tennant A. F., Backer D., Pulone L., Testa V., Weisskopf M. C., 2003, *ApJ*, 594, 798
- Becker W., Weisskopf M. C., Tennant A. F., Jessner A., Dyks J., Harding A. K., Zhang S. N., 2004, *ApJ*, 615, 908
- Bedding T. R., Zijlstra A. A., Jones A., Foster G., 1998, *MNRAS*, 301, 1073
- Beskin V. S., 1982, *Soviet Ast.*, 26, 443
- Beskin V. S., Gurevich A. V., Istomin Y. N., 1993, Physics of the Pulsar Magnetosphere. Cambridge University Press
- Bhat N. D. R., Gupta Y., Kramer M., Karastergiou A., Lyne A. G., Johnston S., 2007, *A&A*, 462, 257
- Bhat N. D. R., Rao A. P., Gupta Y., 1999a, *ApJS*, 121, 483
- Bhat N. D. R., Rao A. P., Gupta Y., 1999b, *ApJ*, 514, 272
- Biggs J. D., 1992, in Hankins T. H., Rankin J. M., Gil J. A., eds, The Magnetospheric Structure and Emission Mechanisms of Radio Pulsars, IAU Colloquium 128 Meridional Compression of Radio Pulsar Beams. Pedagogical University Press, Zielona Góra, Poland, pp 22–25
- Blandford R. D., Applegate J. H., Hernquist L., 1983, *MNRAS*, 204, 1025
- Blandford R. D., Romani R. W., 1988, *MNRAS*, 234, 57P
- Boriakoff V., Ferguson D. C., Slater G., 1981, in Sieber W., Wielebinski R., eds, Pulsars, IAU Symposium 95 Pulsar microstructure quasi-periodicity. Reidel, Dordrecht, pp 199–204
- Box G. E. P., Jenkins G. M., 1976, in G. E. P. Box & G. M. Jenkins ed., Holden-Day Series in Time Series Analysis, Revised ed., San Francisco: Holden-Day, 1976 Time series analysis. Forecasting and control
- Buccheri R., Bennett K., Bignami G. F., Caraveo P. A., Bloemen J. B. G. M., Hermsen W., Boriakoff V., Kanbach G., Manchester J. L., Masnou J. L., 1983, *A&A*, 128, 245
- Burke-Spoliar S., Bailes M., 2010, *MNRAS*, 402, 855
- Burke-Spoliar S., Bailes M., Johnston S., Bates S. D., Bhat N. D. R., Burgay M., D'Amico N., Jameson A., Keith M. J., Kramer M., Levin L., Milia S., Possenti A., Stappers B., van Straten W., 2011, *MNRAS*, 416, 2465
- Burke-Spoliar S., Johnston S., Bailes M., Bates S. D., Bhat N. D. R., Burgay M., Champion D. J., D'Amico N., Keith M. J., Kramer M., Levin L., Milia S., Possenti A., Stappers B., van Straten W., 2012, *MNRAS*, p. 2900
- Cairns I. H., 2004, *ApJ*, 610, 948
- Cairns I. H., Johnston S., Das P., 2001, *ApJ*, 563, L65

- Camilo F., Ransom S. M., Chatterjee S., Johnston S., Demorest P., 2012, ApJ, 746, 63
- Chen J. L., Wang H. G., Wang N., Lyne A., Liu Z. Y., Jessner A., Yuan J. P., Kramer M., 2011, ApJ, 741, 48
- Chen K., Ruderman M., 1993, ApJ, 408, 179
- Chen W. C., Li X. D., 2006, A&A, 450, L1
- Cheng A. F., Ruderman M., 1977, ApJ, 212, 800
- Cheng A. F., Ruderman M. A., 1980, ApJ, 235, 576
- Cheng K. S., Gil J., Zhang L., 1998, ApJL, 493, L35
- Cheng K. S., Ho C., Ruderman M., 1986a, ApJ, 300, 500
- Cheng K. S., Ho C., Ruderman M., 1986b, ApJ, 300, 522
- Chukwude A. E., Baiden A. A., Onuchukwu C. C., 2010, A&A, 515, A21+
- Clegg A. W., Fiedler R. L., Cordes J. M., 1993, ApJ, 409, 691
- Cole T. W., Hesse H. K., Page C. G., 1970, Nature, 225, 712
- Contopoulos I., 2005, A&A, 442, 579
- Contopoulos I., 2007, A&A, 466, 301
- Contopoulos I., Kazanas D., Fendt C., 1999, ApJ, 511, 351
- Cordes J. M., 1978, ApJ, 222, 1006
- Cordes J. M., 1979, Space Sci. Rev., 24, 567
- Cordes J. M., 1993, in Phillips J. A., Thorsett S. E., Kulkarni S. R., eds, Planets around Pulsars The detectability of planetary companions to radio pulsars. Astron. Soc. Pac. Conf. Ser. Vol. 36, pp 43–60
- Cordes J. M., Downs G. S., 1985, ApJS, 59, 343
- Cordes J. M., Lazio T. J. W., 2002, ArXiv Astrophysics e-prints
- Cordes J. M., Shannon R. M., 2008, ApJ, 682, 1152
- Cordes J. M., Shannon R. M., 2010, ArXiv e-prints
- Craft H. D., Comella J. M., Drake F., 1968, Nature, 218, 1122
- Craft H. D., Lovelace R. V. E., Sutton J. M., , 1968
- Daubechies I., 1992, Ten Lectures On Wavelets. Society for Industrial and Applied Mathematics, Philadelphia
- Daugherty J. K., Harding A. K., 1986, ApJ, 309, 362
- Daugherty J. K., Harding A. K., 1996, ApJ, 458, 278
- Davis M. M., Taylor J. H., Weisberg J. M., Backer D. C., 1985, Nature, 315, 547
- Deich W. T. S., Cordes J. M., Hankins T. H., Rankin J. M., 1986, ApJ, 300, 540
- Demorest P. B., Pennucci T., Ransom S. M., Roberts M. S. E., Hessels J. W. T., 2010, Nature, 467, 1081

REFERENCES

- Deshpande A. A., Rankin J. M., 2001, MNRAS, 322, 438
- Deutsch A. J., 1955, Annales d'Astrophysique, 18, 1
- Drake F. D., Craft H. D., 1968, Nature, 220, 231
- Dyks J., Rudak B., 2003, ApJ, 598, 1201
- Dyks J., Zhang B., Gil J., 2005, ApJ, 626, L45
- Edwards R. T., Stappers B. W., 2002, A&A, 393, 733
- Edwards R. T., Stappers B. W., 2003, A&A, 407, 273
- Edwards R. T., Stappers B. W., van Leeuwen A. G. J., 2003, A&A, 402, 321
- Efron B., 1979, The Annals of Statistics, 7, 1
- Esamdin A., Lyne A. G., Graham-Smith F., Kramer M., Manchester R. N., Wu X., 2005, MNRAS, 356, 59
- Espinoza C. M., Lyne A. G., Kramer M., Manchester R. N., Kaspi V. M., 2011, ApJL, 741, L13+
- Everett J. E., Weisberg J. M., 2001, ApJ, 553, 341
- Filippenko A. V., Radhakrishnan V., 1982, ApJ, 263, 828
- Flowers E., Ruderman M. A., 1977, ApJ, 215, 302
- Force M. M., Rankin J. M., 2010, MNRAS, 406, 237
- Foster G., 1996, Astron. J., 112, 1709
- Frescura F., Flanagan C. S., 2003, in M. Bailes, D. J. Nice, & S. E. Thorsett ed., Radio Pulsars Vol. 302 of Astronomical Society of the Pacific Conference Series, Precession in Pulsars. pp 237–+
- Fung P. K., Khechinashvili D., Kuijpers J., 2006, A&A, 445, 779
- Gabor D., 1946, J. Inst. Electr. Eng., 93, 429
- Geppert U., Rheinhardt M., 2002, A&A, 392, 1015
- Geppert U., Rheinhardt M., Gil J., 2003, A&A, 412, L33
- Gil J., Haberl F., Melikidze G., Geppert U., Zhang B., Melikidze Jr. G., 2008, ApJ, 686, 497
- Gil J., Melikidze G., Zhang B., 2006, ApJ, 650, 1048
- Gil J., Melikidze G. I., Geppert U., 2003, A&A, 407, 315
- Gil J., Mitra D., 2001, ApJ, 550, 383
- Gil J. A., Jessner A., Kijak J., Kramer M., Malofeev V., Malov I., Seiradakis J. H., Sieber W., Wielebinski R., 1994, A&A, 282, 45
- Gil J. A., Melikidze G. I., Mitra D., 2002, A&A, 388, 235
- Gil J. A., Sendyk M., 2000, ApJ, 541, 351
- Glendenning N. K., 2000, Compact stars : nuclear physics, particle physics, and general relativity. Springer, New York

- Goldreich P., Julian W. H., 1969, ApJ, 157, 869
- Goldreich P., Reisenegger A., 1992, ApJ, 395, 250
- Gruzinov A., 1999, ArXiv Astrophysics e-prints
- Guillemot L., Johnson T. J., Venter C., Kerr M., Pancrazi B., Livingstone M., Janssen G. H., Jaroenjittichai P., Kramer M., Cognard I., Stappers B. W., Harding A. K., et al. 2012, ApJ, 744, 33
- Gunn J. E., Ostriker J. P., 1969, Nature, 221, 454
- Gupta Y., Gil J., Kijak J., Sendyk M., 2004, A&A, 426, 229
- Gwinn C. R., Taylor J. H., Weisberg J. M., Rawley L. A., 1986, AJ, 91, 338
- Haberl F., Schwope A. D., Hambaryan V., Hasinger G., Motch C., 2003, A&A, 403, L19
- Hall P., 1992, The Bootstrap and Edgeworth Expansion. Springer-Verlag, New York
- Hankins T. H., 1971, ApJ, 169, 487
- Hankins T. H., Eilek J. A., 2007, ApJ, 670, 693
- Hankins T. H., Kern J. S., Weatherall J. C., Eilek J. A., 2003, Nature, 422, 141
- Harding A. K., Contopoulos I., Kazanas D., 1999, ApJ, 525, L125
- Helpman D. J., Manchester R. N., Taylor J. H., 1975, ApJ, 198, 661
- Hesse K. H., Wielebinski R., 1974, A&A, 31, 409
- Hewish A., Bell S. J., Pilkington J. D. H., Scott P. F., Collins R. A., 1968, Nature, 217, 709
- Hirotani K., 2008, ApJL, 688, L25
- Hobbs G., Lyne A., Kramer M., 2006, Chin. J. Astron. Astrophys., Suppl. 2, 6, 169
- Hobbs G., Lyne A. G., Kramer M., 2010, MNRAS, 402, 1027
- Hobbs G., Lyne A. G., Kramer M., Martin C. E., Jordan C., 2004, MNRAS, 353, 1311
- Hobbs G. B., Edwards R. T., Manchester R. N., 2006, MNRAS, 369, 655
- Högbom J. A., 1974, A&AS, 15, 417
- Hotan A. W., van Straten W., Manchester R. N., 2004, PASA, 21, 302
- Hui C. Y., Becker W., 2007, A&A, 467, 1209
- Illarionov A. F., Sunyaev R. A., 1975, A&A, 39, 185
- Istomin Y. N., Sobyanin D. N., 2011, Astronomy Letters, 37, 468
- Jackson J. D., 1962, Classical Electrodynamics. Wiley
- Janssen G. H., Stappers B. W., Kramer M., Nice D. J., Jessner A., Cognard I., Purver M. B., 2008, A&A, 490, 753

REFERENCES

- Johnston S., Galloway D., 1999, MNRAS, 306, L50
- Johnston S., Romani R., 2002, MNRAS, 332, 109
- Johnston S., van Straten W., Kramer M., Bailes M., 2001, ApJ, 549, L101
- Jones P. B., 1988, MNRAS, 233, 875
- Jones P. B., 2011, MNRAS, 414, 759
- Kalapotharakos C., Contopoulos I., 2009, A&A, 496, 495
- Kalapotharakos C., Kazanas D., Harding A., Contopoulos I., 2011, ArXiv e-prints
- Kargaltsev O., Pavlov G. G., Garmire G. P., 2006, ApJ, 646, 1139
- Karuppusamy R., Stappers B. W., Lee K. J., 2012, A&A, 538, A7
- Karuppusamy R., Stappers B. W., van Straten W., 2010, A&A, 515, A36+
- Kaspi V. M., 2010, Proceedings of the National Academy of Science, 107, 7147
- Keane E. F., 2010, PhD thesis, The University of Manchester
- Keane E. F., Kramer M., 2008, MNRAS, 391, 2009
- Keane E. F., Kramer M., Lyne A. G., Stappers B. W., McLaughlin M. A., 2011, MNRAS, 415, 3065
- Keane E. F., Ludovici D. A., Eatough R. P., Kramer M., Lyne A. G., McLaughlin M. A., Stappers B. W., 2010, MNRAS, 401, 1057
- Keane E. F., McLaughlin M. A., 2011, Bulletin of the Astronomical Society of India, 39, 333
- Kloumann I. M., Rankin J. M., 2010, MNRAS, 408, 40
- Knight H. S., 2007, MNRAS, 378, 723
- Komissarov S. S., 2002, MNRAS, 336, 759
- Komissarov S. S., 2006, MNRAS, 367, 19
- Kramer M., 2008, in C. Bassa, Z. Wang, A. Cumming, & V. M. Kaspi ed., 40 Years of Pulsars: Millisecond Pulsars, Magnetars and More Vol. 983 of AIPC, Observations of Pulsed Emission from Pulsars. pp 11–19
- Kramer M., 2009, in IAU Symposium Vol. 259 of IAU Symposium, Pulsars Magnetars. pp 485–492
- Kramer M., Johnston S., van Straten W., 2002, MNRAS, 334, 523
- Kramer M., Lyne A. G., O'Brien J. T., Jordan C. A., Lorimer D. R., 2006, Science, 312, 549
- Kuijpers J. M. E., 2009, in W. Becker ed., Astrophysics and Space Science Library Vol. 357 of Astrophysics and Space Science Library, Physics of Drifting Sub-pulses in Radio Pulsars. p. 543
- Kuzmin A. D., 2007, Ap&SS, 308, 563
- Kuzmin A. D., Ershov A. A., 2004, A&A, 427, 575
- Labrecque D. R., Rankin J. M., Cordes J. M., 1994, AJ, 108, 1854

- Lange C., Kramer M., Wielebinski R., Jessner A., 1998, A&A, 332, 111
- Lattimer J. M., Prakash M., 2007, Phys. Rep., 442, 109
- Lee K. J., Du Y. J., Wang H. G., Qiao G. J., Xu R. X., Han J. L., 2010, MNRAS, 405, 2103
- Li J., Spitkovsky A., Tchekhovskoy A., 2012a, ArXiv e-prints
- Li J., Spitkovsky A., Tchekhovskoy A., 2012b, ApJ, 746, 60
- Li X.-H., Lu F.-J., Li Z., 2008, ApJ, 682, 1166
- Link B., 2006, A&A, 458, 881
- Liu K., Keane E. F., Lee K. J., Kramer M., Cordes J. M., Purver M. B., 2012, MNRAS, 420, 361
- Livingstone M. A., Kaspi V. M., Gavriil F. P., Manchester R. N., Gotthelf E. V. G., Kuiper L., 2007, Astrophys. Space Sci., 308, 317
- Lommen A. N., Zepka A., Backer D. C., McLaughlin M., Cordes J. M., Arzoumanian Z., Xilouris K., 2000, ApJ, 545, 1007
- Lorimer D. R., 1994, PhD thesis, The University of Manchester
- Lorimer D. R., 2008, Living Reviews in Relativity, 11, 8
- Lorimer D. R., Faulkner A. J., Lyne A. G., Manchester R. N., Kramer M., McLaughlin M. A., Hobbs G., Possenti A., Stairs I. H., Camilo F., Burgay M., D'Amico N., Corongiu A., Crawford F., 2006, MNRAS, 372, 777
- Lorimer D. R., Kramer M., 2005, Handbook of Pulsar Astronomy. Cambridge University Press
- Lundgren S. C., Cordes J. M., Ulmer M., Matz S. M., Lomatch S., Foster R. S., Hankins T., 1995, ApJ, 453, 433
- Lyne A., 1999 Glitches and Timing Noise. p. 141
- Lyne A., Hobbs G., Kramer M., Stairs I., Stappers B., 2010, Science, 329, 408
- Lyne A. G., Ashworth M., 1983, MNRAS, 204, 519
- Lyne A. G., Pritchard R. S., Graham-Smith F., Camilo F., 1996, Nature, 381, 497
- Lyne A. G., Pritchard R. S., Shemar S. L., 1995, J. Astrophys. Astr., 16, 179
- Lyne A. G., Pritchard R. S., Smith F. G., 1993, MNRAS, 265, 1003
- Lyne A. G., Shemar S. L., Smith F. G., 2000, MNRAS, 315, 534
- Lyne A. G., Smith F. G., 2006, Pulsar Astronomy, 3rd ed.. Cambridge University Press, Cambridge
- Maciesiak K., Gil J., 2011, MNRAS, 417, 1444
- Mallat S., 1999, A Wavelet Tour of Signal Processing, 2nd ed.. Academic Press
- Malov I. F., 2007, Astronomy Reports, 51, 477
- Manchester R. N., Hobbs G. B., Teoh A., Hobbs M., 2005, AJ, 129, 1993

REFERENCES

- Manchester R. N., Taylor J. H., 1977, Pulsars. Freeman, San Francisco
- Maron O., Kijak J., Kramer M., Wielebinski R., 2000, A&AS, 147, 195
- Matsakis D. N., Taylor J. H., Eubanks T. M., 1997, A&A, 326, 924
- McLaughlin M. A., Cordes J. M., 2003, ApJ, 596, 982
- McLaughlin M. A., Lyne A. G., Lorimer D. R., Kramer M., Faulkner A. J., Manchester R. N., Cordes J. M., Camilo F., Possenti A., Stairs I. H., Hobbs G., D'Amico N., Burgay M., O'Brien J. T., 2006, Nature, 439, 817
- Mdzinarishvili T. G., Melikidze G. I., 2004, A&A, 425, 1009
- Melatos A., Peralta C., Wyithe J. S. B., 2008, ApJ, 672, 1103
- Melikidze G., Gil J., 2006, Chinese Journal of Astronomy and Astrophysics Supplement, 6, 020000
- Meyer D. M., Lauroesch J. T., 1999, ApJ, 520, L103
- Michel F. C., 1982, Reviews of Modern Physics, 54, 1
- Miralles J. A., Pons J. A., Urpin V. A., 2000, ApJ, 543, 1001
- Muslimov A. G., Harding A. K., 2003, ApJ, 588, 430
- Muslimov A. G., Harding A. K., 2004, ApJ, 606, 1143
- O'Brien J. T., Kramer M., Lyne A. G., Lorimer D. R., Jordan C. A., 2006, Chinese Journal of Astronomy and Astrophysics Supplement, 6, 020000
- Ostriker J. P., Gunn J. E., 1969, ApJ, 157, 1395
- Otazu X., Ribó M., Paredes J. M., Peracaula M., Núñez J., 2004, MNRAS, 351, 215
- Pacini F., 1967, Nature, 216, 567
- Page C. G., 1973, MNRAS, 163
- Palliyaguru N. T., McLaughlin M. A., Keane E. F., Kramer M., Lyne A. G., Lorimer D. R., Manchester R. N., Camilo F., Stairs I. H., 2011, MNRAS, 417, 1871
- Papoulis A., 1962, The Fourier Integral and Its Applications. New York: McGraw-Hill
- Petrova S. A., 2004, A&A, 417, L29
- Politis, D.N. Romano, J.P. Wolf, M. 1999, Subsampling. Springer-Verlag, New York
- Popov M. V., Bartel N., Cannon W. H., Novikov A. Y., Kondratiev V. I., Altunin V. I., 2002, A&A, pp 171–187
- Porat B., 1997, A Course In Digital Signal Processing. John Wiley & Sons, Inc.
- Press W. H., Teukolsky S. A., Vetterling W. T., Flannery B. P., 1992, Numerical Recipes: The Art of Scientific Computing, 2nd edition. Cambridge University Press, Cambridge

- Purver M. B., 2010, PhD thesis, The University of Manchester
- Qiao G. J., Zhang B., 1996, A&A, 306, L5+
- Radhakrishnan V., Cooke D. J., Komesaroff M. M., Morris D., 1969, Nature, 221, 443
- Rankin J. M., 1986, ApJ, 301, 901
- Rankin J. M., Ramachandran R., van Leeuwen J., Suleymanova S. A., 2006, A&A, 455, 215
- Rankin J. M., Wright G. A. E., 2007, MNRAS, 379, 507
- Rankin J. M., Wright G. A. E., 2008, MNRAS, 385, 1923
- Rathnasree N., Rankin J. M., 1995, ApJ, 452, 814
- Rea N., Kramer M., Stella L., Jonker P. G., Bassa C. G., Groot P. J., Israel G. L., Méndez M., Possenti A., Lyne A., 2008, MNRAS, 391, 663
- Redman S. L., Wright G. A. E., Rankin J. M., 2005, MNRAS, 357, 859
- Rheinhardt M., Konenkov D., Geppert U., 2004, A&A, 420, 631
- Rickett B. J., 1977, Ann. Rev. Astr. Ap., 15, 479
- Rickett B. J., 1990, Ann. Rev. Astr. Ap., 28, 561
- Rickett B. J., Coles W. A., Bourgois G., 1984, A&A, 134, 390
- Rickett B. J., Hankins T. H., Cordes J. M., 1975, ApJ, 201, 425
- Ritchings R. T., 1976, MNRAS, 176, 249
- Romani R., Johnston S., 2001, ApJ, 557, L93
- Rosen R., McLaughlin M. A., Thompson S. E., 2011, ApJL, 728, L19
- Ruderman M., 2005, ArXiv Astrophysics e-prints
- Ruderman M. A., Sutherland P. G., 1975, ApJ, 196, 51
- Sallmen S., Backer D. C., 1995, in Fruchter A. S., Tavani M., Backer D. C., eds, Millisecond Pulsars: A Decade of Surprise Single pulse statistics for PSR 1534+12 and PSR 1937+21. Astron. Soc. Pac. Conf. Ser. Vol. 72, pp 340–342
- Sallmen S., Backer D. C., Hankins T. H., Moffett D., Lundgren S., 1999, ApJ, 517, 460
- Scargle J. D., 1982, ApJ, 263, 835
- Scheuer P. A. G., 1968, Nature, 218, 920
- Sedrakian A., Wasserman I., Cordes J. M., 1999, ApJ, 524, 341
- Serylak M., 2011, PhD thesis, The University of Amsterdam
- Serylak M., Stappers B. W., Weltevrede P., Kramer M., Jessner A., Lyne A. G., Jordan C. A., Lazaridis K., Zensus J. A., 2009, MNRAS, 394, 295
- Shalybkov D. A., Urpin V. A., 1997, A&A, 321, 685

REFERENCES

- Shao, J. Tu, D. 1995, The Jackknife and the Bootstrap. Springer-Verlag, New York
- Shao, J. Wu, C.F. 1989, Annals of Statistics, 17, 1176
- Shapiro I. I., 1964, Phys. Rev. Lett., 13, 789
- Shapiro S. L., Teukolsky S. A., 1983, Black Holes, White Dwarfs and Neutron Stars. The Physics of Compact Objects. Wiley–Interscience, New York
- Shearer A., Stappers B., O'Connor P., Golden A., Strom R., Redfern M., Ryan O., 2003, Science, 301, 493
- Smith F. G., 2003, Reports on Progress in Physics, 66, 173
- Spitkovsky A., 2006, ApJ, 648, L51
- Spruit H. C., 2008, in C. Bassa, Z. Wang, A. Cumming, & V. M. Kaspi ed., 40 Years of Pulsars: Millisecond Pulsars, Magnetars and More Vol. 983 of American Institute of Physics Conference Series, Origin of neutron star magnetic fields. pp 391–398
- Stella L., Campana S., Colpi M., Mereghetti S., Tavani M., 1994, ApJL, 423, L47
- Stella L., White N. E., Rosner R., 1986, ApJ, 308, 669
- Sturrock P. A., 1971, ApJ, 164, 529
- Sun X. H., Han J. L., 2004, MNRAS, 350, 232
- Tagliaferri R., Ciaramella A., Barone F., Longo G., Milano L., 2001, in A. J. Banday, S. Zaroubi, & M. Bartelmann ed., Mining the Sky Neural Networks for Spectral Analysis of Unevenly Sampled Data. p. 386
- Takata J., Cheng K. S., Taam R. E., 2012, ApJ, 745, 100
- Taylor J. H., Manchester R. N., 1977, ApJ, 215, 885
- Taylor J. H., Manchester R. N., Huguenin G. R., 1975, ApJ, 195, 513
- Templeton M., 2004, Journal of the American Association of Variable Star Observers (AAVSO), 32, 41
- Templeton M. R., Mattei J. A., Willson L. A., , 2005, Secular Evolution in Mira Variable Pulsations
- Tepedelenlioğlu E., Ögelman H., 2005, ApJL, 630, L57
- Thorsett S. E., Dewey R. J., 1993, ApJ, 419, L65
- Timokhin A. N., 2006, MNRAS, 368, 1055
- Timokhin A. N., 2010, MNRAS, pp L133+
- Tukey J., 1958, Annals of Statistics, 29, 614
- Tutukov A. V., 2005, Astronomy Reports, 49, 548
- Urpin V., Gil J., 2004, A&A, 415, 305
- Urpin V. A., Muslimov A. G., 1992, MNRAS, 256, 261
- van Leeuwen A. G. J., Kouwenhoven M. L. A., Ramachandran R., Rankin J. M.,

- Stappers B. W., 2002, A&A, 387, 169
- van Leeuwen A. G. J., Stappers B. W., Ramachandran R., Rankin J. M., 2003, A&A, 399, 223
- van Leeuwen J., Stappers B. W., 2010, A&A, 509, A7
- van Leeuwen J., Timokhin A. N., 2012, ArXiv e-prints
- Venter C., Johnson T. J., Harding A. K., 2012, ApJ, 744, 34
- Viganò D., Pons J. A., Miralles J. A., 2011, A&A, 533, A125
- Wada T., Shibata S., 2011, MNRAS, 418, 612
- Wang N., Manchester R. N., Johnston S., 2007, MNRAS, 377, 1383
- Wang N., Manchester R. N., Johnston S., Rickett B., Zhang J., Yusup A., Chen M., 2005, MNRAS, 358, 270
- Watters K. P., Romani R. W., 2011, ApJ, 727, 123
- Watters K. P., Romani R. W., Weltevrede P., Johnston S., 2009, ApJ, 695, 1289
- Welch P. D., 1967, IEEE Trans. Audio Electroacoustics, 15, 70
- Weltevrede P., Edwards R. T., Stappers B. W., 2006, A&A, 445, 243
- Weltevrede P., Johnston S., Espinoza C. M., 2011, MNRAS, 411, 1917
- Weltevrede P., Stappers B. W., Edwards R. T., 2007, A&A, 469, 607
- Weltevrede P., Stappers B. W., Rankin J. M., Wright G. A. E., 2006, ApJ, 645, L149
- Weltevrede P., Wright G. A. E., Stappers B. W., Rankin J. M., 2006, A&A, 458, 269
- Wright G. A. E., 1981, MNRAS, 196, 153
- Wu F., Xu R. X., Gil J., 2003, A&A, 409, 641
- Xu R. X., Qiao G. J., 2001, ApJL, 561, L85
- Young M. D., Manchester R. N., Johnston S., 1999, Nature, 400, 848
- Zhang B., Gil J., 2005, A&A, 631, L143
- Zhang B., Gil J., Dyks J., 2007, MNRAS, 374, 1103
- Zhang B., Harding A. K., 2000, ApJ, 535, L51
- Zhang B., Harding A. K., Muslimov A. G., 2000, ApJ, 531, L135
- Zhang B., Qiao G. J., Lin W. P., Han J. L., 1997, ApJ, 478, 313
- Zhang B., Sanwal D., Pavlov G. G., 2005, ApJL, 624, L109
- Zhong C.-X., Yang T.-G., 2007, Chinese Astronomy and Astrophysics, 31, 443
- Zoubir, A.M. Iskander, D.R. 2004, Bootstrap Techniques for Signal Processing. Cambridge University Press, Cambridge